

**FACILE SYNTHESIS OF PLASMONIC NANOMATERIALS WITH  
IMPROVED CHARACTERISTICS FOR BIO-PHOTONIC  
APPLICATIONS**

**Thesis Submitted to AcSIR for the Award of the Degree of  
DOCTOR OF PHILOSOPHY  
in Chemical Sciences**



**By**

**SAJITHA M. J.**

**Registration No: 10CC14J39006**

**Under the guidance of**

**Dr. K. YOOSAF**



**CSIR-NATIONAL INSTITUTE FOR INTERDISCIPLINARY  
SCIENCE AND TECHNOLOGY (CSIR-NIIST)  
THIRUVANANTHAPURAM-695 019, KERALA, INDIA**

**September, 2019**

*Dedicated to*

*My Beloved Family and*

*Friends*

## DECLARATION

I hereby declare that the matter embodied in the thesis entitled: “*Facile Synthesis of Plasmonic Nanomaterials with Improved Characteristics for Bio-Photonic Applications*” is the result of the investigations carried out by me at the Photosciences and Photonics Section, Chemical Sciences and Technology Division, CSIR-National Institute for Interdisciplinary Science and Technology (CSIR-NIIST), Thiruvananthapuram, under the supervision of Dr. K. Yoosaf and the same has not been submitted elsewhere for any other degree.

In keeping with the general practice of reporting scientific observations, due acknowledgement has been made wherever the work described is based on the findings of other investigators.



**Sajitha M.J.**



CSIR- NATIONAL INSTITUTE FOR INTERDISCIPLINARY SCIENCE AND TECHNOLOGY

सी एस आर-राष्ट्रीय अंतर्विषयी विज्ञान तथा प्रौद्योगिकी संस्थान

Council of Scientific & Industrial Research

वैज्ञानिक तथा औद्योगिक अनुसंधान परिषद

Industrial Estate P. O., Trivandrum – 695 019, Kerala, INDIA

Tel : 91-471-2515477 (O) Fax : +91-471-2490186 / 2491712

E-mail: [voosafk@gmail.com](mailto:voosafk@gmail.com), [voosafk@niist.res.in](mailto:voosafk@niist.res.in)



AcSIR

Dr. K. YOOSAF

SENIOR SCIENTIST

Chemical Sciences & Technology Division

September 25, 2019

### CERTIFICATE

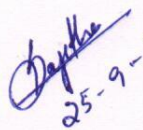
This is to certify that the work embodied in the thesis entitled, “*Facile Synthesis of Plasmonic Nanomaterials with Improved Characteristics for Bio-Photonic Applications*” submitted by **Ms. Sajitha M. J.** to Academy of Scientific and Innovative Research (AcSIR), in partial fulfilment of the requirements for the award of the **Degree of Doctor of Philosophy in Chemical Sciences**, has been carried out under my supervision and guidance at the Chemical Sciences and Technology Division of the CSIR-National Institute for Interdisciplinary Science and Technology (CSIR-NIIST), Thiruvananthapuram. I further certify that this work has not been submitted to any other University or Institution in part or full for the award of any degree or diploma.

डॉ. युसफ करुवाथ / Dr. YOOSAF KARUVATH

वरिष्ठ वैज्ञानिक / Senior Scientist

रसायन विज्ञान तथा प्रौद्योगिकी प्रभाग  
Chemical Sciences & Technology Division

सी एस आर- राष्ट्रीय अंतर्विषयी विज्ञान तथा प्रौद्योगिकी संस्थान  
CSIR-National Institute for Interdisciplinary  
Science and Technology, Govt. of India  
तिरुवनन्तपुरम / Thiruvananthapuram-695 019, Kerala

  
25-9-19  
SAJITHA M. J.





K. Yoosaf

(Thesis Supervisor)



## **ACKNOWLEDGEMENTS**

*I have great pleasure in placing on record my deep sense of gratitude to my research supervisor, Dr. K. Yoosaf, for suggesting the research problem, for his valuable guidance, support and encouragement, leading to the successful completion of this work.*

*I would like to express my sincere thanks to Professor M. V. George for his encouragement, inspiration and motivation the tenure of this work.*

*I thank Dr. A. Ajayaghosh, Director, Dr. Suresh Das, former Director and Dr. Gangan Pratap, former Acting Director of the CSIR-National Institute for Interdisciplinary Science and Technology (NIIST), Thiruvananthapuram, for providing the necessary facilities for carrying out this work.*

*My sincere thanks are also due to:*

❖ *Dr. P. Sujatha Devi, Head, Chemical Sciences and Technology Division, CSIR-National Institute for Interdisciplinary Science and Technology (NIIST), Dr. C. H. Suresh, AcSIR co-ordinator and Dr. R. Luxmi Varma and Dr. Mangalam S. Nair, former AcSIR co-ordinator.*

❖ *Dr. K. George Thomas, Dr. D. Ramaiah, Dr. K. R. Gopidas, Dr. D. Ramaiah, Dr. J. D. Sudha, Dr. Biswapriya Deb, Dr. V. Karunakaran, Dr. Suraj Soman and Dr. V. K. Praveen present and former scientists of the Photosciences and Photonics Section, Chemical Sciences and Technology Division, for their help and support.*

❖ *Dr. Narayanan Unni K.N., Dr. Joshy Joseph and Dr. C. Vijayakumar, my DAC members.*

❖ *Dr. K. K. Maiti, Dr. Nisha N., Mrs. Saranya Giridharan for biological studies.*

❖ *Mr. Robert Philip and Mr. M. Kiran for TEM analysis.*

❖ *Mr. M. Aswin for AFM and Mr. N. Prathviraj for XRD analyses.*

- ❖ *Group members, Dr. Arun Gopi, Mrs. Vindhya S., Mr. Renjith, Mr. Listo V., Mrs. Reethu H., Ms. Bamisha B., Mrs. Neethu, Ms. Raji, Mr. Sanoop and Mr. Sree Nandhu*
- ❖ *Project students Mrs. K.C. Sharika, Mrs. S. Anjali, and Mrs. C. Rasitha, for their help and cooperation.*
- ❖ *My friends: Mr. M. Sreejith, Mrs. A. Silja, Mrs. P. Gayathri, Mr. K. V. Sandeepa, Mr. K. C. Naeem, Mr. T. Shameel, Mr. Mathews Manayani and Mrs. Athira, Mrs. I. Vijitha, for their constant help, inspiration and support.*
- ❖ *All other members of Photosciences and Photonics section, and friends at CSIR-NIIST, Thiruvananthapuram for their help.*
- ❖ *All my classmates for their love and inspiration.*
- ❖ *Council of Scientific and Industrial Research (CSIR) for financial assistance.*

*I am deeply grateful to my parents for their constant source of love and support which have been great inspiration for these efforts. I would like to thank my husband (Sumith), and my family members for their excellent support, understanding and encouragement. I take this opportunity to pay respect to my parents and teachers starting from my school days to those at NIIST, who motivated and blessed me. Without them I would not be in this present situation. With my whole heart I owe them what I am. Finally, I thank God for having given me everything.*

**Sajitha M.J.**

## CONTENTS

	<b>Page</b>
<b>Declaration</b>	<b>i</b>
<b>Certificate</b>	<b>ii</b>
<b>Acknowledgements</b>	<b>iii</b>
<b>Preface</b>	<b>xxix</b>
<b><i>Chapter 1. Plasmonic nanostructures and their bio-applications: An overview</i></b>	
<b>1.1.</b> General introduction to nanoscience and nanotechnology	<b>1</b>
<b>1.2.</b> Plasmonic nanostructures	<b>2</b>
<b>1.2.1.</b> Plasmonic metal nanoparticles	<b>2</b>
<b>1.3.</b> Surface plasmon resonance	<b>3</b>
<b>1.3.1.</b> Factors affecting SPR	<b>4</b>
<b>1.3.1.1.</b> Size	<b>4</b>
<b>1.3.1.2.</b> Shape	<b>5</b>
<b>1.4.</b> Plasmonic sensors	<b>7</b>
<b>1.4.1.</b> Colorimetric detection	<b>8</b>
<b>1.4.2.</b> Surface plasmon resonance sensors	<b>9</b>
<b>1.4.3.</b> Fluorescent sensors	<b>10</b>
<b>1.4.4.</b> Electrochemical sensors	<b>11</b>
<b>1.5.</b> Anisotropic nanomaterials	<b>12</b>
<b>1.5.1.</b> Importance of anisotropic nanoparticles	<b>12</b>
<b>1.5.1.1.</b> High extinction coefficient	<b>12</b>
<b>1.5.1.2.</b> High scattering efficiency	<b>14</b>



<b>1.6.</b>	Localization of fields	<b>15</b>
<b>1.6.1.</b>	Impacts of field localization	<b>16</b>
<b>1.6.1.1.</b>	Absorption and fluorescence	<b>16</b>
<b>1.6.1.2.</b>	Raman spectroscopy	<b>17</b>
<b>1.6.1.2.1.</b>	Principle of Raman scattering	<b>19</b>
<b>1.6.1.2.2.</b>	Pros and cons	<b>19</b>
<b>1.6.1.3.</b>	Surface-Enhanced Raman Scattering (SERS)	<b>20</b>
<b>1.6.1.3.1.</b>	Enhancement mechanism in SERS	<b>20</b>
<b>1.6.1.3.2.</b>	Factors affecting SERS	<b>21</b>
<b>1.7.</b>	Applications of anisotropic nanomaterials	<b>24</b>
<b>1.7.1.</b>	Bio-imaging	<b>24</b>
<b>1.7.2.</b>	Photothermal cancer therapy	<b>25</b>
<b>1.8.</b>	Synthesis of metal nanoparticles	<b>27</b>
<b>1.8.1.</b>	Synthesis of anisotropic nanostructures	<b>28</b>
<b>1.8.1.1.</b>	Synthesis of gold nanorods	<b>30</b>
<b>1.8.1.2.</b>	Synthesis of gold nanostar	<b>31</b>
<b>1.8.1.3.</b>	Growth mechanism of AuNRs	<b>33</b>
<b>1.9.</b>	SERS substrates	<b>34</b>
<b>1.10.</b>	The objective of the present work	<b>38</b>
<b>1.11</b>	References	<b>38</b>
 <b><i>Chapter 2. Synthesis of biocompatible gold nanorods and its application in cancer nanotheranostics</i></b>		
<b>2.1.</b>	Abstract	<b>50</b>
<b>2.2.</b>	Introduction	<b>51</b>

<b>2.2.1.</b>	<b>Synthetic approaches</b>	<b>52</b>
<b>2.2.1.1.</b>	<b>The major challenges</b>	<b>54</b>
<b>2.2.1.1.1.</b>	<b>Need for the high concentration of CTAB</b>	<b>54</b>
<b>2.2.1.1.2.</b>	<b>Demerits of post-synthetic method</b>	<b>55</b>
<b>2.2.1.2.</b>	<b>New synthetic strategies</b>	<b>56</b>
<b>2.3.</b>	<b>Experimental section</b>	<b>58</b>
<b>2.3.1.</b>	<b>Materials and method</b>	<b>58</b>
<b>2.3.2.</b>	<b>Characterization</b>	<b>58</b>
<b>2.3.3.</b>	<b>Synthesis of gold nanorods</b>	<b>60</b>
<b>2.4.</b>	<b>Results and discussion</b>	<b>62</b>
<b>2.4.1.</b>	<b>Characterization of seed</b>	<b>62</b>
<b>2.4.2.</b>	<b>Absorption and morphological characterization of AuNRs</b>	<b>63</b>
<b>2.4.3.</b>	<b>The effect of seed nanoparticles</b>	<b>65</b>
<b>2.4.4.</b>	<b>The effect of AgNO<sub>3</sub></b>	<b>67</b>
<b>2.4.5.</b>	<b>Studies on reducing CTAB concentration in AuNRs synthesis</b>	<b>68</b>
<b>2.4.6.</b>	<b>Morphological studies</b>	<b>70</b>
<b>2.4.7.</b>	<b>Mechanism of AuNRs formation</b>	<b>71</b>
<b>2.4.7.1.</b>	<b>Crystallographic studies</b>	<b>71</b>
<b>2.4.7.2.</b>	<b>Growth kinetics studies</b>	<b>73</b>
<b>2.4.8.</b>	<b>Implications</b>	<b>77</b>
<b>2.4.8.1.</b>	<b>Wider tunable LSPR band</b>	<b>77</b>
<b>2.4.8.2.</b>	<b>Studies on bioavailability</b>	<b>79</b>
<b>2.4.9.</b>	<b>Nanophotonic enhancements</b>	<b>80</b>

2.4.9.1.	Photon to thermal conversion efficiency	80
2.4.9.2.	Signal enhancement of Raman scattering	81
2.4.10.	Application in bio-photonics	82
2.4.10.1.	Photothermal therapy studies on cancer cells	82
2.4.10.2.	SERS fingerprinting on cancerous cells	83
2.5.	Conclusion	84
2.6.	References	85
<b><i>Chapter 3. Developing one-pot synthetic route for multi-branched gold nanocrystals for bio-photonic applications</i></b>		
3.1.	Abstract	91
3.2.	Introduction	92
3.2.1.	Synthetic approaches	93
3.3.	Experimental section	94
3.3.1	Materials and methods	94
3.3.2	Characterization	95
3.3.3	Synthesis of multi-branched gold nanocrystals	96
3.4.	Results and discussion	97
3.4.1.	Morphological evolution of nanocrystals	97
3.4.1.1.	Absorption studies	97
3.4.1.2.	Transmission electron microscopic studies	98
3.4.2.	Kinetic & Mechanistic investigation	100
3.4.2.1.	Role of reagents	100
3.4.2.1.1.	Role of NaOH	100
3.4.2.1.2.	Role of L-DOPA	101



3.4.2.2.	IR studies	102
3.4.2.3.	Effect of L-DOPA concentration on tuning the morphology of nanocrystals	103
3.4.2.4.	Kinetics studies	109
3.4.2.5.	Mechanistic investigation	111
3.4.3.	Applications	115
3.4.3.1.	Nanophotonic enhancements	115
3.4.3.1.1.	SERS efficiency	115
3.4.3.1.1.	Photon to thermal conversion efficiency	116
3.4.3.2.	Theranostics applications	117
3.4.3.2.1.	Cell viability studies	117
3.4.3.2.2.	SERS cell internalization studies	118
3.4.3.2.3.	Apoptosis studies using Live/Dead Cell Assay	120
3.4.3.2.4.	SERS fingerprinting	121
3.5.	Conclusion	122
3.6.	References	123
 <b>Chapter 4. <i>Easy fabrication of SERS substrates through galvanic replacement reaction and its application for creatinine sensing</i></b>		
4.1.	Abstract	127
4.2.	Introduction	128
4.2.1.	Fabrication of SERS substrates	130
4.2.2.	Fabrication techniques	131
4.2.2.1.	Galvanic replacement method	132
4.3.	Experimental section	134
4.3.1.	Materials and methods	134

<b>4.3.2.</b>	<b>Characterization</b>	<b>134</b>
<b>4.3.3.</b>	<b>Fabrication of SERS substrates</b>	<b>135</b>
<b>4.3.4.</b>	<b>Preparation of artificial urine</b>	<b>135</b>
<b>4.4</b>	<b>Results and discussion</b>	<b>135</b>
<b>4.4.1.</b>	<b>Characterization of SERS substrates</b>	<b>135</b>
<b>4.4.2.</b>	<b>Preparation of the Ag-Cu and Au-Cu SERS substrate</b>	<b>138</b>
<b>4.4.2.1.</b>	<b>SEM and EDAX analysis</b>	<b>139</b>
<b>4.4.2.2.</b>	<b>XRD studies</b>	<b>140</b>
<b>4.4.2.3.</b>	<b>Absorption studies</b>	<b>141</b>
<b>4.4.2.4.</b>	<b>SERS studies</b>	<b>142</b>
<b>4.4.2.5.</b>	<b>The effect of concentration on morphological evolution</b>	<b>143</b>
<b>4.4.2.6.</b>	<b>The effect of time on the evolution of Cu-Ag structures</b>	<b>145</b>
<b>4.4.2.7.</b>	<b>The topography transformation mechanism</b>	<b>147</b>
<b>4.4.3.</b>	<b>Fabrication of Cu-Au substrates</b>	<b>149</b>
<b>4.4.3.1.</b>	<b>The effect of concentration on Cu-Au substrates</b>	<b>149</b>
<b>4.4.3.2.</b>	<b>The effect of time on Cu-Au substrates</b>	<b>152</b>
<b>4.4.3.3.</b>	<b>The topography transformation mechanism</b>	<b>155</b>
<b>4.4.4.</b>	<b>The growth mechanism of mesoparticles formation</b>	<b>156</b>
<b>4.4.5.</b>	<b>Uniformity of SERS substrate</b>	<b>157</b>
<b>4.4.6.</b>	<b>Application</b>	<b>158</b>
<b>4.4.6.1.</b>	<b>Detection of creatinine water solutions with different concentrations</b>	<b>159</b>
<b>4.4.6.2.</b>	<b>Detection of creatinine in artificial urine</b>	<b>161</b>
<b>4.5.</b>	<b>Conclusion</b>	<b>162</b>

<b>4.6.</b>	References	<b>162</b>
	List of publications	<b>166</b>
	List of posters and orals presentations	<b>167</b>



## LIST OF FIGURES

		<b>Page</b>
(1)	<b>Figure 1.1.</b> Comparison of size domains of naturally existing systems.	2
(2)	<b>Figure 1.2.</b> Pictorial representation of oscillation of electron cloud in the presence of an electromagnetic radiation.	3
(3)	<b>Figure 1.3.</b> (A) The colour photograph and (B) UV-Visible absorption spectra of differently sized gold nanoparticles solutions.	5
(4)	<b>Figure 1.4.</b> (A) The colour photographs of different anisotropic nanostructures, (B) Schematic representation of the displacement of plasmon resonance relative to the nuclei and (C) Extinction spectra of Au nanorods having different ARs and (D) The plot showing the linear relation between $\lambda_{\max}$ and ARs.	7
(5)	<b>Figure 1.5.</b> (A) Schematic representation of detection of $\text{Hg}^{2+}$ in tap water and (B) Showing their corresponding absorption spectral shift at different concentrations of $\text{Hg}^{2+}$ .	9
(6)	<b>Figure 1.6.</b> (A) Schematic representation of optical measurement of change in the local refractive index while binding analyte to receptor molecule.	9
(7)	<b>Figure 1.7.</b> Schematic representation of (A) FRET-based fluorescent assay for the detection of avidin molecules and their corresponding PL spectra and (B) An amperometric immunosensor for the detection of hepatitis B.	11

- (8) **Figure 1.8.** DDA predicted extinction spectra of AuNRs at different aspect ratio (AR). 13
- (9) **Figure 1.9.** Dark-field images of HeLa cells incubated with (A) 50 nm and (B) 82 nm nanostars 15
- (10) **Figure 1.10.** (A) TEM images and their corresponding field localization and (B) The distribution of electric field on Au star surface. 15
- (11) **Figure 1.11.** PL emission spectra of streptavidin-conjugated AF 750 on Au nanostar substrates 17
- (12) **Figure 1.12.** The plot showing the variation of experimental (black squares) and FDTD calculated (red spheres) Raman signal intensities of R6G adsorbed on Ag NPs with different sizes and irradiated with laser wavelengths: (A) 532 nm; (B) 633 nm; and (C) 785 nm. 21
- (13) **Figure 1.13.** Comparative SERS spectra of MGITC in presence of different nanostructures with laser excitation wavelength (a) 532 nm and (b) 785 nm 22
- (14) **Figure 1.14.** (A) The fabrication of AuNPs array of the sub-10-nm gap by simple drop-casting (B) Enhancement factors obtained under different laser excitations 23
- (15) **Figure 1.15.** (A) Comparative study of the molar heating rate of AuNRs (red) and AuNSs (black) S, M, and L-group represents shorter, medium and longer extinctions wavelengths, respectively and (B) the dark field images of AuNSs on SKOV3 melanoma cells. 26

- (16) **Figure 1.16.** (A) Schematic representation (B) TEM images and (C) color photographs of different types of anisotropic structures. 29
- (17) **Figure 1.17.** SEM (a) and TEM (b-d) images of synthesized AuNSs using different methods (a) CTAB templated, (b) Surfactant-free, (c) Hydroxylamine as reductant and (d) PVP-DMF assisted 31
- (18) **Figure 1.18.** Fabrication of different kinds of SERS active substrates. 36
- (19) **Figure 2.1.** Examples of (A) The colour photograph, (B) The extinction spectra and (C) TEM images of AuNRs with different aspect ratios. 52
- (20) **Figure 2.2.** Schematic representation of CTAB bilayer on the surface of AuNRs. 53
- (21) **Figure 2.3.** Graph showing the cell viability of HCT116 and BEL 7402 cells treated with AuNRs having different surface coatings. 54
- (22) **Figure 2.4.** Schematic representation of surface modification of AuNRs with (A) Polyelectrolyte (B) Silica and (C) Thiol-terminated ligands. 55
- (23) **Figure 2.5.** (a)–(e) TEM images (f) The corresponding UV-Visible spectra of different aspect ratios AuNRs prepared using the additives salicylate. 57
- (24) **Figure 2.6.** (A) TEM image and the corresponding absorption spectrum of nanoseeds prepared via reduction of gold ions by  $\text{NaBH}_4$  62



- (25) **Figure 2.7.** Absorption spectra of AuNRs produced with reducing agents ascorbic acid (black), L-DOPA (red), DHCA (blue) and gallic acid (green); [CTAB] = 0.1 M; [Ag<sup>+</sup>] = 10 μL, [seed] = 160 μL. 63
- (26) **Figure 2.8.** TEM images of nanorods prepared in presence of 1mg (A) Ascorbic acid, (B) DHCA, (C) Gallic acid and (D) L-DOPA in growth solution containing 0.1 M CTAB. 64
- (27) **Figure 2.9.** Absorption spectra of AuNRs prepared by varying the added seed volume at [CTAB] = 0.1 M; [Ag<sup>+</sup>] = 10 μL, [L-DOPA] = 1 mg. 66
- (28) **Figure 2.10.** Absorption spectra of AuNRs prepared by varying the added volumes of AgNO<sub>3</sub> at [CTAB] = 0.1 M; [seed] = 160 μL, [L-DOPA] = 1 mg. 67
- (29) **Figure 2.11.** TEM images of AuNRs prepared by varying the added volumes of AgNO<sub>3</sub> (A) 5 μL, (B) 10 μL, (C) 15 μL and (D) 20 μL at [CTAB] = 0.1 M; [seed] = 160 μL, [L-DOPA] = 1 mg. 67
- (30) **Figure 2.12.** Absorption spectra of nanorods prepared with reductants (A) L-DOPA, (B) DHCA, (C) Gallic acid and (D) Ascorbic acid with varying CTAB concentrations. The other conditions were standard; 0.5 mL 10 mM HAuCl<sub>4</sub>, 9.75 mL CTAB (0.5 mM – 0.1 M), 0.01 mL 0.1 M AgNO<sub>3</sub> and 1 mg reductant. 69
- (31) **Figure 2.13.** (A-E) TEM and (F-J) corresponding size distribution analysis of AuNRs prepared in presence of L-DOPA by varying [CTAB] (A, F) 0.1 M, (B, G) 0.01 M, (C, H) 0.005 M, (D, I) 0.001 M 71

and (E, J) 0.0005 M while keeping all other conditions constant.

- (32) **Figure 2.14.** TEM images of nanorods prepared with reductants (A-B) 71  
DHCA, (C-D) Gallic acid with varying CTAB concentrations (A,C)  
0.05 M and (B, D) 0.01 M.
- (33) **Figure 2.15.** A) HRTEM image, (B) SAED pattern, (C) XRD 72  
spectrum and (D) EDAX of AuNRs prepared in presence of 1 mg L-  
DOPA and 0.1 M CTAB.
- (34) **Figure 2.16.** (A) Evolution of the plasmon absorption during the 74  
formation of Au nanorods and (B) Time dependant absorbance  
changes at 475 (red), 512 (green) and 860 nm (blue).
- (35) **Figure 2.17.** Absorption spectral changes of growth solution 75  
(prepared by mixing HAuCl<sub>4</sub> (0.5 mL, 10 mM), CTAB (9.75 mL, 0.1  
M), and AgNO<sub>3</sub> (0.01 mL, 0.1 M)) after the addition of 1 mg L-  
DOPA.
- (36) **Figure 2.18.** (A), FTIR spectra of AuNRs prepared using L-DOPA (1 77  
mg), HAuCl<sub>4</sub> (0.5 mL, 10 mM), AgNO<sub>3</sub> (0.01 mL, 0.1 M), nanoseed  
solution (0.16 mL) and varying concentration of CTAB (9.75 mL);  
[CTAB] = 0.1 M (dark yellow), 0.01 M (red), 0.0005 M (olive). The  
blue curve represents the FTIR spectrum of AuNRs prepared via  
normal route (AA (1 mg), HAuCl<sub>4</sub> (0.5 mL, 10 mM), AgNO<sub>3</sub> (0.01  
mL, 0.1 M), nanoseed solution (0.16 mL) and CTAB (9.75 mL, 0.1  
M).
- (37) **Figure 2.19.** (A,B) Absorption spectra of AuNRs prepared by varying 78  
the added AgNO<sub>3</sub> volume at different CTAB concentrations. (A)  
[CTAB] = 0.01 M; [Ag<sup>+</sup>] = 1-15 μL (B) [CTAB] = 0.0005 M; [Ag<sup>+</sup>] =

0.5 – 15  $\mu\text{L}$ . (C-F) Representative examples of TEM images of AuNRs produced with (C)  $[\text{CTAB}] = 0.0005 \text{ M}$ ;  $[\text{Ag}^+] = 0.5 \mu\text{L}$ , (E)  $[\text{CTAB}] = 0.1 \text{ M}$ ;  $[\text{Ag}^+] = 0.75 \mu\text{L}$ , (E)  $[\text{CTAB}] = 0.0005 \text{ M}$ ;  $[\text{Ag}^+] = 10 \mu\text{L}$ , (F)  $[\text{CTAB}] = 0.0005 \text{ M}$ ;  $[\text{Ag}^+] = 15 \mu\text{L}$ .

- (38) **Figure 2.20.** (A) Plot showing the cell viability of SKBR3 cells after 79 incubation with AuNRs prepared in the presence of L- DOPA (1 mg) and varying CTAB concentrations (9.75 mL, 0.1 M - 0.0005 M). For comparison, the data of AuNR prepared with AA (1 mg) and CTAB (9.75 mL, 0.1 M) is also provided.
- (39) **Figure 2.21.** Temperature changes of AuNRs solutions upon 80 irradiation with 808 nm laser at a power density of  $0.1 \text{ W/cm}^2$  as a function of time. Water was used as a control.
- (40) **Figure 2.22.** Schematic representation of SERS substrate preparation 82 and Raman spectra of 4-mercaptobenzoic acid adsorbed onto self-assembled monolayers of AuNRs.
- (41) **Figure 2.23.** (A) and (B) are the bright field microscopic images of 82 the cells before and after irradiation. (C) In vitro cytotoxicity before and after laser irradiation (1 min) of SKBR3 cells in the presence of AuNRs prepared with L-DOPA (1 mg) and different CTAB concentrations (9.75 mL, 0.1 M - 0.0005M). Control data is that of cells in the absence of AuNRs.
- (42) **Figure 2.24.** SERS spectra of SKBR3 cells incubated with AuNRs for 84 4 hours as a function of time upon irradiation with 808 nm laser.
- (43) **Figure 3.1.** (A) Electric field distribution on the surface of the Au 93 nanostars with an increasing number of tips and (B) their biomedical

applications.

- (44) **Figure 3.2.** The absorption spectrum of Au nanoparticles in the initial stages (red) and after one hour (purple) prepared by adding 0.2 mM L-DOPA and inset shows their corresponding colour photographs. 98
- (45) **Figure 3.3.** (A-B) TEM images of the obtained nanostars prepared by adding 200  $\mu$ M L-DOPA (C) XRD data illustrating the crystal planes and (D) HRTEM images of the arms and inset shows the diffraction pattern obtained from one of the arms. 99
- (46) **Figure 3.4.** (A) Absorption spectral profile of HAuCl<sub>4</sub> (red), L-DOPA (green) and HAuCl<sub>4</sub> and NaOH (blue) and (B) Time-dependent absorption spectral changes of 0.2 mM HAuCl<sub>4</sub> solution after the addition of 0.2 mM L-DOPA (i.e. in the absence of NaOH). 100
- (47) **Figure 3.5.** FTIR spectra of (A) L-DOPA and (B) Au nanostars (0.2 mM L-DOPA) recorded in KBr. 102
- (48) **Figure 3.6.** (A,B) Color photographs of nanoparticle solutions prepared in presence of different L-DOPA concentrations ([L-DOPA] = 0.03-0.27 mM) taken after (A) 2 minutes and (B) 1 h of mixing the reagents, (C,D) their corresponding absorption spectra. 103
- (49) **Figure 3.7.** The plot showing the variation of the absorption wavelength maximum with respect to L-DOPA concentration. 104
- (50) **Figure 3.8.** Normalized absorption spectra of gold nanoparticles prepared in presence of 0.03 mM (red) and 0.05 mM (wine red) concentration of L-DOPA. 104

- (51) **Figure 3.9.** Representative examples of TEM images of nanocrystals prepared by varying the amount of L-DOPA. 106
- (52) **Figure 3.10.** Graphs showing size distribution analysis of (A-C) the nanoparticles and (D-G) the nanostars obtained in presence of L-DOPA, (A) 0.03 mM, (B) 0.05 mM, (C) 0.07 mM, (D) 0.07 mM, (E) 0.13 mM, (F) 0.20 mM, (G) 0.33 mM. 106
- (53) **Figure 3.11.** Representative examples of TEM images of nanoparticles prepared in the presence of 0.10 mM L-DOPA. 107
- (54) **Figure 3.12.** Representative examples of TEM images of nanoparticles prepared in the presence of 0.27 mM L-DOPA; inset of (F) Shows diffraction pattern obtained from one of the arms. 108
- (55) **Figure 3.13.** (A-C) Time dependent absorption spectral changes of HAuCl<sub>4</sub> solution after the addition of L-DOPA; ([L-DOPA] = (A) 0.05 mM, (B) 0.07 mM, (C) 0.1 mM, (D) 0.13 mM, (E) 0.2 mM, (F) 0.27 mM). 109
- (56) **Figure 3.14.** Evolution of TSPR and LSPR plasmon absorption of gold nanoparticles prepared in presence of varying amounts of L-DOPA; [L-DOPA] = 0.05 mM (A), 0.13 mM (B), 0.2 mM (C) and (D) shows the corresponding comparative evolution of TSPR band alone. 110
- (57) **Figure 3.15.** Representative TEM images displaying the presence of polymeric shell around nanomaterial. 112

- (58) **Figure 3.16.** Schematic representation (up) and illustrative examples of TEM images showing the evolution of branched nanocrystals via particle agglomeration and growth process. 113
- (59) **Figure 3.17.** DLS data showing the variation of particle size during the evolution of the LSPR band. [L-DOPA] = 0.2 mM. 113
- (60) **Figure 3.18.** SERS spectra of MBA molecules on different Au nanocrystals. 116
- (61) **Figure 3.19.** Temperature changes of Au nanocrystals with 808 nm laser at a power density of 0.1 W/ cm<sup>2</sup> as the function of time and water used as the control. 117
- (62) **Figure 3.20.** Plot showing the cell viability of A549 cells after incubation with AuNPs prepared by varying L- DOPA concentrations. 119
- (63) **Figure 3.21.** a) Bright-field and b) Raman images of A549 cells. c) Raman spectra obtained from the marked region of interest. The rows (A) Control, (B) Nanospheres, (C) Nanostars and (D) Nanoflowers. 119
- (64) **Figure 3.22.** Fluorescence images from Live/Dead Cell Assay showing the In vitro cytotoxicity with or without laser irradiation (1 min) in A549 cells in the presence of AuNPs having different morphology. Control data is that of cells in the absence of AuNPs. 121
- (65) **Figure 3.21.** SERS spectra of A 549 cells incubated with Au nanoflowers for 4 hours before and after irradiation with 808 nm laser. 122
- (66) **Figure 4.1.** Pictorial representation of plasmonic nanosubstrates 130

(67)	<b>Figure 4.2.</b> (A) Schematic representation of the nanosphere lithography (B-F) Corresponding microscopic images illustrating the obtained nanostructure at each stage.	132
(68)	<b>Figure 4.3.</b> (A, C) Large area and (B, D-F) higher magnifications SEM images of brass substrate (A, B) before and (C-F) after chemical etching.	135
(69)	<b>Figure 4.4.</b> (A, B) EDS spectra and (C, D) weight percentage composition of brass substrate (A, C) before and (B, D) after chemical etching.	136
(70)	<b>Figure 4.5.</b> (A) Comparative absorption spectra, (B) SERS spectra of brass before and after chemical etching. (C) Illustrates the uniformity of SERS activity of resulting Cu nanostructure.	138
(71)	<b>Figure 4.6.</b> SEM images of (A, B) Cu-Ag and (C, D) Cu-Au substrates.	139
(72)	<b>Figure 4.7.</b> EDS spectra of (A) Cu- Ag and (B) Cu- Au obtained by dipping Cu in 5 mM solutions of respectively AgNO <sub>3</sub> and HAuCl <sub>4</sub> for 3 h.	140
(73)	<b>Figure 4.8.</b> XRD spectra of (A) Cu (B) Cu-Ag and (C) Cu-Au substrates.	141
(74)	<b>Figure 4.9.</b> Absorption spectra of Cu-Ag and Cu-Au substrates.	141
(75)	<b>Figure 4.10.</b> (A) Comparative SERS spectra of Cu, Cu-Ag and Cu-Au	142



substrates.

- (76) **Figure 4.11.** SEM images of silver hemi-mesoparticles obtained by dipping Cu substrates for 5 minutes in different concentrations of  $\text{AgNO}_3$  (A-C) 1 mM, (D-E) 5 mM, (F-H) 10 mM. 143
- (77) **Figure 4.12.** (A) SERS spectra of MPBA molecules on plasmonic substrates prepared by dipping Cu for 5 minutes in different concentrations of  $\text{AgNO}_3$ . (B) Graph showing the variation of  $1590\text{ cm}^{-1}$  with respect to  $[\text{AgNO}_3]$ . 145
- (78) **Figure 4.13.** SEM images of Cu-Ag hemi-mesoparticles obtained by dipping Cu substrates for 3 h in different concentrations of  $\text{AgNO}_3$  (A-C) 1 mM, (D-E) 5 mM and (F-H) 10 mM . 145
- (79) **Figure 4.14.** SERS spectra of Cu-Ag hemi-mesoparticles obtained by dipping Cu substrates for 3 h in different concentrations of  $\text{AgNO}_3$  . 146
- (80) **Figure 4.15.** SEM images of Cu-Ag hemi-mesoparticles obtained by dipping Cu in 5 mM  $\text{AgNO}_3$  at different time intervals (A-C) 5 min, (D-F) 30 min, (G-I) 1 h and (J-L) 2 h. 147
- (81) **Figure 4.16.** SERS spectra of MPBA on Cu-Ag hemi-mesoparticles obtained by dipping Cu in 5 mM  $\text{AgNO}_3$  at different time intervals. 148
- (82) **Figure 4.17.** SEM images of gold hemi-mesoparticles obtained by dipping Cu substrates for 5 minutes in different concentrations of  $\text{Au}^{3+}$  (A-C) 1 mM, (D-E) 5 mM, (F-H) 10 mM. 150
- (83) **Figure 4.18.** (A) SERS spectra of MPBA molecules on plasmonic 151

substrates prepared by dipping etched brass in different concentrations of  $\text{HAuCl}_4$  and (B) The plot showing the variation of intensity change of MPBA Raman bands centered at  $1590\text{ cm}^{-1}$  as a function of  $[\text{HAuCl}_4]$ .

- (84) **Figure 4.19.** The absorption spectrum of gold hemi-mesoparticles obtained by dipping Cu substrates for 5 minutes in different concentrations of  $\text{Au}^{3+}$ . 152
- (85) **Figure 4.20.** SEM images of gold mesoparticles obtained by dipping Cu substrates for 3 h in different concentrations of  $\text{Au}^{3+}$ . (A-C) 1 mM, (D-F) 3 mM, (G-I) 5 mM and (J-L) 10 mM. 153
- (86) **Figure 4.21.** SERS spectra of Cu-Au hemi-mesoparticles obtained by dipping Cu substrates for 3 h in  $\text{HAuCl}_4$  of varying concentrations. 155
- (87) **Figure 4.22.** SEM images of gold mesoparticles obtained by dipping Cu substrates in 5 mM  $\text{Au}^{3+}$  for different time interval (A-C) 5 min, (D-F) 30 min, (G-I) 1 h and (J-L) 3 h. 156
- (88) **Figure 4.23.** SERS spectra of MPBA on (A) Cu (B) Cu-Ag and (C) Cu-Au at different positions and (D-F) their corresponding intensity change of MPBA Raman bands centered at  $1590\text{ cm}^{-1}$ ; substrate preparation condition 5 mM  $\text{AgNO}_3$  or  $\text{HAuCl}_4$  and the dipping time 5 min 157

- (89) **Figure 4.24.** (A, B) The solid-state Raman spectrum of (A) 160 Creatinine, (B) Urea. (C) SERS spectra of different concentrations of creatinine in water and (D) The plot illustrating the linear correlation between  $\log(\text{intensity})$  and  $\log(\text{concentration})$ .
- (90) **Figure 4.25.** (A) SERS spectra of artificial urine containing 161 different concentrations of creatinine and (B) the plot illustrating the linear correlation between  $\log(\text{intensity})$  and  $\log(\text{concentration})$ .

## LIST OF TABLES

		<b>Page</b>
(1)	<b>Table 1.1.</b> Comparative extinction coefficient of organic dyes and gold nanostructures.	13
(2)	<b>Table 1.2.</b> Comparison of experimental VS calculated SERS enhancement factors (EFs) for nanoparticles of different morphologies with three different excitation wavelengths.	23
(3)	<b>Table 2.1.</b> Absorption maxima, aspect ratio and statistical TEM analysis of the yield AuNRs obtained in presence of different reductants.	65
(4)	<b>Table 2.2.</b> Absorption maxima, aspect ratio and statistical TEM analysis of the yield AuNRs obtained in presence of different seed volume.	66
(5)	<b>Table 2.3.</b> EDAX energy values of component elements in AuNRs.	72
(6)	<b>Table 2.4.</b> Statistical TEM analysis of the yield of nanorods obtained in presence of different concentration of CTAB and L-DOPA as the reductant.	75
(7)	<b>Table 4.1.</b> Reduction potentials of metals relative to the standard hydrogen electrode (SHE).	133

## LIST OF ABBREVIATIONS

0D	Zero-dimensional
1D	One-dimensional
2D	Two-dimensional
3D	Three-dimensional
4-MBA	4-mercaptobenzoic acid
4-MPBA	4-mercapto phenyl boronic acid
AA	Ascorbic acid
AFM	Atomic force microscope
APTMS	(3-aminopropyl)trimethoxysilane
ARs	Aspect ratios
AuNPs	Gold nanoparticles
AuNRs	Gold nanorods
AuNSs	Gold nanostars
AuNWs	Gold nanowires
BDAC	Benzylhexadecyldimethylammonium chloride
CE	Chemical enhancement
CNT	Carbon nanotube
CTAB	Cetyltrimethylammonium bromide
DDA	Discrete dipole approximation
DHCA	3,4-dihydroxyhydrocinnamic acid

DLS	Dynamic light scattering
EDAX	Energy dispersive spectroscopy
EME	Electromagnetic enhancement
FRET	Förster resonance energy transfer
GA	Gallic acid
HRTEM	High-resolution transmission electron microscopy
IR	Infrared radiation
LbL	Layer-by-layer assemblies
L-DOPA	L-3,4-dihydroxyphenylalanine
LSPR	Longitudinal plasmon resonance
MGITC	Malachite green isothiocyanate
MNPs	Metal nanoparticles
MPTMS	(3-mercaptopropyl)trimethoxysilane
MTT	[3-(4,5-dimethylthiazol-2-yl)-2,5-diphenyltetrazolium bromide]
MUA	11-mercaptopundecanoic acid
NPs	Nanoparticles
PAA	Poly(acrylic acid)
PAH	Poly(allylamine hydrochloride)
PEG	Polyethylene glycol
PSS	Poly(styrenesulfonate)
PTT	Photothermal therapy
PVP	Polyvinylpyrrolidone
R6G	Rhodamine 6G

SAED	Selected area (electron) diffraction
SERS	Surface-enhanced Raman scattering
SPR	Surface plasmon resonance
SPW	Surface plasmon wave
STEM	Scanning tunneling electron microscopy
TEM	Transmission electron microscopy
TSPR	Transverse surface plasmon resonance
XRD	X-ray powder diffraction



## PREFACE

Plasmonic nanomaterials, due to their unique optical and electronic properties, have emerged as a promising family of nanomaterials for various applications. Their small size, high surface area, brilliant color originating from surface plasmon resonance, which also produces exceptionally localized electromagnetic field, are the main properties which makes them suitable candidate for application such as biosensors, therapeutics, bioimaging, nano-carriers for drug delivery, opto-electronics etc. The easy of synthesis, yield, processability, extent of plasmon tunability and cytotoxicity are the critical parameters for any practical applications. The current thesis makes an effort in exploring new and easy synthetic routes for plasmonic materials (such as nanorods, stars, SERS substrates) with improved characteristics for sensing and photothermal therapy (PTT) applications.

This thesis is organized into four chapters. The first chapter introduces the research background with a brief description of plasmonic nanomaterials, their importance, properties and applications. Further, an outline of the origin of plasmon absorption, factors affecting them and tailoring it for specific applications are also provided. Special attention is given for describing their applications especially in nano-biophotonic areas. This chapter also describes different synthetic strategies that are presently available for plasmonic nanomaterials. Recent developments in this field and major objectives of the current work are also highlighted.

The second chapter deals with a new synthetic strategy for AuNRs with improved yield, plasmon characteristics and biocompatibility and their demonstration in cancer therapeutics. Attempts to prepare nanorods were carried out using four different natural

antioxidant biomolecules and the effect of various parameters on their morphology, optical properties and biocompatibility were studied in detail. Out of these, L-DOPA has evolved as a promising reductant for nanorod synthesis. We were able to achieve reduction in CTAB concentration down to 0.5 mM, which is 200 time less than that of conventional procedure. Also, nanorods are formed in high yields (> 95 %) and their plasmon absorption was highly tunable in both visible as well as NIR region covering both bio-optical windows. The main reason for this is found to be efficient intercalation of L-DOPA with CTAB bilayer and was confirmed through FTIR studies. The evaluation of cytotoxicity illustrated high biocompatibility eliminating the need for further post synthetic treatments. Further, by combing this with their high SERS activity and photon to thermal conversion efficiency, we employed them in destruction of cancer cells and followed the biochemical changes through Raman spectroscopy.

Increasing the number of hot spots in nanomaterials is one of the promising strategies to improve their plasmonic properties. Multi-branched gold nanocrystals, by virtues of its size in the nano domain, morphology providing multiple hotspots, tunability of plasmon absorption in both visible and NIR region, are better candidate for bio-photonic applications. The third chapter describes an easy, one pot and bifunctional biomolecular synthetic strategy for multi-branched gold nanocrystals with excellent plasmon absorption and biocompatibility. Detailed characterization of these nanomaterials and mechanistic studies of their formation were also undertaken in detail. Herein, L-DOPA has been employed as both reductant and capping ligand and morphology of the obtained plasmonic materials were easily tuned from sphere-star-flowers by simply varying the reductant concentration. These nanomaterials showed

better photon to thermal conversion efficiency than gold nanorods due to the more number of sharp tips. In vitro cell internalisation and PTT activity of this nanomaterial was investigated on A549 cancer cell lines. Further, the biochemical changes were studied using Raman spectroscopy.

The major challenge for the wide spread use of SERS technique is the availability of a cheap and reproducible SERS active substrate with high and uniform sensitivity. In chapter 4, we describe an easy SERS substrate fabrication process using a less expensive and readily available material, brass. Brass is an intimate mixture of Cu and Zn. Upon etching with hydrochloric acid, Zn leaches out of the material leaving highly porous and nanostructured Cu substrate, which itself qualify as a suitable platform for SERS. Further, its plasmonic properties can be improved by growing nanocrystals of gold or silver over it. Cu having a lower redox potential, its simple dipping in a solution of either Ag or Au produces their nanostructures via galvanic displacement reaction. The parameters such as reaction time, concentration of the metal ions were optimized so as to obtain plasmonic substrates with high SERS activity. Further to demonstrate its capability for diagnostics, attempts to detect and quantify creatinine from artificial urine has been carried out as it provides first information about kidney functioning. Detection of creatinine from water solutions with good linearity was easily achieved in the concentration range 1 nM to 5 mM. Further, to demonstrate a close to real scenario, the capability of the current substrate for quantification of creatinine from artificial urine was also studied. Thus, the method developed herein will provide a viable alternative for urine creatinine quantification without the need for additional reagents and/or separation techniques.

In summary, herein we try to explore newer and easy synthetic route for plasmonic nanostructures with improved characteristics. Fine tuning their size and morphology via synthetic modulations were attempted so as to obtain materials with enhanced plasmonic properties. Further we evaluated its impact in bio-photonics like sensing and therapeutics.

### **References**

1. Shape controlled synthesis of multi-branched gold nanocrystals through a facile one-pot bifunctional biomolecular approach **M. Sajitha**, A. Vindysarumi, A. Gopi and K. Yoosaf; *RSC Adv.*, **2015**, 5, 98318-98324
2. Making gold nanorod synthesis greener with natural antioxidants and its theranostic application, **M. Sajitha**, N. Narayanan, K.Cottayil, R. B. Nellyil, K. K. Maiti\*, K. Yoosaf\*; Manuscript under submission.
3. Bimetallic hetero structures as sers substrate for creatinine sensing, **M. Sajitha**, R. B. Nellyil and K. Yoosaf \*; Manuscript under preparation.
4. Multi-branched gold nanocrystals for photo - based diagnostic and therapeutic applications, **M. Sajitha**, S. Giridharan, K. K. Maiti\* and K. Yoosaf \*; Manuscript under preparation.
5. Surface-enhanced Raman scattering substrate based on large-area with high uniformity, **M. Sajitha**, A. Soman, K. N. N. Unni\* and K. Yoosaf \*; Manuscript under preparation.

---

# Plasmonic Nanostructures and Their Bio-Applications: An Overview

---

## 1.1 General introduction to nanoscience and nanotechnology

Nanoscience and nanotechnology is the field of study of materials in the 1-100 nm size range and exploring their properties for the benefit of mankind (Figure 1.1). In general, they possess properties that far superior/ different from their isolated state of constituents as well as the bulk systems. Hence, they act as a bridge between atomic/molecular and macroscopic world and open new possibilities for creating advanced technologies. At the nanoscale, the materials possess modified properties such as reactivity, opto-electronics, and magnetism and are due to the electron confinement occurring at the size regime.<sup>1,2</sup> i.e., the holes and electrons are being squeezed into a dimension that approaches below their exciton Bohr radius. Thus, they are mainly dependant on the particle's size, shape, and chemical composition.<sup>3</sup> At the nanoscale building blocks are either of metallic (eg. Au, Ag, Cu, Pt, Pd), inorganic (eg. CdS, CdSe, CdTe, InP, GaN) and organic (eg. CNTs, fullerenes, graphene). In general, nanotechnology refers to the application of nanoscience for the design of custom-built products with enhanced performances in healthcare, materials and other technological areas.

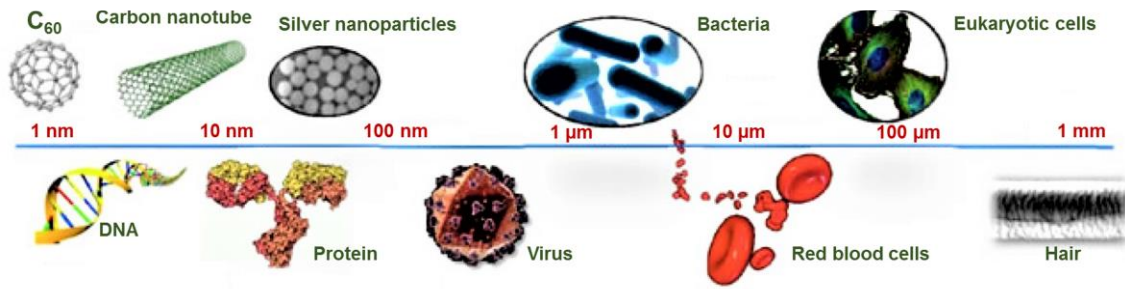


**Figure 1.1.** Comparison of size domains of naturally existing systems(adapted and modified from reference 4).<sup>4</sup>

## 1.2. Plasmonic nanostructures

Among the various, plasmonic nanostructures have obtained a great deal of attention in the field of nanoscience and nanotechnology.<sup>5-7</sup> In plasmonic nanoparticles, electron density can couple with electromagnetic radiation of wavelengths that are far larger than their size. This field of study is called plasmonics. It allows breaking the diffraction limit of light by localizing light into subwavelength dimensions and causes strong field enhancement. Presently, this has been extensively used to enhance the performance of a wide range of devices such as sensors, photocatalysts, photovoltaics, bio-imaging, diagnostics, and therapeutic.

### 1.2.1. Plasmonic metal nanoparticles

Among the widely available plasmonic nanomaterials, the most commonly used are those of the noble metals, gold, and silver. They usually exhibit brilliant colour and is a result of their high absorption and scattering coefficients. Hundreds of years ago, peoples were using these materials as the colouring agents unknowingly. At that time, it was known as the art, and now we call it as nanotechnology. In the 4<sup>th</sup> century, Romans made the Lycurgus Cup, which is one of the best examples of nanotechnology. The glass exhibits different colour upon changing the mode of light irradiation; appears green when lit from outside and reddish when lit from inside. Also, stained glass paintings and

potteries of Italian deruta ceramicists are the other examples. They generated red, yellow and blue colour using gold, silver and copper nanoparticles. Now it is confirmed that red stained glass gets its colour from nanoparticles of gold that are only 20 nm across. Orange glass gets its colour from gold nanoparticles that are of 80 nm across.

### **1.3. Surface plasmon resonance**

In the past two decades, there were plenty of different types of plasmonic nanostructures that have been synthesized, characterized and utilized in different areas. The interaction of light with noble metal nanoparticles causes the collective oscillation of free electrons on the metal surface, giving rise to surface waves, which are known as surface plasmons. An interesting consequence of this is that it can trap light at the metal-dielectric interface resulting in a highly localized and enhanced field. According to Drude and Lorentz model, metal comprises an equal number of conduction electrons and positive ions.<sup>8</sup> The oscillating nature of the electric field of electromagnetic radiation sets

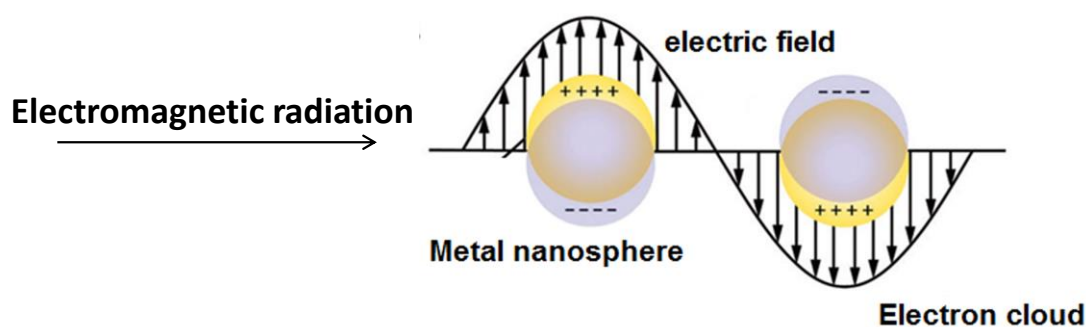


**Figure 1.2.** Pictorial representation of oscillation of electron cloud in the presence of an electromagnetic radiation (adapted and modified from reference 9).<sup>9</sup>

coherent oscillation of the electron cloud over the metal surface. When the frequency of this oscillation is in resonance with that of the incident, absorption occurs and is termed as the surface plasmon resonance (SPR) (Figure 1.2). The wavelength of this absorption is highly dependent on the size, shape, and nature of the material. For Au, Ag and Cu nanoparticles, the absorption generally occurs in the visible range (400-800 nm).

### **1.3.1. Factors affecting SPR**

#### **1.3.1.1. Size**

One easy way to change the colour of the metal nanoparticles is to play with their size. Generally, the plasmon absorption undergoes red-shift as the size of the nanoparticle is increased. In 1999, El-Sayed and co-workers systematically studied the size dependency in plasmon absorption of gold nanoparticles. They noted that when the sizes of gold nanoparticles are varied from 10 nm – 100 nm, their corresponding wavelength of maximum absorption underwent red-shift from ~520 nm to ~580 nm (Figure 1.3).<sup>10</sup> According to Mie theory, the ratio of scattering to total extinction increases with size. The total extinction and scattering increases by 3 fold and 6 fold with respect to the radius of the nanoparticles (Equation 1.1-1.2). Thus, the absorption properties of nanoparticles are influenced by their size (Equation 1.3). Typically, gold nanospheres of size ~ 20 nm primarily have absorbance maximum near 520 nm. However, for smaller particles whose size is less than 10 nm, the plasmon will be highly damped. This is because, at smaller sizes, the rate of electron-surface collisions are higher, which changes the phase of the oscillation. Similarly, for the larger spheres (>100 nm) the absorption bands are highly broadened and shifted towards longer wavelengths. These are mainly due to higher-order electron oscillations. Also, larger spheres scatter light more efficiently than smaller particles as their scattering cross sections increases with size. Thus, Gold nanoparticles are often used as bioimaging tags in darkfield microscopic techniques, where the scattering from individual nanoparticles with diameters larger than 40 nm can be easily observed. In the homogeneous system, the spectral profiles are narrower, but the heterogeneous size distribution always results in peak broadening.



$$C_{\text{ext}} = \frac{24\pi^2 R^3 \epsilon_m^{3/2}}{\lambda} * \frac{\epsilon_p''}{(\epsilon_p' + 2\epsilon_m)^2 + \epsilon_p''^2} \quad \text{--- 1}$$

$$C_{\text{sca}} = \frac{2^7 \pi^5 R^6}{\lambda} * \left| \frac{\epsilon_p' - \epsilon_m}{\epsilon_p' + 2\epsilon_m} \right|^2 \quad \text{--- 2}$$

$$C_{\text{abs}} = C_{\text{ext}} - C_{\text{sca}} \quad \text{--- 3}$$

Where  $R$  is the particle radius and  $\lambda$  is the wavelength of the incident light.

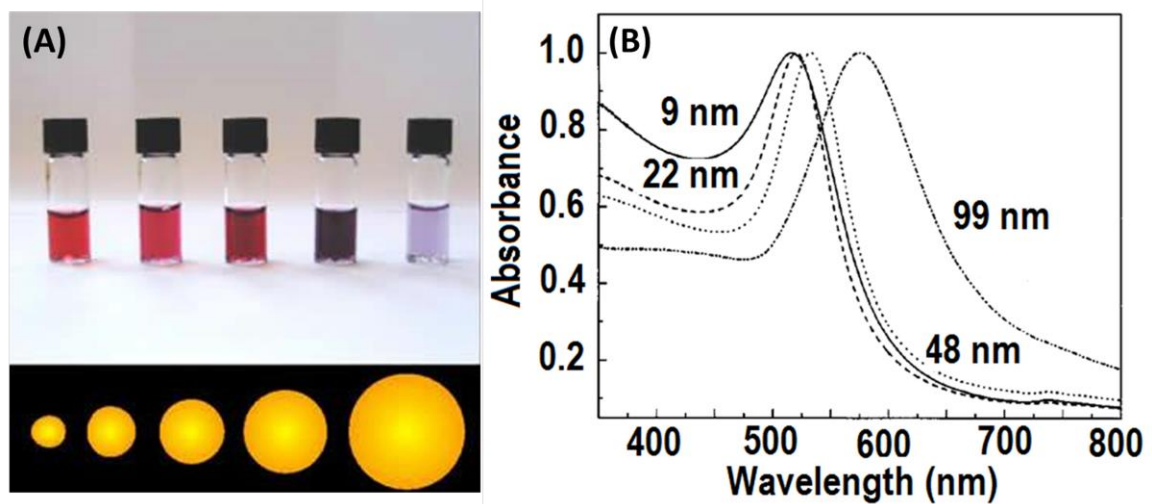


**Figure 1.3.** (A) The colour photograph and (B) UV-Visible absorption spectra of differently sized gold nanoparticles solutions (adapted and modified from reference 10).<sup>10</sup>

### 1.3.1.2. Shape

Comparisons of microscopy and single-particle spectroscopy with theoretical simulations have given a thorough understanding of the relationship between the nanoparticle's shape and their plasmonic properties. Compared to spheres, other 1D, 2D, and 3D nanomaterials exhibit distinctly different plasmonic properties. The nanoparticles with less faces and sharper vertices show resonances in a wider range of wavelengths and hence varying colours (Figure 1.4).<sup>11</sup> For example, the extinction spectra of gold nanorod

possess two plasmon absorption bands corresponding to oscillations across their length (longitudinal axis) and diameter (transverse axis). The former is known as longitudinal plasmon resonance (LSPR), and the latter is termed as transverse surface plasmon resonance (TSPR). AuNRs spectra are described by Gans theory, which is an extension of Mie theory. This theory calculates the depolarization factor along the axis of the spheroid based on the ratio of the semi-major and semi-minor radii. With the increase in this aspect ratio, the longitudinal band along the semi-major axis get red-shifted and the transverse band along the semi-minor axis slightly blue shifted.<sup>12</sup> i.e., in the case of elongated gold nanoparticles the LSPR red shifts by an amount proportional to their aspect ratio. In 2008, Tao et al., studied the influence of AuNRs aspect ratios in LSPR shifts. They observed the obvious LSPR shifts to a longer wavelength region with increasing the aspect ratio of AuNRs.<sup>1</sup>

A similar trend has been observed for particles of other morphologies. For example, in 2004, Hao and co-workers studied the plasmonic properties of multibranch gold nanocrystals which revealed that the optical properties of gold nanostars are highly dependent on dipole excitation from particle tips, which in turn is sensitive to the length as well as the sharpness of the tips.<sup>13</sup>

The other factors that predominantly influence SPR are composition, interparticle distance and dielectric constant of the medium.<sup>14</sup> The sensitivity of SPR towards the dielectric constant of the surrounding medium is described by the Mie theory itself. The increase in the refractive index of the surrounding medium results in a red-shift in SPR. Additionally, capping agents and solvents also influence the surface charge of nanoparticle and change in the wavelength of the surface plasmon resonance.<sup>14,15</sup> In some instances there occurs shift in the resonance wavelength associated with chemical

interaction of molecules with nanoparticles and the modifications in the density of plasma electrons.<sup>16-18</sup>

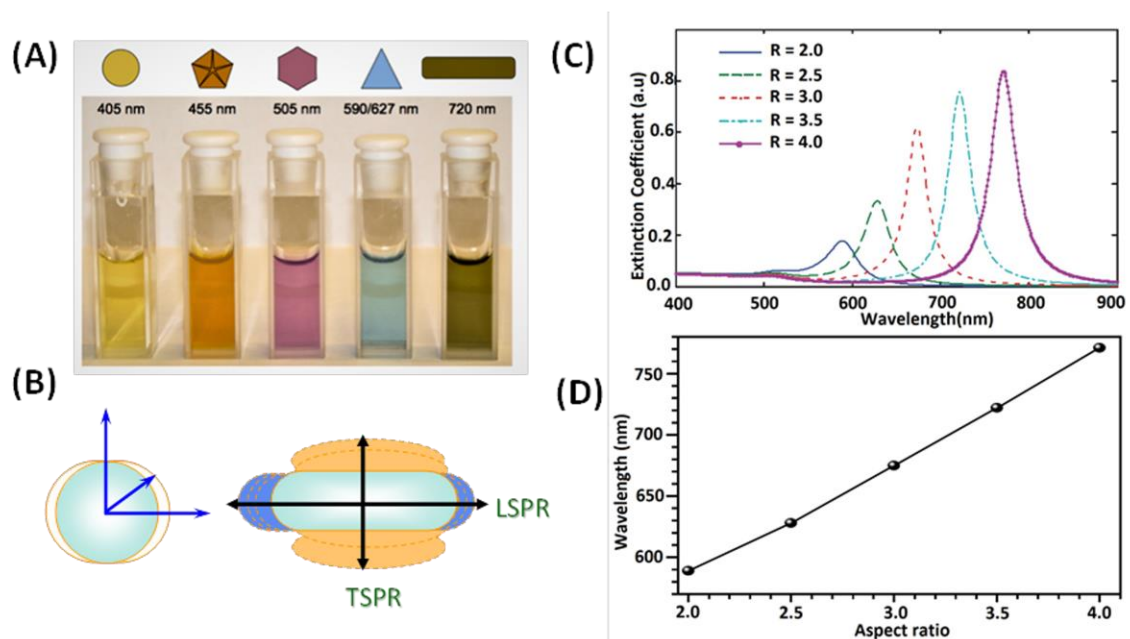


**Figure 1.4.** (A) The colour photographs of different anisotropic nanostructures, (B) Schematic representation of the displacement of plasmon resonance relative to the nuclei and (C) Extinction spectra of Au nanorods having different ARs and (D) The plot showing the linear relation between  $\lambda_{max}$  and ARs (C, D adapted and modified from reference 1).<sup>1,19</sup>

#### 1.4. Plasmonic sensors

Plasmonic sensors can act as the transducer for sensing molecules or analytes by directly detecting the changes in their spectral properties. Plasmonic sensors can be fabricated using metal nanostructures, nanoparticles or a combination of both. Based on the LSPR shift, plasmonic sensors are classified into three: (i) local refractive index changes and associated plasmon shifts induced upon binding of an analyte to the surface of nanoparticle;<sup>56</sup> (ii) either coupling or decoupling of plasmonic fields of multiple nanoparticles in the presence of analyte, causing a shift of the LSPR and thereby a color change.<sup>20-22</sup> (iii) enhancement or quenching of optical properties of other materials in the presence of plasmonic materials. Among the various plasmonic nanoparticles, colloidal

AuNPs are the most commonly used plasmonic transducer because of their chemical stability.

#### **1.4.1. Colorimetric detection**

Colorimetry is the simplest detection technique for analytes in solution. It visualizes the concentration of analytes in a direct way through the changes in colour. Presently, there is a huge drive for using functionalized Au nanoparticles for the detection of heavy metals, small molecules, and biomolecules.<sup>23-25</sup> Compared to the other conventional chromophoric systems, the metal nanoparticles exhibit at least one order of magnitude higher extinction coefficients. Thus, any analyte induced changes in the spectral profile of nanoparticles will be easily reflected as a distinguishable colour change, which can be even noted with the naked eye. In 1998, the Mirkin's group selectively detected polynucleotides through LSPR coupling between Au nanoparticles.<sup>26</sup> Later, Hupp and coworkers widened the scope of colorimetric technique to sense heavy metal ions such as  $Pb^{2+}$ ,  $Hg^{2+}$  and  $Cd^{2+}$  using 11-mercaptopundecanoic acid (MUA) functionalized Au nanoparticle. MUA having carboxylic group binds to the divalent metal ion through an ion-templated chelation process. This causes aggregation of nanoparticles leading to a change in their extinction spectrum.<sup>27</sup> Later, the specificity and sensitivity of colorimetric detection has been improved using DNA as the binding element.<sup>28-30</sup> Also, the use of anisotropic nanomaterials helps to improve the sensitivity of detections. Figure 1.5 represents an illustrative example of colorimetric detection of  $Hg^{2+}$  ions from tap water using AuNRs. When  $Hg^{2+}$  is present in the water, it binds to AuNRs by well-known amalgamation process resulting in the hypsochromic shift to the plasmon absorption and is used for the quantification of  $Hg^{2+}$  ions.<sup>31</sup>

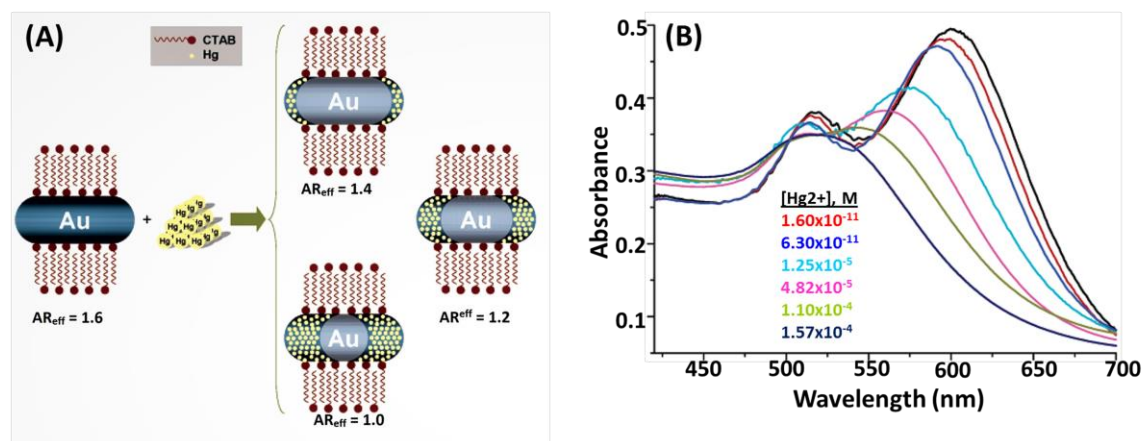


**Figure 1.5.** (A) Schematic representation of detection of  $Hg^{2+}$  in tap water and (B) Showing their corresponding absorption spectral shift at different concentrations of  $Hg^{2+}$  (adapted and modified from reference 31).<sup>31</sup>

#### 1.4.2. Surface plasmon resonance sensors (SPR sensors)

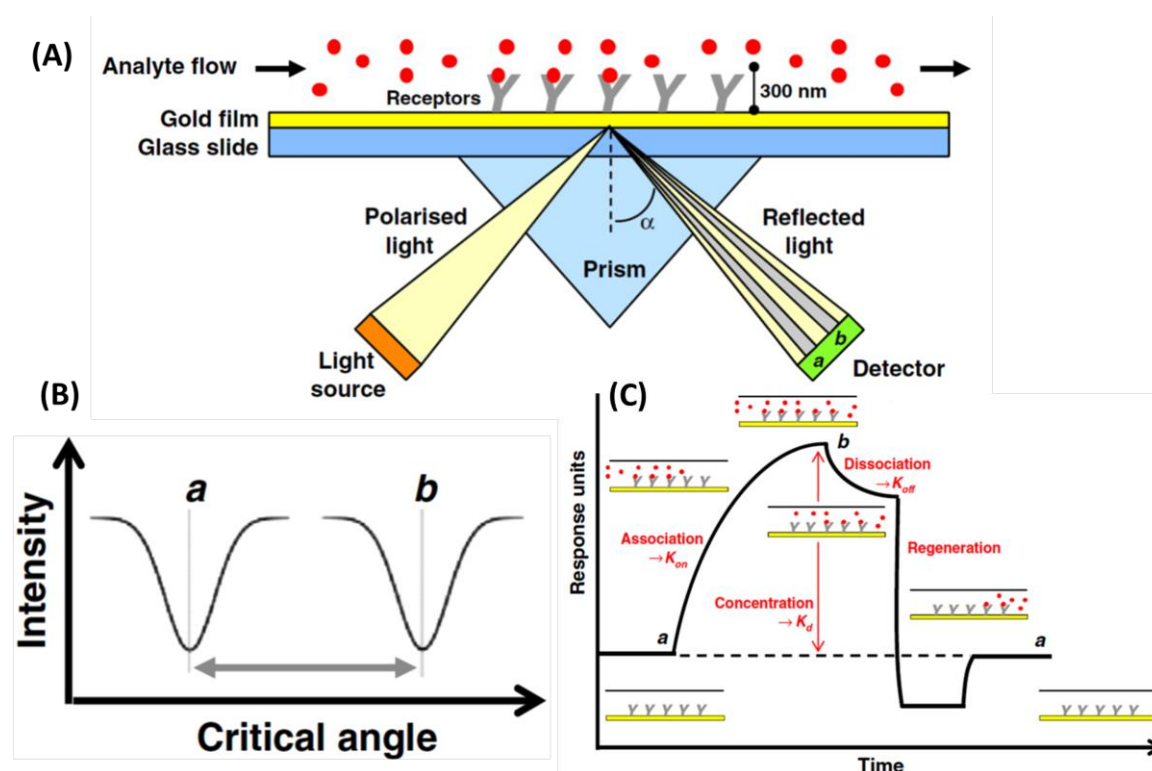


**Figure 1.6.** Schematic representation of optical measurement of change in the local refractive index while binding analyte to receptor molecule (A) Instrumental setup, (B) The graph showing change in critical angle and (C) Senogram (adapted and modified from reference 2).<sup>2</sup>

SPR sensing is an optical method to monitor the binding of the analyte to receptor molecules which are immobilized on the metal surface (Figure 1.6). The sensing is based

on the change in the refractive index of the medium near the metal surface.<sup>32,33</sup> The receptor units present on the metal surface recognize and capture the analyte molecule present in the sample solution. This results in a change in refractive index at the metal surface. The increase in the refractive index gives an increase in the propagation constant of Surface Plasmon Wave (SPW) propagating along the metal surface. This can be measured through optical means.

### **1.4.3. Fluorescent sensors**

The metallic nanoparticles have the ability to alter the fluorophore's emission properties; quenching and enhancement. The general pathways for quenching the dye emission are through electron transfer, energy transfer or by reducing the radiative rate. On the contrary, the phenomenon of fluorescence enhancement occurs by increasing the dye's absorbance and/or radiative rate. It depends on several factors such as (i) the nature of the metal NPs, (ii) fluorophore's closeness with the metal NPs and (iii) the orientation of dye's transition dipole relative to the metal NPs surface. For example, the quenching process is favored if the particle-dye distances are less than 6 nm, whereas the enhancement in fluorescent emission occurs when the particle-dye distances are in between ~ 6-10 nm.<sup>34</sup> By modulating the efficiency of energy transfer, the fluorescent molecules functionalized AuNPs have been used in "turn on" or "turn off" sensing for detection of various analytes including metal ions and biomolecules. In addition to organic chromophores, semiconductor quantum dots (QDs) are also used as fluorophores.<sup>35</sup> In 2005, Kim and co-workers fabricated an inhibition assay using AuNPs and streptavidin loaded QDs as a FRET donor-acceptor couple (Figure 1.7(A)). The specific binding of covalently attached biotin-AuNPs with streptavidin-QDs results in fluorescence quenching. However, due to the strong binding affinity of avidin with biotin, its presence in the solution causes detachment of biotinylated AuNPs from QDs and

yields fluorescence “turn on”. Thus this system can function as a highly specific avidin sensor.<sup>36</sup>

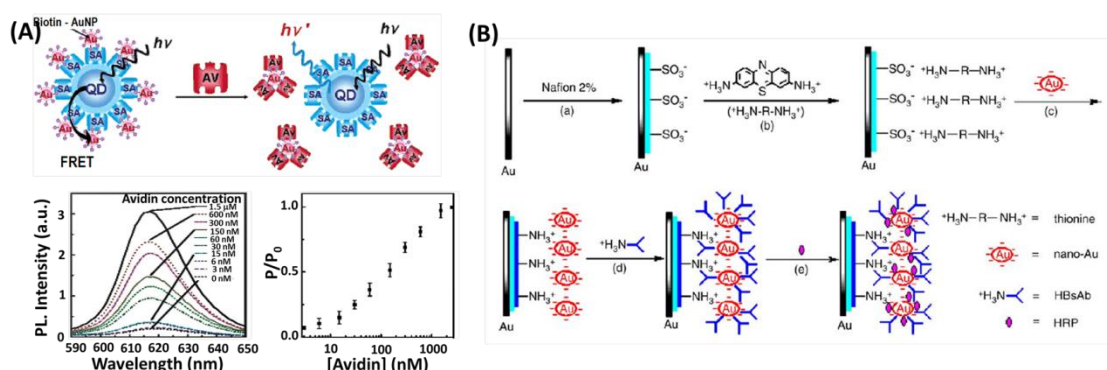


**Figure 1.7.** Schematic representation of (A) FRET-based fluorescent assay for the detection of avidin molecules and their corresponding PL spectra (adapted and modified from reference 36)<sup>36</sup> and (B) An amperometric immunosensor for the detection of hepatitis B.<sup>3</sup>

#### 1.4.4. Electrochemical sensors

AuNPs are the outstanding materials as electrochemical sensors because of their high surface area, exceptional catalytic, and conductivity properties. This makes them an excellent candidate for analytes detection. Functionalized nanomaterials act molecular receptor as well as a signal transducer that simplifies the sensor design without compromising its sensitivity. Yet, factors like the analyte, the recognition element, and the mode of signal transduction can influence the sensitivity of detection.<sup>3</sup> For example, in 2005, Zhuo et al., demonstrated an amperometric immunosensor for hepatitis B using gold electrodes coated with hepatitis B surface antigen (HBsAg) and horseradish peroxidase (HRP) functionalized the gold nanoparticles (Figure 1.7(B)). The presence of HRP helped not only to avoid the nonspecific adsorption but also improved the response of the antigen-antibody reaction thereby yielding high linearity and sensitivity even with clinical samples.<sup>3</sup> In 2016, Munshi et al., fabricated an electrochemical sensor using Fe<sub>3</sub>O<sub>4</sub> coated AuNRs -glassy carbon (GC) electrodes for hydrogen peroxide detection.

They conducted the experiment with two different aspect ratio AuNRs (1.6 and 7.5). These studies show better performance for shorter AuNR-Fe<sub>3</sub>O<sub>4</sub> hydride due to large surface area.<sup>37</sup>

## **1.5. Anisotropic nanomaterials**

Anisotropic nanocrystals of gold and silver are promising candidates for sensing and therapeutic applications because of their high extinction coefficient, increased NIR response and localization of hot spots at their tips.<sup>38,39</sup> The anisotropic Au and Ag NP structures are the sources of the plasmon absorption in the visible to the near-infrared (NIR) region. Importantly, having SPR in the NIR region wherein living tissues show minimal interference are crucial for applications in medical diagnostics and therapeutics.<sup>40,41</sup> Additionally, the shape anisotropy leads to localization of surface plasmon at certain points, especially at tips and edges. When a molecule is placed in these regions, experience a large enhancement in the electric field causing an increase in optical activity such as absorption, fluorescence and Raman scattering. Some of the presently available anisotropic nanostructures are rods, prisms, cubes, pyramids, wires, and polyhedra. But the major challenge of anisotropic nanoparticles is their volume estimation and hence the precise concentration determination due to the irregular shapes and asymmetry.

### **1.5.1. Importance of anisotropic nanoparticles**

#### **1.5.1.1. High extinction coefficient**

Usually, in the case of spectrophotometric analysis, the concentration of the analyte can be determined by knowing its extinction coefficient and the absorbance. One of the methods to calculate the extinction coefficient of anisotropic nanomaterials is through computational models such as discrete dipole approximation (DDA). DDA study the interaction of electromagnetic radiation with particle volume by approximating the



nanoparticles as an array of the point.<sup>42</sup> Generally, it has been found that for MNPs, the extinction coefficient highly depends on its size and morphology.<sup>43</sup> Compared to spherical nanoparticles, anisotropic nanostructures like AuNRs and AuNSs show high extinction coefficient (Table 1.1). Figure 1.8 is an illustrative example of the absorption properties of AuNRs predicted through DDA. From this, it is clear that with an increase in the aspect ratio, both the extinction intensity and the resonant wavelength shift to higher numbers. A similar observation has been made for other anisotropic nanostructures such as nanostar, nanoprisms, etc. This exposed their applications in various biological fields.

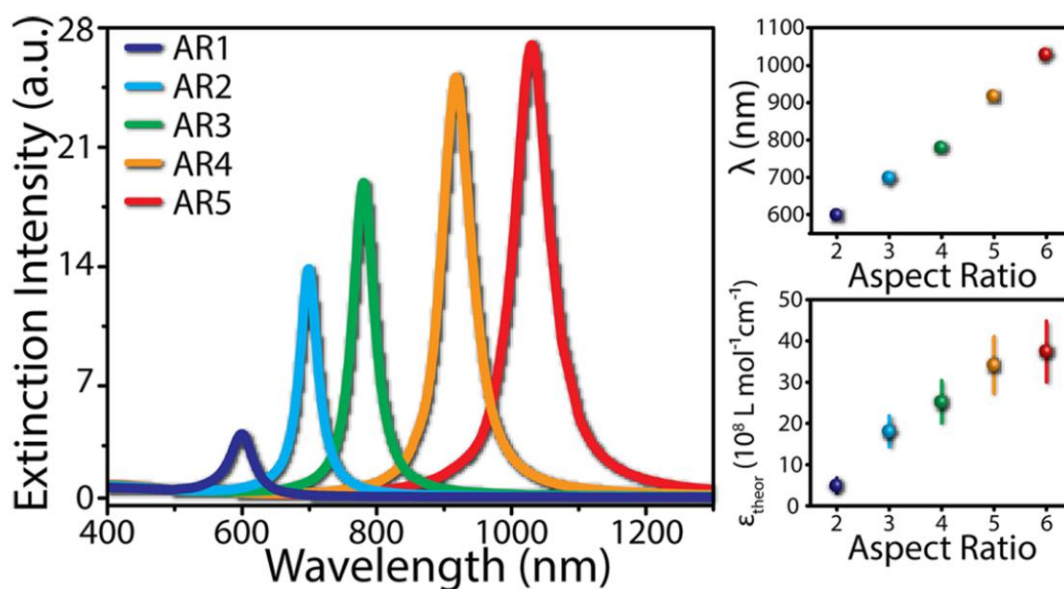


**Figure 1.8.** DDA predicted extinction spectra of AuNRs at different aspect ratio (AR) (adapted and modified from reference 44).<sup>44</sup>

**Table 1.1.** The comparative extinction coefficient of organic dyes and gold nanostructures.<sup>44-46</sup>

Agent	$\epsilon$ (cm <sup>-1</sup> M <sup>-1</sup> )
Organic dyes	10 <sup>4</sup>
AuNPs	10 <sup>6</sup>
AuNRs	10 <sup>8</sup>
AuNSs	10 <sup>9</sup>

### **1.5.1.2. High scattering efficiency**

Compared to organic dyes, metal nanostructures show good scattering efficiency. One of the direct consequences of this is that they can be used as better contrast agents in dark field microscopy (Figure 1.9). Additionally, modulation size and geometry offers the advantage of easy tuning both their scattering colour and efficiency. In 2000, Schultz and co-worker's demonstrated the ability of silver nanoparticles for the detection of single target molecules through dark field microscopy. They found that a single silver nanoparticle provides  $\sim 10^6$  times the signal intensity of a fluorescein (organic) molecule and  $10^5$  times than that of a quantum dot.<sup>47</sup> The studies have shown that anisotropic nanostructures are better scatterers than their spherical counterparts. In one of the pioneering works, El- Sayed, and coworkers used the DDA method to understand the scattering properties of different gold nanostructures. These studies revealed that gold nanospheres of  $\sim 40$  nm shows 5 orders higher absorption cross-section than conventional organic dyes. Also, 80-nm gold nanospheres have 5 orders higher light scattering intensity than the fluorescent emission of the organic dyes. Further, gold nanorods show at least one order of magnitude higher scattering coefficients than those of nanoshells and nanospheres of the same materials.<sup>48</sup> Similarly, one of the recent works Bibikova et al., noted a 3 times increase in the scattering coefficients of AuNSs when their size is varied from 50-80 nm. Further, due to their scattering efficiency, broad and size-tunable plasmon absorption bands results best imaging performance.<sup>49</sup>

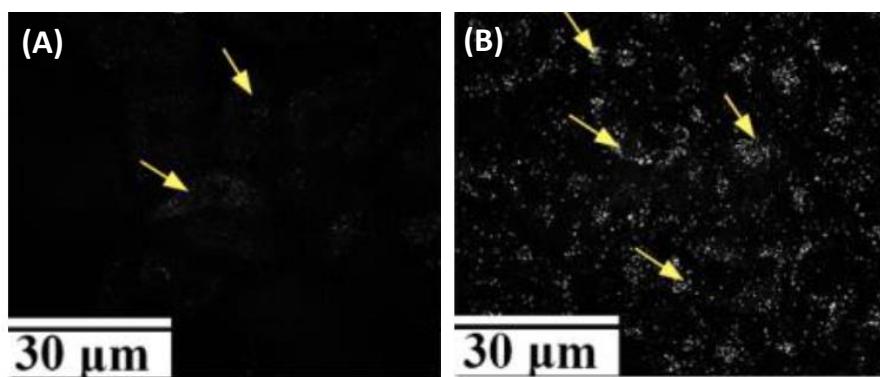


**Figure 1.9.** Dark-field images of HeLa cells incubated with (A) 50 nm and (B) 82 nm nanostars.

49

### 1.6. Localization of fields

One of the interesting aspects of metal nanoparticles is their ability to confine electromagnetic energy, causing strong near-fields enhancement. The areas of such nanomaterials showing high near-field are called hotspots and are generally classified into intrinsic and extrinsic. Intrinsic hot spots are mainly due to virtue of its geometry, the nanoparticles having edges and corners (nanotriangles, nanorods, etc.) always electric fields are more concentrated at tips and vertices (Figure 1.10). While when two nanoparticles are positioned at a short distances (<10 nm) plasmon modes between individual NPs or between a NP and a flat metal surface leads to new modes with highly

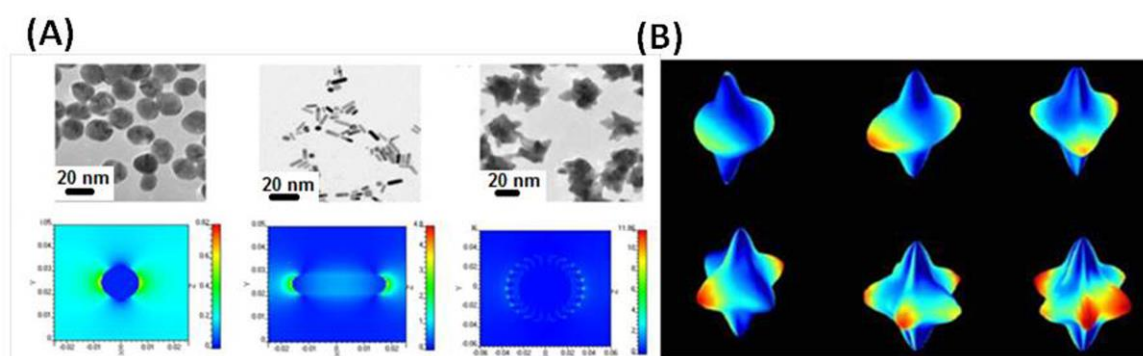


**Figure 1.10.** (A) TEM images and their corresponding field localization(adapted and modified from reference 50)<sup>50</sup> and (B) the distribution of electric field on Au star surface.<sup>19</sup>

localized, intense EM fields at the narrow gaps within the junctions. These are generally termed as extrinsic hotspots. Compared to other anisotropic structures nanostar shows

higher near-field enhancements because of their sharp tips.

### **1.6.1. Impacts of field localization**

#### **1.6.1.1. Absorption and fluorescence**

Metal-enhanced fluorescence or absorption is one of the emerging fields in imaging and sensing technologies. When a molecule interacts with the metal nanoparticle its optical properties are found to enhance due to the influence of SPR and its associated localized fields. Studies have shown that excitation efficiency enhances when SPR is close to the molecule's excitation wavelength. Also, fluorescence enhancement occurs when the emission wavelength of the molecule is close to the plasmon resonance. Compared to the spherical the anisotropic nanostructures show better enhancement due to the higher degree of field localization. Further, they have got multiple resonance wavelengths (for example LSPR and TSPR). Thus, it is possible to simultaneously enhance both the absorption and emission characteristic of the fluorophore through judicious selection of anisotropic nanostructures having LSPR and TSPR matching with that of electronic transitions.<sup>51</sup> For example, AuNRs shows high enhancement of excitation and emitting efficiency due to modes. Usually, fluorescence quenching is the most common phenomenon that occurs when fluorophores are adsorbed onto nanostructured metallic surfaces or nanoparticles. However, under specific conditions, the reverse fluorescence enhancement was noted. This is mainly due to the electric field around the plasmon. A large fluorescence enhancement was observed when the fluorophores interacted with metallic nanoparticles. Gersten and co-worker theoretically studied the fluorescence of a single dye molecule adsorbed on a metal surface, and they found that competition occurs between local field enhancement and the energy transfer to the metal particle from the excited dye molecule.<sup>52</sup> In 2015, Ren et al., studied the fluorescence enhancement of Oxazine 720 AuNRs and Ag coated AuNRs (Au@Ag NRs).

They observed that the fluorescence enhancement factors were increased to about 1.6 and 7.7 for Au NRs and Au@Ag NRs.<sup>53</sup> This increasing order is mainly attributable to the

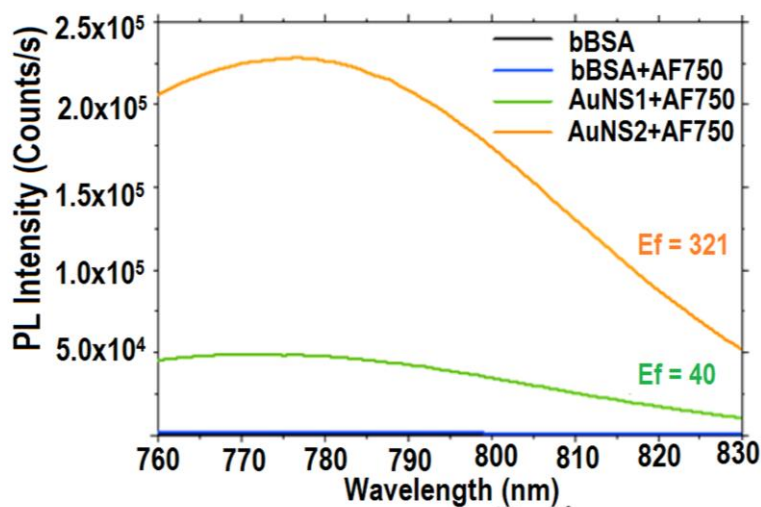


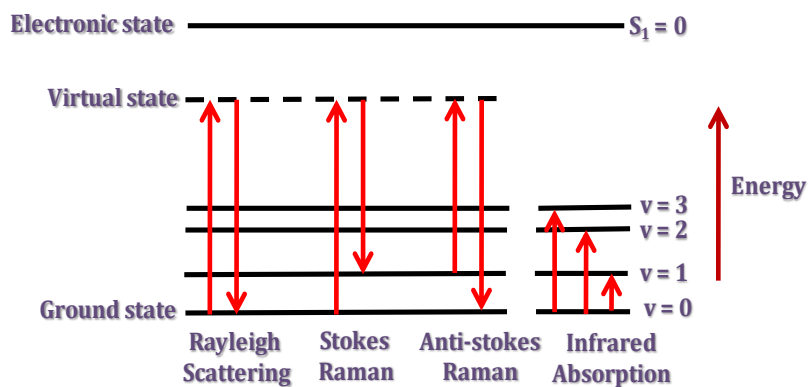
**Figure 1.11.** PL emission spectra of streptavidin-conjugated AF750 on Au nanostar substrates (adapted and modified from reference 54).<sup>54</sup>

better overlap of LSPR with emission wavelengths. In 2017, Ioannis et al., demonstrated the MEF capability of Au stars substrates using NIR dyes such as AF750, AF790, and Ag2S QDs. The result showed that NIR dyes exhibited 320-fold fluorescence enhancement in the presence of Au nanostars arrays than those in their absence (Figure.1.11).<sup>54</sup>

### 1.6.1.2. Raman spectroscopy

In 1928, the Indian physicist C. V. Raman and his student K. S. Krishnan discovered a “new type of secondary radiation”. They observed when monochromatic light is passed through a sample, the scattered radiation contains wavelength shifted photons and is generally known as Raman scattering. He was awarded the Nobel Prize for physics in the year 1930. Raman spectroscopy is a spectroscopic technique based on inelastic scattering of monochromatic light. Raman spectra result from a change in frequency when light is scattered by molecules. When a photon collides with a molecule,

the collision happens either elastically or inelastically. In an elastic collision, the change in the frequency of scattered light is zero and is termed as Rayleigh scattering (Scheme 1.1). The Rayleigh lines are highly intense and are eliminated in an ordinary Raman spectrometer using a specific optical filter (notch, long pass). An inelastic collision can cause a change in the frequency of the scattered light. A small fraction of the photon ( $\sim 1$  in 10 million) are scattered inelastically and has a frequency  $\nu_r$  which is different from that of the incident light  $\nu_0$  and the difference ( $\nu_r - \nu_0 = \Delta\nu$ ), is referred to as the Raman shift. This difference is found to be match with the energy required for particular vibrational or rotational transitions, which are quantized. Thus, the Raman spectrum of the molecule gives fingerprint information. The interaction of the light with a molecule in the ground state transforming to higher energy state, results scattered photons of energy lower than that of the incident photon. This gives rise to Stoke's lines in the Raman spectrum. Instead, if a molecule is already in the excited state, it may relax to lower energy by transferring excess energy to the incident photon, then the scattered radiation will have higher energy, which leads to anti-Stoke's lines in Raman spectrum. Usually, compared to the Stoke's lines, the anti-Stoke's lines are less intense, since at room temperature a very small percentage of molecules are in the excited state. By using Boltzmann's distribution law and by comparing the ratio of the heights of the Stoke's and anti-Stoke's lines, Raman technique can be used as a sensitive temperature probe. Raman spectroscopy gives fingerprint information of the molecule because the shift in frequency is not dependent on the frequency of the incident photon, but the characteristic vibrational levels of the scattering molecule. Thus this can be used as an efficient methodology for the identification and detection of molecular systems.



*Scheme 1.1.* Jablonski diagram representing quantum energy transitions for Rayleigh and Raman scattering.

### 1.6.1.2.1. Principle of Raman scattering

The intensity of the Raman spectrum depends on the light scattering ability of that sample. It depends on the polarizability of the molecule. The induced dipole moment ( $P$ ) in a molecule by an external electric field ( $E$ ) is proportional to the applied field.

$$\mathbf{P} = \alpha \mathbf{E} \quad \text{—————} \quad \mathbf{4}$$

Where  $\alpha$  is the proportionality constant called polarizability. The vibrational motion of the molecule can distort the electron cloud around it and thus leads to change the polarizability. This change can be explained by the polarizability derivative,  $d\alpha/dQ$ , where  $Q$  is the normal coordinate of the vibration. Thus, the selection rule for a Raman-active vibration is

$$\frac{d\alpha}{dQ} \neq 0 \quad \text{—————} \quad \mathbf{5}$$

### 1.6.1.2.2. Pros and cons

Raman spectroscopy has many advantages compared to other spectroscopic techniques. Raman spectrum is highly suitable for organic and inorganic materials for detection that can be solids, liquids, or vapors. It is a non-destructive, specific and sensitive technique with less interference from water. Still, it possesses a lot of limitations

including extremely low scattering cross-section (only one out of  $10^6$  photons are inelastically scattered) contributing to highly weak Raman signal. As a result, it suffers strong interference from highly intense Rayleigh scattering. Efforts have been made to enhance the number of molecules absorbed upon irradiation and thus improving the Raman scattering cross-section. The presently established methods for enhancing Raman signal include Surface Enhanced Raman Scattering (SERS), Resonance Raman Scattering (RRS), and Coherent Anti-stokes Raman Scattering (CARS).

### **1.6.1.3. Surface-enhanced Raman scattering (SERS)**

Surface enhanced Raman scattering was first observed in 1973 by Martin Fleischman et.al in University of Southampton, UK.<sup>55</sup> Intense Raman scattering from an aqueous solution of pyridine was observed when it is adsorbed onto a roughened silver electrode surface. He found that molecules adsorbed on to the electrochemically roughened silver rod yielded more than a million times enhanced Raman signal. Later, Van Duyne and Jeanmaire from Northwestern University and Creighton and Albrecht from the University of Kent also reported similar observations.<sup>56</sup> SERS was one of the revolutions in the field of Raman spectroscopy to overcome the inherent problems associated with low signal to noise ratio. Currently, this has emerged as a powerful tool for detecting a wide range of molecules in various fields.<sup>57</sup>

#### **1.6.1.3.1. Enhancement mechanism in SERS**

Enhancement of Raman signal operates mainly through two mechanisms, namely (i) electromagnetic enhancement<sup>58,59</sup> (EME)<sup>58,59,103,104</sup> [Schatz 1984 and Moskovits 2005] (ii) chemical enhancement (CE)<sup>60,61</sup> [Otto 1992 and Otto 2005]. The electromagnetic enhancement is due to the increase in the electromagnetic field strength at the surface caused by the excitation of surface plasmons. The degree of this



increase depends greatly on the proximity of the molecule to the metallic surface. The other mechanism involved is the chemical enhancement. The exact mechanism involved in chemical enhancement is still not understood. The CE mechanism arises due to the chemical interaction between the adsorbates and the metal surface. It is based on the charge transfer interaction. It involves the photoinduced electron transfer from the Fermi level of the metal to an unoccupied molecular orbital (LUMO) of the adsorbate or vice versa. However, for this to occur, the molecule must be chemically adsorbed to the surface of the metallic nanoparticles. CE increases the Raman signal but extends of increment is much less than the electromagnetic enhancement ( $10-10^2$ ). The simultaneous operation of these two enhancements in a system can create a signal intensity in the order of  $10^5$  to  $10^6$ . The electromagnetic enhancement is dependent on the roughness of the metal surface, while the chemical enhancement involves changes in the electronic states of the adsorbate due to chemisorptions of the analyte onto the surface.<sup>62</sup>

### 1.6.1.3.2. Factors affecting SERS

Localization and enhancement of the near electromagnetic fields due to plasmon excitations is the key principle of surface enhanced Raman spectroscopic (SERS) technique.<sup>63</sup> Recent studies have brought out that one method to obtain maximum

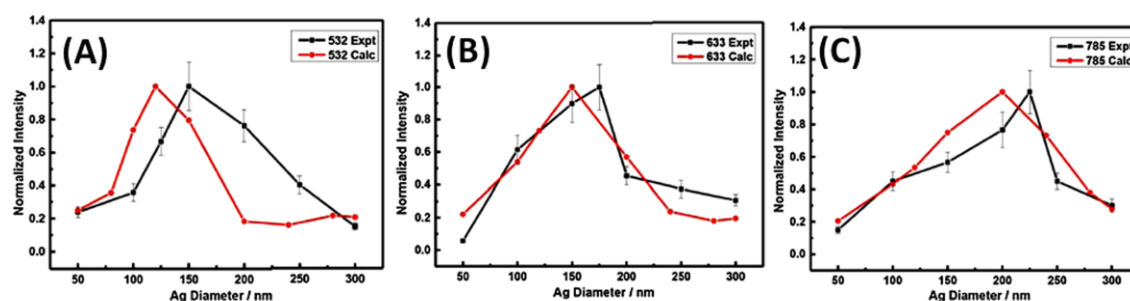


**Figure 1.12.** The plot showing the variation of experimental (black squares) and FDTD calculated (red spheres) Raman signal intensities of R6G adsorbed on AgNPs with different sizes and irradiated with laser wavelengths: (A) 532 nm; (B) 633 nm; and (C) 785 nm.<sup>64</sup>

enhancement is by choosing an excitation wavelength shorter but close to LSPR such that wavelength of the scattered photon appears above LSPR.<sup>65,66</sup> The other important factor is the size. Generally, particles in the size range of 20-200 nm show good SERS activity compared to microstructures. This has been beautifully illustrated by Yang Zhao et al., where they studied the SERS activity of R6G molecule with respect to Ag nanoparticle diameter and excitation wavelength.<sup>64</sup> The nanoparticle size in the range of ~150, ~175, and ~225 nm showed the highest SERS activities with the excitation wavelength of 532, 633, and 785nm, respectively (Figure 1.12).

The third important factor is the shape, Li et al., investigated the SERS properties of three types of nanoparticle (nanospheres, nanorods, and nanostars) under excitation with laser wavelengths 532 nm and 785 nm (Figure 1.13). They observed that the nanostars show the strongest SERS signal enhancement compared to spheres and rods

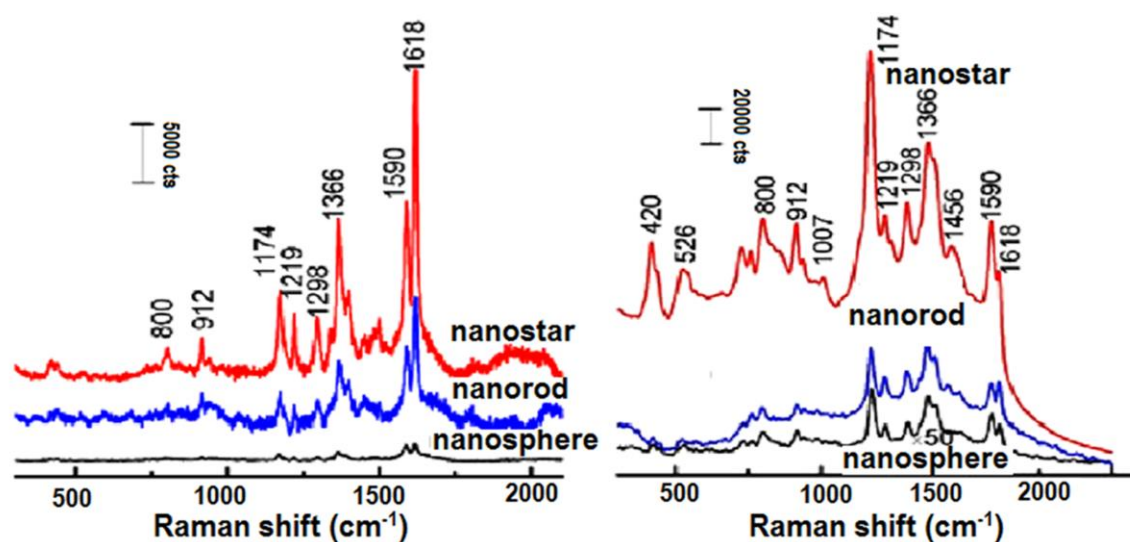


**Figure 1.13.** Comparative SERS spectra of MGITC in presence of different nanostructures with laser excitation wavelength (A) 532 nm and (B) 785 nm (adapted and modified from reference 67).<sup>67</sup>

(Table 1.2). The results indicated the high ability of sharp geometric components to concentrate LSPR and thus were responsible for higher enhancement.<sup>67</sup> Liu et al., investigated the size and shape-dependent SERS activity of plasmonic nanorattles

**Table 1.2.** Comparison of experimental VS calculated SERS enhancement factors (EFs) for nanoparticles of different morphologies with three different excitation wavelengths.<sup>67</sup>

Sample	Experimental EF		Calculated EF	
	532 nm	785 nm	532 nm	785 nm
Nanosphere	$5.1 \times 10^2$	$3.8 \times 10^2$	$8.7 \times 10^2$	$8.3 \times 10^2$
Nanorod	$1.6 \times 10^3$	$5.1 \times 10^4$	$1.5 \times 10^3$	$1.6 \times 10^4$
Nanostar	$3.9 \times 10^3$	$1.0 \times 10^5$	$3.0 \times 10^3$	$8.9 \times 10^4$

comprised of Au nanospheres and nanorods as cores and porous Au nanocubes and cuboids as shells.<sup>68</sup> The SERS signals got enhanced with increase in edge length of the cubic shell of Au nanorattles. On the other hand, the SERS activity of Au cuboid nanorattles with AuNR core was found to decrease with increase in the size of the cuboid shell

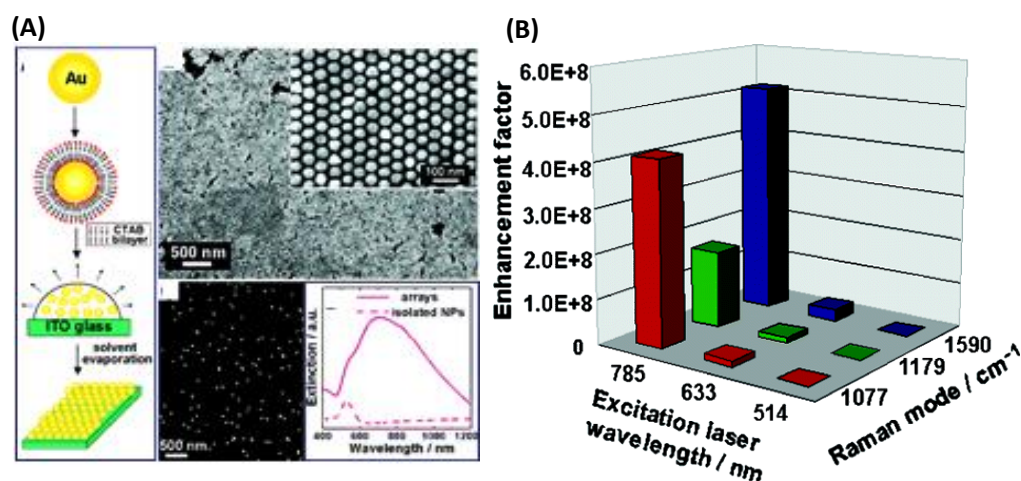


**Figure 1.14.** (A) The fabrication of AuNPs array of the sub-10-nm gap by simple drop-casting (B) Enhancement factors obtained under different laser excitations((B)adapted and modified from reference 69).<sup>69</sup>

The other method to increase the SERS effect is through the creation of hot spots by plasmon coupling. Shalaev's group extensively studied both theoretically and experimentally about the hot spot and attained general consensus that they incline to form in areas where the neighboring particles are nearly touching or allowing for maximum plasmonic coupling. In hot spot regions, the local electric field intensity is enhanced by several orders of magnitude.<sup>70</sup> Wang et al., fabricated highly ordered NP arrays with sub-10-nm gaps through self-assembly. In this work, CTAB-capped Au NPs have been used for the preparation of SERS substrates and obtained high enhancement, stability, and reproducibility (Figure 1.14).<sup>69</sup>

## **1.7. Applications of anisotropic nanomaterials**

### **1.7.1. Bio-imaging**

Cell imaging is mainly done by using conventional contrast agents such as organic fluorophores and lanthanide complexes. But the organic fluorophores suffers lots of limitations including broad emission window, low quantum yields, and photobleaching and lanthanides suffer nonselectivity. Now a day, the anisotropic metal nanoparticles are gaining attention as contrast agents for NIR bioimaging applications. These are due to their ease of functionalization with specific targeting and biocompatible ligands, strong and NIR tunable SPR, large scattering cross-sections, etc.. In 2006, Huang and coworkers first used AuNRs as a contrast agent in dark-field imaging. They conjugate AuNRs with EGFR antibodies (anti-epidermal growth factor receptor) for specific binding. In 2016, Bibikova et al., studied the efficiency of nanostar as contrast agent by preparing nanostars of varying particle size. The results showed that the scattering efficiency increases with their size. Also, their broad plasmon absorption makes them the best contrast agents in darkfield microscopy.<sup>49</sup>

### **1.7.2. Photothermal cancer therapy**

Yet, another important aspect of plasmonic nanomaterials is their ability to convert light energy into heat. The nonradiative relaxation of photoexcited plasmons produces highly localized heat, which is sufficient to kill living cells and is the basis of photothermal therapy (PTT). The main reason for the production heat is the electron-phonon interactions by colliding with the gold lattice, which produces heat in the order of several thousand degrees. This heat is then transferred to the surroundings through phonon-phonon interactions. Thus, when irradiated with a suitable laser, the photothermal heating occurs only around the gold nanoparticles and temperature can rise in a short time scale. This has been found to be efficient in treating various cancers<sup>71</sup> as the heat produced from AuNPs can be utilized in cancer therapy to destroy the cancer cells. The major difference between photothermal therapy and traditional hyperthermia is that the first one is more targets specific. This led to reducing the negative side effects of cancer therapies. In 2003, West and co-workers gave the first example of using gold nanoparticle for cancer treatment.<sup>72</sup> They prepared gold nanoshells over a 110 nm sized silica particle which is then functionalized with polyethylene glycol (PEG) to make it biocompatible, reduce aggregation and increase the half-life of blood circulation. The major limitations of this experiment were the fast diffusion of the nanoshells throughout the tumor and a relatively low depths of treatment, 4-6 mm. Later in 2006, El-Sayed et al., demonstrated a targeted PTT by functionalizing anti-epidermal growth factor receptor (EGFR) monoclonal antibodies to AuNPs which facilitated their uptake and binding with overexpressed EGFR.<sup>73</sup> This has helped to improve the specificity and the nanoparticles being highly concentrated in the cancer cells the treatment can be done with less laser power and reduced time. This help to avoid the destruction of normal cells.

Though the spherical nanoparticles perform well in PTT treatment, the main limitations are (i) the absorption below 600 nm wherein biological tissues have got good absorbance, the irradiation at this wavelength may cause damage to healthy cells as well, (ii) low penetration depth because of the shorter wavelength. However, anisotropic nanostructures such as nanorods, nanostars, nanocages, and nanoshells help to overcome this by having tunable absorption towards NIR region. Additionally, they also have better light-harvesting capability, which helps to reduce the amount of nanoparticle as well as the laser power required for effective treatment. There have been several efforts to study and compare the PTT effect of nanoparticles of different morphologies and sizes. In 2014, Wang et al., made a comparative study of the photothermal effect of differently sized gold nanorods and nanostars. They observed that compared to smaller, bigger particles exhibit a higher photothermal heating effect. Though gold nanostars and gold nanorods having similar plasmon absorption exhibited the same heating effects, the molar heating rates were much higher for gold nanostars (Figure 1.15(A)).<sup>74</sup> Yuan et al. demonstrated that

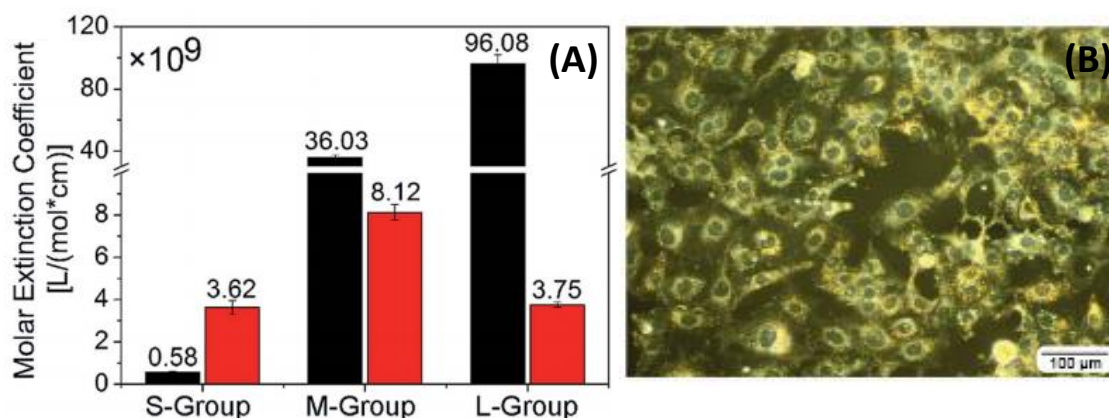


**Figure 1.15.** (A) Comparative study of the molar heating rate of AuNRs (red) and AuNSs (black) S, M, and L-group represents shorter, medium and longer extinction wavelengths, respectively<sup>74</sup> and (B) the dark field images of AuNSs on SKOV3 melanoma cells.<sup>75</sup>

AuNSs functionalized TAT cell-penetrating peptide (CPP) resulted in high cellular uptake in BT549 breast cancer cells and observed efficient photothermolysis with one of the lowest laser irradiation power (0.2 mW) (Figure 1.15 (B)).<sup>76</sup>

## **1.8. Synthesis of metal nanoparticles**

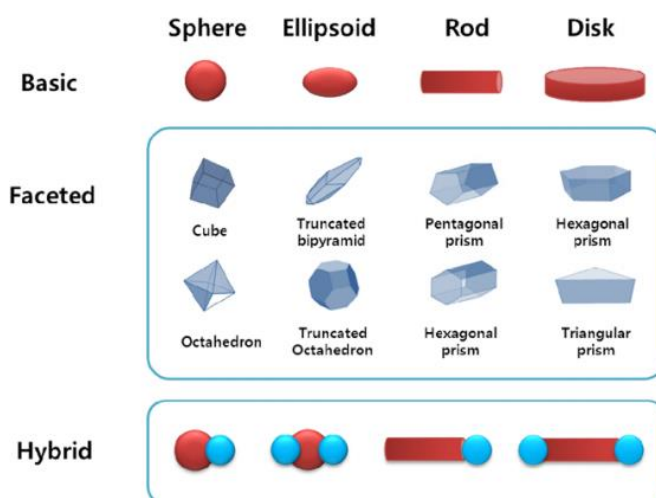
With the recent developments in the field, many synthetic procedures are available for producing plasmonic nanostructures with well-controlled size and shapes and hence for the precise tuning the surface, electronic optical and catalytic properties. These can be generally classified into two; (i) top-down and (ii) bottom-up approaches.<sup>77,78</sup>

Photolithography<sup>79</sup> and electron beam lithography<sup>80,81</sup> are the two main top-down strategies practiced by physicists to fabricate nanostructures while chemists are more comfortable with wet chemical methodologies (bottom-up) nanoparticle synthesis. This involves the reduction of a metal salt by either one of the chemical,<sup>82</sup> sonochemical,<sup>83</sup> electrochemical<sup>84</sup> and photochemical<sup>85</sup> methods, usually in the presence of capping agents having the main roles of (i) providing colloidal stability through preventing precipitation via particle agglomerations and (ii) arresting the further enlargement of nanoparticles. Chemical methods are more attractive because tuning the size and shape of nanomaterials are easily achievable through controlling reaction parameters such as relative concentrations of ingredients, dilution, temperature and time. One of the pioneering but still popular methods for the synthesis of spherical metal nanoparticles is the boiling of an aqueous solution of their salt (e.g. H<sub>2</sub>AuCl<sub>4</sub> for Au) with a natural reductant, sodium citrate which is first reported by Turkevich in 1951. In this method, one could easily assess the progress of reaction and hence formation of nanoparticles through the emergence of characteristic color (deep wine for Au and yellow for Ag) in the medium. By changing the concentration of gold salt and sodium citrate, it is

possible to tune the average particle diameter over a wide range (~10-100 nm). However, particles with more polydispersity both in terms of size and shape are the inevitable consequences when one attempt to prepare particles bigger than 30 nm through this original method.<sup>86</sup>

Later Schiffrin, Brust, and coworkers came up with a two-phase reduction strategy which allowed exploration of Au nanoparticles in organic media. Herein, tetraoctylammonium bromide (TOAB) is a phase transfer agent that extracts  $\text{AuCl}_4^-$  from water to the organic phase in the form of an ionic salt. An almost 25 times higher concentrated sodium borohydride solution is taken as a strong reducing agent to convert  $\text{Au}^{3+}$  ions into nanoparticles. The thioalkanes or amino alkanes present in the medium form a capping layer around Au nanoparticles through Au-S or Au-N bond. Herein also the variation of particle size can be affected by modulating the molar ratios of the gold salt, capping agent and the reductant.<sup>87</sup> Later several researchers have attempted to modify this strategy and still serving as the most popular ways for accessing metal NPs in non-aqueous medium.

### 1.8.1. Synthesis of anisotropic nanostructures



*Scheme 1.2. Schematic diagram of anisotropic nanoparticles*



The first anisotropic AuNPs such as hexagonal (icosahedral) and pentagonal (decahedral) shapes were synthesized in 1979 and 1981 by vapour phase deposition.<sup>88</sup> The first attempt to prepare rod-shaped AuNPs was reported by Wiesner and Wokaun in 1989, and involve the reduction of H<sub>2</sub>AuCl<sub>4</sub> solutions in presence of nanoparticle seeds.<sup>89</sup> The modern concept of seed-mediated synthesis was introduced by Murphy and co-workers. They synthesized AuNRs by treating nanoseeds (obtained via citrate reduction),

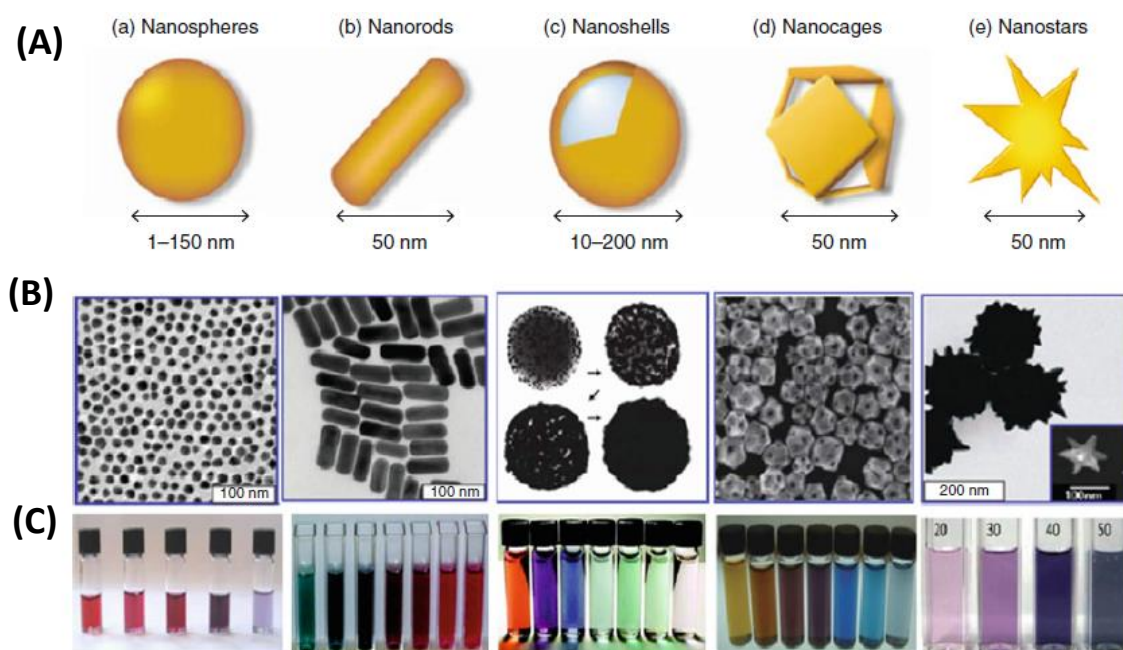


**Figure 1.16.** (A) Schematic representation (B) TEM images and (C) Color photographs of different types of anisotropic structures.<sup>90</sup>

Au(I) growth solution containing cetyltrimethyl ammonium bromide (CTAB) and Ag<sup>+</sup> ions.<sup>91</sup> Here in ascorbic acid was used as the reducing agent for the conversion of Au(III) to Au(I) and further conversion of which to AuNRs in presence of nanoseed. Till date, this method remains as the most efficient and popular one to synthesize anisotropic nanoparticles of desired shapes in high yields (Scheme1.2, Figure 1.16)

### **1.8.1.1. Synthesis of gold nanorods**

Generally, the synthesis of rod-shaped metal nanoparticles involves the reduction of their corresponding metal salts in presence of either rigid or soft templates and are called as 'hard template synthesis' and 'soft template synthesis' respectively. Both chemical and electrochemical reduction strategies have found to be effective in nanorods formation.<sup>95,96</sup> In electrochemical methods the cationic surfactants which favors the rod formation through soft templating also act the supporting electrolyte. The commonly used rigid templates include cylindrical pores of oxide or polymeric membranes.<sup>92,93</sup> Where as soft template utilizes neutral or charged surfactants which form rod-shaped hollow micelles under specific conditions/additives.<sup>94,95</sup> The most commonly used surfactants are of cationic nature, examples are cetyltrimethylammonium bromide (CTAB) (hydrophilic) and tetradecyl ammonium bromide (TDAB) (hydrophobic). In addition to these the other reported methods for Au nanorods are combined chemical-photochemical, solid support growth, and bio-reduction processes, etc. For example, Yamada and co-workers have suggested a combined chemical-photochemical method, wherein ascorbic acid first reduces  $\text{Au}^{\text{III}}$  to  $\text{Au}^{\text{I}}$  and its further conversion to  $\text{Au}^0$  was effected by UV light irradiation.<sup>96</sup>

Markovich and co-workers reported a surface assisted yet seed-mediated method for the preparation of gold nanorods. They produced nanorods directly on mica surfaces even without the need of silver nitrate<sup>97</sup> and the process was simple, it involves dipping of seed particles loaded mica into growth solution. They noted almost 15 % conversion of surface-bound seeds into nanorods and attributed this high yield to the change in the probability of nanoseeds to develop twinning defects. Later, Wei and coworkers have explored this method to grow nanorods on glass surfaces using a different linker molecule, MPTMS.<sup>98</sup>

### 1.8.1.2. Synthesis of gold nanostar

Similar to AuNRs another nanostructure that has emerged as a potential candidate is those having star-like shapes. Morphologically they consist of a central spherical core around which multiple numbers of sharp arms are protruding outside. With the recent advancements in the field large variety of procedures are available for efficient synthesis in solution.<sup>99</sup> As in the case of 1 D nanostructures the first attempts for their preparation were revolving around seed mediated growth process and considerable success has been made.<sup>100</sup> Vo-Dinh and coworkers demonstrated a simple and surfactant-free wet chemistry method for the production of monodisperse gold nanostars in high yield arise groups have attempted modifications using different surfactants and polymers (Figure 1.17). In addition to the surfactant other shapes directing agent,  $\text{AgNO}_3$ , also influence the size and morphology of the obtained AuNSs.<sup>101,102</sup>

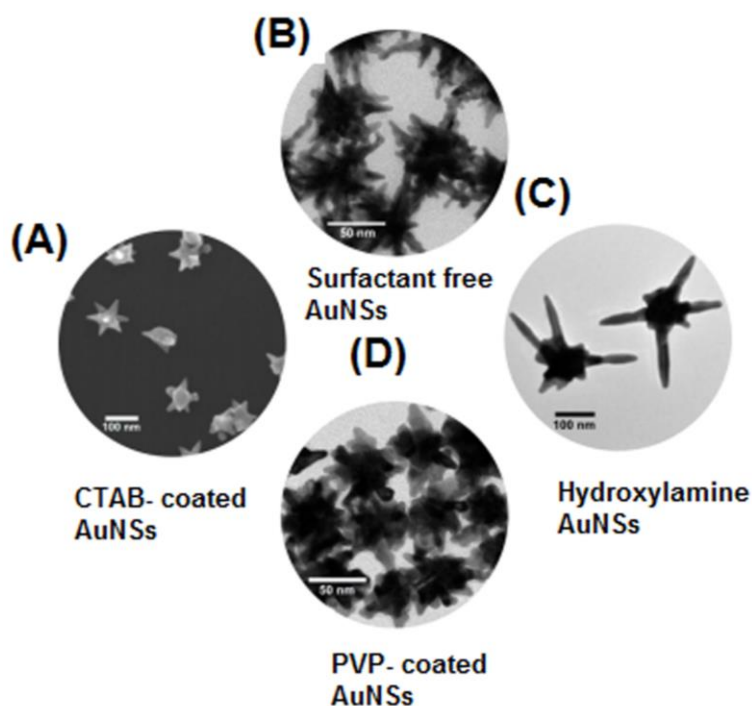


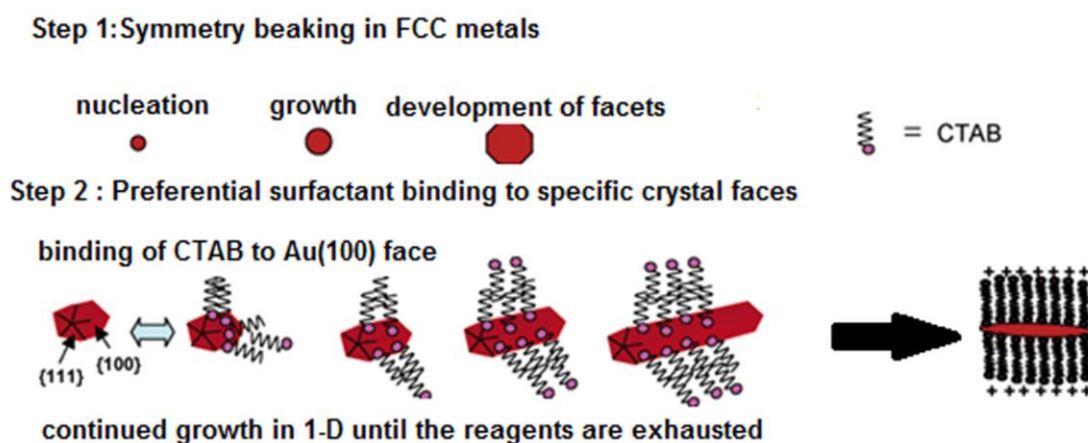
**Figure 1.17.** SEM (A) and TEM (B-D) images of synthesized AuNSs using different methods (A) CTAB templated, (B) Surfactant-free, (C) Hydroxylamine as reductant and (D) PVP-DMF assisted (adapted and modified from reference 103).<sup>103</sup>

Barbosa et al., reported an elegant method for the production of AuNSs in good yield and high monodispersity. This involves the reduction of  $\text{HAuCl}_4$  using a combination of N,N-dimethylformamide (DMF) and poly(vinylpyrrolidone) (PVP) in the presence of PVP-coated Au nanoseeds.<sup>104</sup> It was found that the reduction kinetics of  $\text{AuCl}_4^-$  on the Au seed surface plays a key role in the anisotropic growth, which in turn depends on the relative concentrations of DMF and PVP. Herein, also the ratio of  $[\text{AuCl}_4^-]/[\text{Au seed}]$  ratio also greatly influences the morphology, a decrease in the value yielded smaller particles. Further, the same method has been successfully extended to AuNWs or AuNRs for growing tips on them.<sup>105</sup>

However, one of the practical issues of using these surfactants/ polymers is that the resulting nanostructure will be inherently toxic limiting their bio-medical applications. This has necessitated the search for alternative synthetic strategies surfactant-free. Success has been made to produce star shaped nanoparticles without the aid of any shape directing surfactants. For instance, hydroxylamine has been used as a reducing agent for growing citrate stabilized gold nanoseeds into AuNSs.<sup>102,106</sup> Vo-Dinh and coworkers reported a simple, fast high yield, and surfactant-free wet synthesis procedure for AuNSs.<sup>76</sup> This involves the reduction of  $\text{HAuCl}_4$  with AA and  $\text{AgNO}_3$  in the absence of any other surfactant. Herein, in addition to  $\text{Ag}^+$  ions, hydrochloric acid (HCl) also playing a crucial role in the formation of Au nanostars, this means that as in the case of other halides ions, chlorides play a critical role in the anisotropic growth.<sup>107</sup> Later, This strategy has been successfully extended to produce unusual geometries such as Janus nanostars and others using hybrid nanoseeds.<sup>108,109</sup>

### 1.8.1.3. Growth mechanism of AuNRs

Several attempts have been made by researchers to probe and explain the mechanism pertaining to the 1D growth of Au nanorods (Scheme 1.3). One of the prominent ones is that proposed by Murphy and coworkers where they attribute the preferential 1D growth to a surfactant-mediated process.



**Scheme 1.3.** Schematic representation of different stages of AuNRs growth (adapted and modified from reference 110).<sup>110</sup>

According to this, CTAB has a preferential affinity to the (100) and (110) facets of Au crystals. This leaves only (111) edges for further addition of Au atoms and hence growth occurs only along this direction eventually leading to the 1D nanostructure.<sup>111</sup> Later, Perez-Juste et al. came up with an alternate pathway wherein electric field has a major role in the growth of Au nanorods. According to them, Au<sup>III</sup> ions are bound to the CTAB as an ionic pair which leaves reduced Au<sup>I</sup> ions confined in CTAB micelle.<sup>112</sup> For any further conversion of Au<sup>I</sup> to Au<sup>0</sup> requires its collision with nanoparticles. The slow collision rate as a result of bound Au<sup>I</sup>-CTAB state and the chances of higher electric fields at the already formed tips favours Au<sup>I</sup> reduction primarily at the termini promoting growth along one direction.

## **1.9. SERS substrates**

The development of an easy, sensitive and reliable sensing platform capable of detecting and identifying hazards including biological and chemicals, is one of the long-sought problems. In principle, vibrational spectroscopy provides fingerprint information about materials. However, the problem is with its sensitivity requiring large sample quantities and sophisticated equipment. With the recent developments in the field of signal processing methodologies and less expensive portable Raman spectrophotometers, Surface-enhanced Raman spectroscopy has evolved as one of the potential sensing technologies for chemicals and biomolecules.<sup>113,114</sup> This have found wide usability for various fields including the pharmaceutical industry, chemical industry, food industry, environment, pesticides, warfare agents detection, explosives detection, drug detection, and diagnosis. The major challenge here is the availability of a cheap, reproducible SERS active substrate with high uniformity and sensitivity. The available products in the market cost around 20\$ per substrate, which hinders their widespread utility, especially the countries like India. For obtaining the efficient SERS phenomenon, the support is nanoscale rough metal, the most used being silver, gold and to less extent, copper.

The enhancement factor of SERS is governed by a range of factors such as material, size, shape, and inter-plasmon coupling effect. In practice, besides the enhancement factor, many other aspects need to be covered to develop practical SERS substrates. This encompasses reproducibility, repeatability, scalability, throughput, shelf life, and cost. Over the course of the past two decades, numerous nanotechnology-related approaches have been explored in attempting to tackle these challenges.<sup>115</sup> Nanofabrication techniques for SERS substrates can be grouped into three main categories: lithography-based methods, nonlithographic template methods, and direct formation.<sup>116</sup> Various techniques adopted for depositing nanoparticles on to surfaces and thereby converting

them into SERS substrates include drop-casting, soaking, dip coating, filtration, screen-printing and inkjet printing (Figure 1.18).<sup>117</sup> However, major concerns with these simple processes are the random distribution of the generated hot spots over the surface and the reproducibility. To improve the consistency of hotspots, self-assembly and directed assembly techniques have been attempted. For example, Langmuir–Blodgett technique is found to be highly suitable, to create regular nanoparticle arrays.<sup>118</sup> However, the payback here is the introduction of more complexity.

To address this, there has been an immense effort from both academicians and corporates and can be broadly classified as chemical and physical approaches. In the chemical approach, nanoparticles are prepared in solution by chemical reduction method and are transferred to the substrate either by functionalization of the substrate or by optimizing the interparticle and or particle-surface interactions.<sup>119</sup> However, the issue here is to obtain uniform surface coverage with reproducibility. In 1995 Natan's group reported surface polymerization of trialkoxy silanes bearing nanoparticle anchoring groups such as -SH, -NH<sub>2</sub>, -CN or 2-pyridyls and subsequent solution-based self-assembly.<sup>120</sup> The surfaces thus produced had less than 10% variation in the signal intensity along with the different areas of the substrate. Later, several groups have extended this strategy using a different type of nanoparticles to the extent of their usability. The studies have also shown that the underlying substrate need not only be glass but others such as polydimethylsiloxane (PDMS), poly (vinyl alcohol) (PVA) nanofibers etc.<sup>121,122</sup> These enabled their easy integration into various sensing platform such as microfluidics.

In 2001, Nie's group adopted a nanoporous filtration technique wherein the size of pores is smaller than that of nanoparticles, thus producing the nanostructured thin film.<sup>123</sup> Their studies have shown that the SERS activity of the film is not only dependent on the

particle size but also on the laser irradiation wavelength. The substrates thus obtained had higher packing densities of hot spots and hence displayed greater overall SERS enhancement factors. In 2005, Naomi J. Halas and coworkers reported a simple drop-casting technique using 50 nm sized CTAB capped nanoparticles.<sup>69</sup> The electrostatic repulsion between the particles and size of the CTAB layer helped to produce uniform hexagonally packed nanoparticle arrays having <12 % standard deviation in signal intensity from point to point on the substrate and hitting a detection limit of ~50 nM. The other successful approach is the Langmuir–Blodgett method; wherein 2-D arrays of nanostructures can be produced at the air-liquid interface. For example, the group of Peidong Yang used this technique to assemble monolayers of silver nanowires over large areas (~20 cm<sup>2</sup>) with very high reproducibility and enhancement factors (~10<sup>9</sup>).<sup>124</sup> Yet another successful strategy is the printing techniques where presynthesized nanoparticles are first formulated into ink which can then subsequently either inkjet<sup>125</sup> or screen printed<sup>126</sup> on to a wide variety of substrates, then subsequently either either inkjet<sup>125</sup> or

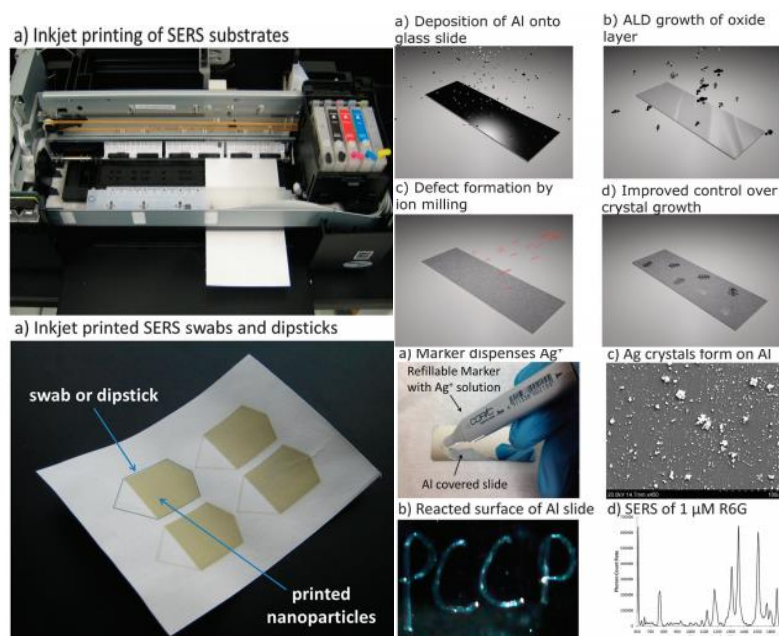


**Figure 1.18.** Fabrication of different kinds of SERS active substrates.<sup>125,126</sup>



screen printed<sup>126</sup> on to a wide variety of substrates, and it has been demonstrated that detection limit can be as low as Femto moles. The main advantage here is high throughput, cost-effectiveness and highly suitable for large-scale productions.

Parallely, there have been attempts to fabricate SERS substrate via physical methods. These mainly include lithographic, and template approaches and the main advantages here are the high levels of control and reproducibility. For example, the anodic membrane of porous aluminum oxide (AAO) has been extensively utilized as a template to prepare aligned nanowires via metal deposition.<sup>127</sup> Van Duyne and co-workers pioneered nanosphere lithography (NSL). This process involves depositing a monolayer of close-packed silica or polystyrene spheres by spin or drop casting onto a substrate followed by metal evaporation. Later, this method has evolved to be as one of the most successful low-cost fabrication techniques yielding  $EF > 10^8$ .<sup>128</sup> The peculiar property of block copolymers in self-assembling to form soft templates of spherical, cylindrical and lamellar morphologies with typical dimensions 5-50 nm have also been employed for the fabrication of SERS substrates. These soft templates can be used to obtain highly ordered metallic nanostructures by several methods, including vapor deposition, electrodeposition, or incorporation of metal nanoparticles.<sup>129</sup>

Electron beam lithography is another powerful tool for making nanoscale patterns with extreme control and precision.<sup>130</sup> Even though scientifically this is an elegant process to create patterns with resolution  $< 1$  nm, from a practical point of view, the drawbacks are slow and high cost. For example, Andrea Toma et al. has fabricated 3D nanostar dimers with a sub 10 nm gap with which they were able to achieve single molecular sensitivity.<sup>131</sup>

## **1.10. The objective of the present work**

The overall focus of this thesis is (i) to exploit the greener synthetic route for the synthesis of anisotropic nanostructures, (ii) to use spectroscopic tools as the first measure for nanoparticle formation and (iii) undertake detailed spectroscopic and morphological studies in light of their potential application in the apt field. The second chapter deals with the synthesis of one-dimensional biocompatible gold nanorods with natural antioxidants. Herein, we utilized photon to the thermal conversion efficiency of nanorods for photothermal treatments. The synthesis of multi-branched gold nanocrystals and their bioimaging and photothermal treatments efficiency are detailed in the third chapter. In both these chapters, we exploited the Raman enhancement capability of these anisotropic nanostructures to study the photo-induced break down of cells. We have designed a low-cost process for the preparation of SERS substrates via galvanic replacement reaction, and its sensing applications are explained in the fourth chapter.

## **1.11 References**

- (1) Jun, T.; Yong-Hua, L.; Rong-Sheng, Z.; Kai-Qun, L.; Zhi-Guo, X.; Zhao-Feng, L.; Sheng-Li, L.; Pei, W.; Hai, M. *Chinese Physics Letters* **2008**, *25*, 4459-4462.
- (2) Patching, S. G. *Biochimica et Biophysica Acta (BBA) - Biomembranes* **2014**, *1838*, 43-55.
- (3) Zhuo, Y.; Yuan, R.; Chai, Y. Q.; Zhang, Y.; Li, X. L.; Zhu, Q.; Wang, N. *Analytica Chimica Acta* **2005**, *548*, 205-210.
- (4) <https://www.azonano.com/article.aspx?ArticleID=3012>.
- (5) Chung, T.; Lee, S. Y.; Song, E. Y.; Chun, H.; Lee, B. *Sensors* **2011**, *11*, 10907-10929.

- (6) Wang, A. X.; Kong, X. M. *Materials* **2015**, *8*, 3024-3052.
- (7) Chao, J.; Lin, Y.; Liu, H.; Wang, L.; Fan, C. *Materials Today* **2015**, *18*, 326-335.
- (8) Alabastri, A.; Tuccio, S.; Giugni, A.; Toma, A.; Liberale, C.; Das, G.; De Angelis, F.; Di Fabrizio, E.; Zaccaria, R. P. *Materials* **2013**, *6*, 4879-4910.
- (9) Cobley, C. M.; Chen, J. Y.; Cho, E. C.; Wang, L. V.; Xia, Y. N. *Chemical Society Reviews* **2011**, *40*, 44-56.
- (10) Link, S.; El-Sayed, M. A. *The Journal of Physical Chemistry B* **1999**, *103*, 4212-4217.
- (11) Noguez, C. *The Journal of Physical Chemistry C* **2007**, *111*, 3806-3819.
- (12) Nehl, C. L.; Hafner, J. H. *Journal of Materials Chemistry* **2008**, *18*, 2415-2419.
- (13) Hao, E.; Bailey, R. C.; Schatz, G. C.; Hupp, J. T.; Li, S. *Nano Letters* **2004**, *4*, 327-330.
- (14) Mulvaney, P. *Langmuir* **1996**, *12*, 788-800.
- (15) Thomas, K. G.; Zajicek, J.; Kamat, P. V. *Langmuir* **2002**, *18*, 3722-3727.
- (16) El-Sayed, M. A. *Accounts of Chemical Research* **2001**, *34*, 257-264.
- (17) Burda, C.; Chen, X.; Narayanan, R.; El-Sayed, M. A. *Chemical Reviews* **2005**, *105*, 1025-1102.
- (18) Shenhar, R.; Rotello, V. M. *Accounts of Chemical Research* **2003**, *36*, 549-561.
- (19) Rodríguez-Oliveros, R.; Sánchez-Gil, J. A. *Optical Express* **2012**, *20*, 621-626.
- (20) Kim, T.; Lee, K.; Gong, M.-s.; Joo, S.-W. *Langmuir* **2005**, *21*, 9524-9528.

- (21) Kim, H. N.; Ren, W. X.; Kim, J. S.; Yoon, J. *Chemical Society Reviews* **2012**, *41*, 3210-3244.
- (22) Liang, H.; Zhao, H.; Rossouw, D.; Wang, W.; Xu, H.; Botton, G. A.; Ma, D. *Chemistry of Materials* **2012**, *24*, 2339-2346.
- (23) Kong, B.; Zhu, A.; Luo, Y.; Tian, Y.; Yu, Y.; Shi, G. *Angewandte Chemie International Edition* **2011**, *50*, 1837-1840.
- (24) Slocik, J. M.; Zabinski Jr., J. S.; Phillips, D. M.; Naik, R. R. *Small* **2008**, *4*, 548-551.
- (25) Daniel, W. L.; Han, M. S.; Lee, J.-S.; Mirkin, C. A. *Journal of the American Chemical Society* **2009**, *131*, 6362-6363.
- (26) Storhoff, J. J.; Elghanian, R.; Mucic, R. C.; Mirkin, C. A.; Letsinger, R. L. *Journal of the American Chemical Society* **1998**, *120*, 1959-1964.
- (27) Kim, Y.; Johnson, R. C.; Hupp, J. T. *Nano Letters* **2001**, *1*, 165-167.
- (28) Giljohann, D. A.; Seferos, D. S.; Daniel, W. L.; Massich, M. D.; Patel, P. C.; Mirkin, C. A. *Angewandte Chemie International Edition* **2010**, *49*, 3280-3294.
- (29) Xue, X.; Wang, F.; Liu, X. *Journal of the American Chemical Society* **2008**, *130*, 3244-3245.
- (30) Chu, J.; Park, C.; Jang, K.; Shim, J. H.; Na, S. *Journal of Mechanical Science and Technology* **2018**, *32*, 799-804.
- (31) Rex, M.; Hernandez, F. E.; Campiglia, A. D. *Analytical Chemistry* **2006**, *78*, 445-451.
- (32) Beseničar, M.; Maček, P.; Lakey, J. H.; Anderluh, G. *Chemistry and Physics of Lipids* **2006**, *141*, 169-178.
- (33) Cooper, M. A. *Journal of Molecular Recognition* **2004**, *17*, 286-315.

- (34) Chowdhury, S.; Wu, Z.; Jaquins-Gerstl, A.; Liu, S.; Dembska, A.; Armitage, B. A.; Jin, R.; Peteanu, L. A. *The Journal of Physical Chemistry C* **2011**, *115*, 20105-20112.
- (35) Medintz, I. L.; Clapp, A. R.; Mattoussi, H.; Goldman, E. R.; Fisher, B.; Mauro, J. M. *Nature Materials* **2003**, *2*, 630-638.
- (36) Oh, E.; Hong, M.-Y.; Lee, D.; Nam, S.-H.; Yoon, H. C.; Kim, H.-S. *Journal of the American Chemical Society* **2005**, *127*, 3270-3271.
- (37) Alagiri, M.; Rameshkumar, P.; Pandikumar, A. *Microchimica Acta* **2017**, *184*, 3069-3092.
- (38) Liu, T. M.; Conde, J.; Lipinski, T.; Bednarkiewicz, A.; Huang, C. C. *Npg Asia Materials* **2016**, *8*.
- (39) Xu, C.; Zhao, C. Q.; Li, M.; Wu, L.; Ren, J. S.; Qu, X. G. *Small* **2014**, *10*, 1841-1847.
- (40) Gobin, A. M.; Watkins, E. M.; Quevedo, E.; Colvin, V. L.; West, J. L. *Small* **2010**, *6*, 745-752.
- (41) Hainfeld, J. F.; O'Connor, M. J.; Lin, P.; Qian, L. P.; Slatkin, D. N.; Smilowitz, H. M. *Plos One* **2014**, *9*, 2
- (42) de Puig, H.; Tam, J. O.; Yen, C.-W.; Gehrke, L.; Hamad-Schifferli, K. *Nanomaterial Interfaces* **2015**, *119*, 17408-17415.
- (43) Park, K.; Biswas, S.; Kanel, S.; Nepal, D.; Vaia, R. A. *The Journal of Physical Chemistry C* **2014**, *118*, 5918-5926.
- (44) Near, R. D.; Hayden, S. C.; Hunter, R. E.; Thackston, D.; El-Sayed, M. A. *The Journal of Physical Chemistry C* **2013**, *117*, 23950-23955.
- (45) Singh, K.; Sandhu, G. K.; Lark, B. S. *Pramana* **2004**, *62*, 1139.

- (46) Tsoulos, T. V.; Han, L.; Weir, J.; Xin, H. L.; Fabris, L. *Nanoscale* **2017**, *9*, 3766-3773.
- (47) Schultz, S.; Smith, D. R.; Mock, J. J.; Schultz, D. A. *Proceedings of the National Academy of Sciences* **2000**, *97*, 996-1001.
- (48) Jain, P. K.; Lee, K. S.; El-Sayed, I. H.; El-Sayed, M. A. *Journal of Physical Chemistry B* **2006**, *110*, 7238-7248.
- (49) Bibikova, O.; Popov, A.; Bykov, A.; Fales, A.; Yuan, H.; Skovorodkin, I.; Kinnunen, M.; Vainio, S.; Vo-Dinh, T.; Tuchin, V. V.; Meglinski, I. *IEEE Journal of Selected Topics in Quantum Electronics* **2016**, *22*, 13-20.
- (50) Reguera, J.; Langer, J.; de Aberasturi, D. J.; Liz-Marzan, L. M. *Chemical Society Reviews* **2017**, *46*, 3866-3885.
- (51) Yu, H.; Peng, Y.; Yang, Y.; Li, Z.-Y. *npj Computational Materials* **2019**, *5*, 45.
- (52) Gersten, J.; Nitzan, A. *The Journal of Chemical Physics* **1981**, *75*, 1139-1152.
- (53) Ren, Z.; Li, X.; Guo, J.; Wang, R.; Wu, Y.; Zhang, M.; Li, C.; Han, Q.; Dong, J.; Zheng, H. *Optics Communications* **2015**, *357*, 156-160.
- (54) Theodorou, I. G.; Jawad, Z. A. R.; Jiang, Q.; Aboagye, E. O.; Porter, A. E.; Ryan, M. P.; Xie, F. *Chemistry of Materials* **2017**, *29*, 6916-6926.
- (55) Fleischmann, M.; Hendra, P. J.; McQuillan, A. J. *Chemical Physics Letters* **1974**, *26*, 163-166.
- (56) Jeanmaire, D. L.; Van Duyne, R. P. *Journal of Electroanalytical Chemistry and Interfacial Electrochemistry* **1977**, *84*, 1-20.
- (57) Sharma, B.; Frontiera, R. R.; Henry, A.-I.; Ringe, E.; Van Duyne, R. P. *Materials Today* **2012**, *15*, 16-25.

- (58) Schatz, G. C. *Accounts of Chemical Research* **1984**, *17*, 370-376.
- (59) Martin, M. *Journal of Raman Spectroscopy* **2005**, *36*, 485-496.
- (60) Otto, A.; Mrozek, I.; Grabhorn, H.; Akemann, W. *Journal of Physics: Condensed Matter* **1992**, *4*, 1143.
- (61) Andreas, O. *Journal of Raman Spectroscopy* **2005**, *36*, 497-509.
- (62) S., Y. Y.; Tamitake, I. *Journal of Raman Spectroscopy* **2016**, *47*, 78-88.
- (63) Mosier-Boss, P. A. *Nanomaterials* **2017**, *7*, 142.
- (64) Zhao, Y.; Zhang, Y. J.; Meng, J. H.; Chen, S.; Panneerselvam, R.; Li, C. Y.; Jamali, S. B.; Li, X.; Yang, Z. L.; Li, J. F.; Tian, Z. Q. *Journal of Raman Spectroscopy* **2016**, *47*, 662-667.
- (65) Ding, S. Y.; You, E. M.; Tian, Z. Q.; Moskovits, M. *Chemical Society Reviews* **2017**, *46*, 4042-4076.
- (66) Israelsen, N. D.; Hanson, C.; Vargis, E. *The Scientific World Journal* **2015**, *2015*, 12.
- (67) Ming, L.; Scott, K. C.; Jianming, Z.; Jessica, L.; Zoraida, P. A.; Dongling, M.; Nianqiang, W. *Nanotechnology* **2012**, *23*, 115501.
- (68) Liu, K.-K.; Tadepalli, S.; Wang, Z.; Jiang, Q.; Singamaneni, S. *Analyst* **2017**, *142*, 4536-4543.
- (69) Wang, H.; Levin, C. S.; Halas, N. J. *Journal of the American Chemical Society* **2005**, *127*, 14992-14993.
- (70) Brouers, F.; Blacher, S.; N. Lagarkov, A.; Sarychev, A.; Gadenne, P.; M. Shalaev, V. *Theory of giant Raman scattering from semicontinuous metal films*, 1997; Vol. 55.
- (71) Ren, Y. T.; Chen, Q.; Qi, H.; Ruan, L. M. *Nanomaterials* **2017**, *7*, 416.

- (72) Hirsch, L. R.; Stafford, R. J.; Bankson, J. A.; Sershen, S. R.; Rivera, B.; Price, R. E.; Hazle, J. D.; Halas, N. J.; West, J. L. *Proceedings of the National Academy of Sciences of the United States of America* **2003**, *100*, 13549-13554.
- (73) El-Sayed, I. H.; Huang, X. H.; El-Sayed, M. A. *Cancer Letters* **2006**, *239*, 129-135.
- (74) Wang, X.; Li, G.; Ding, Y.; Sun, S. *RSC Advances* **2014**, *4*, 30375-30383.
- (75) D'Hollander, A.; Mathieu, E.; Jans, H.; Vande Velde, G.; Stakenborg, T.; Van Dorpe, P.; Himmelreich, U.; Lagae, L. *Int J Nanomedicine* **2016**, *11*, 3703-3714.
- (76) Yuan, H.; Khoury, C. G.; Hwang, H.; Wilson, C. M.; Grant, G. A.; Vo-Dinh, T. *Nanotechnology* **2012**, *23*, 075102-075102.
- (77) Wang, Y.; Xia, Y. *Nano Letters* **2004**, *4*, 2047-2050.
- (78) Biswas, A.; Bayer, I. S.; Biris, A. S.; Wang, T.; Dervishi, E.; Faupel, F. *Advances in Colloid and Interface Science* **2012**, *170*, 2-27.
- (79) Sun, S.; Mendes, P.; Critchley, K.; Diegoli, S.; Hanwell, M.; Evans, S. D.; Leggett, G. J.; Preece, J. A.; Richardson, T. H. *Nano Letters* **2006**, *6*, 345-350.
- (80) Corbierre, M. K.; Beerens, J.; Lennox, R. B. *Chemistry of Materials* **2005**, *17*, 5774-5779.
- (81) Yue, W. S.; Wang, Z. H.; Yang, Y.; Chen, L. Q.; Syed, A.; Wong, K.; Wang, X. B. *Journal of Micromechanics and Microengineering* **2012**, *22*, 125007.
- (82) Wang, H.; Qiao, X.; Chen, J.; Ding, S. *Colloids and Surfaces A: Physicochemical and Engineering Aspects* **2005**, *256*, 111-115.



- (83) Saez, V.; Mason, T. J. *Molecules* **2009**, *14*, 4284-4299.
- (84) Khaydarov, R. A.; Khaydarov, R. R.; Gapurova, O.; Estrin, Y.; Scheper, T. *Journal of Nanoparticle Research* **2009**, *11*, 1193-1200.
- (85) Scaiano, J. C.; Billone, P.; Gonzalez, C. M.; Maretta, L.; Marin, M. L.; McGilvray, K. L.; Yuan, N. *Pure and Applied Chemistry* **2009**, *81*, 635-647.
- (86) Turkevich, J.; Stevenson, P. C.; Hillier, J. *Discussions of the Faraday Society* **1951**, *11*, 55-75.
- (87) Brust, M.; Walker, M.; Bethell, D.; Schiffrin, D. J.; Whyman, R. *Journal of the Chemical Society, Chemical Communications* **1994**, 801-802.
- (88) Renou, A.; Gillet, M. *Surface Science* **1981**, *106*, 27-34.
- (89) Wiesner, J.; Wokaun, A. *Chemical Physics Letters* **1989**, *157*, 569-575.
- (90) Kumar, A.; Liang, X.-J. In *Encyclopedia of Metalloproteins*; Kretsinger, R. H., Uversky, V. N., Permyakov, E. A., Eds.; Springer New York: New York, NY, 2013; pp 875-887.
- (91) R., J. N.; L., G.; J., M. C. *Advanced Materials* **2001**, *13*, 1389-1393.
- (92) Li, Z.; Kübel, C.; Pârvulescu, V. I.; Richards, R. *ACS Nano* **2008**, *2*, 1205-1212.
- (93) Xie, Y. D.; Kocaefe, D.; Chen, C. Y.; Kocaefe, Y. *Journal of Nanomaterials* **2016**, *2016*, 1-10.
- (94) Pallares, R. M.; Su, X.; Lim, S. H.; Thanh, N. T. K. *Journal of Materials Chemistry C* **2016**, *4*, 53-61.
- (95) Kang, L.; Yanru, B.; Yuanhui, Z.; Xuchuan, J.; Aibing, Y.; Huanting, W. *Chemistry – A European Journal* **2017**, *23*.

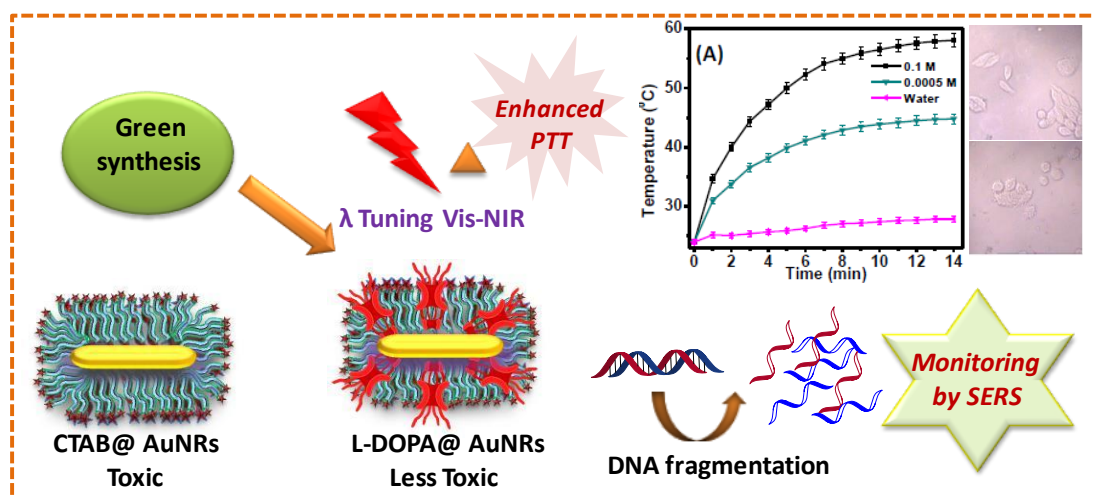
- (96) Niidome, Y.; Nishioka, K.; Kawasaki, H.; Yamada, S. *Chemical Communications* **2003**, 2376-2377.
- (97) Taub, N.; Krichevski, O.; Markovich, G. *The Journal of Physical Chemistry B* **2003**, *107*, 11579-11582.
- (98) Wei, Z.; Mieszawska, A. J.; Zamborini, F. P. *Langmuir* **2004**, *20*, 4322-4326.
- (99) Dondapati, S. K.; Sau, T. K.; Hrelescu, C.; Klar, T. A.; Stefani, F. D.; Feldmann, J. *ACS Nano* **2010**, *4*, 6318-6322.
- (100) Nikoobakht, B.; El-Sayed, M. A. *Chemistry of Materials* **2003**, *15*, 1957-1962.
- (101) Wu, H.-L.; Chen, C.-H.; Huang, M. H. *Chemistry of Materials* **2009**, *21*, 110-114.
- (102) Yuan, H.; Ma, W.; Chen, C.; Zhao, J.; Liu, J.; Zhu, H.; Gao, X. *Chemistry of Materials* **2007**, *19*, 1592-1600.
- (103) Nehl, C. L.; Liao, H.; Hafner, J. H. *Nano Letters* **2006**, *6*, 683-688.
- (104) Barbosa, S.; Agrawal, A.; Rodríguez-Lorenzo, L.; Pastoriza-Santos, I.; Alvarez-Puebla, R. A.; Kornowski, A.; Weller, H.; Liz-Marzán, L. M. *Langmuir* **2010**, *26*, 14943-14950.
- (105) Pazos-Pérez, N.; Barbosa, S.; Rodríguez-Lorenzo, L.; Aldeanueva-Potel, P.; Pérez-Juste, J.; Pastoriza-Santos, I.; Alvarez-Puebla, R. A.; Liz-Marzán, L. M. *The Journal of Physical Chemistry Letters* **2010**, *1*, 24-27.
- (106) Pandian, S.; Pastoriza-Santos, I.; Rodríguez-González, B.; Garcia de Abajo, J.; Liz-Marzán, L. *High-yield synthesis and optical response of gold nanostars*, 2008; Vol. 19.

- (107) Marek, G.; Ana, S. I.; Benito, R. G.; Ramón, A. P.; Jorge, P. J.; M., L. M. *L. Advanced Functional Materials* **2008**, *18*, 3780-3786.
- (108) Rodriguez-Fernandez, D.; Altantzis, T.; Heidari, H.; Bals, S.; Liz-Marzan, L. M. *Chemical Communications* **2014**, *50*, 79-81.
- (109) Sanz-Ortiz, M. N.; Sentosun, K.; Bals, S.; Liz-Marzán, L. M. *ACS Nano* **2015**, *9*, 10489-10497.
- (110) Li, N.; Zhao, P. X.; Astruc, D. *Angewandte Chemie-International Edition* **2014**, *53*, 1756-1789.
- (111) Murphy, C. J.; Sau, T. K.; Gole, A. M.; Orendorff, C. J.; Gao, J.; Gou, L.; Hunyadi, S. E.; Li, T. *The Journal of Physical Chemistry B* **2005**, *109*, 13857-13870.
- (112) J., P. J.; M., L. M. L.; S., C.; C., C. D. Y.; P., M. *Advanced Functional Materials* **2004**, *14*, 571-579.
- (113) Patra, P. P.; Chikkaraddy, R.; Tripathi, R. P. N.; Dasgupta, A.; Kumar, G. V. P. *Nature Communications* **2014**, *5*, 4357.
- (114) Wang, Y.; Irudayaraj, J. *Philosophical Transactions of the Royal Society B: Biological Sciences* **2013**, *368*, 20120026.
- (115) Sun, X.; Li, H. *Current Nanoscience* **2016**, *12*, 175-183.
- (116) Mosier-Boss, P. A. *Nanomaterials* **2017**, *7*.
- (117) Betz, J. F.; Yu, W. W.; Cheng, Y.; White, I. M.; Rubloff, G. W. *Physical Chemistry Chemical Physics* **2014**, *16*, 2224-2239.
- (118) Mahmoud, M. A.; Tabor, C. E.; El-Sayed, M. A. *Journal of Physical Chemistry C* **2009**, *113*, 5493-5501.
- (119) Bich, H. N.; Van Hieu, N.; Hong, N. T. *Advances in Natural Sciences-Nanoscience and Nanotechnology* **2016**, *7*.

- (120) Freeman, R. G.; Grabar, K. C.; Allison, K. J.; Bright, R. M.; Davis, J. A.; Guthrie, A. P.; Hommer, M. B.; Jackson, M. A.; Smith, P. C.; Walter, D. G.; Natan, M. J. *Science* **1995**, *267*, 1629-1632.
- (121) Fortuni, B.; Inose, T.; Uezono, S.; Toyouchi, S.; Umemoto, K.; Sekine, S.; Fujita, Y.; Ricci, M.; Lu, G.; Masuhara, A.; Hutchison, J. A.; Latterini, L.; Uji-i, H. *Chemical Communications* **2017**, *53*, 11298-11301.
- (122) He, D.; Hu, B.; Yao, Q.-F.; Wang, K.; Yu, S.-H. *ACS Nano* **2009**, *3*, 3993-4002.
- (123) Maxwell, D. J.; Emory, S. R.; Nie, S. M. *Chemistry of Materials* **2001**, *13*, 1082-1088.
- (124) Tao, A.; Kim, F.; Hess, C.; Goldberger, J.; He, R. R.; Sun, Y. G.; Xia, Y. N.; Yang, P. D. *Nano Letters* **2003**, *3*, 1229-1233.
- (125) Yu, W. W.; White, I. M. *Analytical Chemistry* **2010**, *82*, 9626-9630.
- (126) Qu, L. L.; Li, D. W.; Xue, J. Q.; Zhai, W. L.; Fossey, J. S.; Long, Y. T. *Lab on a Chip* **2012**, *12*, 876-881.
- (127) Lee, S. J.; Morrill, A. R.; Moskovits, M. *Journal of the American Chemical Society* **2006**, *128*, 2200-2201.
- (128) McFarland, A. D.; Young, M. A.; Dieringer, J. A.; Van Duyne, R. P. *Journal of Physical Chemistry B* **2005**, *109*, 11279-11285.
- (129) Shen, Y.; Liu, Y.; Wang, W.; Xu, F.; Yan, C.; Zhang, J.; Wang, J.; Yuan, A. *Rsc Advances* **2016**, *6*, 38716-38723.
- (130) Gunnarsson, L.; Bjerneld, E. J.; Xu, H.; Petronis, S.; Kasemo, B.; Kall, M. *Applied Physics Letters* **2001**, *78*, 802-804.

- (131) Chirumamilla, M.; Toma, A.; Gopalakrishnan, A.; Das, G.; Zaccaria, R. P.; Krahne, R.; Rondanina, E.; Leoncini, M.; Liberale, C.; De Angelis, F.; Di Fabrizio, E. *Advanced Materials* **2014**, *26*, 2353-2358.

## Synthesis of Biocompatible Gold Nanorods and its Application in Cancer Nanotheranostics



### 2.1. Abstract

Gold nanorods (AuNRs) are one of the important classes of nanomaterials being widely utilized in areas like sensing, imaging, photo-electronics and therapeutics. The major drawback of the presently available methodologies for its synthesis is the use of high concentration of CTAB which is known to be cytotoxic. Herein, we investigate the efficacy of three natural antioxidants, L-DOPA, DHCA and gallic acid, in nanorod synthesis. The initial studies revealed that, among the three, L-DOPA supports the formation of longer rods with highly red-shifted plasmon absorption ( $LSPR_{max} = 930 \text{ nm}$ ). Also, through systematic experiments, nanorods were prepared at CTAB concentrations down to 0.5 mM which is  $\sim 200$  times less than the conventional procedure. Notably, the nanorods formed here are thinner (6-10 nm diameter) and the LSPR absorption underwent a gradual shift to  $>1100 \text{ nm}$ . Further, the wider tunability of plasmon absorption in both bio-optical windows (630 nm to 1260 nm) was demonstrated by

*modulating the added volumes of AgNO<sub>3</sub>. However, at reduced CTAB concentrations, blueshift in LSPR position with diminishing nanorod yield have been observed for ascorbic acid, gallic acid and DHCA. Additionally, IR analysis clearly implied efficient intercalation of L-DOPA with CTAB layer. This helped to considerably reduce CTAB concentration thus making nanorods synthesis greener. Also, AuNRs produced herein exhibits superior SERS activity with a decrease in CTAB concentration. Further, by combing this with their high SERS activity and photon to thermal conversion efficiency, employed them in the destruction of cancer cells and followed the biochemical changes through Raman spectroscopy.*

## **2.2. Introduction**

Among the plasmonic nanomaterials of gold, nanorods are one dimensional systems having promising optical properties which are highly utilized in various fields including sensing, imaging, photo-electronics and therapeutics.<sup>1-6</sup> The light absorption range can be widely tuned in the VIS-NIR range just by adjusting its aspect ratio (Figure 2.1).<sup>7-9</sup> The other advantages are (i) efficient large-scale synthesis, (ii) easy functionalization, and (iii) colloidal stability.<sup>10-12</sup> Also, when irradiated with suitable light, AuNRs exhibits high photon-to-thermal conversion efficiency. This is due to the nonradiative relaxation of excited plasmons which makes them wonderful candidate for photothermal therapeutics and found to be efficient in treating various cancers.<sup>1,13-15</sup>

The gold nanorods possess a high extinction coefficient and scattering efficiency compared to spherical nanoparticles. Plasmon excitation of gold nanorods results in the generation of high optical near fields and localized electric fields. Materials placed in such near field exhibit high enhancement in optical

activities such as absorption, fluorescence and Raman scattering.<sup>16-18</sup> This has resulted in high sensitivity and the detection limit can be pushed even to single molecular level. They also have been applied in boosting the efficiency of advanced optoelectronic devices such as solar cells and light-emitting diodes.

### 2.2.1. Synthetic approaches

The unique one dimensional morphology imposes challenges to its preparation. Compared to their spherical counterparts, 1D nanostructures are energetically less favoured. Hence inducing anisotropy during nanoparticle growth is challenging. The seed mediated method introduced by Jana et al. in 2001 was one of the breakthroughs for AuNRs synthesis. Till now, due to its simplicity and scalability, this remains the most efficient and commonly used synthetic methods.<sup>19</sup>

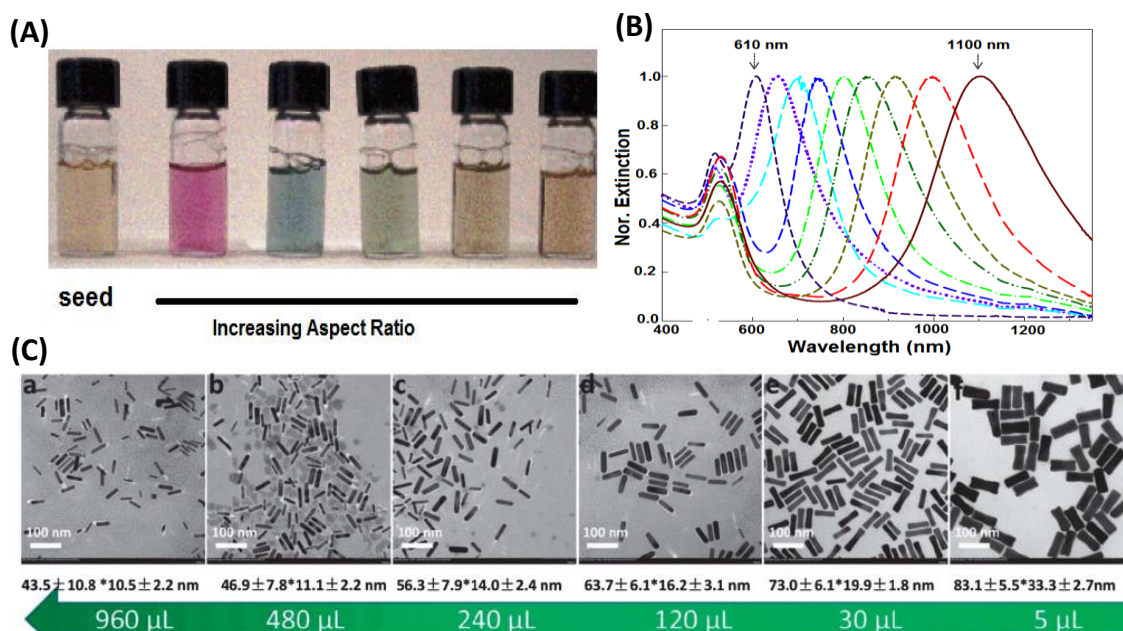


**Figure 2.1.** Examples of (A) The colour photograph,<sup>20</sup> (B) The extinction spectra<sup>21</sup> and (C) TEM images<sup>22</sup> of AuNRs with different aspect ratios.



The major ingredients used herein are nanoseed, Au (III) ions, ascorbic acid (reductant), the surfactant CTAB, and AgNO<sub>3</sub> (the last two act as shape directing agents).

In 2003, Nikoobakht and El-Sayed achieved a significant improvement in seed mediated synthesis by introducing CTAB capped seed instead of citrate.<sup>23</sup> The cationic surfactant, cetyltrimethylammonium bromide (CTAB) consists of a polar quaternary ammonium head group and a 16 carbon long tail. This forms a bilayer structure around AuNRs, in an interdigitating fashion pointing out the polar head groups on either side. Most probably the inner layer is bound to the NRs surface through the head groups and is linked to the outer layer via interdigitation of the alkyl chains through hydrophobic interactions. Thus, the polar head groups of the outer layer are free to interact with the water molecules of the aqueous medium (Figure 2.2).<sup>24</sup> The main advantage of capping seed with CTAB instead of citrated is that it helps to increase the compatibility with the soft template which is CTAB itself. Thus, the seed can easily migrate to it, become part of it and facilitate the growth through diffusion of gold atoms into the template. This improves the quality, yield, and tunability of aspect ratio of AuNRs.

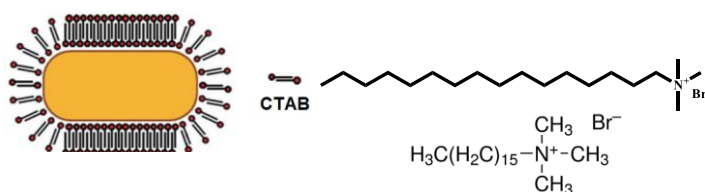


**Figure 2.2.** Schematic representation of CTAB bilayer on the surface of AuNRs.<sup>25</sup>

### 2.2.1.1. The major challenges

However, there are a few drawbacks to this well exploited synthetic approach and are explained as follows.

2.2.1.1.1. **Need for the high concentration of CTAB:** Though the critical micellar concentration of CTAB is 1 mM at 25 °C,<sup>26</sup> an almost 100 times higher concentration is required for the preparation of AuNRs in reasonable yield and its stabilization in aqueous medium. CTAB is known to be a toxic surfactant, posing both environmental as well as occupational health issues. Moreover, it prevents the direct utilization of gold nanorods into bio-phonic applications. Studies have clearly nailed down to the conclusion that the toxicity of AuNRs arises from its capping ligand CTAB. Therefore, many post-synthetic treatments have been proposed and successfully employed. One approach is the surface coating of AuNRs with biocompatible molecules such as PEG, PSS,<sup>8</sup> PAH, PAA<sup>27</sup> or their combinations which considerably enhanced cell viability. In 2015, Wen et al., compared the toxicity of CTAB capped AuNRs and surface modifications with other polymers in HCT116 colon cancer cells and BEL 7402 human hepatocellular cancer cells. They found that only 20-40 % of cells are viable when interacting with CTAB-AuNRs whereas the cell viability considerably increased upon surface overcoating (Figure 2.3).<sup>28</sup>

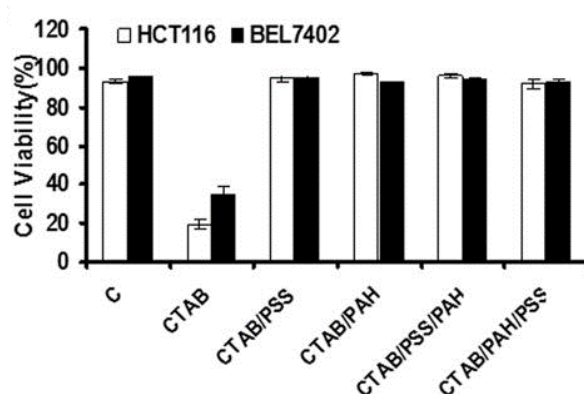


**Figure 2.3.** Graph showing the cell viability of HCT116 and BEL 7402 cells treated with AuNRs having different surface coatings.<sup>28</sup>

Yet, another approach is to coat with inorganic passivates, one example is silica coating reported by Liz-Marzán et al.<sup>29</sup> on AuNRs surface to form an Au/silica

core/shell structure. This can be done by the reagents such as (3-mercaptopropyl) trimethoxysilane (MPTMS) solution or 3-mercaptopropyl triethoxysilane (MPTES) (Figure 2.4). In 2015 An et al., done the detailed studies on the biocompatibility of silica-coated AuNRs and found that the toxicity effect of CTAB can be reduced by coating with silica polymer.<sup>30</sup>

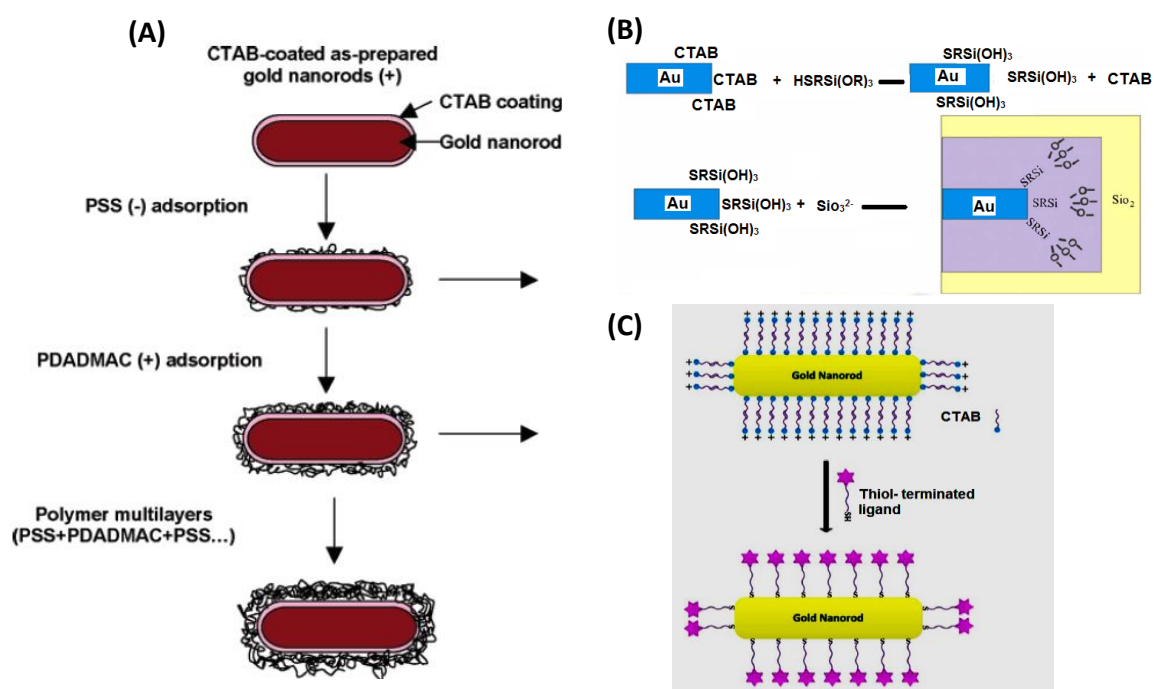


**Figure 2.4.** Schematic representation of a surface modification of AuNRs with (A) Polyelectrolyte<sup>31</sup> (B) Silica(adapted and remodified from reference 32)<sup>32</sup> and (C) Thiol-terminated ligands.<sup>6</sup>

### 2.2.1.1.2. Demerits of post-synthetic method

Upon the replacement of surfactant with thiol-terminated ligands that strongly bind to the AuNRs surface via Au-S covalent bonds, the chances of aggregation become higher due to the loss of CTAB protective layer. Another issue is the bigger size of the thiolated PEGs poses a challenge to penetrate the dense CTAB bilayer and reach AuNRs surface. This leads to incomplete removal of

CTAB. Additionally, it increases the distance between the analytes and AuNR surface, which will reduce the sensitivity of LSPR biosensors. In addition to these, high power NIR laser irradiation leads to structural deformation of PEG which causes uncontrolled aggregation of AuNRs.<sup>33</sup> To overcome this, small thiol terminated ligands such as 11-mercaptopundecanoic acid (MUA) and cysteamine are used preferably for complete removal of CTAB.<sup>34</sup> But the hydrophobic nature of the MUA creates a major challenge because the CTAB-capped AuNRs are very unstable in organic media thereby posing limitations for the place exchange.

Other drawbacks of the conventional procedures are (i) the low yield, the best yield obtained is only  $\geq 75\%$ . (ii) less tunability of plasmon absorption, the maximum tunability is 600-800 nm. Though with co-surfactants such as BDAC it is possible to tune the plasmon wavelengths up to about 1100-1300 nm, it is also toxic.<sup>23,35</sup>

### **2.2.1.2. New synthetic strategies**

Today the researches are more interested to reduce the CTAB concentration in the synthesis process itself. Even decades ago, it was noted that the presence of additives could alter the micellization behaviour of surfactants. Both the hydrophilicity and Coulombic charge of additives critically influences the micellar packing parameters. For example, aromatic additives like salicylate are known to promote the formation of elongated CTAB micelles. By taking advantage of this, Ye et al., for the first time, succeeded in synthesising gold nanorods in 0.05 M CTAB growth solution which is two times less than the conventional procedure (Figure 2.5).<sup>36</sup> Later, Su et al. reported the formation of AuNRs at further reduced concentrations (four times) using dopamine as the reductant as well as additive.<sup>37</sup>

To the best of our knowledge, the only attempt which made some success to produce AuNRs in the absence of CTAB was by using an amino acid, lysine. Though there was the formation of rod-shaped nanoparticles, the yield and quality were remarkably poor.<sup>38</sup>

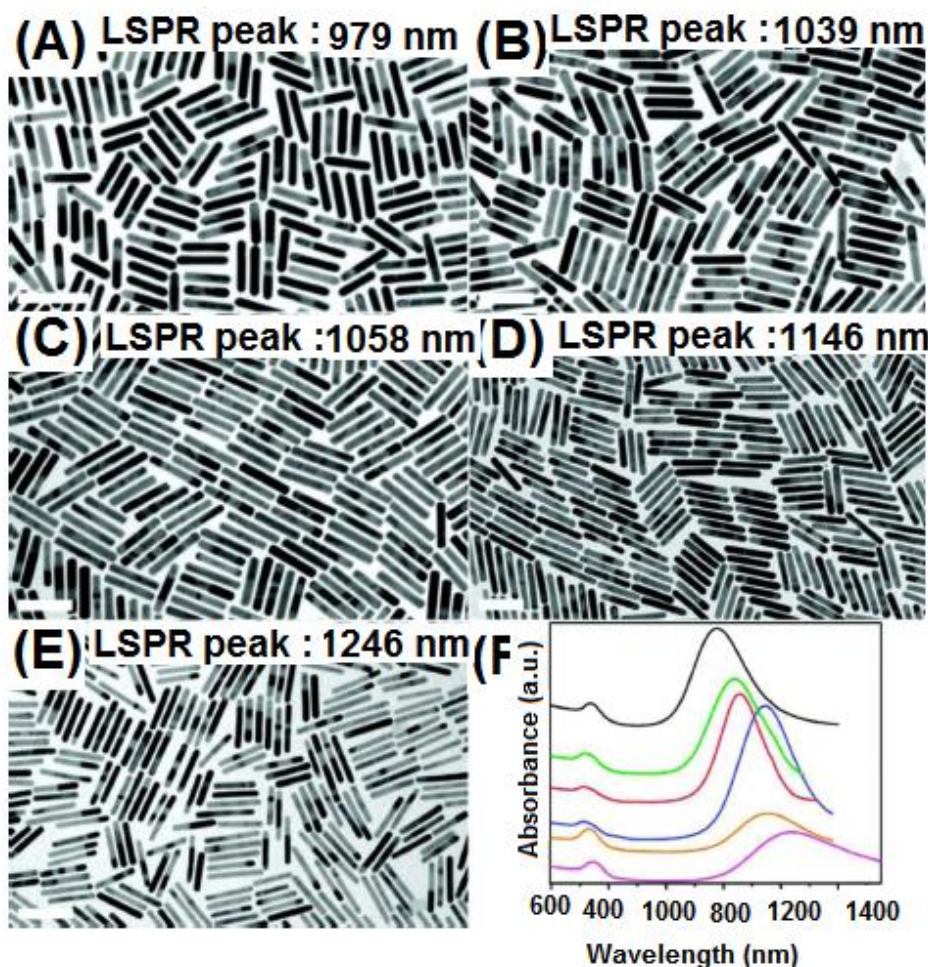


**Figure 2.5.** (A)–(E) TEM images (F) The corresponding UV-Visible spectra of different aspect ratios AuNRs prepared using the additives salicylate (adapted and modified from reference 39).<sup>39</sup>

Thus, it is clear that the way forward towards nanorod synthesis with low CTAB concentration is through the use of aromatic additives. Herein, we present the results of the studies of the influence of three natural antioxidants in the formation of AuNRs. The additives chosen for present studies are, three

structurally similar natural antioxidants namely, Gallic acid (GA), 3,4-dihydroxyhydrocinnamic acid (Dihydrocaffeic acid, DHCA) and L-DOPA and the obtained data were also compared with the conventional procedure using ascorbic acid (AA). Our studies have shown that among these, L-DOPA is highly efficient in promoting the synthesis of nanorods with low CTAB concentrations and wider tunability of plasmon absorption.

## **2.3. Experimental section**

### **2.3.1 Materials and methods**

Hydrogen tetrachloroaurate(III)trihydrate ( $\text{HAuCl}_4 \cdot 3\text{H}_2\text{O}$ , ACS reagent), L-DOPA, DHCA, Gallic acid were procured from Ms. Sigma-Aldrich. Silver nitrate ( $\text{AgNO}_3$ , >99.5%, emparata® ACS) was obtained from Ms. Merck Pvt. Ltd. Cetyltrimethylammonium bromide (CTAB, >98%), sodium borohydride ( $\text{NaBH}_4$ , >98%) and ascorbic acid were purchased from Ms. Spectrochem Pvt. Ltd. All chemicals were used without further purification. Water used for all experiments was doubly distilled.

### **2.3.2 Characterization**

UV-visible absorption spectra were obtained either using a UV-VIS-NIR (UV-3101PC, M/s. Shimadzu Corporation, JAPAN) or diode array (UV-VIS 8453, M/s. Agilent Technologies Inc. USA) spectrophotometers. All measurements were performed in a quartz cuvette (1 cm).

TEM studies were carried out on an FEI's 300 kV high resolution (FEI-Tecnaï G2-30 with EDAX) transmission electron microscope by drop-casting nanorod solution onto a carbon-coated Cu grid.

For XRD, samples were prepared by repeated drop-casting of Au nanorod solutions onto a clean glass plate and data were acquired using a Panalytical PW 3040/60 X'Pert Pro powder diffractometer and Cu K $\alpha$ 1 radiation.

For IR studies, the purified nanorods were dispersed in KBr and carried out measurements in diffused reflectance mode using IR Prestige-21 Fourier transform IR spectrophotometer, Ms. Shimadzu Corporation, Japan. The spectra thus obtained were converted into transmittance mode through Kubelka-Munk operation.

For ICP-MS analysis, 4 ml of Au nanorods were initially microwave digested using Anton Paar's Multiwave 3000, after mixing with 8 ml aqua regia, then diluted to 100 mL with Type 1 water (Thermo Scientific, Barnstead, Smart 2 pure). The experiment was conducted using ICAP Qc (Thermo scientific) with a plasma power of 1548.6 W. The typical measurement parameters were cool flow read back- 13.67 L/min, nebulizer flow - 1.0180 L/min, auxiliary flow read back- 0.796 L/min, integration time – 10 s.

Raman spectra were collected using Confocal Raman Microscope (Alpha 300 R, WiTech, Germany) through 20x objective lens and samples were irradiated with 633 nm laser and spectra were collected on Princeton Instruments spectrograph having 600 lines/mm grating. The data were acquired using 0.5 s as integration time and averaged over 10 accumulations.

### **2.3.3. Synthesis of gold nanorods**

For refining AuNR's synthesis, we adopted modification to the well-exploited two-step procedure involving the first synthesis of nanoseeds followed by its anisotropic overgrowth.

**Step (i) nanoseed preparation:** In a typical experiment, 0.25 mL of 10 mM HAuCl<sub>4</sub> solution was mixed with 9.5 mL of 0.1 M CTAB solution. To this, an ice-cold solution of freshly prepared NaBH<sub>4</sub> (0.6 mL, 0.01 M) was injected under vigorous stirring. The formation of Au(0) and subsequently smaller Au nanoparticles was evident from the immediate color change of the solution to dark brown. The solution was further stirred for 2 minutes and Ostwald ripened at room temperature for 1 h.

**Step (ii) nanorod preparation:** In the second step, the growth solution was prepared by mixing HAuCl<sub>4</sub> (0.5 mL, 10 mM), CTAB (9.75 mL, 0.1- 0.0005 M) and AgNO<sub>3</sub> (0.01 mL, 0.1 M). To this 1 mg of reductant (L-DOPA, DHCA, Gallic acid or ascorbic acid) was added and kept undisturbed. The solution became colourless indicating the reduction of Au(III) to Au(I) ions. Then 0.16 mL of initially prepared seed solution was added, mixed well and incubated for 15 minutes. The colour of the solution gradually turned to wine red indicating the formation of gold nanorods.

**Step (iii) purification:** The obtained nanorods were initially centrifuged at ~7500 rpm for 10 minutes and the collected supernatant was then centrifuged at least 3 times at ~13500 rpm for 20 minutes and the residue was collected.

**SERS substrate preparation:** To prepare a monolayer of AuNRs on glass plates, APTMS strategy was adopted.<sup>40,41</sup> This involves functionalization of the glass



surface with APTMS followed by AuNRs self-assembly. Initially, glass plates were successively ultrasonicated in absolute ethanol and ultrapure water which is then treated with 3:7 (v/v) mixture solution of H<sub>2</sub>O<sub>2</sub> (30%) and H<sub>2</sub>SO<sub>4</sub> (98%) for ~ 4 h. These substrates were thoroughly cleaned with ultrapure water and purged with N<sub>2</sub> gas. Afterward, they were immersed in an aqueous solution of 0.2% (v/v) APTMS for ~ 24 h. Subsequently, cleaned with ultrapure water and baked for ~ 30 min at 110 °C. Finally, a monolayer of gold nanorods was self-assembled by dipping these glass plates in its solution for ~12 h. Any excess of physisorbed AuNRs were removed by running ultrapure water.

**Cell Culture:** Human breast adenocarcinoma cell line, SKBR3 was obtained from American Type Culture Collection (ATCC, USA). The cells were maintained in DMEM media supplemented with 10% fetal bovine serum and antibiotics (100U mL<sup>-1</sup> penicillin/100 µg mL<sup>-1</sup> streptomycin mixture) in a 5% CO<sub>2</sub> incubator at 37 °C.

**Cell viability assay:** On attaining 80% confluency, the cells were trypsinized, centrifuged and seeded at a density of 10<sup>4</sup> cells/well in two 96 well plates and incubated at 37 °C for sufficient growth. AuNRs were added to the wells at a concentration of 10 µM in each plate and incubated for 4 hours. One of the plates was then irradiated with 808 nm laser (0.1 W/cm<sup>2</sup>) for 1 minute. 100 µL MTT (0.5 mg/mL) was added to each well and the purple colour formation after the addition of DMSO was measured colorimetrically at 570 nm. Percentage cell viability was calculated as the ratio of absorbance of samples to the absorbance of the control (medium alone).

**SERS spectral analysis:** SKBR3 cells were cultured in 4 well chamber slide made of glass. AuNRs was added to the wells and incubated at 37 °C for 4 h together

with control (media alone). Further, the cells were irradiated with 808 nm laser (0.1 W/cm<sup>2</sup>, 1 min) and investigated for the spectral fingerprint on confocal Raman microscope. Suitable cells were focused using the integrated video camera and scanned with an integration time of 0.5 s.

## 2.4. Results and discussion

### 2.4.1. Characterization of seed

Figure 2.6 displays the representative TEM image and optical absorption spectral profile of synthesized seed gold nanoparticles. Detailed cross-sectional analysis of these microscopic images showed the presence of mainly spherical nanoparticles of the size 2-3 nm (Figure 2.6 A). While they exhibited broad absorption band without any characteristic peaks except small bump around 380 nm and 480 nm (Figure 2.6 B). These are mainly due to their small size and it is in

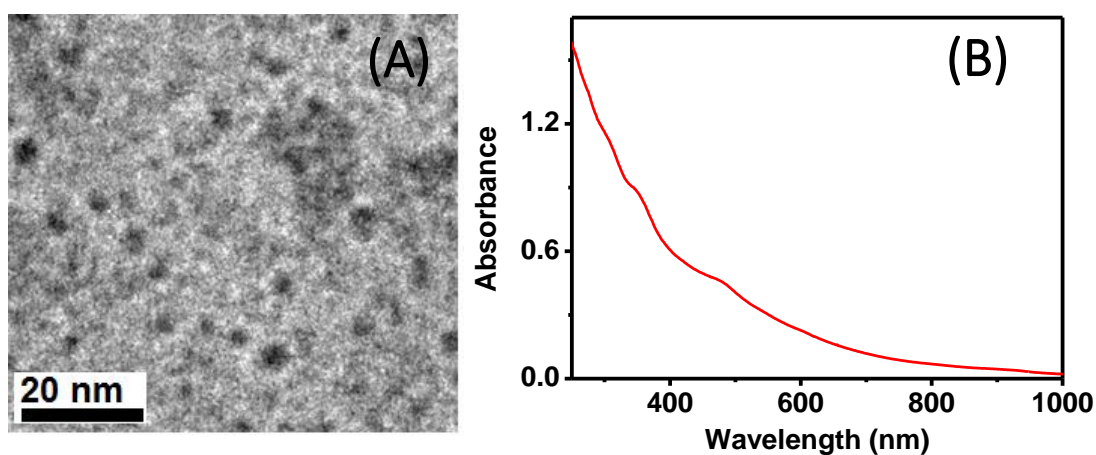


**Figure 2.6.** (A) TEM image and (B) The corresponding absorption spectrum of nanoseeds prepared via reduction of gold ions by NaBH<sub>4</sub>.

accordance with literature reports. For gold, clear plasmon absorption features stems out when the particles sizes are higher than ~ 5 nm.

### 2.4.2. Absorption and morphological characterization of AuNRs

Figure 2.7 represents the comparative absorption spectra of AuNRs prepared in presence of different reductants. Spectroscopically, they all displayed similar absorption spectral profiles with two distinguishable absorption bands corresponding to LSPR and TSPR. However, there were a few noticeable differences. (i) The position of LSPR bands appeared at ~930 nm, 860 nm, 815 nm and 765 nm respectively for those prepared in the presence of L-DOPA, DHCA, and 765 nm respectively for those prepared in the presence of L-DOPA, DHCA,

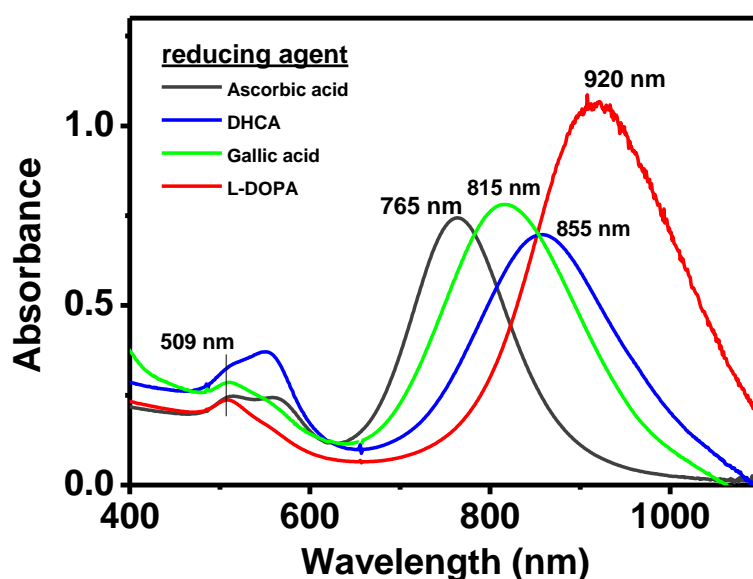


**Figure 2.7.** Absorption spectra of AuNRs produced with reducing agents ascorbic acid (black), L-DOPA (red), DHCA (blue) and gallic acid (green); [CTAB] = 0.1 M; [Ag<sup>+</sup>] = 10  $\mu$ L, [seed] = 160  $\mu$ L.

GA and AA. Thus, it could be noted that among these, AuNRs synthesised in the presence of L-DOPA has the most red-shifted plasmon absorption with highest optical density, whereas those with AA (conventional reductant) has the bluest. This indicates the formation of longer nanorods with L-DOPA and shorter ones with AA. Also, the absorption profile of the AuNRs made by employing DHCA or

AA as the reductant exhibited a considerable absorption at  $\sim 550$  nm indicating the coexistence of spherical and other morphology nanoparticles.

To have a further clear picture, the morphology and size distribution of the produced AuNRs were estimated through TEM analysis, and the results are presented in figure 2.8. In the case of ascorbic acid, the nanorods formed were highly nonuniform with wide variation in their both length and width. Typically, the length varied from  $\sim 15$  to 60 nm and width from  $\sim 5$  to 20 nm. In addition to this, a considerable percentage of nanoparticles of other morphologies were also present. In DHCA, compared to ascorbic acid, nanorods formation is more uniform and the length varied from  $\sim 40$  to 60 nm and width from  $\sim 10$  to 15 nm. Still, the yield of AuNRs are less, a large percentage of spherical, cube-shaped and other nanostructures have been found. Among these only 69% particles were of rod-shaped. In the case of gallic acid, the rods are formed in higher yields with less

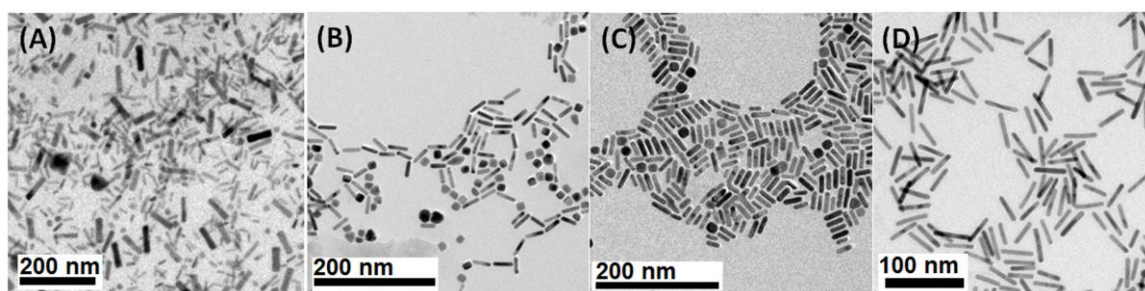


**Figure 2.8.** TEM images of nanorods prepared in presence of 1mg (A) Ascorbic acid, (B) DHCA, (C) Gallic acid and (D) L-DOPA in growth solution containing 0.1 M CTAB.

number of spherical nanoparticles and length varied from  $\sim 20$ -30 nm and width from  $\sim 5$ -10 nm. In L-DOPA, more monodispersed nanorods are formed in high yield ( $>90\%$ ) with length  $\sim 35 - 45$  nm and width  $\sim 6$ -10 nm. It can also be noted that the nanorods formed with aromatic reductants are thinner in diameter than that of ascorbic acid. Above

90 % of rod-shaped particles formation was observed in L- DOPA and gallic acid (Table 2.1).

**Table 2.1.** Absorption maxima, aspect ratio and statistical TEM analysis of the yield AuNRs obtained in presence of different reductants.

P;Sl. No.	Conc. of CTAB (M)	Reductant	$\lambda_{\max}$ (nm)	Aspect Ratio (AR)	Yield of AuNRs (%)
1	0.1	DHCA	856	3.8	69
2	0.1	Gallic acid	815	4.2	93
3	0.1	L-DOPA	920	4.5	95

The nanorods produced in presence of L-DOPA have the highest aspect ratio of 4.5, while 3.8 and 4.2 have been obtained for gallic acid and DHCA respectively (Table 2.1). Thus, both the absorption and TEM results gave the first glimpses of the efficiency of L-DOPA in promoting lengthier nanorod growth (Figure. 2.11). From these studies it is clear that, when compared to other ligands, L-DOPA outperform as a reductant as well as an additive in synthesis of AuNRs. Therefore, further detailed studies were focused on optimizing the conditions to extract the best possible one.

#### 2.4.3. The effect of seed nanoparticles

Figure 2.9 represents the effect of seed concentration on the absorption spectral features of AuNRs prepared using L-DOPA as reductant and while maintaining all other conditions standard. At 50  $\mu$ L seed solution, both TSPR and LSPR bands are highly broad with lower optical densities indicating the low yield of nanorods formation. Also, it has the most red shifted LSPR band suggesting the formation of longer nanorods. The low yield of nanorods is due to insufficient number of seed particles for effective nucleation and overgrowth. The longer nanorods are due to high  $\text{Au}^{3+}$  to seed ratio. When the seed concentration raising to 80  $\mu$ L, the increased nucleation rate results in

more number of nanorod formation as indicated by increased optical density. Further enhancement in optical density and slight blue shift in LSPR absorption was noted when

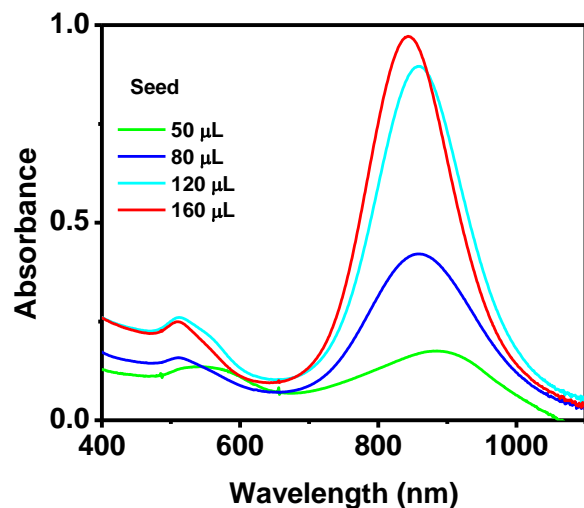


**Figure 2.9.** Absorption spectra of AuNRs prepared by varying the added seed volume at  $[CTAB] = 0.1 M$ ;  $[Ag^+] = 10\mu L$ ,  $[L-DOPA] = 1mg$ .

**Table 2.2.** Absorption maxima, aspect ratio and statistical TEM analysis of the yield AuNRs obtained in presence of different seed volume.

Sl. No.	Volume of seed ( $\mu L$ )	$\lambda_{max}$ (nm)	Aspect Ratio (AR)	Yield of AuNRs (%)
1	50	887	6	56
2	80	860	5.2	74
3	160	840	4.5	95

the seed concentration was raised to 120  $\mu L$ . Above this, not much change in the optical density was observed other than hypsochromic shift. This suggested that the minimum required seed concentration for maximum  $Au^{3+}$  to nanorod conversion is in the range 120  $\mu L$  -160  $\mu L$  (Table 2.2).

#### 2.4.4. The effect of $\text{AgNO}_3$

It is well known that  $\text{Ag}^+$  ions play an important role in nanorod growth and tuning the aspect ratio. It has been hypothesized that  $\text{Ag}^+$ , in the form of  $\text{AgBr}$  ( $\text{Br}^-$  from CTAB and  $\text{Ag}^+$  from  $\text{AgNO}_3$ ), preferentially adsorbs at (100) plane of the nanoseeds and restricts the growth along this direction. Thus, the growth occurs mainly at (111) facets by deposition of  $\text{Au}(0)$  yielding unique one-dimensional nanostructures. Thus, to attempt the tuning of the LSPR band, systematically

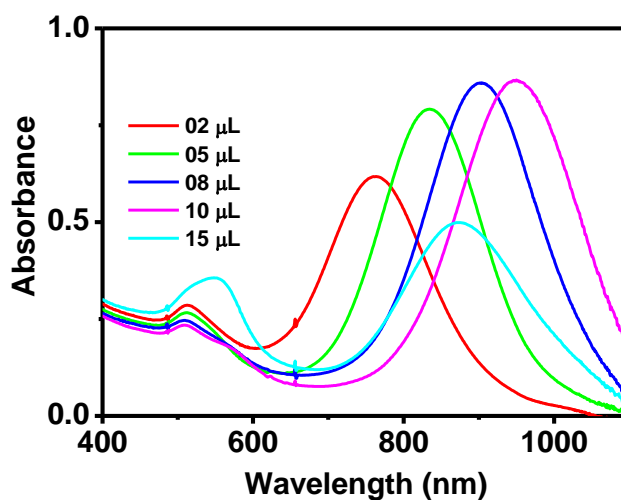


**Figure 2.10.** Absorption spectra of AuNRs prepared by varying the added volumes of  $\text{AgNO}_3$  at  $[\text{CTAB}] = 0.1 \text{ M}$ ;  $[\text{seed}] = 160 \mu\text{L}$ ,  $[\text{L-DOPA}] = 1 \text{ mg}$ .

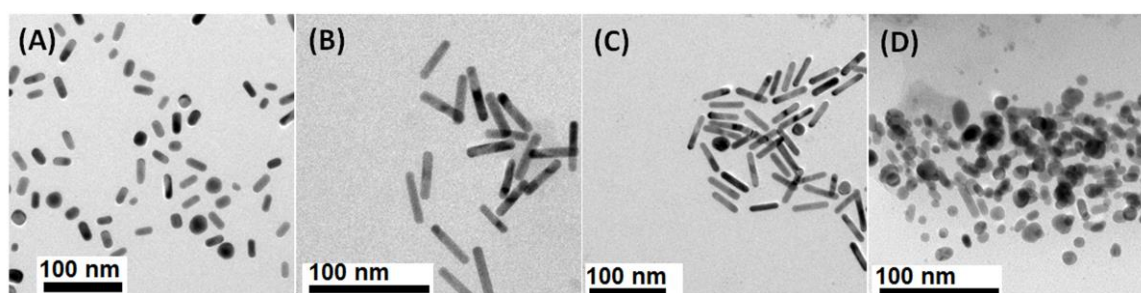


**Figure 2.11.** TEM images of AuNRs prepared by varying the added volumes of  $\text{AgNO}_3$  (A)  $5 \mu\text{L}$ , (B)  $10 \mu\text{L}$ , (C)  $15 \mu\text{L}$  and (D)  $20 \mu\text{L}$  at  $[\text{CTAB}] = 0.1 \text{ M}$ ;  $[\text{seed}] = 160 \mu\text{L}$ ,  $[\text{L-DOPA}] = 1 \text{ mg}$ .

varied the amount of  $\text{AgNO}_3$  while keeping all other parameters constant and the obtained results are provided in figure 2.10. It was interesting to note that, LSPR absorption of nanorods are highly tunable in the range 600-950 nm when the  $\text{Ag}^+$  ion is varied from 2  $\mu\text{L}$  – 10  $\mu\text{L}$ . At its lower amounts, the AuNRs formed are shorter and has an average length of around 20 nm (aspect ratio  $\sim 2$ ). There was a consistent rise in aspect ratio and consequently LSPR position linearly red-shifted with its increasing volumes. Further increasing the volume results a blue shift in absorption spectra as it gives shorter nanorods. At very high concentration of  $\text{AgNO}_3$ , spherical nanoparticles are formed instead of rods (Figure 2.11). This is due to (i) the increased ionic strength and (ii) the adsorption of excess  $\text{Ag}^+$  on (111) facets thereby blocking effective 1 D growth.

#### **2.4.5. Studies on reducing CTAB concentration in AuNRs synthesis**

Further efforts were focused on studying the effect of CTAB concentration in AuNRs synthesis. The main intention was to see if this could help to reduce the percentage of undesirable surfactant during synthesis itself. If successful, this may pave the way to more ecofriendly route to AuNRs and help in eliminating the need for post-synthetic treatments. With this aim, we conducted systematic experiment by varying the CTAB concentration and keeping all other conditions constant and the obtained data are presented in figure 2.13. When L-DOPA was employed, LSPR band underwent a prominent and continuous bathochromic shift 805 nm - 1120 nm as CTAB concentration varied from 0.1 M to 0.001 M. This implies the formation of longer nanorods reinforcing the argument of L-DOPA's ability to support rod-shaped micelles even at CTAB concentrations lower than the conventional. When its amount was further reduced to 0.5 mM, the plasmon



absorption experienced a slight blue shift to 1010 nm, below which AuNR's formation may be less favoured. However, in all other cases an opposite trend was noted. For example, with conventional reductant AA, attempts to lower CTAB concentration landed in the continuous blue shift to the LSPR absorption from 815 nm to 645 nm along with decrease in optical density. Consequently, formation of

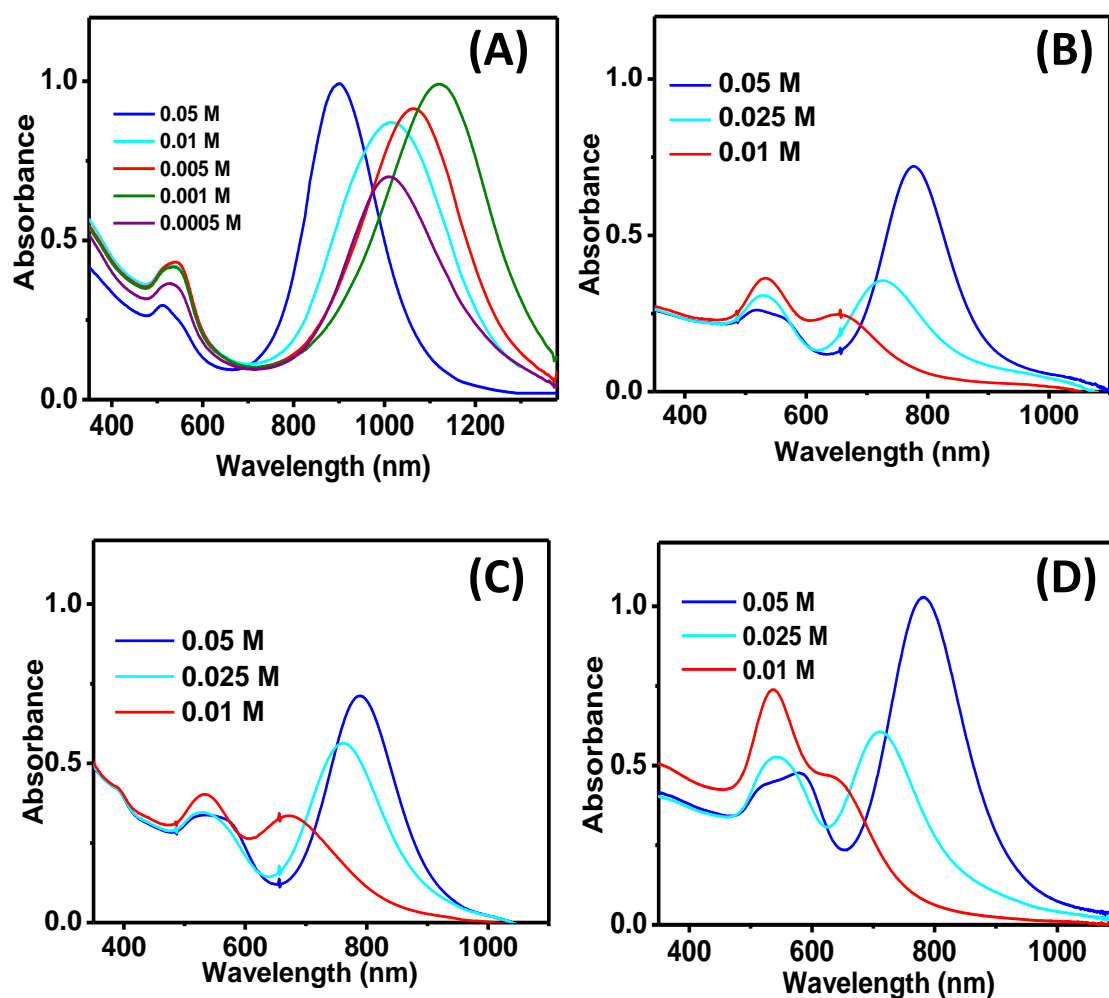


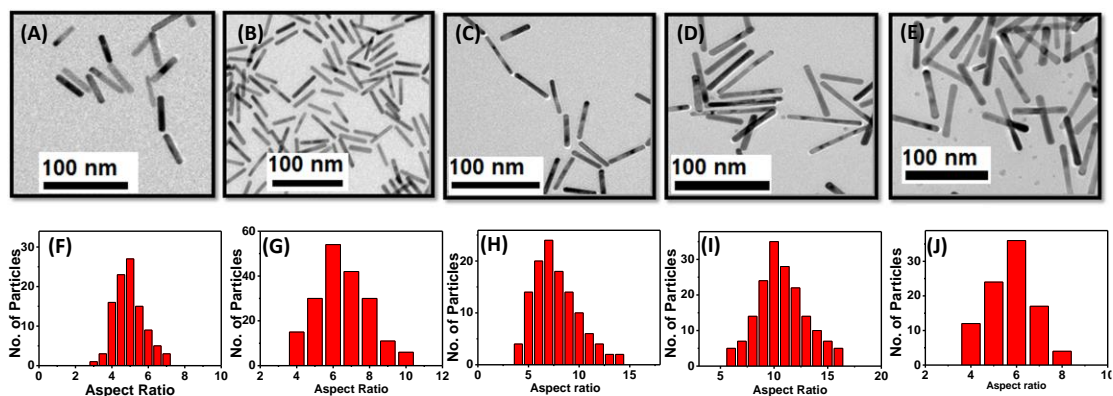
**Figure 2.12.** Absorption spectra of nanorods prepared with reductants (A) L-DOPA, (B) DHCA, (C) GA and (D) AA with varying CTAB concentrations. The other conditions were standard; 0.5 mL 10 mM HAuCl<sub>4</sub>, 9.75 mL CTAB (0.5 mM – 0.1 M), 0.01 mL 0.1 M AgNO<sub>3</sub> and 1 mg reductant.

new band at 580 nm and considerable broadening was noted for TSPR band. The hypsochromic shift to the LSPR band is an indication of the formation of shorter AuNRs, and the TSPR broadening is due to the increased percentage of nanoparticles of other morphologies.<sup>42</sup> These observations suggest their ineffectiveness to induce anisotropic growth at low CTAB concentrations. Similarly, in the case of DHCA the hypsochromic shift and decreasing optical density were observed when the concentration varied from 0.1 M - 0.01 M. At 0.01 M, the optical density of TSPR band is higher compared to LSPR band which indicated more number of spherical particles than rods. Similar results are obtained while synthesizing AuNRs at reduced CTAB concentrations in presence of GA as the reductant (Figure 2.12).

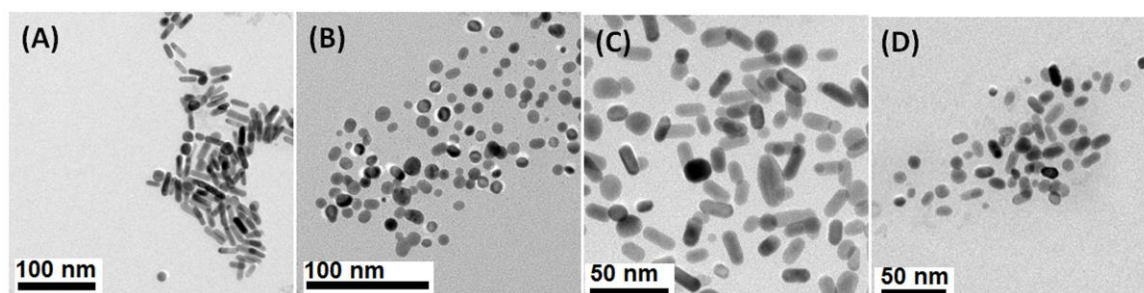
#### **2.4.6. Morphological studies**

Figure 2.13 and 2.14 shows the comparative TEM studies illustrating the effect of CTAB concentration on the morphology of resulting AuNRs. With L-DOPA as the reductant, the purified AuNRs displayed almost the same width (~8 nm) and is not much influenced by the CTAB concentration. However, the length of the AuNRs perpetually increased (from 45 nm to above 75 nm) with CTAB's diminishing quantities. For example, the length of AuNRs produced at 0.1, 0.01 and 0.001 M were respectively 45, 55 and 75 nm. Instead, it got reduced to ~ 50 nm when the concentration reached 0.0005 M, and there occurred more spherical particles as is evident from TEM images. Below this, nanomaterials formed were highly polydisperse. However, with other reductants such as DHCA, GA, and AA, lowering of CTAB concentration always accompanied a drop in the aspect ratio and elevated polydispersity (Figure 2.14). These studies clearly disclose that using

L-DOPA as the reductant AuNRs could be produced at CTAB concentrations down to 0.0005 M which is ~200 times lower than the standard conditions.



**Figure 2.13.** (A-E) TEM and (F-J) corresponding size distribution analysis of AuNRs prepared in presence of L-DOPA by varying [CTAB] (A, F) 0.1 M, (B, G) 0.01 M, (C, H) 0.005 M, (D, I) 0.001 M and (E, J) 0.0005 M while keeping all other conditions constant.



**Figure 2.14.** TEM images of nanorods prepared with reductants (A-B) DHCA, (C-D) Gallic acid with varying CTAB concentrations (A,C) 0.05 M and (B,D) 0.01 M.

## 2.4.7. Mechanism of AuNRs formation

### 2.4.7.1. Crystallographic studies

Crystallographic studies were conducted using both HRTEM and XRD. From the HRTEM images, the d spacing values were extracted as 0.235 nm and 0.201 nm which corresponds to (111) and (200) planes of gold atoms in the fcc crystal lattice (Figure 2.15 A, B). Similar results were obtained from XRD measurements (Figure 2.15 C) which

inferred the predominant (111) facets of nanocrystals. The EDAX analysis confirmed their main composition as Au atoms with a minor contribution from Ag (Figure 2.15 D and Table 2.3).

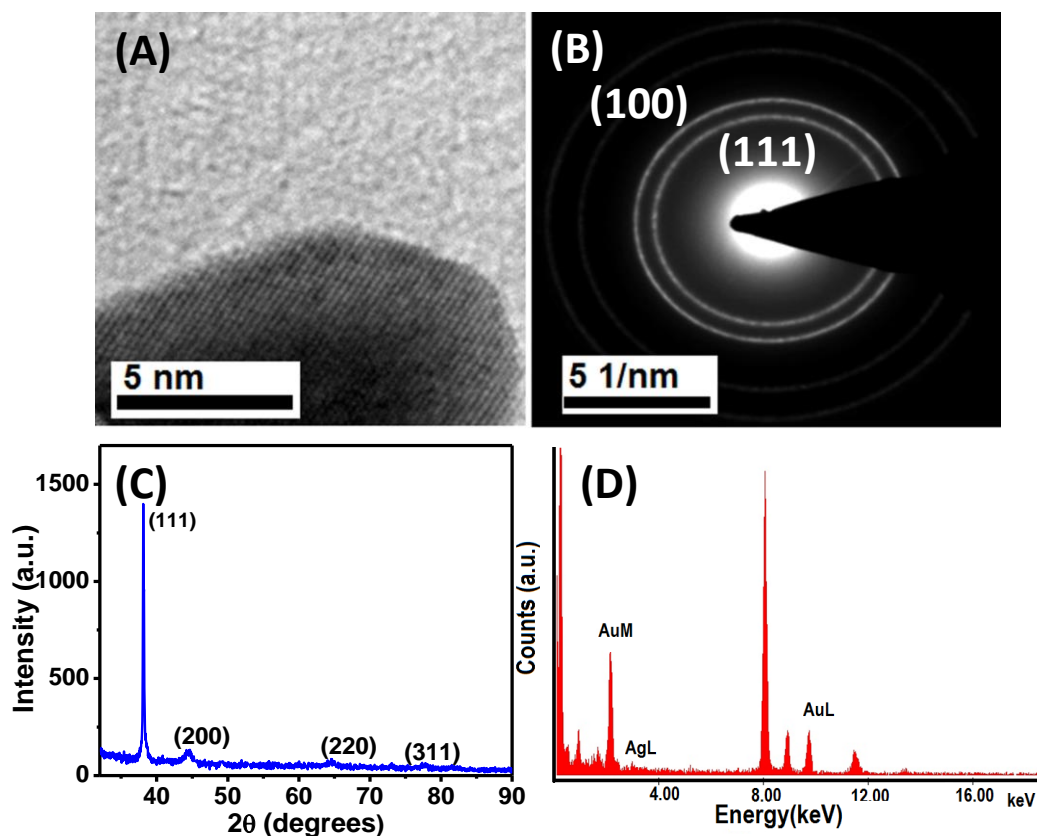


**Figure 2.15.** A) HRTEM image, (B) SAED pattern, (C) XRD spectrum and (D) EDAX of AuNRs prepared in presence of 1 mg L-DOPA and 0.1 M CTAB

**Table 2.3.** EDAX energy values of component elements in AuNRs

Elements	Energy value in keV	
	K $\alpha$	L $\alpha$
Ag	22.163	2.983
Au	M $\alpha$	L $\alpha$
	2.123	9.713

#### **2.4.7.2. Growth kinetics studies**

It is well established in the colloidal synthesis that the size and shape distribution of any nanoparticles formed is primarily determined by their growth rate. To gain an insight into this aspect, the absorption spectral changes occurred during the nanorod formation were recorded and is presented in figure 2.16. At least three stages of nanorod growth can be identified from a close analysis of the data. (i) In the first five minutes, there was decrease in the nanoseed centered absorption at around 475 nm and broadening of the spectral profile indicating the overgrowth of the nanoseeds. (ii) In the next 20 minutes there was fast exponential raise in the plasmon absorption corresponding to both TSPR (512 nm) and LSPR bands (860 nm) and involves transformation nanoseeds into nanorods. (iii) After 20 minutes, growth becomes slower and attains a saturation stage. Along with these spectral changes, during the first 6-10 minutes, the LSPR peaks showed a fast red shift from 730 nm to 860 nm suggesting the construction of anisotropic structures (nanorods). During the initial stages, the concentration of  $\text{Au}^{3+}$  ions and shape directing agents ( $\text{AgNO}_3$  and CTAB) are higher and hence larger nanorods are formed as is evident from the bathochromic shift in the LSPR absorption. In the later stages, as the effective concentration of reactant and shape directing agents are less, and the rate of nanorod formation is slow and will have smaller sizes as is indicated by slow raise in plasmon absorption and blue shift in the LSPR band. Upon keeping the solution at room temperature for 12 h, the LSPR peak showed a further slight blue shift in its absorption maximum. Due to the fast formation rate, there will be atomic defects on the unstable facets of nanorod surface, and the atoms on the nanorod would reconstruct and the size of the particles changes slightly in this stage.

Earlier studies have brought out that natural antioxidants having a polyphenolic moiety, can reduce  $\text{Au}^{3+}$  and  $\text{Ag}^+$  ions.<sup>43-47</sup> Structurally, L-DOPA and DHCA contain two

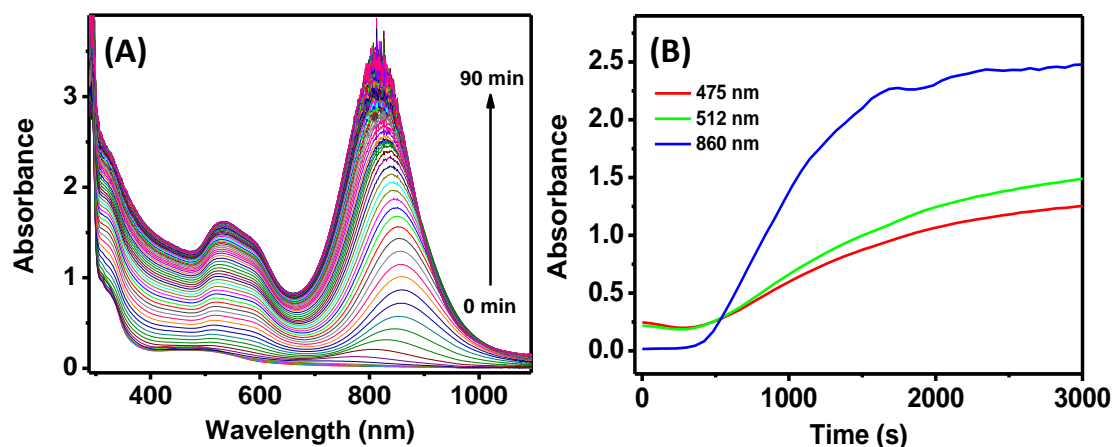


**Figure 2.16.** (A) Evolution of the plasmon absorption during the formation of Au nanorods and (B) Time-dependent absorbance changes at 475 (red), 512 (green) and 860 nm (blue).

two o-phenolic hydroxyl groups and GA has three hydroxyl groups. All of them have got lower redox potential than Au(III) ions, and hence its conversion to Au(0) is thermodynamically feasible.<sup>49,50</sup> In the present case, the growth solution has a light yellow colour originating from the absorption band at  $\sim 395$  nm of Au(III)-CTAB complex. Addition of either of these reductant molecules to the growth solution induced fading of the yellow colour owing to continuous recession in optical density at 395 nm (Figure 2.17). This is a clear indication of the conversion of Au(III) to Au(I) ions. Later, the addition of nanoseeds to this solution yielded wine-red colour owing to the evolution of plasmon absorption. Thus, it can be inferred that nanoseeds has triggered the further conversion of Au(I) to Au(0) and the anisotropic overgrowth resulted in the formation of 1D nanorods. This was evident from the presence of both LSPR and TSPR band in the absorption spectrum, and predominantly rod-shaped particles in the TEM images. Further, it has also been noticed that the addition of nanoseeds to the growth solution in the absence of these biomolecules did not bring any of these changes. From these, it can be concluded that hydroxy phenols participate in the AuNR's growth and

involves at least two stages (Fig. 2.15 B); (i) reduction of Au(III) ions to Au(I) and (ii) further conversion of Au(I) ions to Au(0) catalysed by nanoseeds and

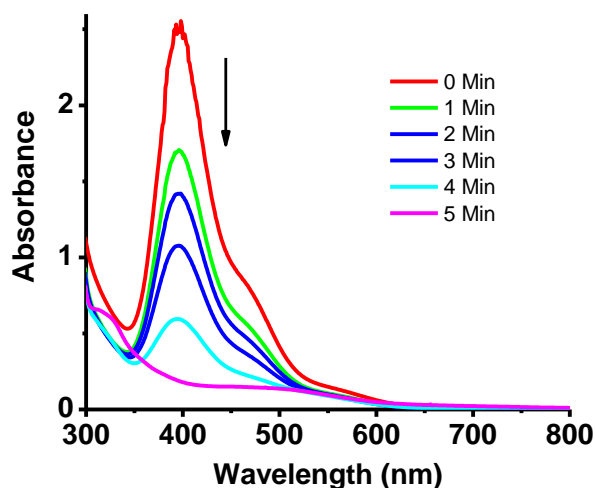


**Figure 2.17** Absorption spectral changes of growth solution (prepared by mixing  $\text{HAuCl}_4$  (0.5 mL, 10 mM), CTAB (9.75 mL, 0.1 M), and  $\text{AgNO}_3$  (0.01 mL, 0.1 M)) after the addition of 1 mg L-DOPA.

subsequent formation of AuNRs. ICP-MS analysis indicated more than 93 % conversion of Au(III) to Au(0) in the presence of L-DOPA. Out of these, the yield of nanorods obtained was estimated (from detailed TEM analysis) to be ~ 95 %, 92 %, 88 % and 80 % at CTAB concentrations 0.1 M, 0.01 M, 0.001 M and 0.0005 M respectively (Table 2.4). Though their exact role is still under debate,<sup>48-55</sup> CTAB and  $\text{AgNO}_3$  are known to be the essential components that direct the one-dimensional growth of AuNRs.

**Table 2.4.** The statistical TEM analysis of the yield of nanorods obtained in the presence of different concentration of CTAB and L-DOPA as the reductant.

Sl. No.	Conc. of CTAB (M)	Reductant	Yield of AuNRs (%)
1	0.1	L-DOPA	95
2	0.01	L-DOPA	92
3	0.001	L-DOPA	88
4	0.0005	L-DOPA	80

CTAB mainly serves the roles of (i) soft elongated template promoting 1D growth and (ii) the capping ligand that prevents nanorods from aggregation. Even though the critical micellar concentration of CTAB is  $\sim 1$  mM in water at 25 °C, almost 100 times higher amount is required for efficient AuNR synthesis. Herein, AuNRs formed in the presence of L-DOPA have red-shifted LSPR bands when compared to that of other ligands. Also, even longer nanorods are obtained at reduced CTAB concentrations (Scheme 2.1). These prompted us to believe that, in addition to reductant, L-DOPA may also have the role of an additive having better compatibility with CTAB layer. In one of the earlier works, Yoo et al. reported that aromatic additives such as salicylate support the formation of elongated micelles at low CTAB concentrations.<sup>56</sup> Therefore, we argue that L-DOPA assists the growth of AuNRs even at extremely low CTAB concentrations by serving as an auxiliary capping ligand. To prove this, IR spectrum of purified AuNRs were recorded as a function of used CTAB concentration and the obtained data is presented in figure 2.18 A. The peaks corresponding to the asymmetrical ( $\bar{\nu}_{as}$  CH<sub>2</sub>) and symmetrical ( $\bar{\nu}_{s}$  CH<sub>2</sub>) stretching vibrations of methylene groups of CTAB were clearly visible at 2922 cm<sup>-1</sup> and 2850 cm<sup>-1</sup> respectively. With the reduction in CTAB concentrations, the relative intensities of these peaks were progressively diminished when compared to those characteristic C-O and aromatic C-H vibrations ( $\bar{\nu} = 1710-1750$  cm<sup>-1</sup>, 1400-1540 cm<sup>-1</sup> and 900-1170 cm<sup>-1</sup>). This served as proof for the substitution of CTAB with L-DOPA through efficient intercalation within the capping layer (Figure 2.18 B, C).



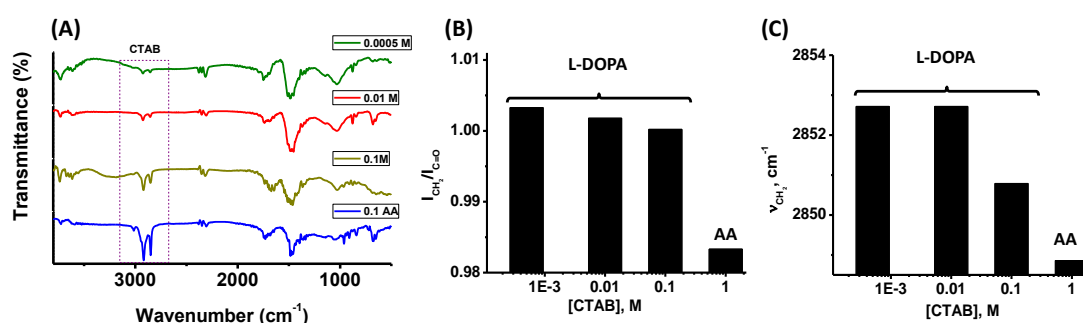
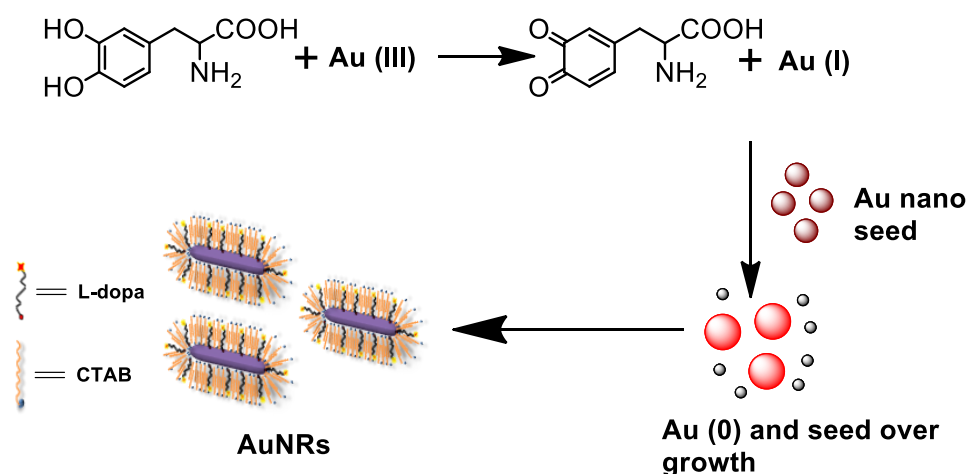


**Figure 2.18.** (A), FTIR spectra of AuNRs prepared using L-DOPA (1 mg), HAuCl<sub>4</sub> (0.5 mL, 10 mM), AgNO<sub>3</sub> (0.01 mL, 0.1 M), nanoseed solution (0.16 mL) and varying concentration of CTAB (9.75 mL); [CTAB] = 0.1 M (dark yellow), 0.01 M (red), 0.0005 M (olive). The blue curve represents the FTIR spectrum of AuNRs prepared via normal route (AA (1 mg), HAuCl<sub>4</sub> (0.5 mL, 10 mM), AgNO<sub>3</sub> (0.01 mL, 0.1 M), nanoseed solution (0.16 mL) and CTAB (9.75 mL, 0.1 M).



**Scheme 2.1.** Schematic representation showing the conversion of Au(III) to Au(0) through Au(I) and the subsequent 1D growth yielding AuNRs.

## 2.4.8. Implications

### 2.4.8.1. Wider tunable LSPR band

Having realized the lowering of CTAB concentration, our next curiosity was to see the versatility of the procedure. To tap the full potential of AuNRs in a variety of fields, its plasmon absorption should be tunable as wide as possible. Ag<sup>+</sup>

ions are known to have a pronounced effect on the aspect ratio of AuNRs. However, for AuNRs prepared with normal CTAB concentrations (0.1 M) LSPR was tunable only to the maximum extent of  $\sim 950$  nm and its length reaches  $\sim 50$  nm. Yet, it is almost 150 nm red-shifted when compared to that maximum achievable with the conventional procedure. Promisingly, the extensibility of plasmon absorption augmented at lower CTAB concentrations. LSPR band went up to  $\sim 1260$  nm (AR = 10) when the surfactant concentration is 0.01 M which is close to the highest value reported for AuNRs prepared using other methods (Figure 2.19 A).<sup>9,23,57</sup> Similar observation was made even for very low CTAB concentrations (0.5 mM) (Figure 2.19 B). Thus, it is evident that the present

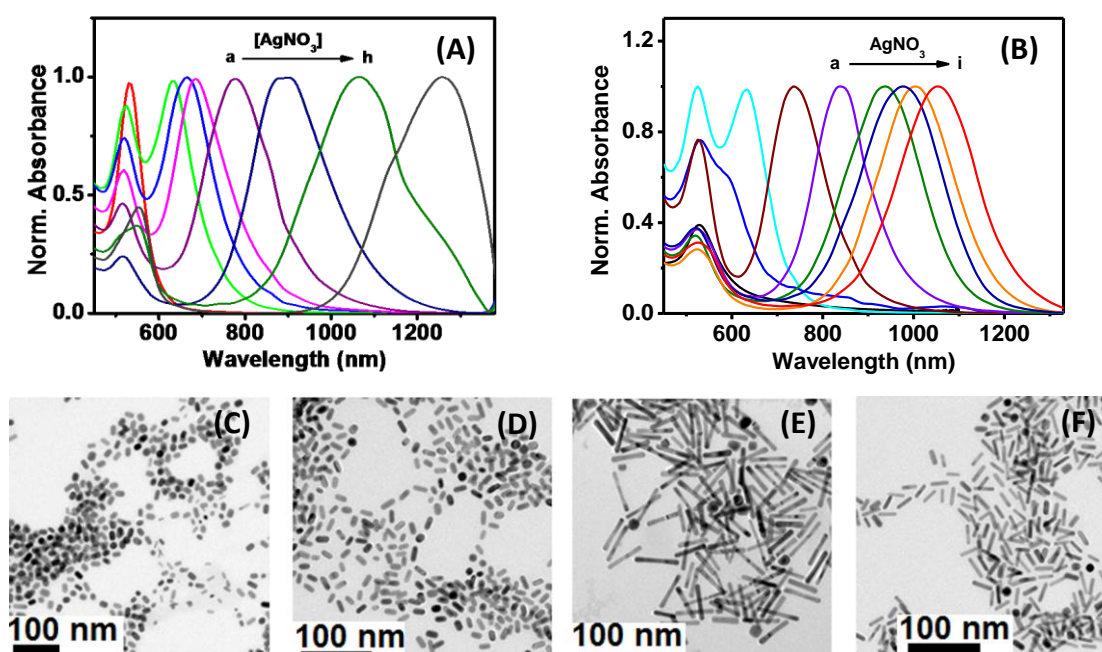


**Figure 2.19.** (A,B) Absorption spectra of AuNRs prepared by varying the added  $\text{AgNO}_3$  volume at different CTAB concentrations. (A)  $[\text{CTAB}] = 0.01 \text{ M}$ ;  $[\text{Ag}^+] = 1\text{-}15 \mu\text{L}$  (B)  $[\text{CTAB}] = 0.0005 \text{ M}$ ;  $[\text{Ag}^+] = 0.5 - 15 \mu\text{L}$ . (C-F) Representative examples of TEM images of AuNRs produced with (C)  $[\text{CTAB}] = 0.0005 \text{ M}$ ;  $[\text{Ag}^+] = 0.5 \mu\text{L}$ , (E)  $[\text{CTAB}] = 0.1 \text{ M}$ ;  $[\text{Ag}^+] = 0.75 \mu\text{L}$ , (E) $[\text{CTAB}] = 0.0005 \text{ M}$ ;  $[\text{Ag}^+] = 10 \mu\text{L}$ , (F)  $[\text{CTAB}] = 0.0005 \text{ M}$ ;  $[\text{Ag}] = 15 \mu\text{L}$ .

methodology not only offers the advantage of reducing toxic surfactants to a greater extent but also allows tuning of plasmon absorption in both the bio-optical windows. Along with the bathochromic shift in the LSPR absorption, increase in optical density was quite often and is mainly attributable to higher extinction coefficient of larger AuNRs. Above a certain  $\text{AgNO}_3/\text{CTAB}$  ratio, we observed a blue shift in the LSPR absorption along with broadened TSPR band. This is because AgBr if present in excess amounts can also adsorb to the (111) plane restricting the preferential 1D growth and hence diminished AuNR formation yield (Figure 2.19 C-F).

#### 2.4.8.2. Studies on bioavailability

Our next interest was to see the impact of these surface-modified nanorods in biological environments, and hence therapeutic applications. In this context, we initiated the evaluation of AuNR's cytotoxic potential in SKBR3 cells by MTT assay and the results are displayed in figure. 2.20. As reported by others, we also noted high

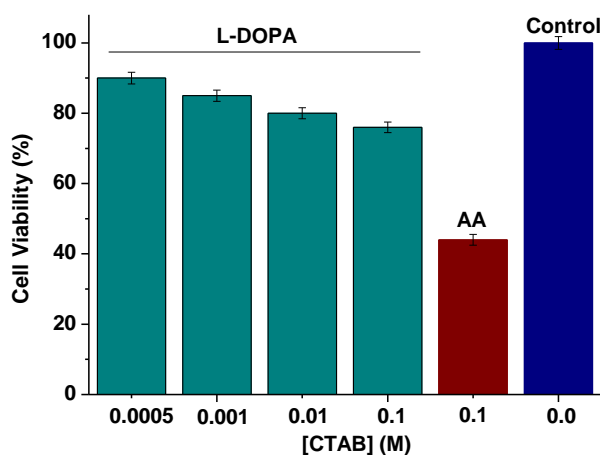


**Figure 2.20.** (A) Plot showing the cell viability of SKBR3 cells after incubation with AuNRs prepared in the presence of L- DOPA (1 mg) and varying CTAB concentrations (9.75 mL, 0.1 M- 0.0005 M). For comparison, the data of AuNR prepared with AA (1 mg) and CTAB (9.75 mL, 0.1 M) is also provided.

cytotoxicity for the AuNRs, cell viability was estimated to be only ~ 40 % for those prepared via normal procedure. On the contrary, cell viability got greatly enhanced to ~ 75 % while using L-DOPA in AuNR's synthesis. Moreover, there was a consistent reduction in cytotoxicity with a decrease in toxic surfactant concentration. Cell viability > 85 % has been achieved for AuNRs prepared at 0.5 mM CTAB, thus eliminating the need for any further treatment for improving their bio-utility.

## 2.4.9. Nanophotonic enhancements

### 2.4.9.1. Photon to thermal conversion efficiency

Photothermal therapy (PTT) is one of the viable technologies for cancer treatment in which metallic nanomaterials can transform NIR light into thermal energy causing cell death via hyperthermia. Like any other plasmonic materials, AuNRs are well known for their ability to perform as photothermal transducers. The photothermal conversion

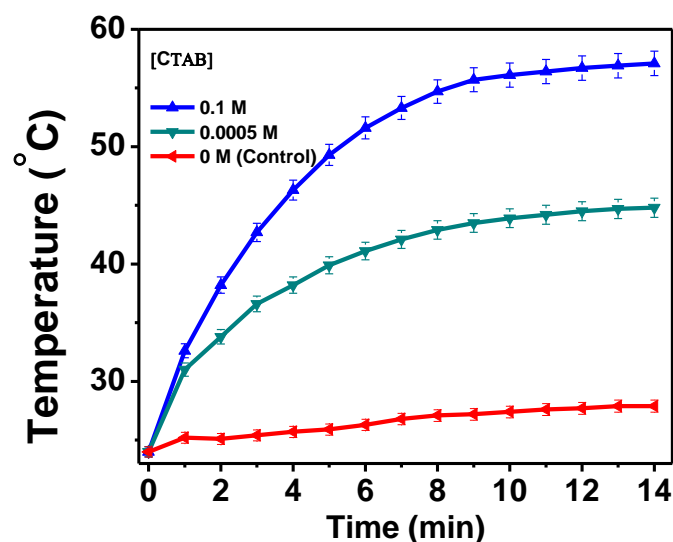


**Figure 2.21.** Temperature changes of AuNRs solutions upon irradiation with 808 nm laser at a power density of  $0.1 \text{ W/cm}^2$  as a function of time. Water was used as a control.

efficiency of synthesised AuNRs was investigated by recording the temperature changes with time using a multimeter integrated to thermocouple under 808 nm laser ( $0.1 \text{ W/cm}^2$ )

irradiation. Generally, an increase in the temperature of the system to 58 °C was attained upon laser irradiation for 13 minutes. While no such heating effect was observed for control experiments (water alone) (Figure. 2.21). Such an elevation of temperature can cause irreversible damages to cells and hence cell death.

#### **2.4.9.2. Signal enhancement of Raman scattering**

Plasmonic materials can enhance the Raman scattering efficiency of molecules through surface plasmon-induced electromagnetic enhancement mechanism.<sup>58</sup> When compared to spherical particles, anisotropic nanostructures such as nanorods and stars causes several fold increase in SERS signal intensity and are suitable for sensing and diagnostic platforms.<sup>18,61-63</sup> Herein, we estimated the SERS activity of these newly synthesised AuNRs. To avoid any unambiguity, and have uniform AuNRs concentration in the probe volume, we first prepared its self-assembled monolayer on the glass substrate via APTMS functionalization. These monolayered substrates were then treated with equal volumes of the reporter molecule, 4-mercaptobenzoic acid (4-MBA), and washed properly to remove any unbound molecules. Figure 2.22 represents the Raman spectra of 4-MBA acquired from the functionalized substrate. Mainly the peaks corresponding to aromatic ring vibrations at 1590 cm<sup>-1</sup> and 1090 cm<sup>-1</sup> are highly enhanced in the presence of AuNRs. The AuNRs prepared with 0.1 M CTAB showed the lowest SERS activity. With the decrease in CTAB concentration, there was an increase in SERS signal intensity, and the best results are obtained for that prepared at 0.001 M CTAB. This can be understood by the fact that with the decrease in CTAB concentration there is an increase in aspect ratio. The longest AuNRs supports more electromagnetic field due to the increase in its extinction coefficient.

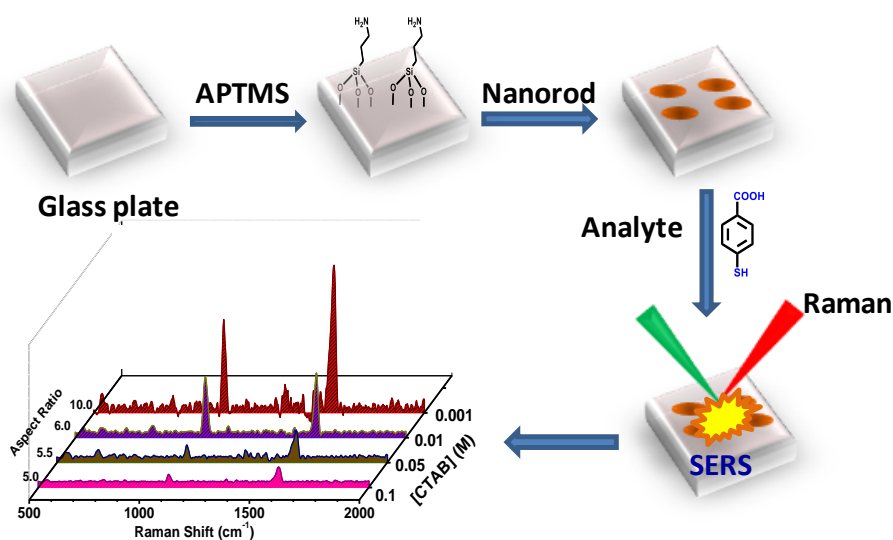


**Figure 2.22.** Schematic representation of SERS substrate preparation and Raman spectra of 4-mercaptobenzoic acid adsorbed onto self-assembled monolayers of AuNRs.

## 2.4.10. Application in bio-photonics

### 2.4.10.1. Photothermal therapy studies on cancer cells

To demonstrate the usefulness of these improved and multi-characteristics of AuNRs in a close to a real scenario, as a next step, the PTT efficiency of synthesized AuNRs was evaluated in breast cancer (SKBR3) cells (Figure. 2.23). Upon irradiation

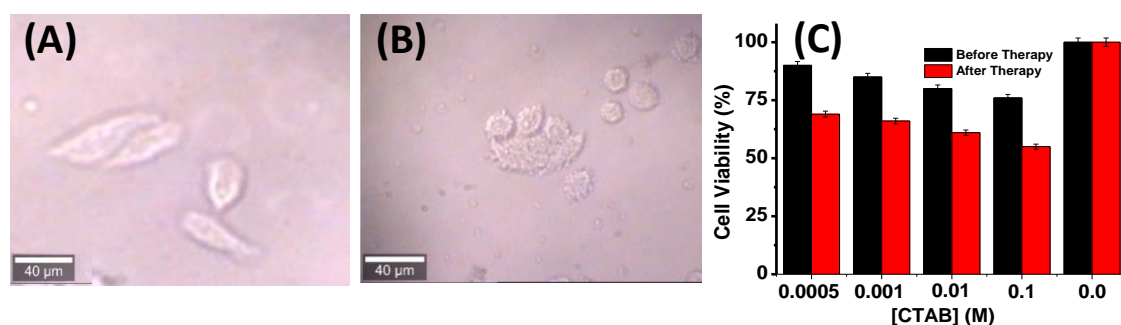


**Figure 2.23.** (A) and (B) are the bright-field microscopic images of the cells before and after irradiation. (C) In vitro cytotoxicity before and after laser irradiation (1 min) of SKBR3 cells in the presence of AuNRs prepared with L- DOPA (1 mg) and different CTAB concentrations (9.75 mL, 0.1 M-0.0005M). Control data is that of cells in the absence of AuNRs.

with 808 nm laser, the cells lost their normal spindle-shaped morphology indicating the progression of cell death. More quantitative data are obtained from MTT assay. In all the cases, the viability of cells (incubated with AuNRs 4 h) got drastically reduced upon laser irradiation (for 1 min). The maximum cytotoxic effect observed for AuNRs with 0.1 M CTAB is due to (i) high surfactant concentration, (ii) better overlap with the used laser excitation.

#### **2.4.10.2. SERS fingerprinting on cancerous cells**

In addition to MTT and visual analysis, attempts were made to monitor cell death through spectroscopy. Though Raman analysis has emerged as an authentication tool for chemical entities, its low scattering efficiency, has obstructed the real-time study of molecular-level changes associated with cell destruction. However, herein, by taking advantage of the AuNR's ability to amplify the Raman signal through SERS mechanism, we were able to analyse the minute alterations in biochemical components of sub-cellular malieu upon photothermal therapy. SERS spectra of SKBR3 cells prior to and after laser irradiation are presented in figure 2.24. Careful inspection of these spectral patterns revealed significant changes corresponding to various bond vibrations nucleic acids and proteins. Generally, important peaks appeared at around 520, 830, 1163, 1265, 1372, 1542 and 1595  $\text{cm}^{-1}$  which were assigned to disulfide bond (S-S) of proteins, O-P-O (DNA backbone), tyrosine C-H bending, C-C<sub>6</sub>-H<sub>5</sub> stretching mode in Phe, amide III, C=C bending mode of Phe and guanine and adenine (N<sub>7</sub>-H stretches) respectively. After laser irradiation, we noted decline of the band intensity corresponding to the O-P-O (~ 830  $\text{cm}^{-1}$ ) and enhancement of peak at 1595  $\text{cm}^{-1}$  (N<sub>7</sub>-H vibrations). The DNA dissociated from histone proteins during cell death exposed as guanine and adenine to the plasmonic field of AuNRs which results in an increase in SERS intensity after therapy.

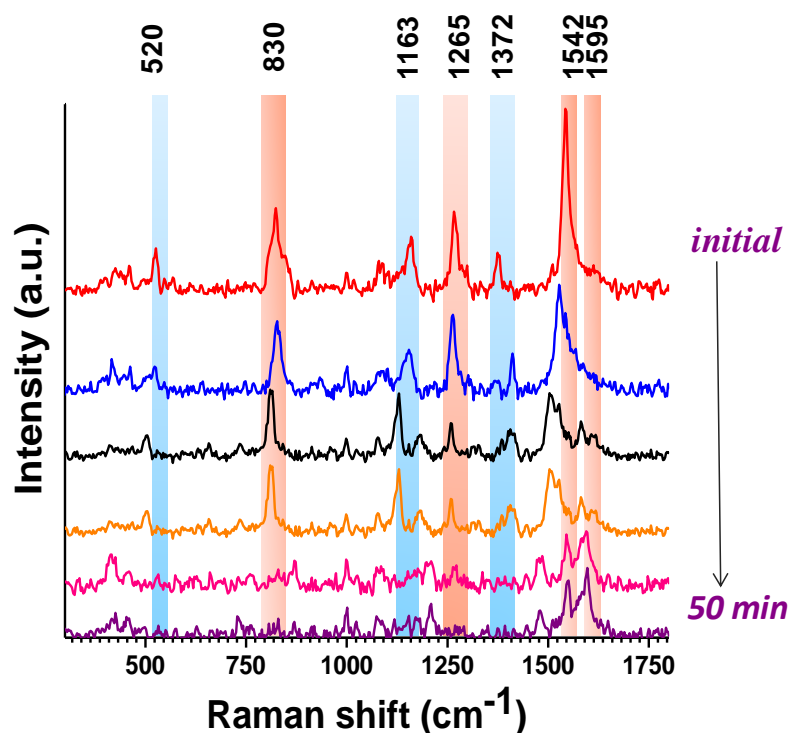


**Figure 2.24.** SERS spectra of SKBR3 cells incubated with AuNRs for 4 hours as a function of time upon irradiation with 808 nm laser.

## 2.5. Conclusion

In summary, the studies presented herein illustrate the capability of L-DOPA to produce AuNRs at extremely low CTAB concentrations. Compared to the conventional procedure the AuNRs produced herein have more uniformity and better yield. One possible reason could be L-DOPA's efficient intercalation with CTAB bilayer. This may serve as one of the first steps towards developing a completely greener synthetic route which is considered to be a holy grail in the field. Cytotoxic experiments indicated the improvement of cell viability up to 85 % for AuNRs prepared through this novel route. In addition to the reduction in the use of toxic chemicals in the preparation stage, the current method also offers the advantage of eliminating the need for post-synthetic treatment for bio-photonics,



like photothermal therapy of cancer. Moreover, the LSPR plasmon absorption of the AuNRs with lower CTAB molar ratios is widely tunable in the Vis-NIR region extending up to 1260 nm. In particular, this covers both the bio-optical windows which further adds up their value. Thus, it will promote bio and therapeutic utility by allowing to use NIR light which has more penetration capability. Furthermore, we have demonstrated the photothermal efficiency of AuNRs in the presence of NIR laser irradiation (808 nm) and extended the PTT effect on breast tumor cells, SKBR3 which showed significant cell death. Their high Raman enhancing capability enabled us to monitor minute biochemical changes in sub-cellular component through SERS fingerprinting and imaging modality. Therefore, the synthesised AuNRs have evolved as a promising nanomaterial towards bio-nanophotonics, especially cancer therapy.

## **2.6. Reference**

- (1) Abadeer, N. S.; Murphy, C. J. *Journal of Physical Chemistry C* **2016**, *120*, 4691-4716.
- (2) Yang, X.; Yang, M. X.; Pang, B.; Vara, M.; Xia, Y. N. *Chemical Review* **2015**, *115*, 10410-10488.
- (3) Gao, N.; Chen, Y.; Li, L.; Guan, Z.; Zhao, T.; Zhou, N.; Yuan, P.; Yao, S. Q.; Xu, Q.-H. *Journal of Physical Chemistry C* **2014**, *118*, 13904-13911.
- (4) Peng, Y.; Xiong, B.; Peng, L.; Li, H.; He, Y.; Yeung, E. S. *Analytical Chemistry* **2015**, *87*, 200-215.
- (5) Kumar, A.; Kim, S.; Nam, J.-M. *Journal of the American Chemical Society* **2016**, *138*, 14509-14525.

- (6) Cao, J.; Sun, T.; Grattan, K. T. V. *Sensors and Actuators B: Chemical* **2014**, *195*, 332-351.
- (7) Ni, W.; Kou, X.; Yang, Z.; Wang, J. F. *Acs Nano* **2008**, *2*, 677-686.
- (8) Chen, H.; Shao, L.; Li, Q.; Wang, J. *Chemical Society Reviews* **2013**, *42*, 2679-2724.
- (9) Ratheesh, K. M.; Prabhathan, P.; Seah, L. K.; Murukeshan, V. M. *Biomedical Physics and Engineering Express* **2016**, *2*, 055005.
- (10) Qiu, L.; Larson, T. A.; Vitkin, E.; Guo, L. Y.; Hanlon, E. B.; Itzkan, I.; Sokolov, K. V.; Perelman, L. T. *Biomedical Optics Express* **2010**, *1*, 135-142.
- (11) Tong, L.; Wei, Q. S.; Wei, A.; Cheng, J. X. *Photochemistry and Photobiology* **2009**, *85*, 21-32.
- (12) Boustany, N. N.; Boppart, S. A.; Backman, V. *Annual Review of Biomedical Engineering* **2010**, *12*, 285-314.
- (13) Ali, M. R. K.; Rahman, M. A.; Wu, Y.; Han, T. G.; Mackeya, M. H.; Mackey, M. A.; Wang, D. S.; Shin, H. J.; Chen, Z. G.; Xiao, H. P.; Wu, R. H.; Tang, Y.; Shin, D. M.; El-Sayed, M. A. *Proceedings of the National Academy of Sciences of the United States of America* **2017**, *114*, E3110-E3118.
- (14) Liu, Z. M.; Ye, B. G.; Jin, M.; Chen, H. L.; Zhong, H. Q.; Wang, X. P.; Guo, Z. Y. *Nanoscale* **2015**, *7*, 6754-6761.
- (15) Tsai, M. F.; Chang, S. H. G.; Cheng, F. Y.; Shanmugam, V.; Cheng, Y. S.; Su, C. H.; Yeh, C. S. *Acs Nano* **2013**, *7*, 5330-5342.
- (16) Yuan, H.; Khatua, S.; Zijlstra, P.; Yorulmaz, M.; Orrit, M. *Angewandte Chemie International Edition* **2013**, *52*, 1217-1221.

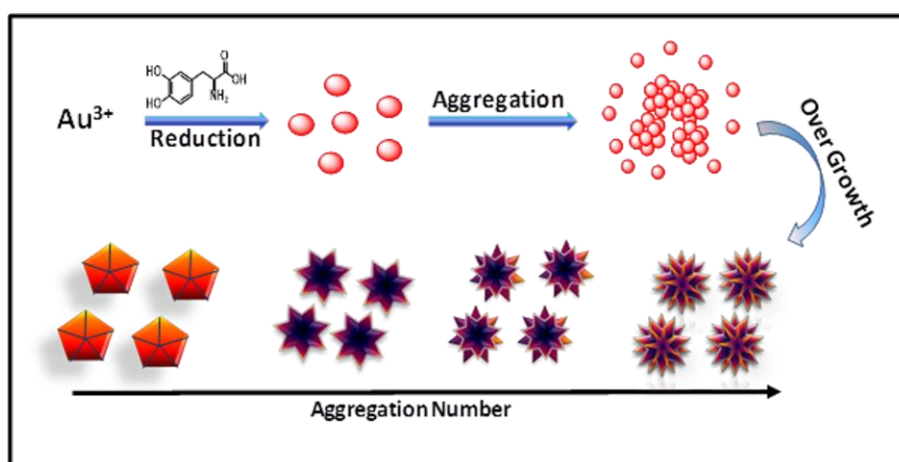
- (17) Khatua, S.; Paulo, P. M. R.; Yuan, H.; Gupta, A.; Zijlstra, P.; Orrit, M. *ACS Nano* **2014**, *8*, 4440-4449.
- (18) Wang, Y. Q.; Yan, B.; Chen, L. X. *Chemical Review* **2013**, *113*, 1391-1428.
- (19) R., J. N.; L., G.; J., M. C. *Advanced Materials* **2001**, *13*, 1389-1393.
- (20) Murphy, C. J.; Sau, T. K.; Gole, A. M.; Orendorff, C. J.; Gao, J.; Gou, L.; Hunyadi, S. E.; Li, T. *The Journal of Physical Chemistry B* **2005**, *109*, 13857-13870.
- (21) Zhu, J.; Yong, K.-T.; Roy, I.; Hu, R.; Ding, H.; Zhao, L.; Swihart, M. T.; He, G. S.; Cui, Y.; Prasad, P. N. *Nanotechnology* **2010**, *21*, 285106.
- (22) Xu, X.; Zhao, Y.; Xue, X.; Huo, S.; Chen, F.; Zou, G.; Liang, X.-J. *Journal of Materials Chemistry A* **2014**, *2*, 3528-3535.
- (23) Nikoobakht, B.; El-Sayed, M. A. *Chemistry of Materials* **2003**, *15*, 1957-1962.
- (24) Nikoobakht, B.; El-Sayed, M. A. *Langmuir* **2001**, *17*, 6368-6374.
- (25) Park, W. M.; Choi, B. G.; Huh, Y. S.; Hong, W. H.; Lee, S. Y.; Park, T. J. *ChemPlusChem* **2013**, *78*, 48-51.
- (26) Huang, X.; Yang, J.; Zhang, W.; Zhang, Z.; An, Z. *Journal of Chemical Education* **1999**, *76*, 93.
- (27) Vieira, S.; Vial, S.; Maia, F. R.; Carvalho, M.; Reis, R. L.; Granja, P. L.; Oliveira, J. M. *RSC Advances* **2015**, *5*, 77996-78005.
- (28) Wan, J.; Wang, J.-H.; Liu, T.; Xie, Z.; Yu, X.-F.; Li, W. *Scientific Reports* **2015**, *5*, 11398.
- (29) Pastoriza-Santos, I.; Pérez-Juste, J.; Liz-Marzán, L. M. *Chemistry of Materials* **2006**, *18*, 2465-2467.

- (30) Das, M.; Yi, D.; An, S. *International Journal of Nanomedicine*, **2015**, *10*, 1521-1545
- (31) Gole, A.; Murphy, C. J. *Chemistry of Materials* **2005**, *17*, 1325-1330.
- (32) Pérez-Juste, J.; Pastoriza-Santos, I.; Liz-Marzán, L. M.; Mulvaney, P. *Coordination Chemistry Reviews* **2005**, *249*, 1870-1901.
- (33) Yu, C.; Varghese, L.; Irudayaraj, J. *Langmuir* **2007**, *23*, 9114-9119.
- (34) Xiaohua, H.; Svetlana, N.; A., E. S. M. *Advanced Materials* **2009**, *21*, 4880-4910.
- (35) Kozek, K. A.; Kozek, K. M.; Wu, W. C.; Mishra, S. R.; Tracy, J. B. *Chemistry of Materials* **2013**, *25*, 4537-4544.
- (36) Ye, X. C.; Gao, Y. Z.; Chen, J.; Reifsnnyder, D. C.; Zheng, C.; Murray, C. B. *Nano Letters* **2013**, *13*, 2163-2171.
- (37) Su, G.; Yang, C.; Zhu, J.-J. *Langmuir* **2015**, *31*, 817-823.
- (38) Sebastián, V.; Lee, S.-K.; Zhou, C.; Kraus, M. F.; Fujimoto, J. G.; Jensen, K. F. *Chemical Communications* **2012**, *48*, 6654-6656.
- (39) Ye, X.; Jin, L.; Caglayan, H.; Chen, J.; Xing, G.; Zheng, C.; Doan-Nguyen, V.; Kang, Y.; Engheta, N.; Kagan, C. R.; Murray, C. B. *ACS Nano* **2012**, *6*, 2804-2817.
- (40) Nath, N.; Chilkoti, A. *Analytical Chemistry* **2004**, *76*, 5370-5378.
- (41) Zheng, X.-S.; Hu, P.; Zhong, J.-H.; Zong, C.; Wang, X.; Liu, B.-J.; Ren, B. *Journal of Physical Chemistry C* **2014**, *118*, 3750-3757.
- (42) Harris-Birtill, D.; Singh, M.; Zhou, Y.; Shah, A.; Ruenraroengsak, P.; Gallina, M. E.; Hanna, G. B.; Cass, A. E. G.; Porter, A. E.; Bamber, J.; Elson, D. S. *Plos One* **2017**, *12*, e0185990-e0185990.

- (43) Yoosaf, K.; Ipe, B. I.; Suresh, C. H.; Thomas, K. G. *Journal of Physical Chemistry C* **2007**, *111*, 12839-12847.
- (44) Sajitha, M.; Vindhyasarumi, A.; Gopi, A.; Yoosaf, K. *RSC Advances* **2015**, *5*, 98318-98324.
- (45) Baron, R.; Zayats, M.; Willner, I. *Analytical Chemistry* **2005**, *77*, 1566-1571.
- (46) Willner, I.; Baron, R.; Willner, B. *Advanced Materials* **2006**, *18*, 1109-1120.
- (47) Lee, H.; Dellatore, S. M.; Miller, W. M.; Messersmith, P. B. *Science* **2007**, *318*, 426-430.
- (48) Meena, S. K.; Celiksoy, S.; Schafer, P.; Henkel, A.; Sonnichsen, C.; Sulpizi, M. *Physical Chemistry Chemical Physics* **2016**, *18*, 13246-13254.
- (49) Burrows, N. D.; Harvey, S.; Idesis, F. A.; Murphy, C. J. *Langmuir* **2017**, *33*, 1891-1907.
- (50) Thomas, N.; Mani, E. *RSC Advances* **2016**, *6*, 30028-30036.
- (51) Park, K.; Hsiao, M. S.; Koerner, H.; Jawaid, A.; Che, J.; Vaia, R. A. *Journal of Physical Chemistry C* **2016**, *120*, 28235-28245.
- (52) Burrows, N. D.; Lin, W.; Hinman, J. G.; Dennison, J. M.; Vartanian, A. M.; Abadeer, N. S.; Grzincic, E. M.; Jacob, L. M.; Li, J.; Murphy, C. J. *Langmuir* **2016**, *32*, 9905-9921.
- (53) Walsh, M. J.; Barrow, S. J.; Tong, W.; Funston, A. M.; Etheridge, J. *ACS Nano* **2015**, *9*, 715-724.
- (54) Toussi, S. M.; Zanella, M.; Abdelrasoul, G. N.; Athanassiou, A.; Pignatelli, F. *Journal of Photochemistry and Photobiology A* **2015**, *311*, 76-84.

- (55) Indrasekara, A. S. D. S.; Wadams, R. C.; Fabris, L. *Particle & Particle Systems Characterization* **2014**, *31*, 819-838.
- (56) Yoo, H.; Sharma, J.; Yeh, H. C.; Martinez, J. S. *Chemical Communication*. **2010**, *46*, 6813-6815.
- (57) Xu, X.; Zhao, Y.; Xue, X.; Huo, S.; Chen, F.; Zou, G.; Liang, X.-J. *Journal of Materials Chemistry A* **2014**, *2*, 3528-3535.
- (58) Wang, A.; Kong, X. *Materials* **2015**, *8*, 3024-3052.

## Developing One-Pot Synthetic Route for Multi-Branched Gold Nanocrystals for Bio-Photonic Applications



### 3.1. Abstract

*Multi-branched gold nanocrystals are promising candidates for sensing and therapeutic applications because of their high extinction coefficient, increased NIR response and localization of hot spots at their sharp tips. Herein, we investigated a viable room temperature synthetic strategy to prepare multi-branched gold nanocrystals of varying morphologies without the aid of additional nanoseeds or shape directing agents. By systematically modulating the bifunctional ligand to  $\text{Au}^{3+}$  ion molar ratio ( $[\text{L-DOPA}]/[\text{HAuCl}_4] = 0.15-1$ ), the plasmon absorption was tuned from visible (530 nm) to NIR (930 nm). The corresponding microscopic studies showed a gradual transformation of the nanomaterial's morphology from multiply twinned spheres to branched stars and flowers. The detailed spectroscopic and microscopic studies have revealed that the*

*evolution of these branched nanocrystals proceeds through aggregation and subsequent overgrowth of initially produced spherical particles. Gold nanostars, with multi-sharp branches, have greater tip-enhanced plasmonic properties in the NIR tissue optical window, which is suitable for in vivo biomedical applications. Further, by combining this with their high SERS activity and photon to thermal conversion efficiency, we employed them in the destruction of human lung adenocarcinoma cancer cells (A549) and followed the biochemical changes through Raman spectroscopy.*

### **3.2. Introduction**

Multi-branched gold nanocrystals such as gold nanostars (AuNS), a new type of gold nanostructures, have demonstrated potential applications especially in biomedical areas due to their several outstanding properties. These are highly anisotropic NPs composed of a small core with a large number of sharp tips.<sup>1,2</sup> Their morphology gives unique physicochemical and optical properties that can be controlled even with small shape modifications. Compared to other anisotropic structures, these NPs will exhibit good plasmon absorption due to the hybridizations of the plasmons of the core and the tips of varying sizes. This results in more number of hot spots per nanoparticle due to lightning rod effect and they exhibit very high extinction coefficients of the order of  $10^8$ - $10^9$   $M^{-1} cm^{-1}$ .<sup>3</sup> This makes them an excellent candidate for the detection of biomolecules and other analytes with single molecular sensitivity.<sup>4-6</sup> In addition to lightning rod effect, AuNS's tunable plasmon absorption with increased NIR response makes them highly suitable for multifunctional theranostics such as photothermal therapy and Raman bioimaging (Figure 3.1).<sup>7,8</sup>



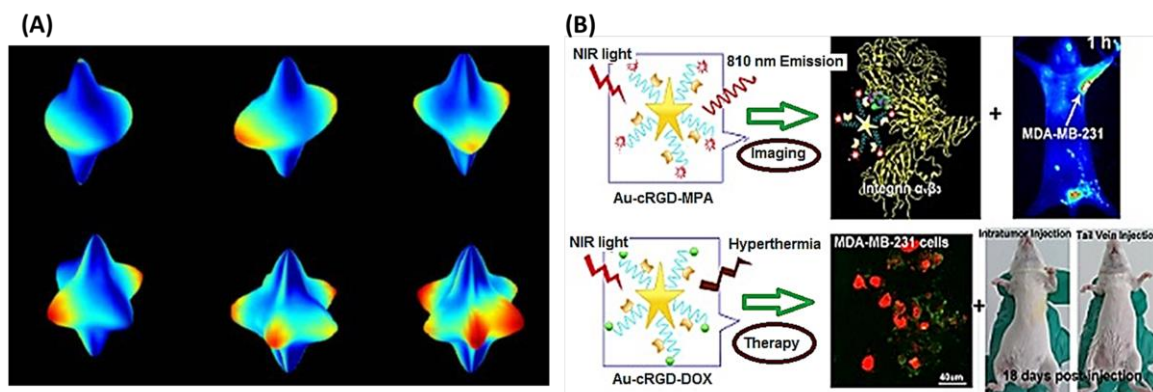


**Figure 3.1.** (A) Electric field distribution on the surface of the Au nanostars with an increasing number of tips<sup>9</sup> and (B) their biomedical applications (adapted and modified from reference 10).<sup>10</sup>

### 3.2.1. Synthetic Approaches

However, at present, only a few synthetic routes are available to prepare these promising classes of materials. There are several synthetic factors that can critically influence the efficiency of the synthesis and the quality of nanostars produced. These include (i) the dielectric environment (ii) quality of nanoseed and (iii) nature of the surfactant or such shape directing agents. The most common and well-exploited methodologies include seed-mediated growth and seedless method. The polymeric surfactant such as PVP or CTAB hinders surface functionalization and effective chemisorptions of analyte molecules. Also, they cause toxicity to biological samples which limits its practical applications. Another method for the synthesis is surfactant-less synthesis. But the major drawbacks of these are of their poor stability, which causes morphology transformation (reshaping) from star shape to other and corresponding blue shifts or loss of LSPR band. The poor stability is due to dominant van der Waals attractions resulting in particle agglomeration. These findings evidence the important role of that AuNS's surface properties in the stability and are pertinent to the SERS applications.

There were a few attempts to synthesize branched nanocrystals using classes of molecules like di/trihydroxybenzene or dopamine. Urchin like structures was obtained when hydroquinone was used as a secondary reducing agent along with citrate.<sup>11</sup> S. Yi *et al.* reported the formation of snowflake-like Au nanoparticles<sup>12</sup> as a result of dopamine oxidative polymerization into highly branched polydopamine structures.<sup>13</sup> However, these reactions were carried out either in the presence of nanoseeds or at boiling conditions. The resulting nanocrystals have the size of a few micrometers and are unsuitable for *in vivo* applications. Therefore, developing a simple room temperature one-pot surfactant-free synthetic methodology for multi-branched nanocrystals having size < 100 nm is highly desirable.

Herein, we illustrate, a simple one-pot procedure for the preparation of multi-branched gold nanocrystals using a bifunctional and bio-relevant molecule, namely L-DOPA. The approach presented here is more environmentally benign as we are using one of the naturally occurring antioxidants which function both as reducing and shape-directing agent. We also demonstrate tuning the size and morphology of the resulting nanocrystals from spherical to stars to flower by simple alteration of the reductant concentration.

### **3.3. Experimental section**

#### **3.3.1. Materials and methods**

Chemicals such as hydrogen tetrachloroaurate trihydrate (HAuCl<sub>4</sub>.3H<sub>2</sub>O) and L-3,4-dihydroxyphenylalanine (L-DOPA) were purchased from Ms. Sigma Aldrich. Sodium hydroxide was obtained from Ms. Sd fine Chem. Ltd. and were used as received without further purification. All glass wares were cleaned using

aqua regia prior to use and the experiments were performed in Millipore water (18.2 M $\Omega$ ).

### **3.3.2 Characterization**

UV-visible absorption spectra were obtained using a UV- 3101PC UV-VIS-NIR (Ms. Shimadzu Corporation, JAPAN) and diode array (UV-VIS 8453, M/s. Agilent Technologies Inc. USA) spectrophotometer. All measurements were performed in a quartz cuvette (1 cm).

TEM studies were carried out on a FEI's 300 kV high resolution (FEI-Tecnai G2-30 with EDAX) transmission electron microscope by drop-casting nanoparticle solution onto a carbon-coated Cu grid.

For XRD, samples were prepared by repeated drop-casting of Au nanoparticle solutions onto a clean glass plate and data were acquired using a Panalytical PW 3040/60 X'Pert Pro powder diffractometer and Cu K $\alpha$ 1 radiation.

For IR studies, nanoparticles were dispersed in KBr and carried out measurements in diffused reflectance mode using IR Prestige-21 Fourier transform IR spectrophotometer, Ms. Shimadzu Corporation, Japan. The spectra thus obtained were converted into transmittance mode through Kubelka-Munk operation.

Dynamic light scattering (DLS) was carried out using Zetasizer nanoseries, (Zeta Nano-ZS, Ms. Malvern Instruments, UK). A minimum of six measurements was taken for each sample to ensure statistical significance.

Raman spectra were collected using portable QE Pro-Raman spectrometer with 785 nm laser as the excitation source and mercaptobenzoic acid (MBA) as the Raman reporter.

The fluorescent images were collected using a Nikon inverted microscope model TS-100 FLED (Nikon Corporation, Japan).

**3.3.3. Synthesis of multi-branched gold nanocrystals:** In a typical experiment, 15 mL of 0.2 mM HAuCl<sub>4</sub> solution was mixed with 50 μL of 10 mM L-DOPA solution and 10 μL of 0.15 M NaOH solution. The formation of Au(0) and subsequently smaller Au nanoparticles was evident from the immediate color change of the solution.

**Cell culture:** The A549 cancer cell line (human lung adenocarcinoma) was procured from the American Type Culture Collection (ATCC, Manassas, VA, USA) and preserved in Dulbecco's Modified Eagle Medium (DMEM) supplemented with fetal bovine serum (FBS, 10%) at 37 °C and under an atmosphere of 5% CO<sub>2</sub>. Glass bottom, 96-well plates, and 4-well chamber slides were used for culturing the cells.

**MTT assay for cytotoxicity studies:** The potential of different gold nanoconstructs for inhibiting cell growth were evaluated against A549 cells. The principle of MTT assay relies on the cleavage of a tetrazolium salt by mitochondrial dehydrogenase enzyme in viable cells. 100 μL of the cell suspension containing  $\sim 5 \times 10^4$  cells/well were seeded into a 96-well glass plate, mixed with various concentrations of nanoconstructs and incubated for 4 h at 37 °C in a CO<sub>2</sub> incubator. Subsequently, each well is treated with 20 μL MTT (5 mg/mL) and further incubated for 2 h. This resulted in the formation of insoluble formazan crystals. These were solubilized with 100 μL MTT lysis buffer and incubation continued for an additional 4 h. Later, a microplate spectrophotometer was employed for measuring absorbance at 570 nm from which the quantification of cell viability was carried out.

**SERS cell imaging studies:** Cells seeded in 4-well chamber slides were first treated with the different gold nanoconstructs and 10  $\mu\text{M}$  SERS reporter molecules (Rhodamine B) for 2 hours. Excess probes from the medium were then washed off twice with PBS (pH 7.4). SERS imaging studies were carried out with WI-Tec confocal Raman microscope (WI-Tec, Inc., Germany). The data were collected over an area 50  $\mu\text{m}$  x 50  $\mu\text{m}$  with 150 x 150 points per line in both directions and integration time of 0.02 s.

**SERS spectral analysis:** A549 cells were cultured in 4 well chamber slide made of glass. Gold nanoconstructs were added to the wells and incubated at 37°C for 4 h together with control (media alone). Further, the cells were irradiated with 808 nm laser (0.1  $\text{W}/\text{cm}^2$ , 1 min) and investigated with the spectral fingerprint and mapping image on confocal Raman microscope. Suitable cells were focused on using the integrated video camera and scanned with an integration time of 0.5 s and averaged over 10 accumulations.

**Live dead assay:** After the laser irradiation and subsequent treatment with 200  $\mu\text{L}$  of 1:1 mixture of acridine orange and ethidium bromide (100  $\mu\text{g}/\text{mL}$ ) and 96-well plate containing cells and nanoconstructs were washed two times using PBS solution. Then the fluorescence images were taken under a FITC filter wherein live cells appeared as green and dead cells stained orange.

## **3.4. Results and discussion**

### **3.4.1. Morphological evolution of nanocrystals**

#### **3.4.1.1. Absorption studies**

Figure 3.2 illustrates the observed colour changes and corresponding absorption spectrum of the nanoparticles produced by mixing of 0.2 mM L-DOPA

and 0.1 mM NaOH and 15 mL aqueous solution of HAuCl<sub>4</sub> (0.2 mM). Initially, the solution attained a red colour which after one hour gradually changed to purple. The optical measurements done by UV-Visible spectrophotometer showed only a single absorption maximum centered around 530 nm in the initial stages. While two peaks (~530 nm and ~710 nm) were clearly evident after the colour change. In the case of the gold, isotropic spherical nanoparticles usually exhibit only one plasmon (centered around 520 nm) whereas anisotropic nanostructures such as nanorods, nanostars display multiple absorption maxima corresponding to different (transverse and longitudinal) modes of plasmon oscillation.<sup>3,14-22</sup> Therefore, we argue that during the first one hour of reaction mainly spherical nanoparticles are formed which eventually transform to anisotropic nanostructures.

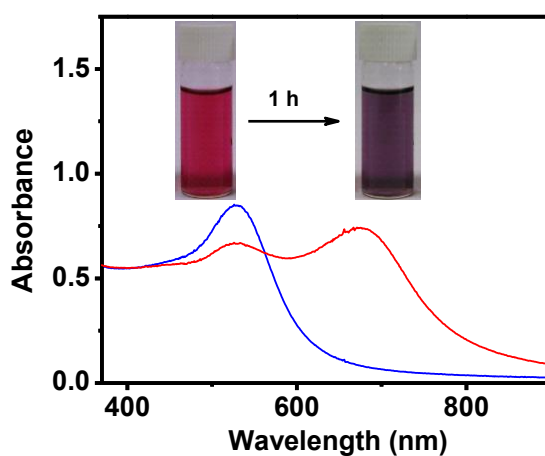


**Figure 3.2.** The absorption spectrum of Au nanoparticles in the initial stages (red) and after one hour (purple) prepared by adding 0.2 mM L-DOPA and the inset shows their corresponding colour photographs.

### **3.4.1.2. Transmission electron microscopic studies**

In order to understand the origin of these absorption spectral profiles and hence to characterize the produced nanoparticles, TEM studies were performed. TEM images recorded from different areas of the sample confirmed the occurrence of more than 95 %

multiply branched nanocrystals (Figure. 3.3A). Also, we found that the nanomaterials thus produced have the size in the range 30-50 nm with the majority having dimension ~35 nm (Figure.3.3B). The no. of arms of each nanocrystal varies from 3-7 and have a length of around 10 nm. The absorption properties of gold nanostars are known to arise from the combinations of plasmons localized at their core and tips. In the present case, the absorption peak at ~ 530 nm (Figure. 3.2.) is mainly assigned to the TSPR of the core and tips. In addition this may also have contribution from any spherical particles present in the solution. While the lower energy band centered at ~710 nm arises from LSPR of the elongated branches.<sup>4,8,10,23-25</sup> From the HRTEM images the d spacing values were

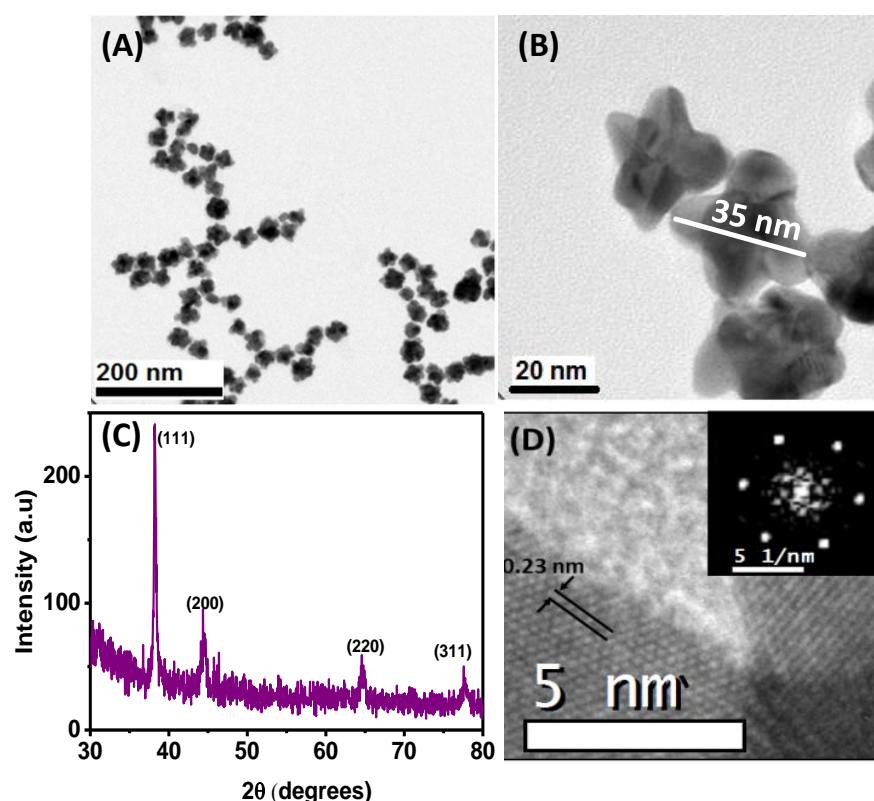


**Figure 3.3.** (A-B) TEM images of the obtained nanostars prepared by adding 200  $\mu$ M L-DOPA (C) XRD data illustrating the crystal planes and (D) HRTEM images of the arms and inset shows the diffraction pattern obtained from one of the arms.

extracted as 0.235 nm and 0.201 nm (Figure. 3.4D). This corresponds to (111) and (200) planes of gold atoms in the fcc crystal lattice. Similar results were obtained from XRD measurements (Figure. 3.3C) which inferred the predominant (111) facets of nanocrystals.

### 3.4.2. Kinetic & mechanistic investigation

#### 3.4.2.1. Role of reagents

##### 3.4.2.1.1. Role of NaOH

All three reagents are highly important for the synthesis of multi-branched nanoparticles. NaOH plays a crucial role in producing quality nanoparticles. The  $\text{HAuCl}_4$  solution exhibit a broad absorption in 250 nm – 350 nm range with a shoulder around 280 nm which got disappeared upon the addition of NaOH. While L- DOPA exhibit two prominent peaks at 225 nm and 280 nm (Figure 3.6 A). Upon mixing, the two the band corresponding to L-DOPA continually decreased

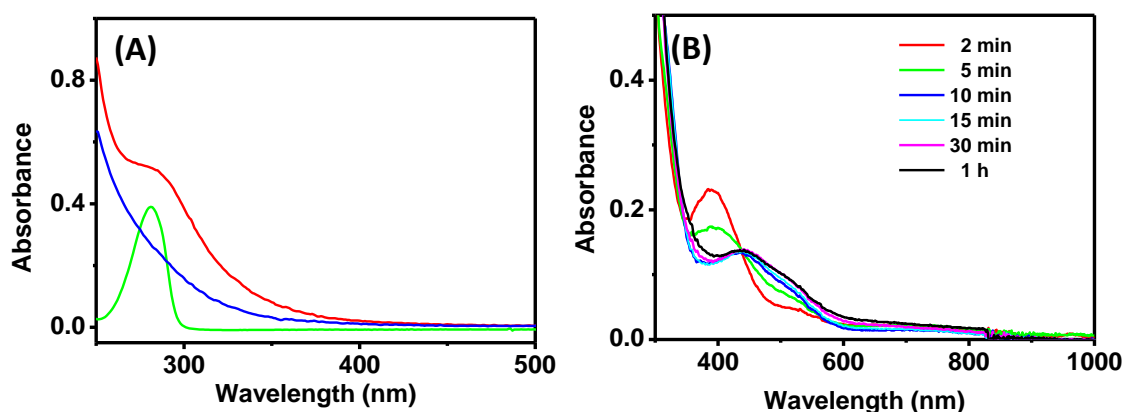


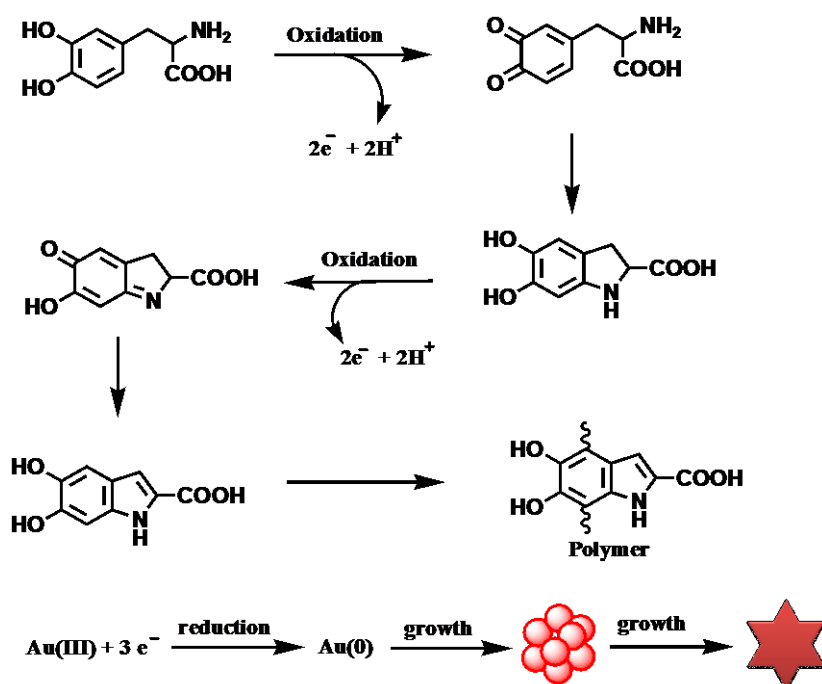
**Figure 3.4.** (A) Absorption spectral profile of  $\text{HAuCl}_4$  (red), L-DOPA (green) and  $\text{HAuCl}_4$  and NaOH (blue) and (B) Time-dependent absorption spectral changes of 0.2 mM  $\text{HAuCl}_4$  solution after the addition of 0.2 mM L-DOPA (i.e. in the absence of NaOH).



with the concomitant emergence of red-shifted absorption above 450 nm (Figure 3.6 B). This suggests the oxidation L-DOPA into its quinone form. However, no evolution of plasmon absorption was noted even after one hour. This may be due to the fact that  $\text{Au}^{3+}$  ions might have reduced to  $\text{Au}^+$  and not to  $\text{Au}^0$ . This indicates that L-DOPA alone with gold solution is insufficient for nanoparticle generation. Interestingly, addition of NaOH to this solution yielded facile generation of nanoparticles.

### 3.4.2.1.2. Role of L-DOPA

Structurally, L-DOPA contains a catechol unit and zwitterionic amino acid part. Dihydroxy benzene unit of these types of biomolecules are known to undergo oxidation producing dopaquinone, dopachrome and other polymeric structures (Scheme 3.1).<sup>42,49-51</sup> The electrons released during this process can be involved in the reduction of metal



*Scheme 3.1. Representation of L-DOPA oxidation and  $\text{Au}^{3+}$  reduction reactions resulting in the formation of polymer and branched Au nanocrystals.*

cations. In the present case, the redox potential of L-DOPA is at least 0.3 V negative than Au(III)/Au(0) system and hence the reduction reaction is thermodynamically feasible.<sup>52,53</sup> It is reported that the redox potentials of catechols shift to lower values with increase in pH.<sup>53</sup> Therefore, the rapid addition of NaOH raises the local pH, causing a faster reduction rate. The oxidized product thus produced may bind with nanoparticle surface and establish a capping layer.

### 3.4.2.2. IR studies

The IR spectrum of L-DOPA displayed numerous peaks corresponding to different modes of stretching and bending vibrations (Fig. 3.5). Most of these peaks were absent in the IR spectrum of gold nanostars. For example, only a broad band in the region 3000-3600  $\text{cm}^{-1}$  was obtained for Au nanostars whereas clear peaks corresponding to OH, CH, and NH vibrations were present for L-DOPA. In particular, the IR spectrum of the nanocrystals has quite a resemblance with that reported for melanin like structures.<sup>26-28</sup>

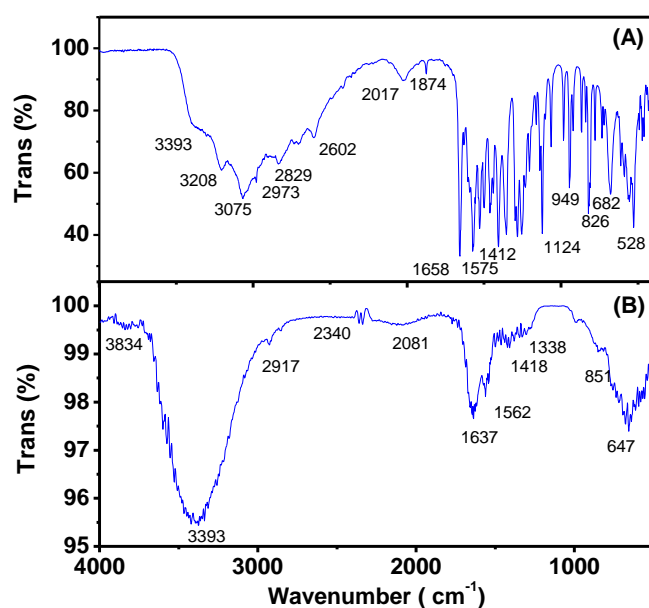


**Figure 3.5.** FTIR spectra of (A) L-DOPA and (B) Au nanostars (0.2 mM L-DOPA) recorded in KBr.

This indicates the polymeric nature of surface-bound ligands. Hence, fostering of branched Au nanocrystals may occur through the shape directing action of produced polymeric structures. Such instances have been reported in similar cases. Further to understand the role of L-DOPA and hence to gain insight on the nanoparticle growth mechanism, performed detailed absorption and microscopic studies.

### 3.4.2.3. Effect of L-DOPA concentration on tuning the morphology of nanocrystals

Since L-DOPA plays the role of both reducing and stabilizing agent, we thought that the modulation of its molar ratio could be a viable strategy to tune the morphology of the nanocrystals. Figure. 3.6 shows the colour photograph of the solution and corresponding absorption spectra of nanoparticles prepared in the presence of varying

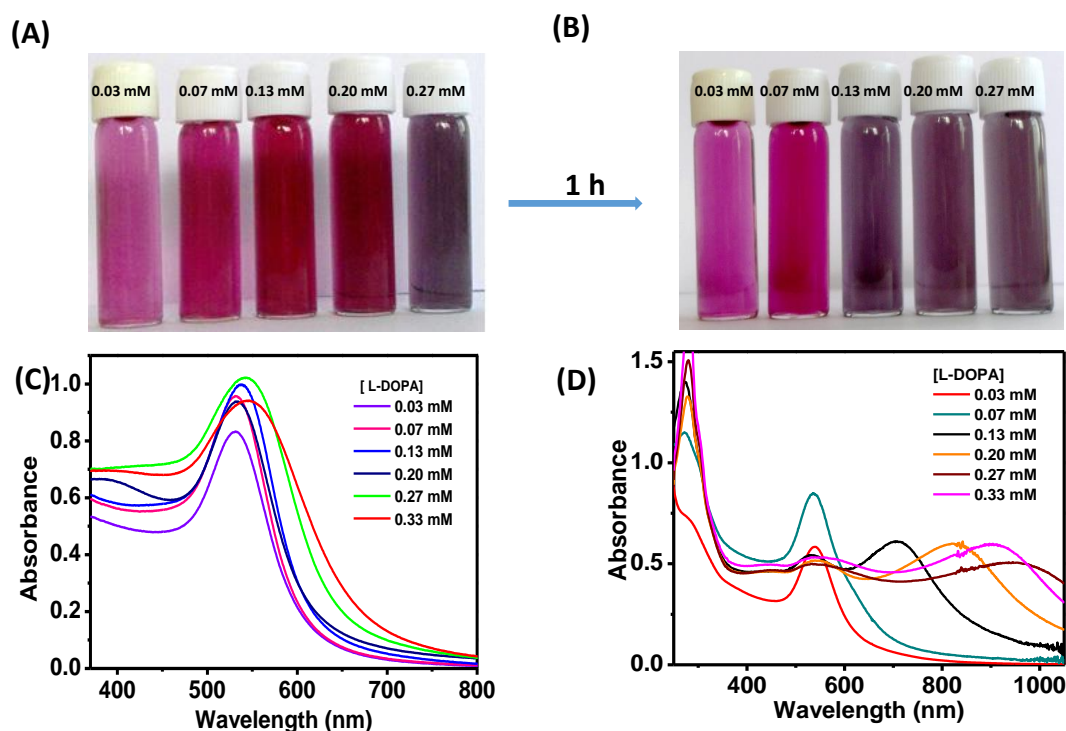


**Figure 3.6.** (A,B) Color photographs of nanoparticle solutions prepared in presence of different L-DOPA concentrations ( $[L-DOPA] = 0.03-0.27$  mM) taken after (A) 2 minutes and (B) 1 h of mixing the reagents, (C,D) their corresponding absorption spectra.

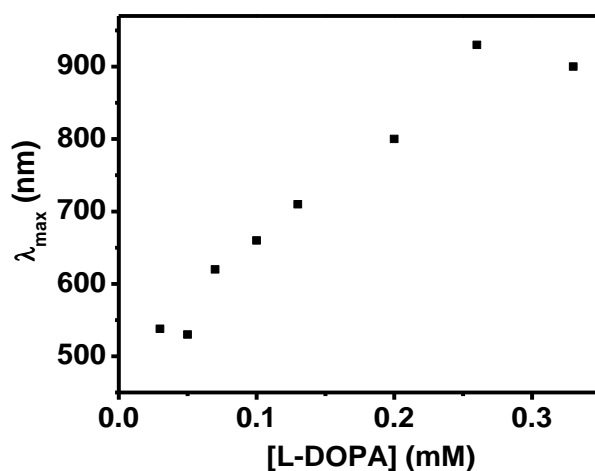


**Figure 3.7.** The plot showing the variation of the absorption wavelength maximum with respect to L-DOPA concentration.

amounts of L-DOPA while maintaining all other conditions constant. In about ~ 2 minutes almost all the solutions developed wine red colour, except that above 0.20 mM. As time progresses, there were drastic colour changes to each of these solutions (Figure 3.6 A, 3.6 B). At very low concentrations (0.03 mM L-DOPA) solution developed red colour that got intensified over a period of 15 minutes. Only a single plasmon band with a  $\lambda_{\max} \sim 540$  nm appeared in the equivalent absorption spectrum. A similar observation was

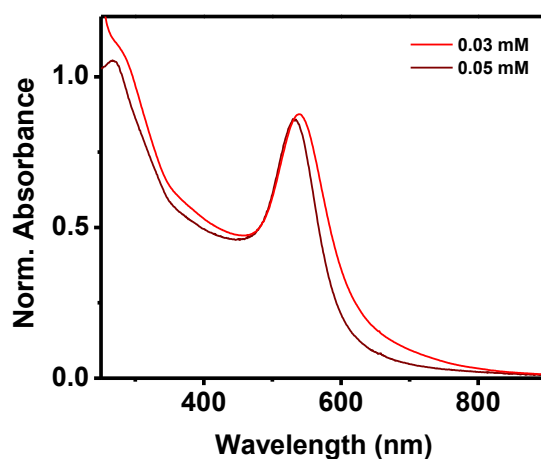


**Figure 3.8.** Normalized absorption spectra of gold nanoparticles prepared in presence of 0.03 mM (red) and 0.05 mM (wine red) concentration of L-DOPA.

noticed when the amount of L-DOPA was raised to 0.05 mM. The solution initially attained wine red color which deepened in about 15 minutes and absorption maximum got blue-shifted to ~ 530 nm with narrowing of the bandwidth (Figure. 3.8). Along with this, the optical density (OD) improved from 0.6 to 0.9 (Figure 3.6D) supporting the reducing action of L-DOPA. Wherein, the raise of reductant concentration resulted in the conversion of larger percentage of Au<sup>3+</sup> ions to Au(0) thus producing more number of Au nanoparticles. The hypsochromic shift in absorption maximum bestows to the evolution of nanoparticles having smaller sizes. Whereas decrease in the full width at half maximum (FWHM) of the band may imply the more uniform size distribution of the nanocrystals (*vide infra*). However, with any further increase in molar ratio, over a period of time, the initially generated wine red color gradually changes to purple and grey. The optical measurements recorded after 1 hour showed a decrease in the OD at 530 nm and a new red-shifted band appeared (Figure 3.6 D). The position of this band underwent a gradual and linear red-shift along with added reductant volume (Figure 3.7). For example, the nanomaterials prepared in the presence of 0.07 mM L-DOPA have major absorption peak at ~ 530 nm and shoulder at ~ 620 nm. Bathochromically shifted clear new peaks at 660, 710, 800 and 930 nm were produced when the amount of reductant reaches 0.1, 0.13, 0.2, and 0.26 mM respectively. Any further increase in molar ratio brought blue shift to the absorption maximum ( $\lambda_{\text{max}} = 900$  nm for 0.33 mM). These spectral changes could be attributed to the formation of anisotropic nanostructures having different size and morphology which were further detailed through microscopic studies. Represented in figure 3.9 are the examples of TEM images of nanocrystals synthesized by varying the amount of L-DOPA and figure 3.10 are their corresponding statistical analysis. Nanomaterials of average size ~ 40 nm having spherical and multiply twinned

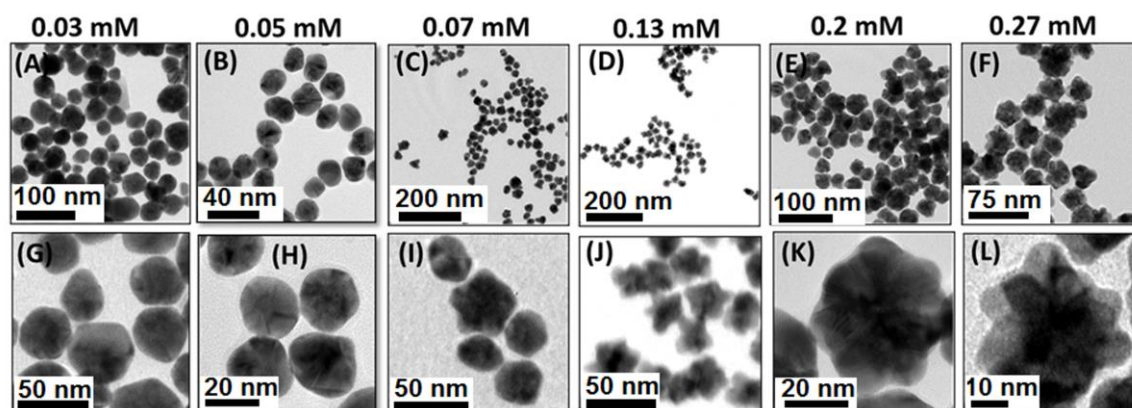


**Figure 3.9.** Representative examples of TEM images of nanocrystals prepared by varying the amount of L-DOPA.

structures were obtained at very low molar percentages (0.03 mM). Whereas raising in L-DOPA concentration to 0.05 mM materialized particles with more uniform sizes and reduced dimensions (~ 35 nm) (Figure 3.10 A,B).

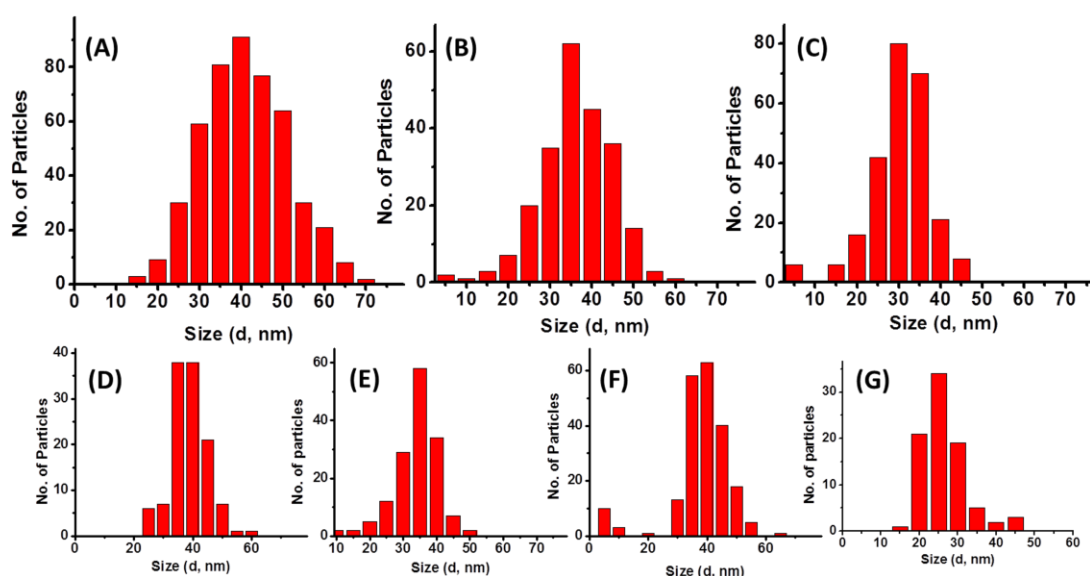


**Figure 3.10.** Graphs showing size distribution analysis of (A-C) the nanoparticles and (D-G) the nanostars obtained in presence of L-DOPA, (A) 0.03 mM, (B) 0.05 mM, (C) 0.07 mM, (D) 0.07 mM, (E) 0.13 mM, (F) 0.20 mM, (G) 0.33 mM.

This is inconsistent with our observed blue shift in the absorption maximum and shrunken FWHM value (vide supra) which corroborates with earlier literature reports. Hence, this

also substantiates the capping role of the reductant. Thus, at smaller molar ratios the amount of protecting ligand is insufficient to properly cover the nanoparticle surface thus resulting in more polydispersity. In addition, at this molar ratio, a minute percentage of (~ 5 %) tiny particles (< 10 nm) also coexists. This may additionally contribute to the obtained hypsochromic shift in the absorption maximum. Interestingly, the gradual evolution of nanoparticles having other morphologies such as nanostars and nanoflowers were evident with more added volumes of L-DOPA. For example, about 30 % of the particles formed have multiple arms when the concentration reaches ~ 0.07 mM (Figure 3.10 B, G). The size of the spherical nanoparticles is determined as 30-35 nm from TEM

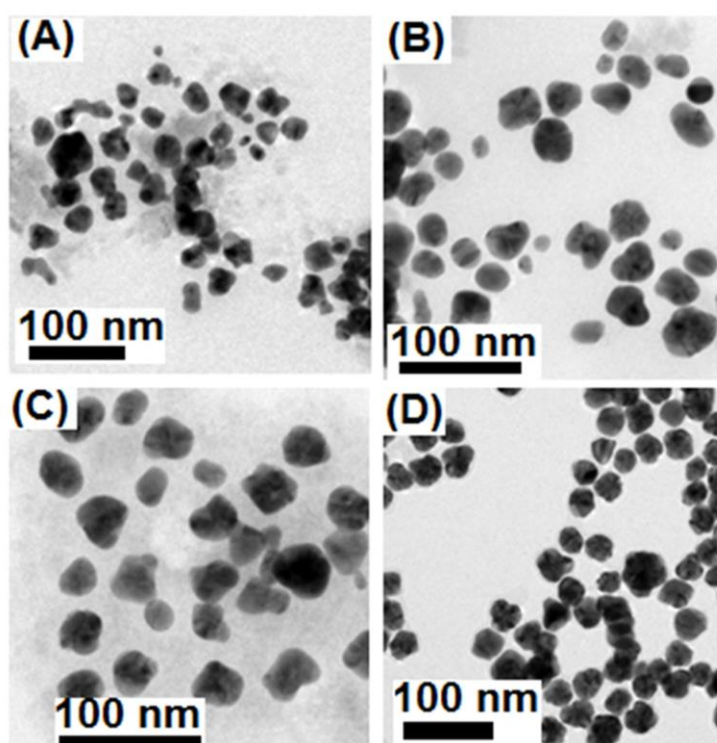


**Figure 3.11.** Representative examples of TEM images of nanoparticles prepared in the presence of 0.10 mM L-DOPA.

images. On the other hand, contemporary nanostars are slightly bigger in dimensions (Figure 3.10 C-D). Furthermore, in this case the percentage of smaller particles having dimensions < 10 nm has considerably increased when compared to that at 0.05 mM. A



further increase in fraction of star-shaped particles ( $> 50\%$ ) has been observed when the concentration reaches  $0.1\text{ mM}$ . However, most of the nanocrystals have  $< 4$  number of branches and the protrusions are mainly underdeveloped (Figure 3.11). Therefore, it is not surprising that this solution exhibit the lowest LSPR peak position ( $\lambda_{\text{max}} = 670\text{ nm}$ ). More than  $90\%$  of star-shaped particles (size  $\sim 35\text{ nm}$ ) were obtained when the reductant was further increased to  $0.13\text{ mM}$ . Whereas, higher molar ratios resulted in flower-like morphologies with many numbers of arms (petals). For example, along with star-shaped materials, flowers having, mainly two layers of petals were obtained in the presence of  $0.2\text{ mM}$  L-DOPA (Figure 3.9 D, I). The size distribution analysis gave dimensions of  $\sim 40\text{ nm}$  for these nanostructures (Figure 3.10 F). A further increase in size (to  $\sim 50\text{ nm}$ )

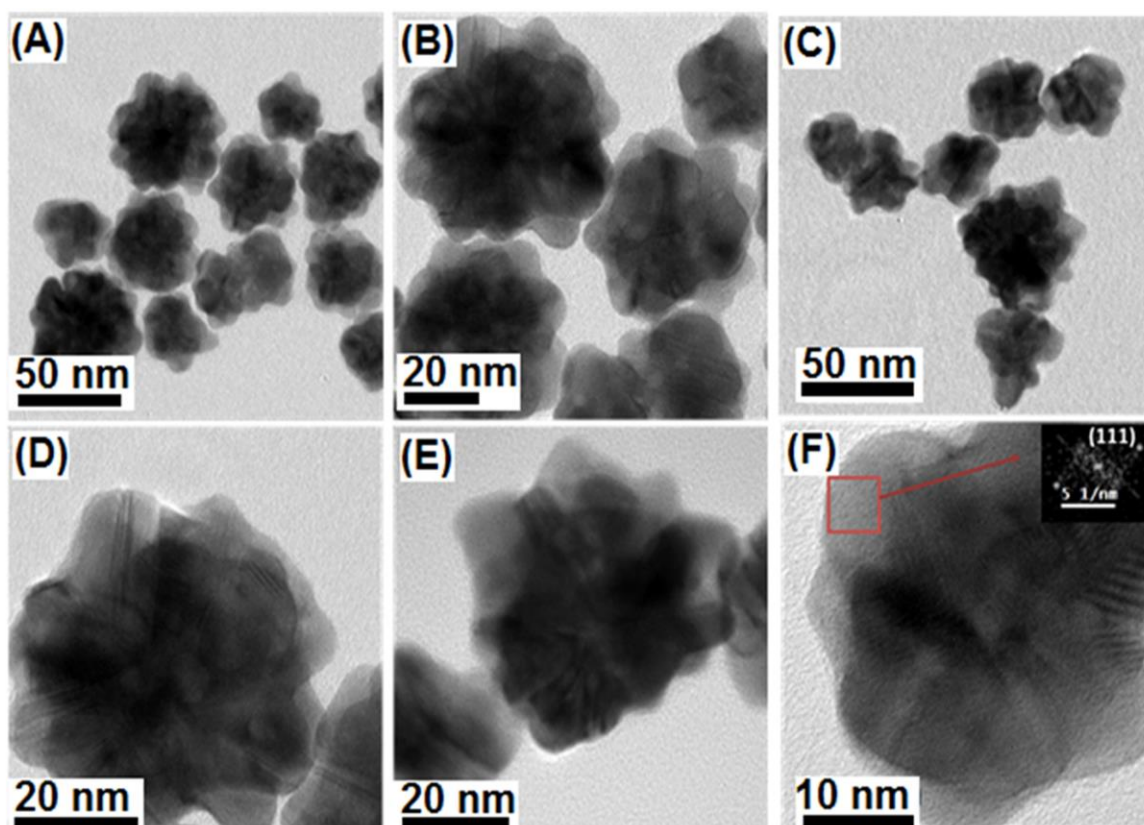


**Figure 3.12.** Representative examples of TEM images of nanoparticles prepared in the presence of  $0.27\text{ mM}$  L-DOPA; inset of (F) shows diffraction pattern obtained from one of the arms.



and the number of petals was perceived when the concentration reaches 0.27 mM. This is inconsistent with redshift in the absorption maximum from 800 to 930 nm. HRTEM images, reveals the flower-like morphologies are having arms with mainly (111) planes (Figure 3.12). Further raise in reductant concentration caused a decrease in the percentage of nanoflowers and most of the nanostructures have star-shaped morphologies with size ~ 30 nm (Figure 3.10 G) This is in accordance with the observed blue shift in LSPR band.

#### 3.4.2.4. Kinetics studies

To gain further insight on the mechanistic aspects of multiple types of nanoparticles realization, absorption spectral changes as a function of time were recorded for each of the solutions. Upon mixing the three reagents, plasmon absorption above 530 nm was obvious in all the cases. For example, at 0.05 mM, initially, the broad band was appeared at around 540 nm. With time this peak got intensified and blueshifted (to 530 nm) along with peak width sharpening. These spectral changes attained saturation stage in

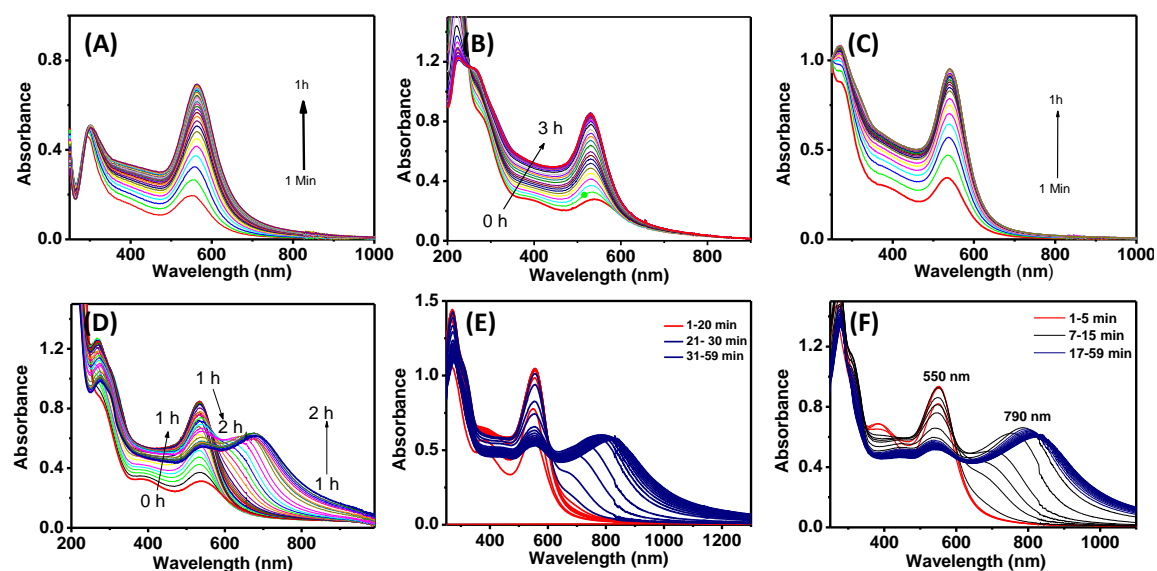


**Figure 3.13.** (A-C) Time dependent absorption spectral changes of  $\text{HAuCl}_4$  solution after the addition of L-DOPA;  $[\text{L-DOPA}] =$  (A) 0.05 mM, (B) 0.07 mM, (C) 0.1 mM, (D) 0.13 mM, (E) 0.2 mM, (F) 0.27 mM).

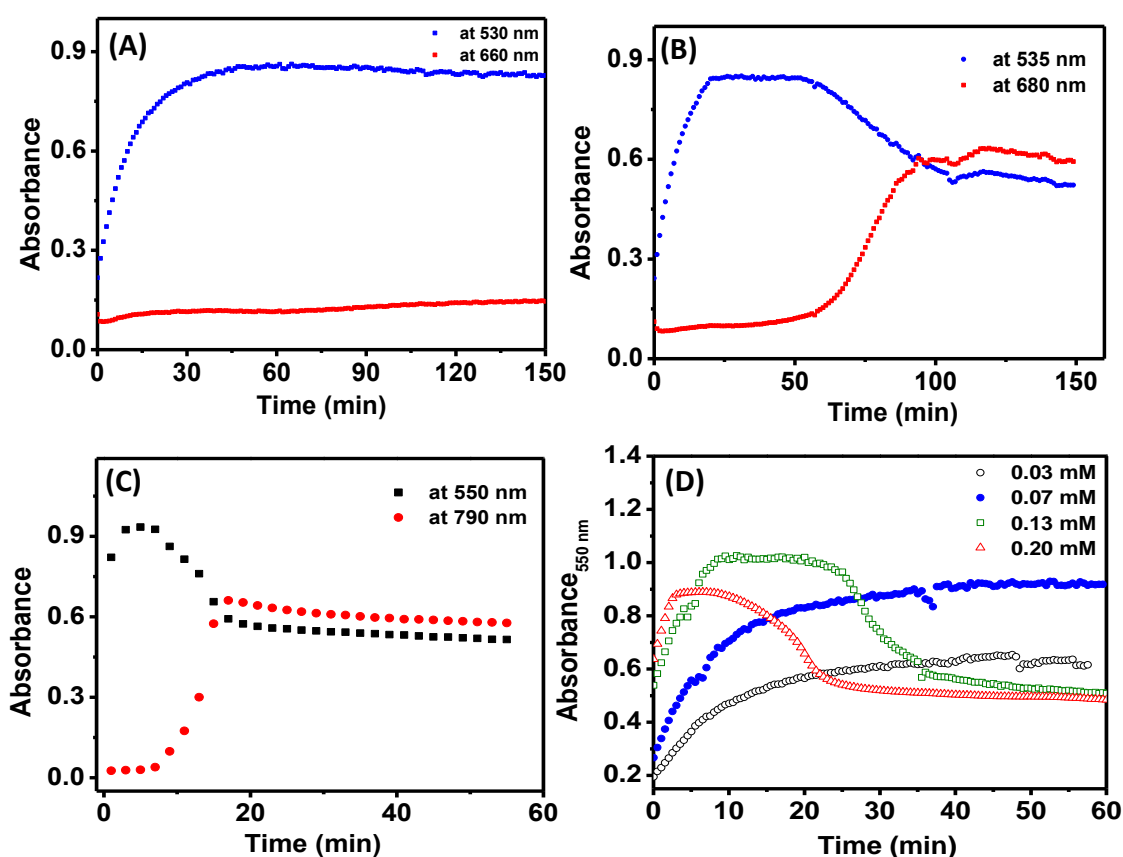


**Figure 3.14.** Evolution of TSPR and LSPR plasmon absorption of gold nanoparticles prepared in presence of varying amounts of L-DOPA; [L-DOPA] = 0.05 mM (A), 0.13 mM (B), 0.2 mM (C) and (D) shows the corresponding comparative evolution of TSPR band alone.

a period of about 1 hour. This implies that initially formed nanoparticles may be having wide size distribution. As the reaction progresses more nanoparticles with uniform dimensions are evolved due to continuous reduction of  $\text{Au}^{3+}$  ions and the reorganization of the initially formed nanoparticles (vide supra). A similar trend has been perceived in other samples. However, at concentrations higher than 0.13 mM, more red-shifted and broad spectra were obtained for the beginning of the reaction as well as at the first saturation period. The time required for reaching the first saturation period got diminished to ~50, 20, 8 and 3 minutes respectively for 0.05, 0.1, 0.13 and 0.2 mM concentrations (Figure 3.13 and Figure 3.14). As a result of this fast reduction rate, nanoparticles formed could be ill-defined and are more polydisperse. After the initial saturation period, the

absorption profile of nanoparticles having 0.03 and 0.05 mM L-DOPA did not undergo any considerable change. In contrast, those containing L-DOPA concentrations above 0.07 mM, exhibited a continuous drop of the peak intensity at 530 nm and a new band has concomitantly emerged at lower energies. The simultaneous occurrence of both these processes indicates transformation of initially formed nanoparticles to anisotropic nanostructures.

#### **3.4.2.5. Mechanistic investigation**

Understanding the nanoparticle formation mechanism is highly essential to materialize control over their size and morphology and tailoring their properties to desired applications.<sup>45,57-59</sup> However, the limitations posed by (i) the absence of a well-defined externally added seed, (ii) relatively faster reaction rate, (iii) the inability to trap the intermediate stages of growth and (iv) and the possible solid-state reactions/coalescence occurred during solvent evaporation and drying on TEM grid has restricted us in arriving at any concrete assumption on the mechanism. From the microscopic studies, it was evident that spheroid nanostructures are produced at lower molar ratios and multi-branched particles at higher ones. This may signify the soft templating role of the capping ligand. In fact, the nature of surface-bound ligands is estimated from IR studies as polymeric product of L-DOPA oxidation (*vide supra*). This is also fortified by the detection of an organic shell around nanoparticles in majority of the TEM images (Figure 3.15). Formation of anisotropic nanostructures has been reported in presence of such biopolymeric materials. In most of the well-established procedures, the synthesis of anisotropic nanostructures was achieved by the overgrowth of small nanoparticles

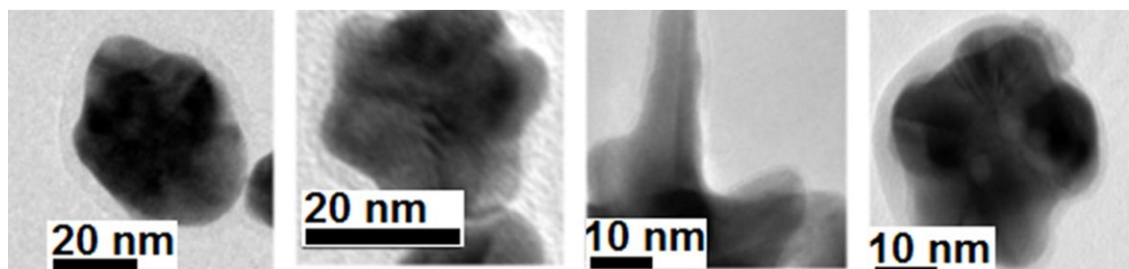


**Figure 3.15.** Representative TEM images displaying the presence of polymeric shell around nanomaterial.

(commonly termed as nanoseeds) with the aid of soft templates like CTAB and  $\text{AgNO}_3$ . In such instances, shape directing agents adsorb on certain planes of the nanoseeds thus blocking further growth along these sides. Then the formation of anisotropic nanostructure occurs via expansion of the exposed facets. This is accompanied by a continuous and simultaneous progression of absorption in the entire plasmon region. Because the anisotropic nanostructures have a much higher extinction coefficient compared to the spherical nanoparticles of the same size. On the other hand, the approach described here is devoid of the use of nanoseeds or any conventional shape directing agents. Even if nanoseeds are produced in the initial stages of the reaction, and the anisotropic nanostructures are generated via their simple overgrowth, one would expect similar trend in the absorption spectra. However, in the present case, it is noticed (i) first the evolution of a band around 530 nm, indicating that the initially formed nanoparticles are spherical in shape (ii) which then gradually decreases in intensity along with the concomitant formation of low energy absorption. Earlier theoretical and experimental studies have given evidence to the red-shifting of absorption maximum when two nanoparticles come close to each other. The peak position of this new band is highly dependent on the number of particles and the distance between them. The sigmoidal nature of the LSPR evolution indicates the multi-branched nanostructure realization

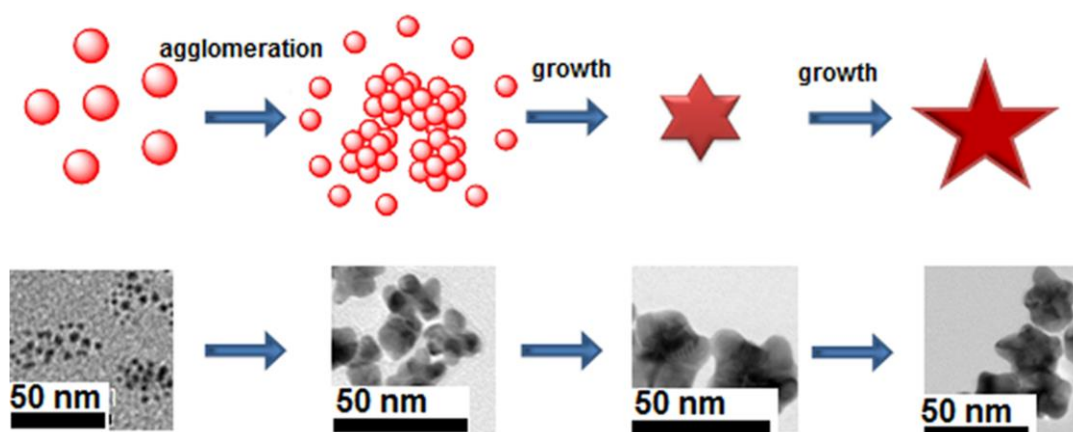


**Figure 3.16.** Schematic representation (up) and illustrative examples of TEM images showing the evolution of branched nanocrystals via particle agglomeration and growth process.

described here is autocatalytic in nature. This involves at least three stages (Figure 3.16) (i) Booming of smaller nanoparticles having size  $< 10$  nm (ii) their agglomeration and (iii) followed by their overgrowth to well-defined nanostructures. This proposition is reinforced by several facts and is detailed as follows. (i) A large percentage of smaller particles has been found both in the DLS and TEM images at the

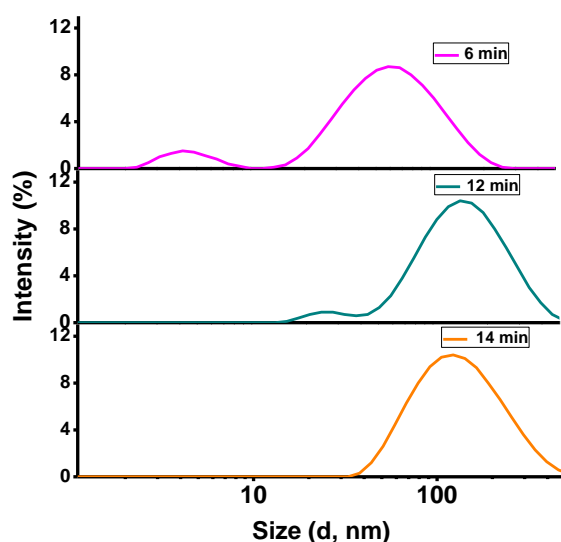


**Figure 3.17.** DLS data showing the variation of particle size during the evolution of the LSPR band.  $[L\text{-DOPA}] = 0.2$  mM.

first saturation period. (ii) Several distinct agglomerates of small particles were observed in different areas of TEM grid. The analysis of the kinetic data disclosed minimum of 2.5

times higher rate for increase in LSPR absorption than the drop of optical density at 530 nm. This is because the formation of one nanostar requires agglomeration of many numbers of particles. Hence the absorption spectral changes due to a decrease in the number of individualized small particles overwhelm the effect caused by high extinction coefficient of branched nanocrystals. (iii) A systematic examination of both TEM images and DLS data illustrated a rise in overall size in the LSPR growth stage along with time (Figure. 3.17). Thus according to this mechanism it could be assumed that the morphology of final nanostructure is dictated by the initial aggregation number. The kinetic studies expressed an increase in reaction rate with raise in L-DOPA concentration. This implies the number of particles present at a particular time in a given volume will be proportional to the reductant concentration. This in turn affects the initial aggregation number which varies in the order  $0.03 > 0.05 > 0.1 > 0.13 > 0.16 > 0.2 > 0.27$  mM. After this initial aggregation process, growth process occurs mainly at the exposed facets and the HRTEM images revealed, the arms of the multi-branched nanocrystals are mainly (111) facets. It could also be pointed out that effect of L-DOPA concentration on the size of nanocrystals may appear self-contradictory. There was a reduction in the average particle size from 40 nm to 35 nm when the L-DOPA concentration was raised from 0.03 to 0.05 mM. Thereafter particle size got steadily increased to 40 and 50 nm for 0.2 and 0.27 mM reductant concentrations respectively (vide supra). However it is to be noted that the particle morphology is entirely different for these concentration regimes. Only spheroid particles are observed at lower concentrations whereas the nanocrystals formed have multiple arms that above 0.1 mM. Moreover the kinetic studies presented here (Figure 3.13-3.14) demonstrate a clear difference in their formation mechanism. Only continuous evolution plasmon absorption at  $\sim 530$  nm was observed for spheroid particles. i.e. they are formed by the overgrowth of initially formed nuclei. On the

contrary, at concentration above 0.1 mM, the kinetic plot shows three distinct stages (i) fast raise in absorbance at  $\sim 530$  nm (ii) then an induction period (iii) followed by evolution of low energy LSPR band by the deprivation of the initially formed peak at 530 nm. Thus the multi-branched nanocrystals are materialized through an aggregative growth mechanism at the expense of the initially formed spherical particles which serve as seeds.<sup>58,59</sup> Hence it could be argued that the final size and morphology of these nanocrystals is dictated by the aggregation number rather than only capping ligand concentration (*vide supra*). The average number of arms of the produced nanocrystals varies as 0, 5, 12 and 18 for concentrations 0.03 (and 0.05), 0.13, 0.2 and 0.26 mM concentrations respectively and could be grown from an equivalent no. of agglomerating particles. At larger added volumes the diminishing of the particle size could be due to the combined effects of decrease in effective nanoparticle concentration (arising from volume change) and increase in the capping ligand concentrations. In the nanoparticles synthesis it is generally known that large percentage of the capping ligand reduces the particle size.

### **3.4.3. Applications**

#### **3.4.3.1. Nanophotonic enhancements**

##### **3.4.3.1.1. SERS efficiency**

Figure 3.18 represents Raman spectra of mercapto benzoic acid (MBA) taken in the presence of different gold nanostructures. The major peaks of MBA such as  $1074\text{ cm}^{-1}$  and  $1581\text{ cm}^{-1}$  correspond to  $\nu_{\text{sa}}(\text{CC})$  aromatic ring. The other weak bands at about  $1390\text{ cm}^{-1}$  corresponding to  $\nu(\text{COO})$  stretching mode and  $1180\text{ cm}^{-1}$  corresponding to the C–H deformation modes were observed (Figure 3.17). It can be noted that SERS intensity

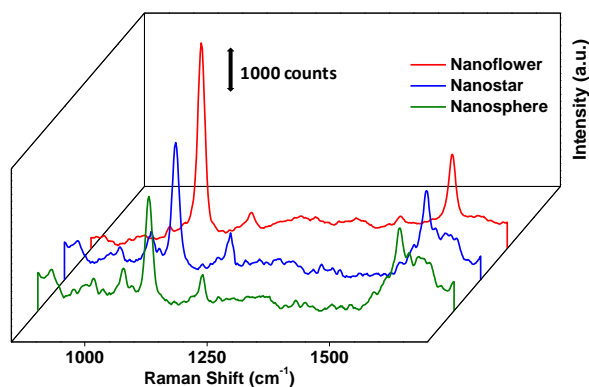


**Figure 3.18.** SERS spectra of MBA molecules on different Au nanocrystals.

increases in the order nanospheres < nanostars < nanoflowers. In the case of spheres, as there are no tips the signal intensity is weak. As the number of tips got increased and hence the number of hot spots, the nanostars and nanoflowers showed higher Raman signal enhancement.

#### 3.4.3.1.2. Photon to thermal conversion efficiency

Recently photothermal therapy (PTT) has emerged as an encouraging method for cancer therapeutics in which plasmonic nanomaterials convert VIS/NIR radiations into heat resulting in cell death via hyperthermia. The photothermal conversion efficiency of synthesized AuNPs was investigated by recording the temperature changes as a function of time using a multimeter integrated to thermocouple under 808 nm laser ( $0.1 \text{ W/cm}^2$ ) irradiation. From the results, it was observed that compared to spherical nanoparticles gold nanostars and flowers have higher photon to thermal conversion efficiency. i.e., within 3 minutes of laser irradiation nanostar and flower systems attain a temperature of  $56 \text{ }^\circ\text{C}$ . Such an elevation of temperature can cause irreversible damages to cells. The rate of temperature rise increases with increase in the number of arms on the nanocrystals (Figure. 3.19). While the control experiment with water alone showed almost no heating effect.



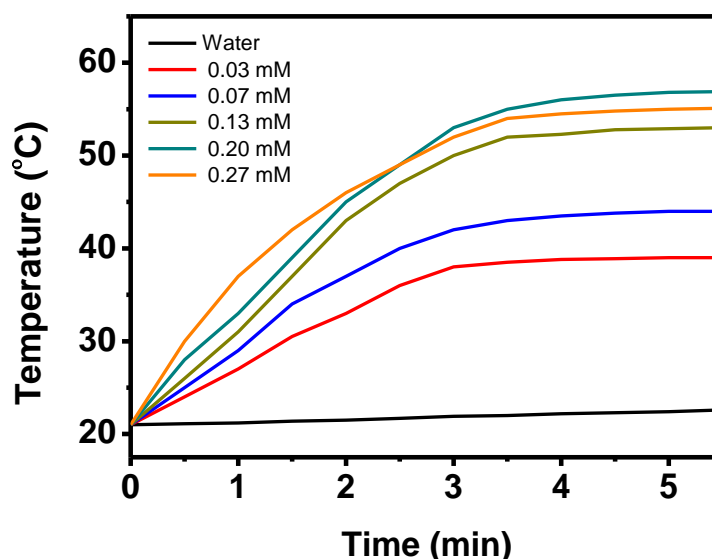


**Figure 3.19.** Temperature changes of Au nanocrystals with 808 nm laser at a power density of 0.1 W/cm<sup>2</sup> as the function of time and water used as the control.

### 3.4.3.2. Theranostics applications

#### 3.4.3.2.1. Cell viability studies

Figure 3.20 illustrates the results of MTT assay showing the comparison of cytotoxicity of gold nanocrystals having different morphologies. Nanosphere exhibit the lowest cell viability and nanoflowers exhibit the highest. The biocompatible L-DOPA's concentration is higher in nanoflowers compared to nanospheres and this will enhance the cell viability. Cell viability > 75 %, 85 %, 92 % has been achieved for AuNPs prepared at 0.03 mM, 0.13 mM, 0.27 mM L-DOPA, thus improving their bio-utility without any further treatment. To tap the full potential of the current system, we investigated its utility in an apt field, i.e, therapeutic ability in cancer treatment.

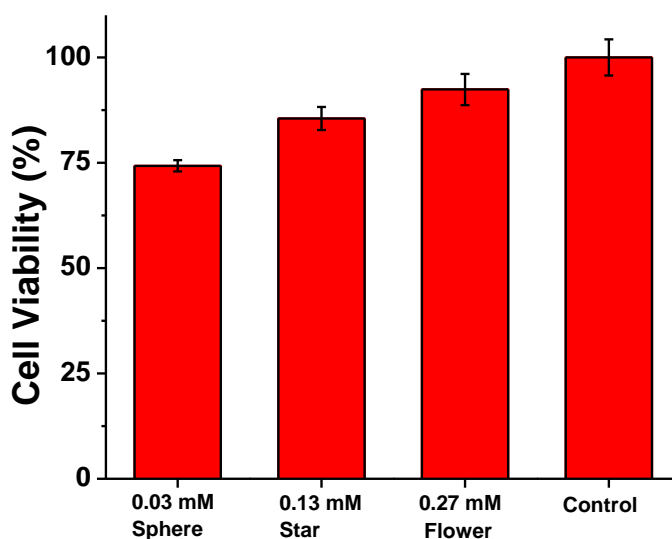


**Figure 3.20.** Plot showing the cell viability of A549 cells after incubation with AuNPs prepared by varying L- DOPA concentrations.

#### 3.4.3.2.2. SERS cell internalization studies

Radioactive tracing techniques and fluorescence labeling have been commonly used to study cellular uptake of nanomaterials such as metal nanoparticles, quantum dots, iron oxide NPs, fullerenes, and carbon nanotubes. However, fluorescent organic dye labeling has inherent limitations such as broad fluorescence, photobleaching, and interference from cellular auto-fluorescence. The radioactive technique is unsafe to animals and humans due to its radiation. Obviously, the development of novel techniques alternative to the conventional fluorescence and radioactive approaches is highly needed. SERS spectroscopy has attracted considerable interest in the field of life science because of its nondestructive and ultrasensitive features. SERS, being Raman spectroscopic technique, gives “molecular fingerprint” that can be used to identify molecules with high specificity. Additionally, it can also provide characteristic intrinsic signals from samples such as cells, or cellular compartments. Yet, the main challenges are cytotoxicity and low level of cellular uptakes and hence the insufficient number of nanoparticles for obtaining a spectral signal through the enhancement of Raman signal. To evaluate the efficiency of

the current system the SERS based studies on the uptake was studied using rhodamine 6G as the reporter molecule. The rationale was that Rhodamine 6G is an organic fluorophore with high Raman scattering cross-section .

For in-vitro studies, we chose A549 cells, a cell line derived from adenocarcinomic human alveolar basal epithelial cells. Our preliminary investigations have shown cellular uptake of R6G-AuNPs as we obtained the well-distributed signal of reporter inside the cells signified through SERS. For control (cell cultures incubated in

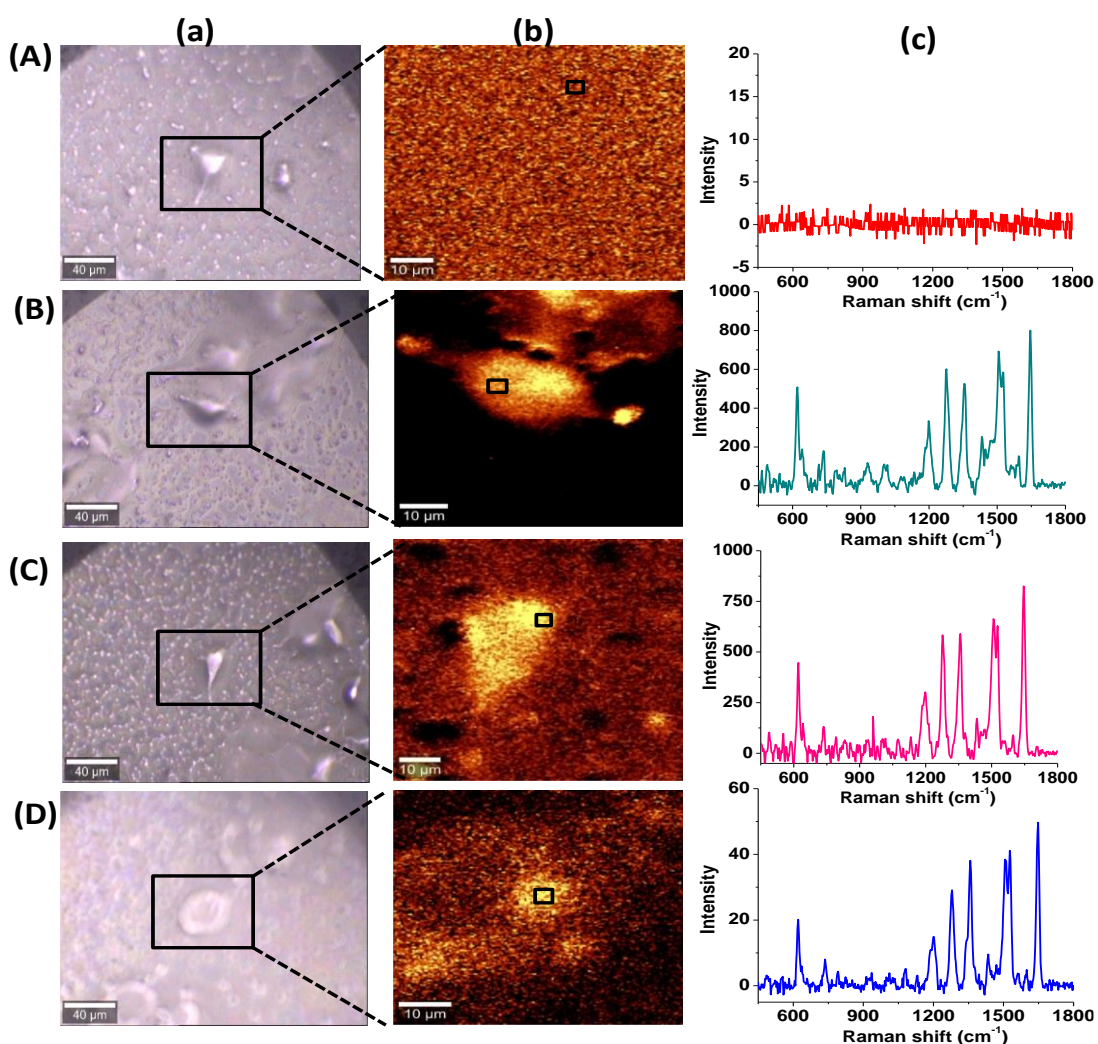


**Figure 3.21.** a) Bright-field and b) Raman images of A549 cells. c) Raman spectra obtained from the marked region of interest. The rows (A) control, (B) nanospheres, (C) nanostars and (D) nanoflowers.

the medium containing R6G alone) experiment, Raman signal was not observed signifying that 633 nm excitation and 0.05 s integration time do not give intracellular information without SERS. The SERS bands of rhodamine 6G are observed in the spectra recorded for the overnight incubation. These studies revealed that the uptake of the dye - Au support is relatively good in the case of Au nanosphere, star, and flower. The relative intensity of SERS signal is higher in nanosphere and star compared to nanoflower and is only due to the mismatch between plasmon absorption (1150 nm) and the applied laser excitation wavelength (633 nm) (Figure.3.21).

#### **3.4.3.2.3. Apoptosis studies using Live/Dead Cell Assay**

The basis of Live/Dead Cell Assay is that viable cells exhibit intact intracellular enzymatic activity and plasma membrane. This assay contains a mixture of two highly fluorescent dyes that label live and dead cells differentially. Live cells are recognized on the basis of intracellular esterase activity which gives green fluorescence in the presence of acridine orange with the excitation maximum and emission maximum are 494 nm and 515 nm, respectively. Dead cells are recognized by the absence of esterase activity and non-intact plasma membrane which give red fluorescence in the presence of ethidium bromide with the excitation maximum and emission maximum are 528 nm and 617 nm, respectively. The photothermal conversion efficiency of synthesized AuNPs was further investigated through the cell viability studies using Live/Dead fluorescent Assay. Before irradiation with 808 nm laser ( $0.1 \text{ W/cm}^2$ ) most of the A549 cells are alive and hence predominantly exhibit green fluorescence. However, after the PTT treatment, the cells exhibited varied fluorescence characteristics and are highly dependent on the particle morphology. For example, in the case of cells incubated with nanospheres, after the laser irradiation, appearance of red fluorescence from only a few cells was noted. However the

PTT treatment yielded almost 50% and 100% red fluorescence cells in the case of nanostars and nanoflowers respectively. ie, compared to nanospheres and nanostars the gold nanoflower shows maximum apoptosis due to high photothermal conversion efficiency under laser irradiation (Figure.3.22).

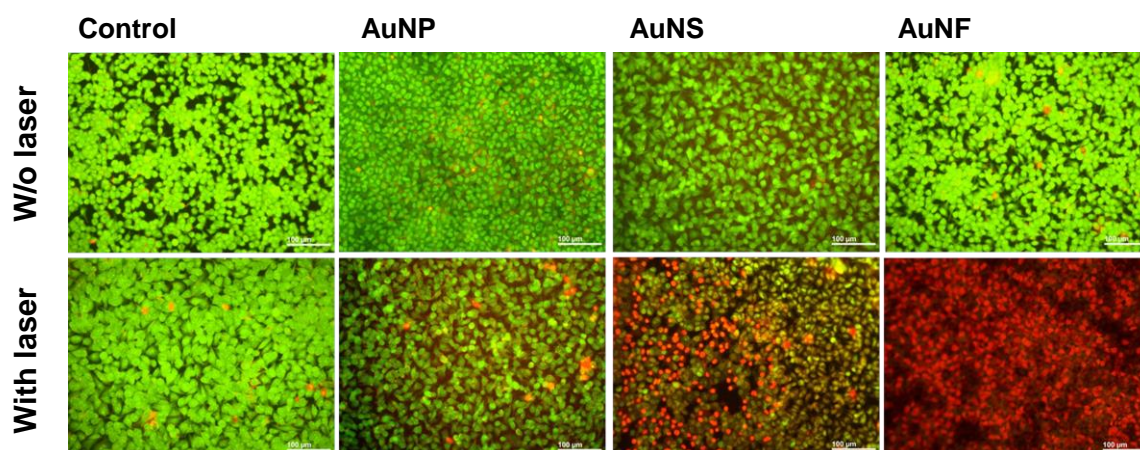


**Figure 3.22.** Fluorescence images from Live/Dead Cell Assay showing the invitro cytotoxicity with or without laser irradiation (1 min) in A549 cells in the presence of AuNPs having different morphology. Control data is that of cells in the absence of AuNPs.

#### **3.4.3.2.4. SERS fingerprinting**

The SERS has emerged as an authentication tool for assessing molecular-level variations of cell death in real-time. Similar to the studies presented in chapter 2, here also we were able to analyse the minuscule alterations in biochemicals of sub-cellular malieu upon photothermal therapy using gold nanoflowers. The obtained SERS spectral profiles of A549 cells before and after laser irradiation are presented in figure 3.23. Careful inspection of these spectral patterns revealed significant changes to the bond vibrations corresponding to nucleic acids as well as proteins. The prominent bands appeared around 828, 935, 1302, 1447 and 1572  $\text{cm}^{-1}$  are respectively attributed to O-P-O (backbone of DNA), C-H bending (tyrosine), C-C<sub>6</sub>-H<sub>5</sub> stretching mode in Phe, amide III, C=C bending mode of Phe and stretching of N<sub>7</sub>-H (guanine and adenine). After laser

irradiation, the intensity at  $\sim 828\text{ cm}^{-1}$  (i.e. band due to O-P-O backbone of DNA) decreased while the band around  $1572\text{ cm}^{-1}$  assigned to N<sub>7</sub>-H vibration of guanine and adenine got considerably enhanced. This is due to DNA detachment from the histone proteins during cell death which exposed guanine and adenine to the plasmonic field of AuNFs. This caused higher SERS intensity after therapy.

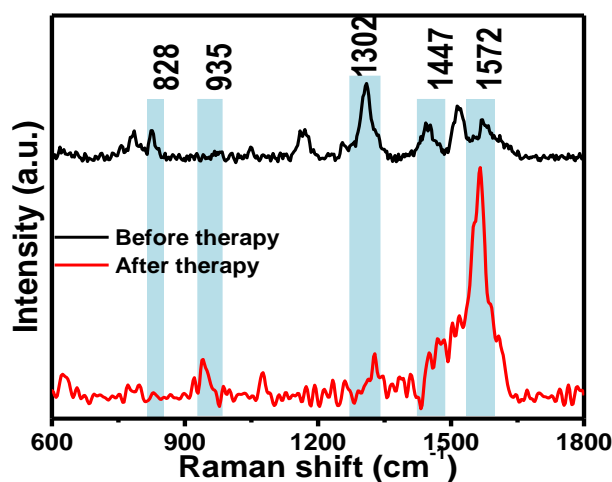


**Figure 3.23.** SERS spectra of A 549 cells incubated with Au nanoflowers for 4 hours before and after irradiation with 808 nm laser.

### **3.5. Conclusion**

In conclusion, the potentiality of L-DOPA for a versatile, seedless and surfactant less one-pot room temperature synthetic strategy for the preparation of multiple types of Au nanocrystals has been developed. Tuning the shape and the optical properties of the nanocrystals were accomplished by simple variation of the reductant concentration. This together with, FTIR studies and the observation of organic shell around the nanomaterials confirm the bifunctional role of L-DOPA. Analysis of the kinetic data and the microscopic images revealed that formation of different types of nanocrystals proceeds through spherical nanoparticles which then aggregates and overgrows into nanoparticles

of specific shape. L-DOPA is an important biomolecule and is a precursor to several neurotransmitters including dopamine. Since the present methodology is devoid of any toxic surfactants and being a biocompatible molecule is used for preparation, the nanomaterials thus produced could be highly suitable for biomedical applications. Together with this, their tunable NIR absorption, relatively smaller sizes (30-60 nm), presence of multiple branches indicate their potential for sensing and therapeutic applications. Both the comparative SERS and photo-thermal conversion studies showed better efficiencies for nanocrystals with multiple branches than their spherical counterparts. These plasmonic effects are found to have a strong correlation with the number of branches in the nanocrystals. These obtained advantageous were translated to study the cellular uptake efficiency, photothermal therapy and the consequent monitoring of the minute biochemical changes in sub-cellular component. Therefore, the methodology presented here opens up newer possibilities of making biocompatible anisotropic nanomaterials with similar biomolecules which may find application in both sensing and bio-medicinal fields.

### **3.6. References**

- (1) Wu, H.-L.; Chen, C.-H.; Huang, M. H. *Chemistry of Materials*. **2009**, *21*, 110-114.
- (2) Zhang, H.; Lu, Y.; Liu, H.; Fang, J. *Rsc Advances* **2014**, *4*, 36757-36764.
- (3) de Puig, H.; Tam, J. O.; Yen, C.-W.; Gehrke, L.; Hamad-Schifferli, K. *J. Journal of Physical Chemistry C* **2015**, *119*, 17408–17415.
- (4) Rodríguez-Lorenzo, L.; Álvarez-Puebla, R. A.; Pastoriza-Santos, I.; Mazzucco, S.; Stéphan, O.; Kociak, M.; Liz-Marzán, L. M.; García de

- Abajo, F. J. *Journal of the American Chemical Society* **2009**, *131*, 4616-4618.
- (5) Chirumamilla, M.; Toma, A.; Gopalakrishnan, A.; Das, G.; Zaccaria, R. P.; Krahne, R.; Rondanina, E.; Leoncini, M.; Liberale, C.; De Angelis, F.; Di Fabrizio, E. *Advanced Materials* **2014**, *26*, 2353-2358.
- (6) Harmsen, S.; Bedics, M. A.; Wall, M. A.; Huang, R.; Detty, M. R.; Kircher, M. F. *Nature Communications* **2015**, *6*, 6570.
- (7) Dykman, L.; Khlebtsov, N. *Chemical Society Reviews* **2012**, *41*, 2256-2282.
- (8) Ng, V. W. K.; Berti, R.; Lesage, F.; Kakkar, A. *Journal of Materials Chemistry B* **2013**, *1*, 9-25.
- (9) Rodriguez-Oliveros, R.; Sanchez-Gil, J. A. *Optical Express* **2012**, *20*, 621-626.
- (10) Chen, H. Y.; Zhang, X.; Dai, S. H.; Ma, Y. X.; Cui, S. S.; Achilefu, S.; Gu, Y. Q. *Theranostics* **2013**, *3*, 633-649.
- (11) Li, J.; Wu, J.; Zhang, X.; Liu, Y.; Zhou, D.; Sun, H.; Zhang, H.; Yang, B. *Journal of Physical Chemistry C* **2011**, *115*, 3630-3637.
- (12) Yi, S.; Sun, L.; Lenaghan, S. C.; Wang, Y.; Chong, X.; Zhang, Z.; Zhang, M. *RSC Advances* **2013**, *3*, 10139-10144.
- (13) Lee, H.; Dellatore, S. M.; Miller, W. M.; Messersmith, P. B. *Science* **2007**, *318*, 426-430.
- (14) Yuan, H.; Khoury, C. G.; Hwang, H.; Wilson, C. M.; Grant, G. A.; Vo-Dinh, T. *Nanotechnology* **2012**, *23*, 075102.
- (15) Kedia, A.; Kumar, P. S. *RSC Advances* **2014**, *4*, 4782-4790.

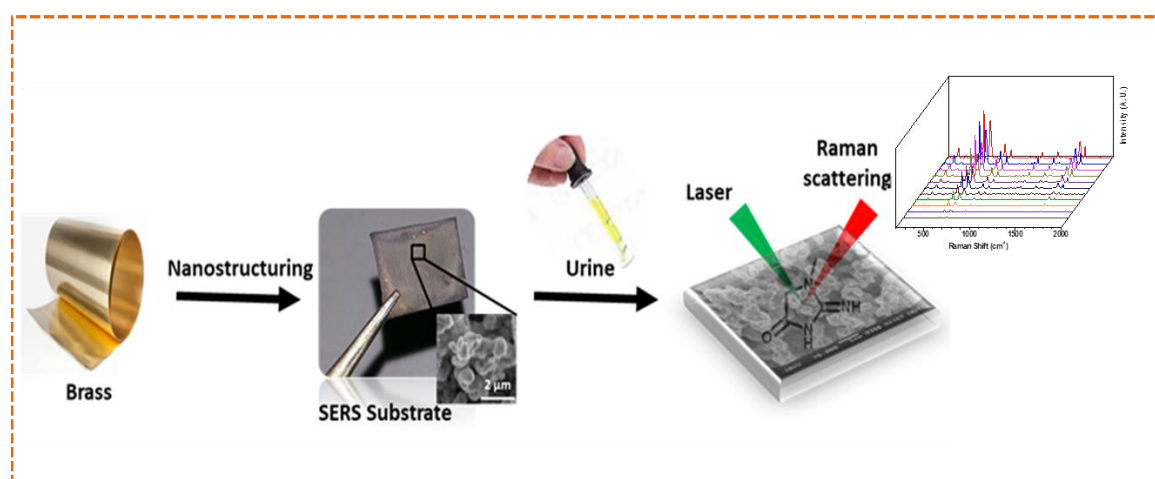


- (16) Rodríguez-Lorenzo, L.; de la Rica, R.; Álvarez-Puebla, R. A.; Liz-Marzán, L. M.; Stevens, M. M. *Nature Materials* **2012**, *11*, 604-607.
- (17) Zhang, Q.; Large, N.; Wang, H. *ACS Applied Materials & Interfaces* **2014**, *6*, 17255-17267.
- (18) He, R.; Wang, Y.-C.; Wang, X.; Wang, Z.; Liu, G.; Zhou, W.; Wen, L.; Li, Q.; Wang, X.; Chen, X.; Zeng, J.; Hou, J. G. *Nature Communications* **2014**, *5*, 4327.
- (19) Xia, Y.; Xiong, Y.; Lim, B.; Skrabalak, S. E. *Angewandte Chemie International Edition* **2009**, *48*, 60-103.
- (20) Manjavacas, A.; García de Abajo, F. J. *Nature Communications* **2014**, *5*, 3548.
- (21) Liu, X.-L.; Wang, J.-H.; Liang, S.; Yang, D.-J.; Nan, F.; Ding, S.-J.; Zhou, L.; Hao, Z.-H.; Wang, Q.-Q. *Journal of Physical Chemistry C* **2014**, *118*, 9659-9664.
- (22) Wang, H.; Brandl, D. W.; Nordlander, P.; Halas, N. J. *Accounts of Chemical Research* **2007**, *40*, 53-62.
- (23) Rodríguez-Oliveros, R.; Sánchez-Gil, J. A. *Optical Express* **2012**, *20*, 621-626.
- (24) Baron, R.; Zayats, M.; Willner, I. *Analytical Chemistry* **2005**, *77*, 1566-1571.
- (25) Rodríguez-Lorenzo, L.; de la Rica, R.; Álvarez-Puebla, R. A.; Liz-Marzán, L. M.; Stevens, M. M. *Nature Materials* **2012**, *11*, 604.
- (26) Banerjee, A.; Supakar, S.; Banerjee, R. *PLoS ONE* **2014**, *9*, e84574.
- (27) Shaaban, M. T.; El-Sabbagh, S. M. M.; Alam, A. *Life Science Journal* **2013**, *10*, 1437-1448.

- (28) Apte, M.; Girme, G.; Bankar, A.; RaviKumar, A.; Zinjarde, S. *J Nanobiotechnology* **2013**, *11*, 2.

## CHAPTER 4

### Easy Fabrication of SERS Substrates through Galvanic Replacement Reaction and its Application for Creatinine Sensing



#### 4.1. Abstract

*The major challenge for the widespread use of SERS technique is the availability of a cheap and reproducible SERS active substrate with high and uniform sensitivity. This chapter describes an easy SERS substrate fabrication process using a less expensive and readily available material, brass. Brass is an intimate mixture of Cu and Zn. Upon etching with hydrochloric acid, Zn leaches out of the material leaving highly porous and nanostructured Cu substrate, which itself qualify as a suitable platform for SERS. Further, its plasmonic properties can be improved by growing nanocrystals of gold or silver over it. As Cu is having a lower redox potential, its simple dipping in a solution of either  $\text{Ag}^+$  or  $\text{Au}^{3+}$  produces their nanostructures via galvanic displacement reaction. The parameters such as reaction time, concentration of the metal ions were optimized as to obtain plasmonic substrates with high SERS activity. The obtained results were also*

*correlated with detailed morphological and spectroscopic data. Further to demonstrate its capability for diagnostics, attempts to detect and quantify creatinine from urine has carried out as it provides primary information about kidney functioning. Detection of creatinine from water solutions with good linearity was easily achieved in the concentration range 1 nM to 5 mM. Further, to demonstrate a close to a real scenario, the capability of the current substrate for sensing of creatinine from artificial urine was also studied.*

## **4.2. Introduction**

Developing easy and accurate detection techniques for chemicals and biological components is one of the thrust areas of research as it can make a large impact on health,<sup>1</sup> forensic<sup>2</sup> and environmental sectors.<sup>3</sup> Most often this requires sophisticated instruments, specific sample preparation procedures, and service of skilled personals adding the cost and time for analysis. It is known that most of the diseases produce chemicals which are normally absent and or present in low concentrations in the body. These are generally called as biomarkers. For example, creatinine is one of the simplest molecules which serve as a biomarker for kidney failure. The presence of elevated percentage of glucose is the sign of diabetes. The precise estimation of these abnormal components helps to efficient disease diagnosis and hence to provide apt therapeutics in time. Recently, Raman spectroscopy has evolved as one of the efficient diagnostic techniques ranging from simple sensing, detection of specific disease biomarkers and pathogen and imaging. Unlike other spectroscopic techniques Raman probes the unique vibrational characteristics of molecules and thus serves as a fingerprint technique to identify the chemicals with great specificity and sensitivity.<sup>4,5</sup> The other

advantages of Raman spectroscopy are since it is based on scattering, it doesn't require any specific sample preparation procedures thus allowing detection directly from body fluids well as *in vivo* conditions. Additionally, water is a weak Raman scatterer and interferes little with the measurements. Further, it can be measured with any monochromatic light source ranging from UV to NIR. Due to these, it is a highly promising technology for diagnostic purposes. However, its practical utility is limited by the weak inelastic scattering efficiency. To overcome this many signal enhancement techniques has been introduced and the most promising is SERS. Studies have revealed that both colloidal solutions metal nanoparticles, as well as nanostructured plasmonic surfaces, have the capability to enhance Raman signal by several orders of magnitude. However, the former has got issues like loss of colloidal stability (less suitable for storage), the presence of capping ligand reduces the access to nanosurface (reduces efficiency), possibility of aggregation in presence of analytes (non-consistency in signal strengths), errors arising from the uncertainties in mixing volume. Thus, solid-state plasmonic substrates are better alternative, and presently many commercial products are available.<sup>6,7</sup> Presently, the cost of commercially available SERS substrate ranges from 5-30 US\$. This limits their application mainly to research purposes and is less preferable in daily usage like diagnosis. The major concerns to be addressed to tap the full potential are fabrication of reproducible, large volume, high enhancement substrates and most importantly the cost.

#### 4.2.1. Fabrication of SERS substrates

SERS active substrate fabrication is highly vital newly emerging field in SERS research. The enhancement of Raman signal greatly depends on the morphology and arrangement of the metal nanoparticles and the excitation wavelength of the incident light

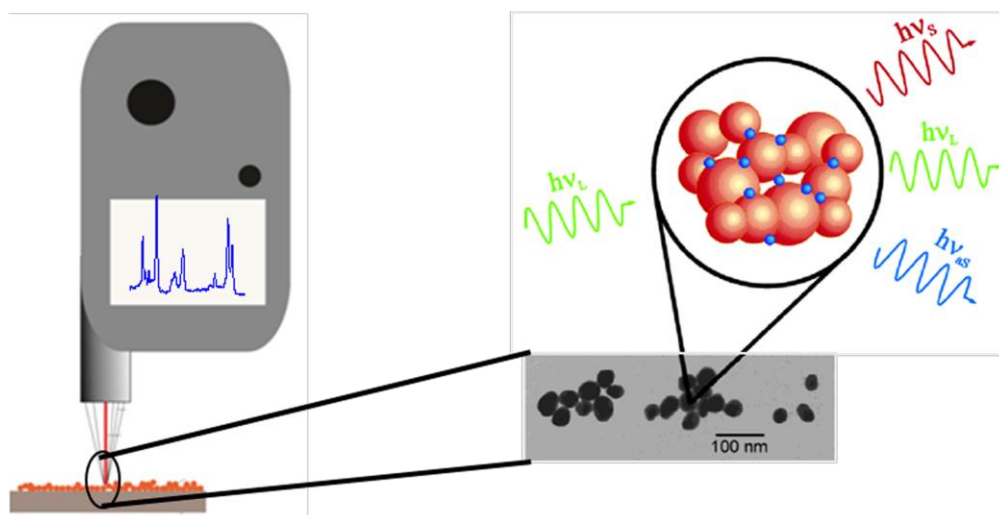


**Figure 4.1.** Pictorial representation of plasmonic nanosubstrates.<sup>8,9</sup>

(Figure. 4.1).<sup>8,9</sup> The metal nanoparticles such as silver, gold, and copper with different size and shape are widely used for fabrication of substrates due to their good SERS activity. The major challenges to be addressed in the fabrication are producing uniform, highly sensitive and reproducible SERS substrates. The Raman enhancement will occur when the molecules attach to the surface of metal nanoparticles and the enhancement factors are mainly depends upon the number of ‘hot spots’ and the field generated therein.<sup>10,11</sup> Thus designing a SERS substrate with the maximum number of hot spots per unit area is highly important.

The major factor that affects SERS enhancement is the nature of materials. Silver metals give more Raman enhancements compared to gold and copper

metals.<sup>12</sup> The two main factors that affect the SERS enhancement are the size and shape of the nanomaterials. Recently, by controlling the size and shape of metal or bimetallic nanostructures there is a number of 1D and 2D SERS substrates have been reported.<sup>13,14</sup> The larger size of nanoparticles will lead to the lower overall efficiency of the enhancement. But if the size is too small will fail to produce electrical conductivity and fail to have an enhancement for the electric field. Normally, nanoparticles are in the range of 20 nm- 200 nm will give higher enhancement compared to bigger or smaller nanoparticles. Anisotropic nanostructures such as nanoparticles having a number of sharp edges will give better enhancement due to the localization of electric fields are more at the tips. Also, high surface area and high uniformity are the other key factors while preparing SERS substrates.<sup>15,16</sup>

#### **4.2.2. Fabrication techniques**

The presently available preparation methodologies for substrate fabrications can be generally classified as chemical as well as physical process and are outlined in chapter 1. The physical method generally involves preparation of nanostructuring of surfaces followed by its conversion into plasmonic substrates via deposition of thin films of metals such as gold, silver or copper. With the advent of nanotechnology different techniques are available for the construction of nanostructured surfaces. These include nanoimprint lithography,<sup>17,18</sup> electron beam lithography,<sup>19,20</sup> ultrafast laser ablation techniques (Figure 4.2). The techniques available for the deposition of metals include thermal evaporation, sputtering, electrodeposition, Atomic layer deposition (ALD), etc., Though these techniques successfully addressed the issue of reproducibility, the major limitation is the high cost associated with nanostructuring as well as metal deposition.<sup>21</sup> Herein we try to

evolve, a simple yet cost-effective way to produce nanostructured plasmonic substrates.

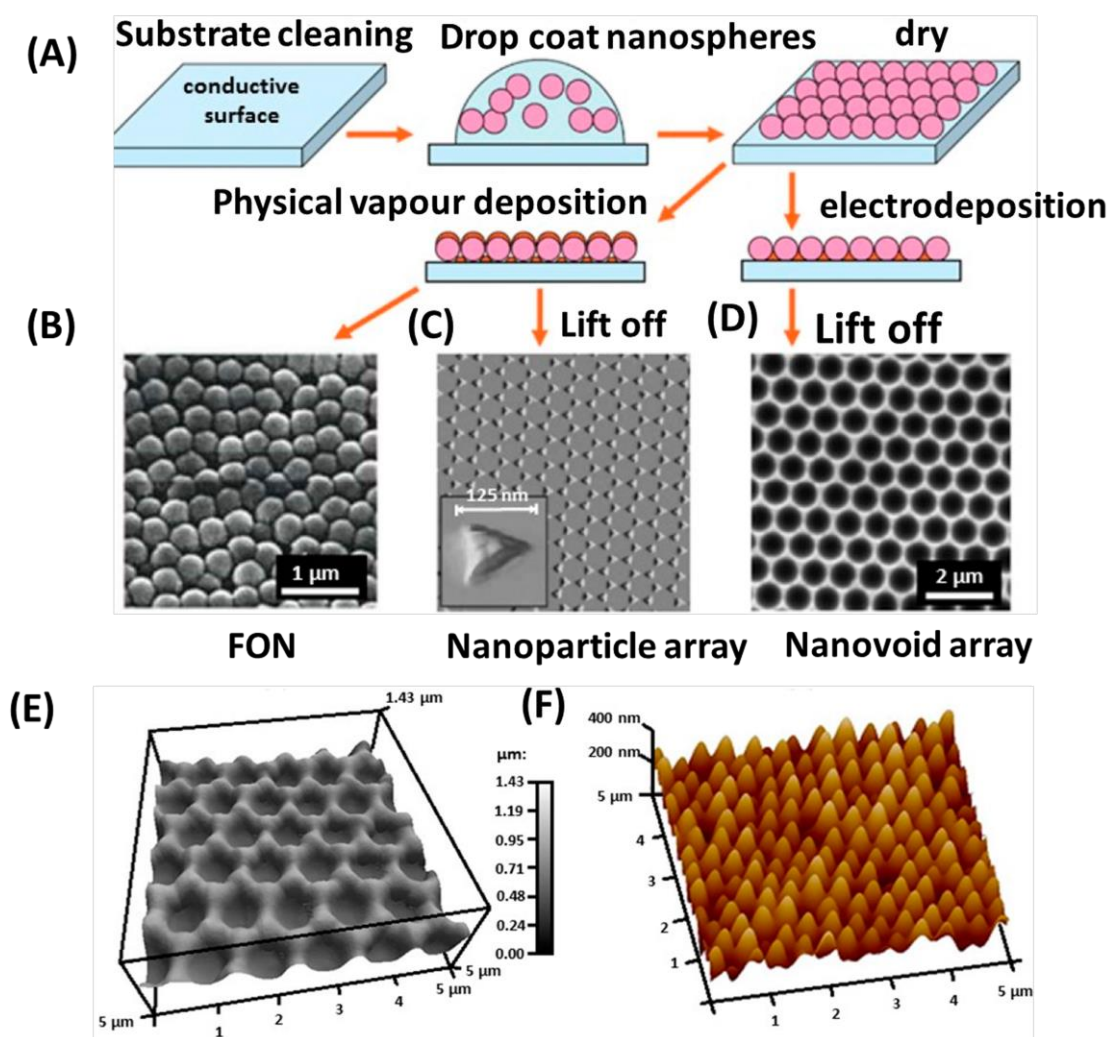


**Figure 4.2.** (A) Schematic representation of the nanosphere lithography (B-F) Corresponding microscopic images illustrating the obtained nanostructure at each stage.<sup>22,23 24</sup>

#### 4.2.2.1. Galvanic replacement method

Galvanic displacement is one of the processes long known in science and is effectively used for different applications. In general galvanic displacement is a process



by which a base material is displaced by another, due to the difference in their electrode potential. Thus, it is an electrochemical process which involves the oxidation of metal called as sacrificial templates by the ions of another metal having higher reduction potential. Some common examples are amalgamation of gold by mercury, use of Zn as

**Table 4.1.** : Reduction potentials of metals relative to the standard hydrogen electrode (SHE).<sup>25</sup>

Reduction Reaction	E <sup>0</sup> (V vs. SHE) <sup>a)</sup>
$\text{Co}^{2+} + 2\text{e}^{-} \longrightarrow \text{Co}$	-0.28
$\text{Cu}^{2+} + 2\text{e}^{-} \longrightarrow \text{Cu}$	0.34
$\text{Rh}^{3+} + 3\text{e}^{-} \longrightarrow \text{Rh}$	0.76
$\text{Ag}^{+} + \text{e}^{-} \longrightarrow \text{Ag}$	0.80
$\text{Pd}^{2+} + 2\text{e}^{-} \longrightarrow \text{Pd}$	0.95
$\text{Ir}^{3+} + 3\text{e}^{-} \longrightarrow \text{Ir}$	1.16
$\text{Pt}^{2+} + 2\text{e}^{-} \longrightarrow \text{Pt}$	1.18
$\text{Au}^{3+} + 3\text{e}^{-} \longrightarrow \text{Au}$	1.50

<sup>a)</sup> For ideal conditions at 25<sup>0</sup>C and 1 atm.

sacrificial electrode to prevent the corrosion of iron. Table 1, summarize the standard reduction potentials of some of the common metals; in principle, any metal can be replaced by one occupying lower position in this table. In the field nanoscience and nanotechnology, this has proven to be highly efficient technique to produce nanomaterials of varying morphologies and composition.<sup>25-27</sup> Recently, the preparation of silver dendrites via galvanic replacement have been reported by several studies using more reactive metals (e.g. Cu, Mg, Al, Zn, Ni, Sn) as base material.<sup>26</sup>

### **4.3. Experimental section**

#### **4.3.1. Materials and methods**

Chemicals such as hydrogen tetrachloroauratetrihydrate ( $\text{HAuCl}_4 \cdot 3\text{H}_2\text{O}$ ) and 4-mercaptophenyl boronic acid were purchased from Ms. Sigma Aldrich. Silver nitrate ( $\text{AgNO}_3$ , >99%) was obtained from Ms. Merck. Brass foil, alloy 260, 0.25 mm thick, 15 cm x 45 cm was procured from Ms. Alfa Aesar. All glasswares were cleaned using aqua regia prior to use and the experiments were performed in Millipore water (18.2 M $\Omega$ ).

#### **4.3.2 Characterization**

UV-visible absorption spectra were obtained using a UV-2401 PC UV-VIS spectrophotometer (Ms. Shimadzu Corporation, JAPAN) with integrating sphere accessory. XRD data were acquired using a Panalytical PW 3040/60 X'Pert Pro powder diffractometer and Cu  $K\alpha 1$  radiation.

SEM images were obtained using a JEOL 5600 LV scanning electron microscope with an accelerating voltage of 12–15 kV after sputtering with gold. EDS was acquired using EVO 18 Special Edition scanning electron microscope (Carl Zeiss, Germany) operated at 20 kV electron source.

Raman spectra were collected using Confocal Raman Microscope (Alpha 300 R, WiTech, Germany) through 20 x objective lens and samples were irradiated with 633 nm laser and spectra were collected on Princeton Instruments spectrograph having grating 600 lines/mm with 0.5 s integration time and 10 accumulations.

### **4.3.3. Fabrication of SERS substrates**

Brass foil from commercial vendors (in its native form) has chosen as the base material for the SERS substrates fabrication. The surface of brass foil was initially rubbed with sandpaper which helps to remove any physical contaminants on the surface. Then the substrate was cleaned via sonication sequentially with water, acetone, and isopropanol. Later, for chemical etching, the substrate was dipped in concentrated HCl and heated for ~ 1 h which yielded highly porous nanostructured substrate. In order to grow nanostructures of gold or silver the substrate was dipped in solutions of either HAuCl<sub>4</sub> or AgNO<sub>3</sub>.

### **4.3.4. Preparation of artificial urine**

To 0.5 L of distilled water, 12 g of urea was added and mixed until it completely dissolved. Then 3.0 g of potassium chloride, 5.0 g of sodium chloride and 3.2 g of sodium phosphate was added to it; mixed until the solution was clear. Then the pH of this solution was adjusted to be within the 5 to 7 and mixed well with 1.33 mg of creatinine and 33.3 mg of albumin. To evaluate the potential of SERS substrates in kidney functioning diagnosis, the above solution was prepared in the absence of creatinine, and its aliquot amounts were added prior to measurements.

## **4.4. Results and discussion**

### **4.4.1. Characterization of SERS substrates**

#### **SEM and EDAX analysis**

Figure 4.3 shows the SEM images of the brass substrate before and after treatment with HCl. The brass in its native form has a slightly yellow colour and

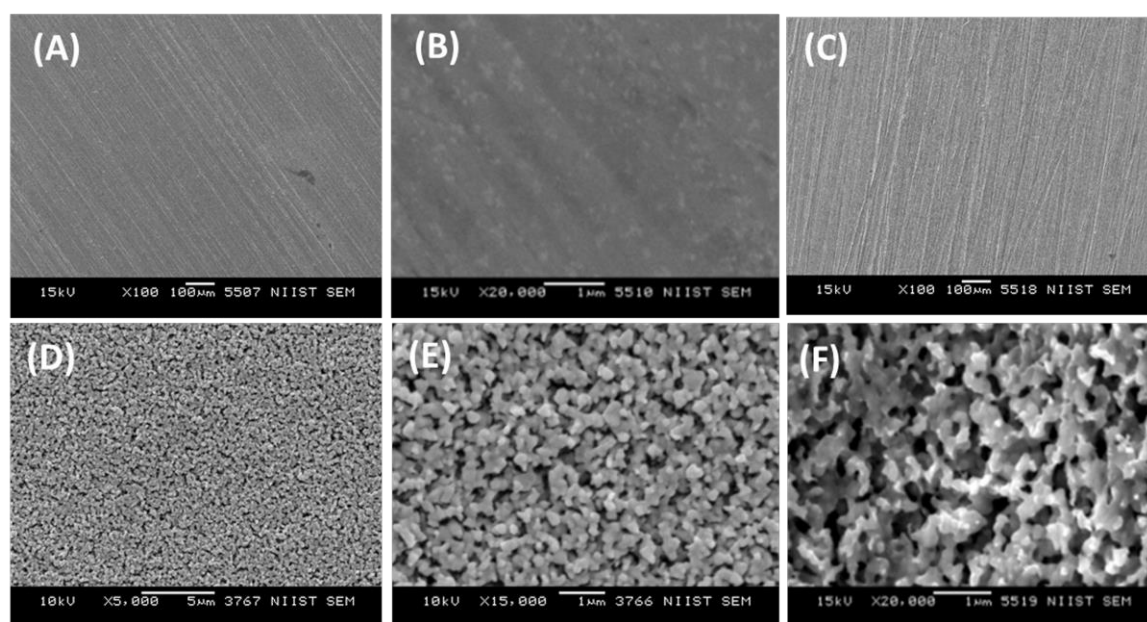


**Figure 4.3.** (A, C) Large area and (B, D-F) higher magnifications SEM images of the brass substrate (A, B) before and (C-F) after chemical etching.

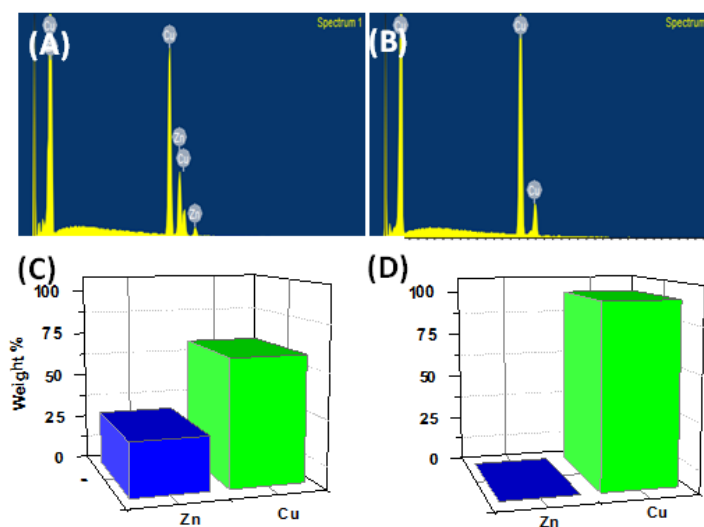


**Figure 4.4.** (A, B) EDS spectra and (C, D) weight percentage composition of the brass substrate (A, C) before and (B, D) after chemical etching.

has got a highly smooth surface and the corresponding SEM images did not show any characteristic nanoscale features. The EDAX based elemental studies confirmed that it is purely a binary form of 70.18 % Cu and 29.82 % Zn (Figure 4.4). After the treatment with concentrated HCl there was the complete

disappearance of Zn signal indicating its dissolution. Consequently, the colour of the corresponding substrate changes to brick red. The corresponding SEM analysis showed evolution of a porous morphology that was uniformly distributed over a large area.

Figure 4.5 A represent the absorption spectral studies of the chemical etching process. Brass before chemical etching exhibit absorption at around 400 nm which explains its yellow colour. Interestingly, after etching the colour of the substrate change to brick red and it showed the absorption band at ~ 540 nm. This may be arising from the plasmon absorption of Cu in the nanosize as is visualized in SEM images. Further, we investigated the possibility of utilizing this nanostructured Cu for Raman enhancement applications. The performance of SERS activity before and after etching was evaluated using 4-Mercapto phenyl boronic acid (MPBA) as Raman reporter (Figure 4.5 B). The characteristic Raman peaks of MPBA appeared at 401, 421, 630, 648, 687, 742, 815, 823, 998, 1018, 1068, 1098, 1168, 1187, 1277, 1469, 1485, 1590  $\text{cm}^{-1}$ . Mainly the peaks corresponding to aromatic ring vibrations appeared at 1590  $\text{cm}^{-1}$  and 1084  $\text{cm}^{-1}$ . Out of these, the peak at 1590  $\text{cm}^{-1}$  is the most prominent and is used for comparisons. The integrated intensities for this band are ~  $8.4 \times 10^2$  and  $8.5 \times 10^3$  respectively before and after etching process. That means the nanostructured Cu substrate shows almost 10 times enhancement in SERS activity when compared to that of parent brass substrate. For any SERS substrate to be used for practical applications in analysis and quantification, it should show nearly uniform SERS activity throughout the substrate. For testing the viability of the present substrate in this context, we collected the spectra from different locations of the same substrate and the data is presented in (Figure. 4.5 C).

A maximum of only 15 % variation in intensities was found between the minimum and maximum values.

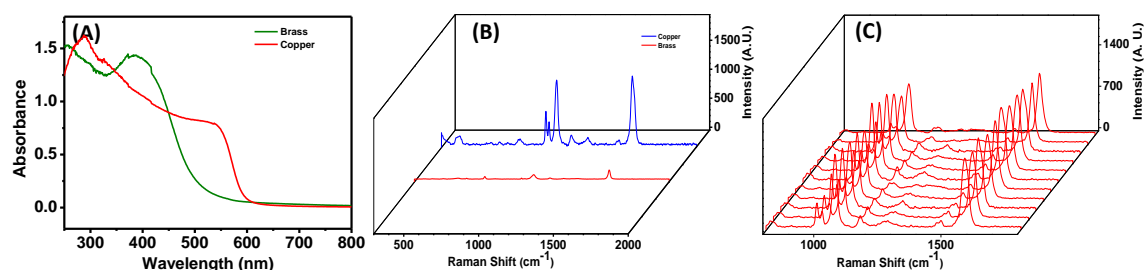
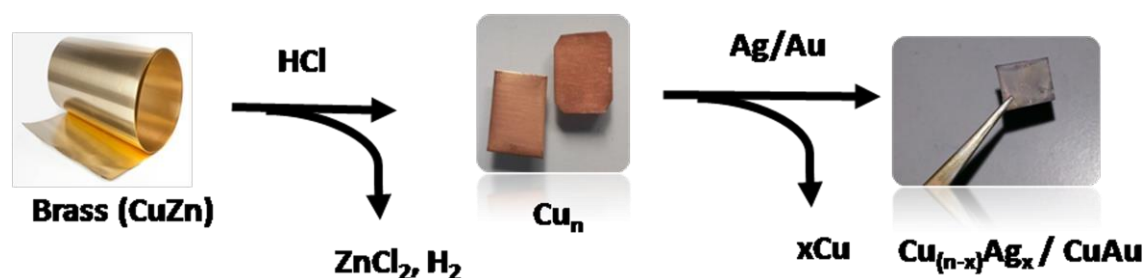


**Figure 4.5.** (A) Comparative absorption spectra, (B) SERS spectra of brass before and after chemical etching. (C) Illustrates the uniformity of SERS activity of resulting Cu nanostructure.

#### 4.4.2. Preparation of the Ag-Cu and Au-Cu SERS substrate

It is known that SERS activity of coinage metals increases in the order  $\text{Cu} < \text{Au} < \text{Ag}$ . Therefore, we thought that one easy way to increase SERS signal intensity is to incorporate Au or Ag to Cu substrates. One of the simplest methods for this is the galvanic replacement reaction. The driving force for the galvanic replacement reaction is the redox potential difference between the sacrificial



**Scheme 4.1.** Schematic representation of fabrication of Cu- Ag and Cu – Au substrates.

template (Cu substrate) and the metal ions ( $\text{Ag}^+$  or  $\text{Au}^{3+}$ ) in solution. Cu has lower reduction potential (+ 0.34 eV) than gold (+ 1.50eV) and silver (+ 0.80 eV). When

treated with metal salt solution, the sacrificial template undergoes oxidation followed by dissolution. Meanwhile, the metal ions from solution undergo reduction and get deposited on the surface of the template (Scheme 4.1).

#### **4.4.2.1. SEM and EDAX analysis**

Figure 4.6 shows the SEM images of Cu-Ag and Cu-Au substrates prepared by dipping nanostructured Cu with 5 mM solutions of  $\text{AgNO}_3$  or  $\text{HAuCl}_4$  for 5 min. It can be found that the morphology of the substrate is entirely different compared to the initial porous structure. The EDS analysis showed the emergence

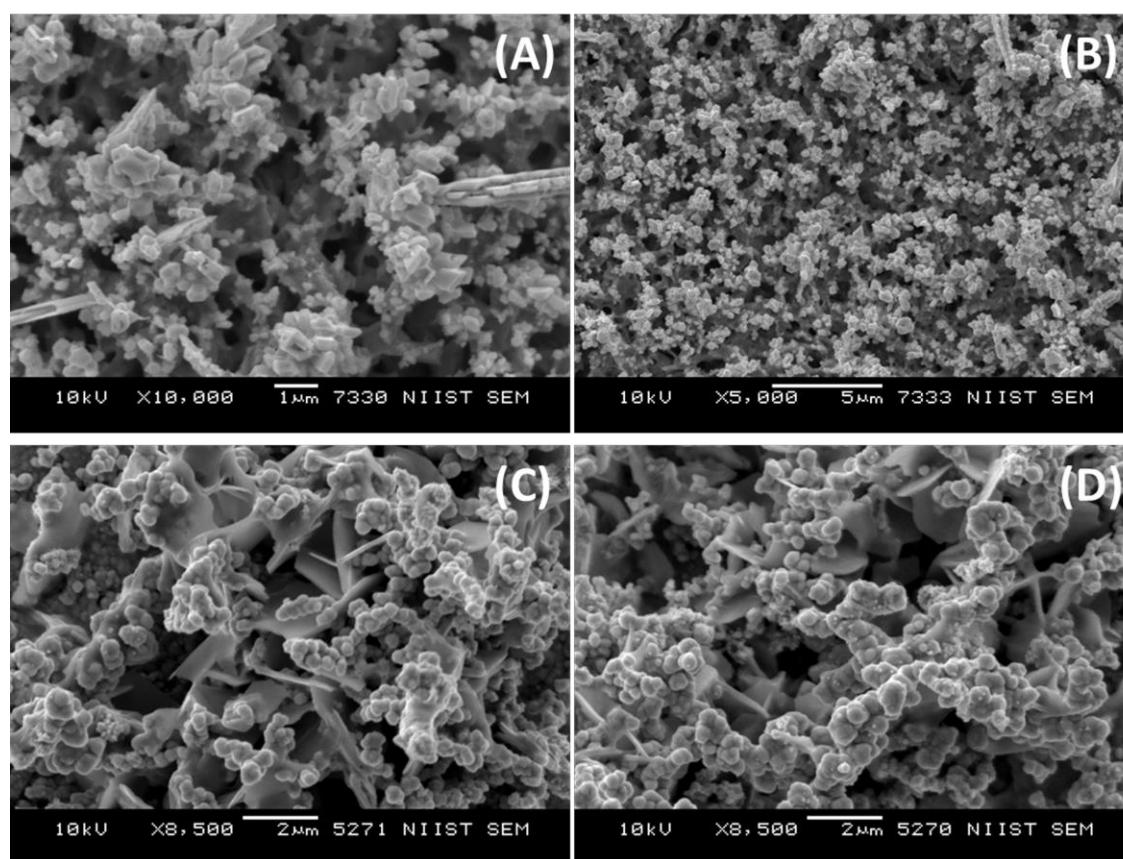


**Figure 4.6.** SEM images of (A, B) Cu-Ag and (C, D) Cu-Au substrates.

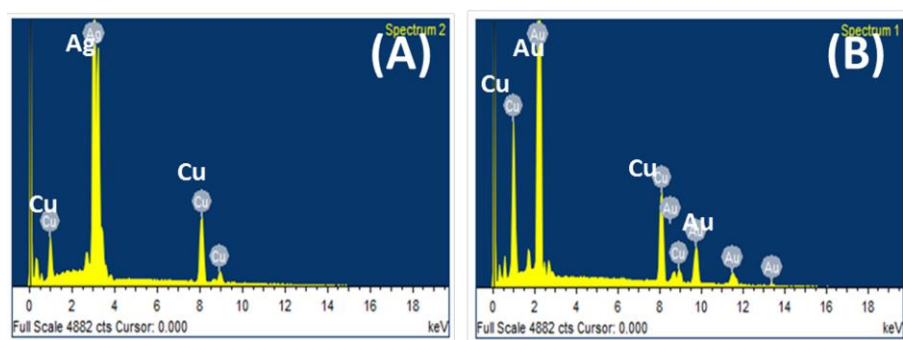


**Figure 4.7.** EDS spectra of (A) Cu- Ag and (B) Cu- Au obtained by dipping Cu in 5 mM solutions of respectively  $\text{AgNO}_3$  and  $\text{HAuCl}_4$  for 3 h.

of the peak corresponding to Au and Ag. In the case of Ag, the evolution of structures resembling that of thrones was noted. The EDS measurements carried out on these evidenced the presence of Ag atoms in addition to Cu. Compositionally this surface consisted of 67 weight percentage of Ag (Figure 4.7). On the contrary galvanic displacement with Au yielded emergence of flower-like budding morphologies with 57 % elemental weight composition of Au.

#### 4.4.2.2. XRD studies

Figure 4.8 represents the comparison of the XRD spectrum of Cu, Cu-Ag and Cu-Au substrates. In the case of Cu, three peaks appeared at  $2\theta$  values of 43.52, 50.68, and 74.33 degree. By comparing it with the standard powder diffraction card of JCPDS, copper file No. 04–0836 these peaks were assigned to (111), (200), and (220) planes. This confirms that the resultant nanostructures possess fcc crystal lattice (Figure. 4.8 A). XRD pattern of Cu-Ag substrates showed additional major peak at 38.4 degree which corresponds to (111) planes of silver atoms in the fcc crystal lattice (Figure. 4.8 B). Similarly, Cu-Au substrates showed additional peaks at 38.2, 44.4, 64.6 and 77.6 correspondings to (111), (200), (220) and (311) planes of Au. (Figure. 4.8 C).



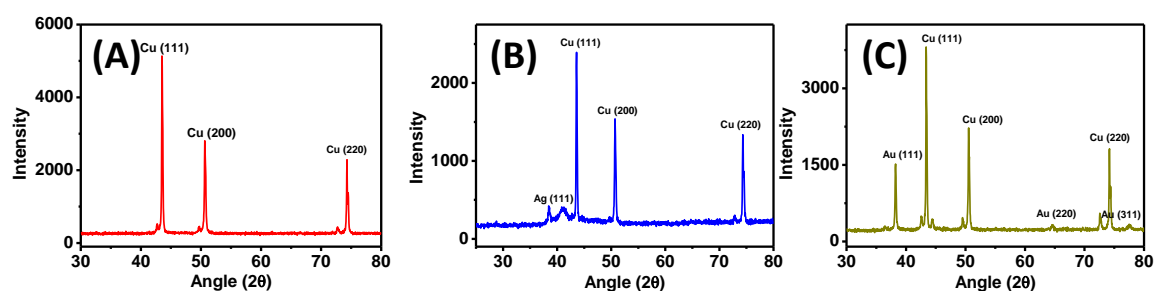


Figure 4.8. XRD spectra of (A) Cu (B) Cu-Ag and (C) Cu-Au substrates.

#### 4.4.2.3. Absorption studies

Figure 4.9 represents the absorption spectra of Cu-Ag and Cu-Au plasmonic substrates obtained through galvanic displacement reaction. Careful inspection of the data revealed the following noticeable differences when compared to that of the initial copper nanostructured surface. After the galvanic displacement reaction, Cu-Au substrates gave a clear band at ~540 nm. This suggests the existence of gold in the nano regime and consequently the evolution of surface plasmon resonance. On the other hand the Cu-Ag

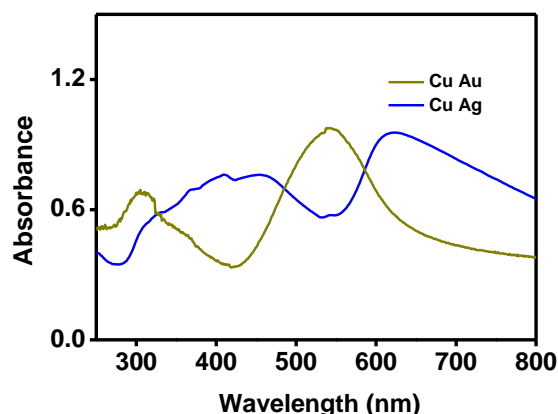


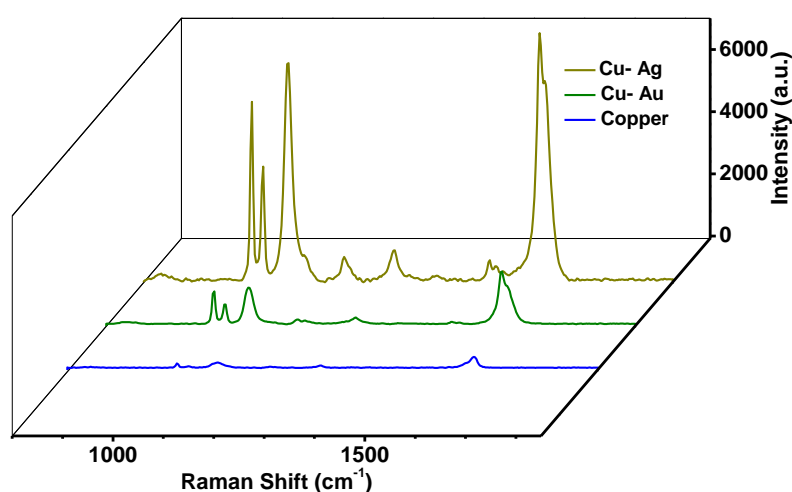
Figure 4.9. Absorption spectra of Cu-Ag and Cu-Au substrates.

substrates showed a continuous absorption in the UV-VIS region with two bands ~ 400 nm and 620 nm. Absorption in 600 nm region indicates the formation of anisotropic

nanostructures and is in accordance with the observed thorn-like structures in the SEM images.

#### 4.4.2.4. SERS studies

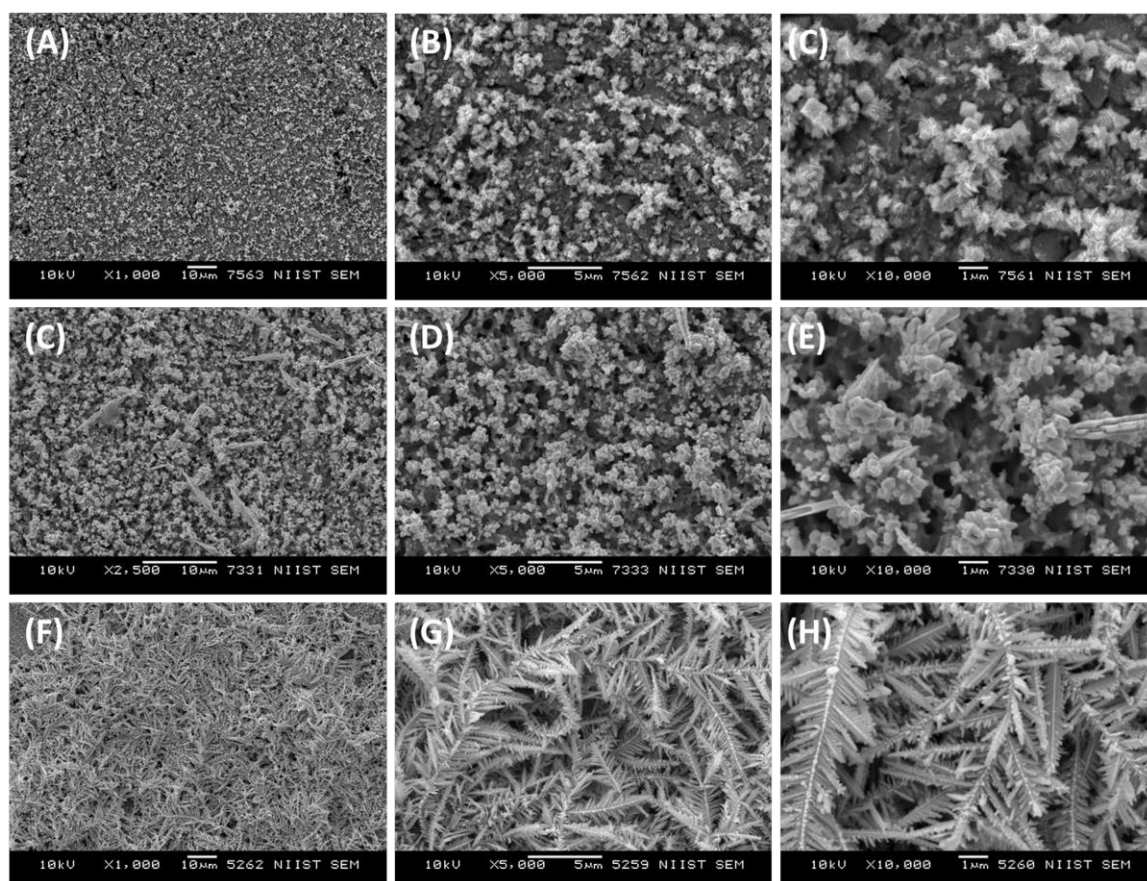
The comparative SERS activity studies were conducted to reveal the influence of galvanic displacement reaction on the efficiencies of Raman signal enhancement. In both cases, the obtained Raman spectrum of MPBA shows quiet resemblance with that collected using parent Cu substrate except in terms of intensities. No considerable change in the Raman shift values was noted indicating the same kind of polarisability and hence the mode of SERS enhancement. The integrated intensities of the prominent peak at  $1590\text{ cm}^{-1}$  are  $5.2 \times 10^4$  and  $2.5 \times 10^5$  respectively for Cu-Au and Cu-Ag substrates. ie., Au substrates exhibited almost 6 times and Ag substrates showed 30 times higher enhancement compared to the parent Cu substrate (Figure 4.10). This is almost 60 times and 300 times higher enhancement than the parent brass substrates. Comparatively, Cu-Ag substrate shows almost 5 times enhancement than Cu-Au substrates.



**Figure 4.10.** (A) Comparative SERS spectra of Cu, Cu-Ag and Cu-Au substrates.

#### 4.4.2.5. The effect of concentration on morphological evolution

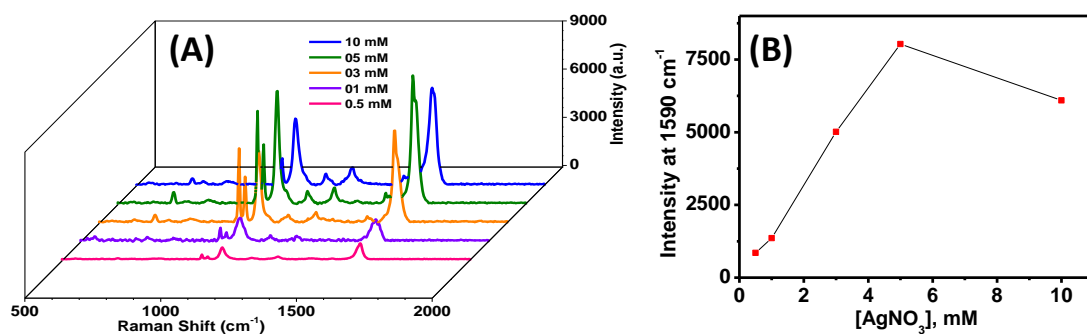
In order to understand the topographical evolution of nanostructures and hence to optimize the conditions for better SERS substrates, we performed a series of experiments and are outlined below. For example, figure 4.10 represent the SEM images of Ag plasmonic substrates obtained by dipping etched brass foils in varying concentrations of  $\text{AgNO}_3$  for a fixed period of time, 5 min. At 1 mM concentrations, the nanopores on the surfaces of the Cu substrate start to disappear and seedling of small plant-like structures of Ag nanoparticles was noticed. In addition to this, small particle-like features were also present. The size of these



**Figure 4.11.** SEM images of silver hemi-mesoparticles obtained by dipping Cu substrates for 5 minutes in different concentrations of  $\text{AgNO}_3$  (A-C) 1 mM, (D-E) 5 mM, (F-H) 10 mM.

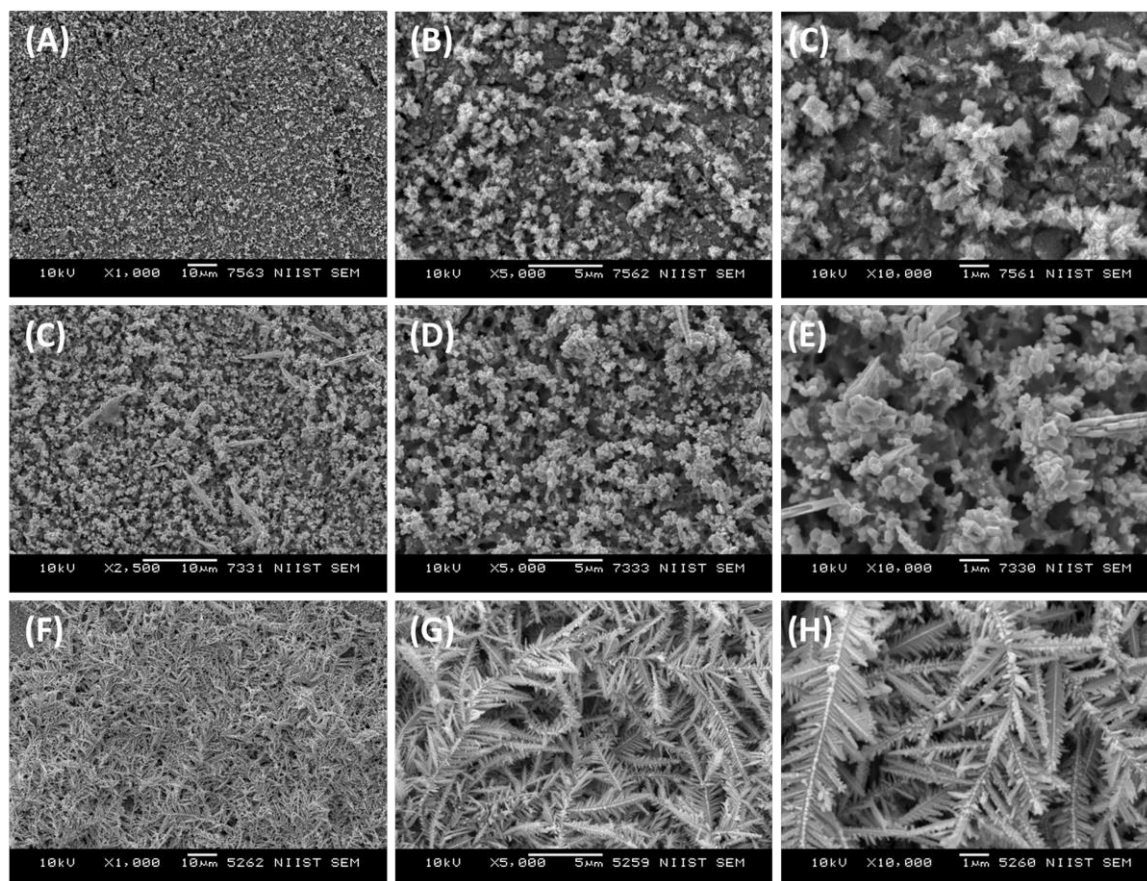
features vary from a few nanometers to a few micrometers. From the SEM images it was noted that almost all the surface of the substrates are bare and only a small portion covered with Ag nanoparticles. In 5 mM concentration, due to the availability of more number of  $\text{Ag}^+$  ions more nanoparticles are formed and appeared different layer like structures with elongated thrones like morphologies. Thus it has got the number of sharp edges. The presences of pores were still visible at this concentration. At higher concentrations such as 10 mM, the well-developed walking fern-like morphology was observed and is completely distributed throughout the substrate.

Figure 4.12 represents SERS studies of Cu-Ag substrates prepared at varying concentrations of  $\text{AgNO}_3$ . All of these substrates showed SERS activity considerably higher than the parent Cu. For example, at lower concentrations, the integrated intensity of  $1590\text{ cm}^{-1}$  peak is  $\sim 2.8 \times 10^4$ ,  $5.4 \times 10^4$  respectively for nanostructures prepared with 0.5 mM and 1 mM  $\text{AgNO}_3$  which is almost 3 and 6 times higher than the Cu substrates. The trend increases linearly with concentration up to 5 mM and afterward, a decrease in the intensity was noted. Of these nanostructures prepared with 3 mM concentration showed higher enhancement in Raman signal with intensity  $1.7 \times 10^5$  which is 20 times more than Cu. Among all, hemi mesoparticles yielded with 5 mM  $\text{AgNO}_3$  exhibited the highest enhancement  $2.5 \times 10^5$  ( $\sim 30$  times higher). This is because of the presence of a large number of hotspots throughout the substrate. However, any further increase in concentration (e.g. 10 mM) did not produce much change in the signal intensity but slightly decreased to  $2.4 \times 10^5$  due to the decrease of hot spots in fully grown leaf-like structures.

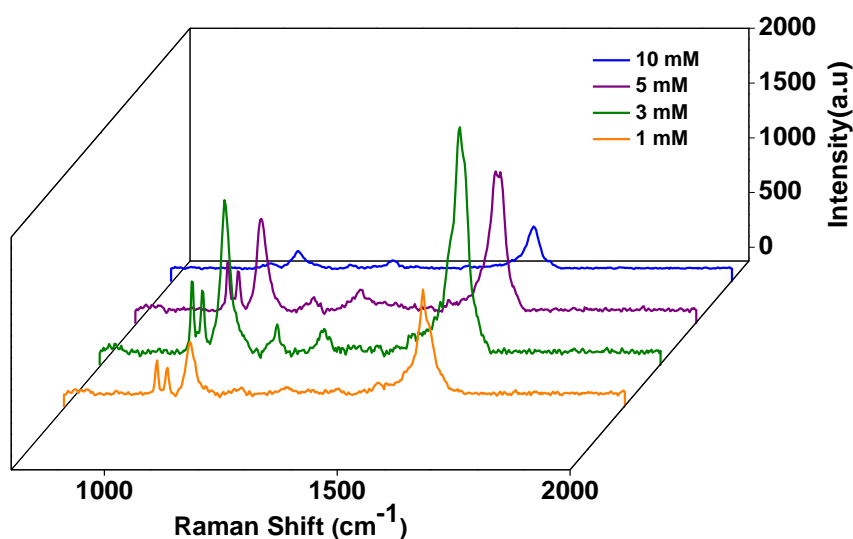


**Figure 4.12.** (A) SERS spectra of MPBA molecules on plasmonic substrates prepared by dipping Cu for 5 minutes in different concentrations of  $\text{AgNO}_3$ . (B) Graph showing the variation of  $1590 \text{ cm}^{-1}$  with respect to  $[\text{AgNO}_3]$ .

#### 4.4.2.6. The effect of time on the evolution of Cu-Ag structures



**Figure 4.13.** SEM images of Cu-Ag hemi-mesoparticles obtained by dipping Cu substrates for 3 h in different concentrations of  $\text{AgNO}_3$  (A-C) 1 mM, (D-E) 5 mM and (F-H) 10 mM .



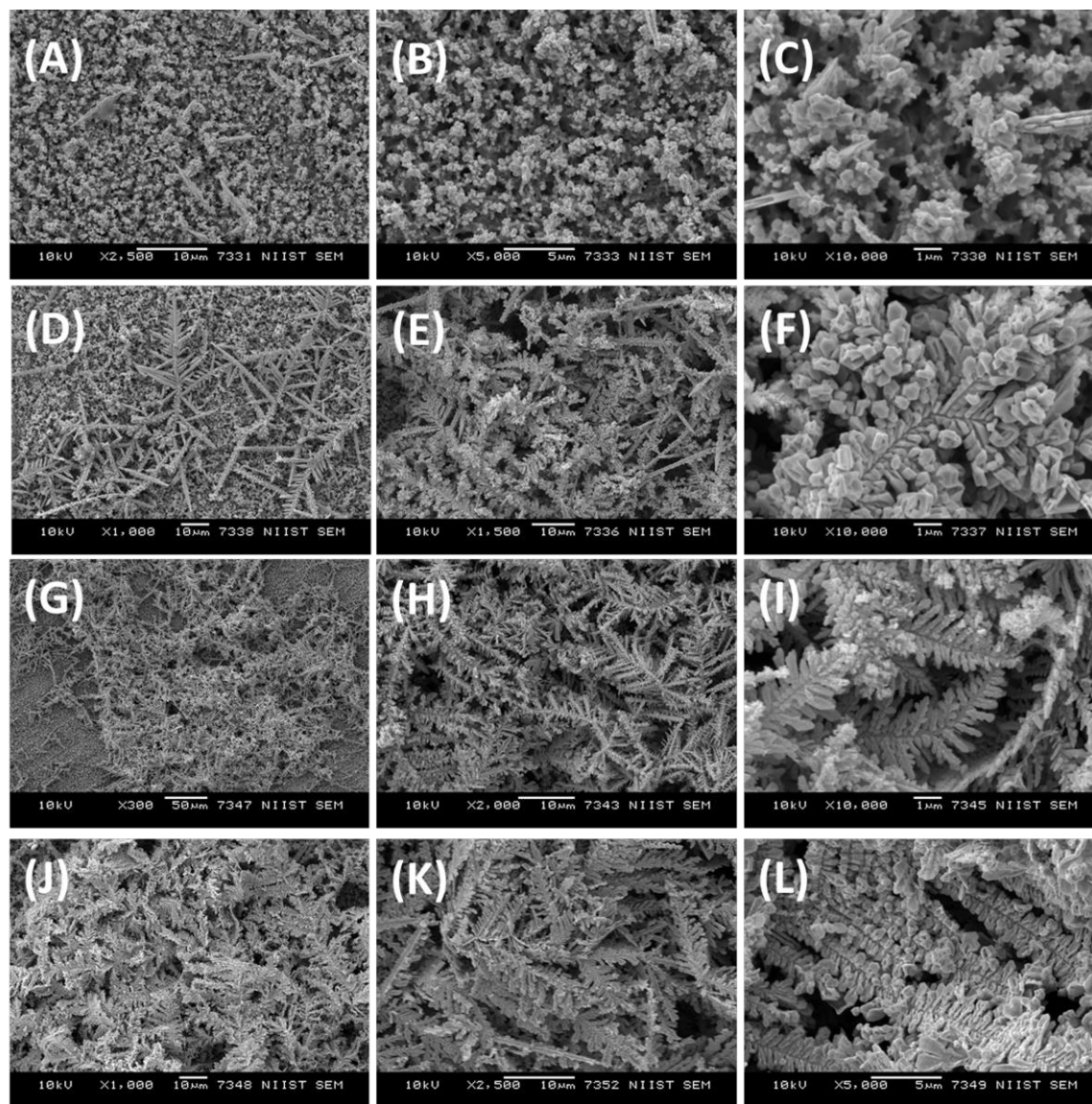
**Figure 4.14.** SERS spectra of Cu-Ag hemi-mesoparticles obtained by dipping Cu substrates for 3 h in different concentrations of  $\text{AgNO}_3$ .

Figure 4.13 represents the morphology of the Cu-Ag nanostructures obtained after dipping Cu for a long period of time (3 h) yet with different concentration of  $\text{AgNO}_3$ . At higher concentrations such as its mM, the mesoparticle formation happens at a faster rate compared to low concentrations due to the availability of a large number of  $\text{Ag}^+$  ions present in the solution. The SEM images of 5 min, 5 mM, and 1 mM, 3 h reactions quite resemble each other. However, the growth is more complete and is more uniformly distributed in the latter case. Similarly, the 5 mM, 3 h reaction yielded more grown structures compared to that of 10 mM, 5 min. Even bigger nanostructures were obtained in 10 mM concentration at 3 h. Detailed SERS studies showed that the nanostructure prepared with 1 mM and 3 mM exhibited almost similar SERS activity (Figure 4.14). The lowest signal intensity was noted at 10 mM 3h reaction. This is because the nanostructures obtained here are bigger and the edges of the leaf are more rounded in shape. While nanostructures of 5 mM concentration exhibited better



signal compared to 10 mM as their leaves are having pentagon like structures with sharp edges.

#### 4.4.2.7. The topography transformation mechanism



**Figure 4.15.** SEM images of Cu-Ag hemi-mesoparticles obtained by dipping Cu in 5 mM  $\text{AgNO}_3$  at different time intervals (A-C) 5 min, (D-F) 30 min, (G-I) 1 h and (J-L) 2 h.

In order to understand how the nanostructures evolved, we monitored the morphological transformations of Ag nanoparticles as a function of time. Figure 4.15 shows the SEM images of Ag particles formed using 5 mM  $\text{AgNO}_3$  at

different time intervals. At 1-5 min reaction time, only particles of smaller dimensions are obtained. As time proceeds, one could see the morphological transformation from small particles to larger leaf-like structures. At 30 min, the elongated leaf-like structure starts to grow and form multi-dimensional edges by depositing more number of nanoparticles on the blade of leaves. When the reaction time reached 1 h, the formed nanoparticles are arranged in a more defined manner to attain walking fern-like structures. At 2 h, they become well-ordered walking fern-like morphology and widely distributed all over the surface.

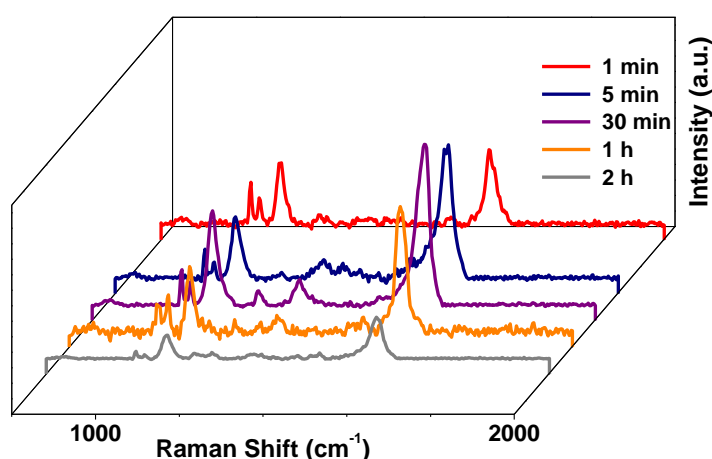


**Figure 4.16.** SERS spectra of MPBA on Cu-Ag hemi-mesoparticles obtained by dipping Cu in 5 mM AgNO<sub>3</sub> at different time intervals.

Figure 4.16 represents the effect of morphological evolution on the SERS activity of Cu-Ag substrates at 5 mM concentration. Among all, the lowest signal intensity was noted for the nanostructures formed at 1 min and 2 h. With increasing the reaction time, such as at 5-30 min there was a steady increase in the Raman signal enhancement. Further increasing the time to 1h and 2h, SERS activity starts



decreasing due to the formation of more rounded shape pinna of leaf instead of the hexagon shape.

#### **4.4.3. Fabrication of Cu-Au substrates**

Inspiring from the previous Cu-Ag SERS substrate results, the following experiments were conducted with  $\text{HAuCl}_4$  solution to improve the signal enhancement on Cu-Au substrates. The Cu substrates were dipped in different concentrations of  $\text{HAuCl}_4$  solutions to develop Cu-Au substrates. As the concentration of Au (III) increases the number of small particles deposited onto the substrates to form urchin-like morphology.

##### **4.4.3.1. The effect of concentration on Cu-Au substrates**

Figure 4.17 shows SEM images of Au plasmonic substrates obtained by dipping etched brass foils in varying concentrations of  $\text{HAuCl}_4$  for a fixed period of time, 5 min. Compared to the Ag galvanic displacement reaction Au yielded different morphologies. At 1 mM concentrations, surfaces of Cu substrate are filled with a large percentage of small particles (< 50 nm) and a minor fraction of bigger particles (~ 250 nm). In addition to this, budding small flower-like features are also noted. In 5 mM concentration, due to the availability of more number of  $\text{Au}^{3+}$  ions more nanoparticles are formed and further grown with a different layer like structures and sea corals like morphology. Mainly, we noted the growth of flake/coral-like structures above the underlying small particles. Onto which there occurs further growth of small ensembles of nanoparticles thus resembling that of flower buds. At higher concentrations such as 10 mM, the well-developed sea

urchins morphology was observed and is completely distributed throughout the Cu substrate.

Figure 4.18 represents SERS studies of Cu-Au substrates prepared at varying concentrations of  $\text{HAuCl}_4$ . Similar to Ag, the plasmonic nanostructures grown with Au showed considerably good SERS activity. For example, at lower concentrations, the integrated intensity of  $1590\text{ cm}^{-1}$  band of MPBA is  $1 \times 10^3$ ,  $3.5 \times 10^3$  respectively for 0.5 mM and 1 mM. The trend increases linearly with concentration up to 5 mM and afterward, a decrease in the intensity was noted. Whereas, those prepared with 3 mM concentration showed good enhancement in Raman signal with the intensity of  $\sim 2.4 \times 10^4$

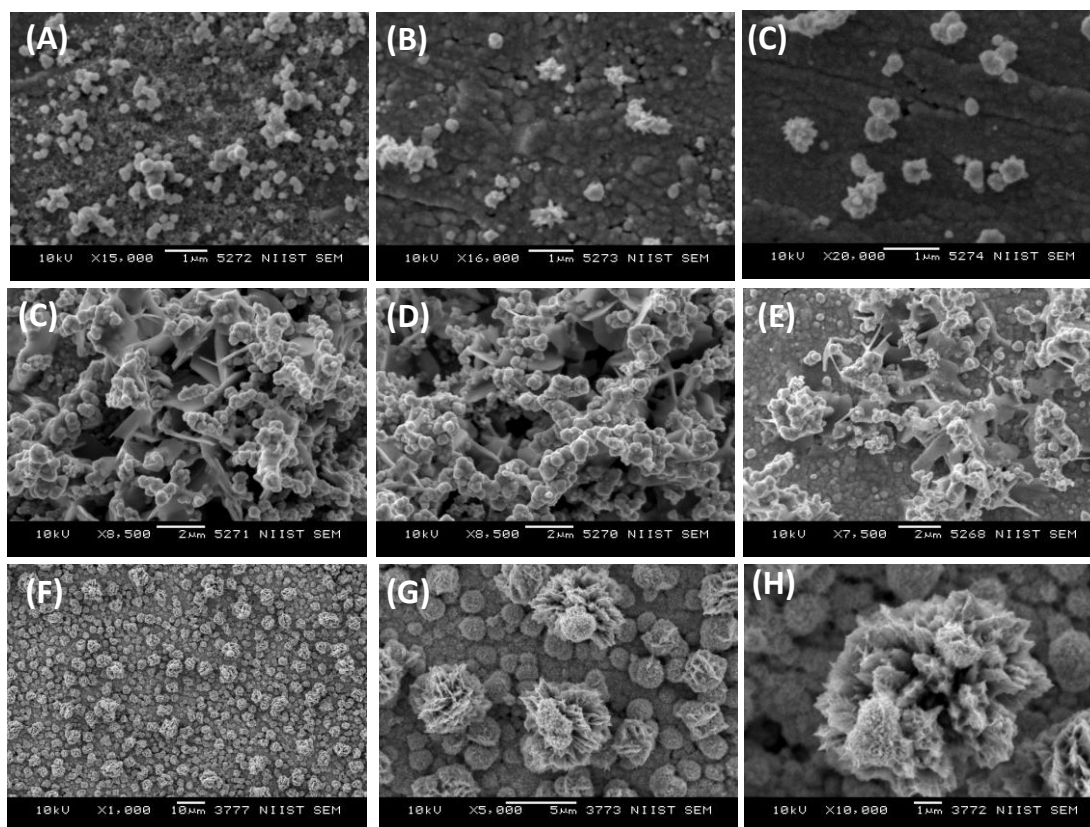


**Figure 4.17.** SEM images of gold hemi-mesoparticles obtained by dipping Cu substrates for 5 minutes in different concentrations of  $\text{Au}^{3+}$  (A-C) 1 mM, (D-E) 5 mM, (F-H) 10 mM.

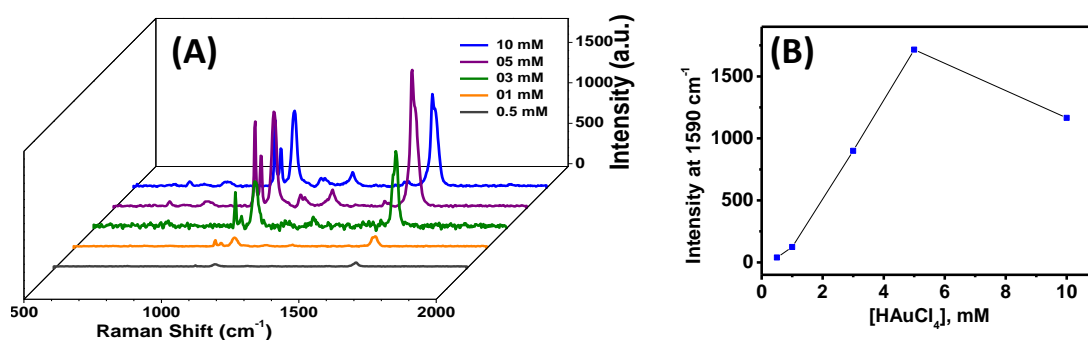


**Figure 4.18.** (A) SERS spectra of MPBA molecules on plasmonic substrates prepared by dipping etched brass in different concentrations of HAuCl<sub>4</sub> and (B) The plot showing the variation of intensity change of MPBA Raman bands centered at 1590 cm<sup>-1</sup> as a function of [HAuCl<sub>4</sub>].

which is 3 times higher and 5 mM concentration exhibited the highest enhancement  $\sim 5.2 \times 10^4$  (6 times). This is because of the presence of large number of hotspots throughout the substrate. Further increasing the concentration to 10 mM did not much influence the signal intensity but a slightly decreased to  $\sim 3.7 \times 10^4$  due to the decrease of hot spots in the fully grown urchin-like structure. The experimentally measured UV-Vis absorption spectra of Au mesoparticles having different morphologies are shown in figure 4.19. The nanostructures formed with 1 mM concentration exhibited an absorption band at 550 nm and have the relatively lower optical density of 0.005. With an increase in the concentration of Au<sup>3+</sup> ions in the reaction medium, generally a continuous blue shift and increase in the optical density were noted. For example, the nanostructures formed with 3 mM and 5 mM concentration exhibited optical densities of 0.01 and 0.017 and absorption maximum 540 nm and 530 nm respectively. However, at higher concentrations (e.g. 10 mM) though there was further slight increase in the optical density (0.02), the absorption maxima underwent red shift to 555 nm with the appearance of broad absorption tailing to NIR range. The increase in optical density suggests the reduction of more and more Au<sup>3+</sup> ions and hence the formation of more Au nanoparticles.

Whereas, the presence of absorption tailing to NIR range is an indication of formation of bigger (above micrometer range) particles and is in accordance with the obtained morphologies in the corresponding SEM images.

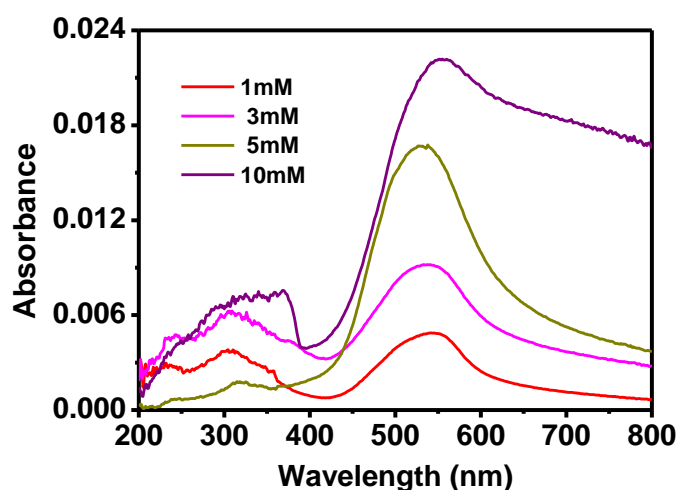


**Figure 4.19.** The absorption spectrum of gold hemi-mesoparticles obtained by dipping Cu substrates for 5 minutes in different concentrations of  $Au^{3+}$ .

#### 4.4.3.2. The effect of time on Cu-Au substrates

At higher concentrations such as 10 mM, the mesoparticle formation happens with a faster rate compared to low concentrations due to the availability of a large number of  $Au^{3+}$  ions present in the solution. For studying the effect of time, we monitored the morphological evolution of nanostructures at a longer period, 3h (Figure 4.20). For 10 mM concentrations, there was not much difference in the morphology between the 5 min and 3 hours reaction except that more percentage of fully developed teddy tear sunflower are noted in the latter case. At low concentrations, (1 mM) with increase in the reaction time from 5 min to 3 h more percentage of bigger particles are formed. In the case of 5 mM concentration, 3 h reaction yielded entirely different morphology when compared to that of 5 min

reaction. Mainly, sea urchins like structures having the size in the range 4-5  $\mu\text{m}$  are evident from the SEM images. Similarly, 3 mM concentration also yielded urchin-like structures, however their size is relatively small ( $< 3 \mu\text{M}$ ) as compared to 5 mM concentration.

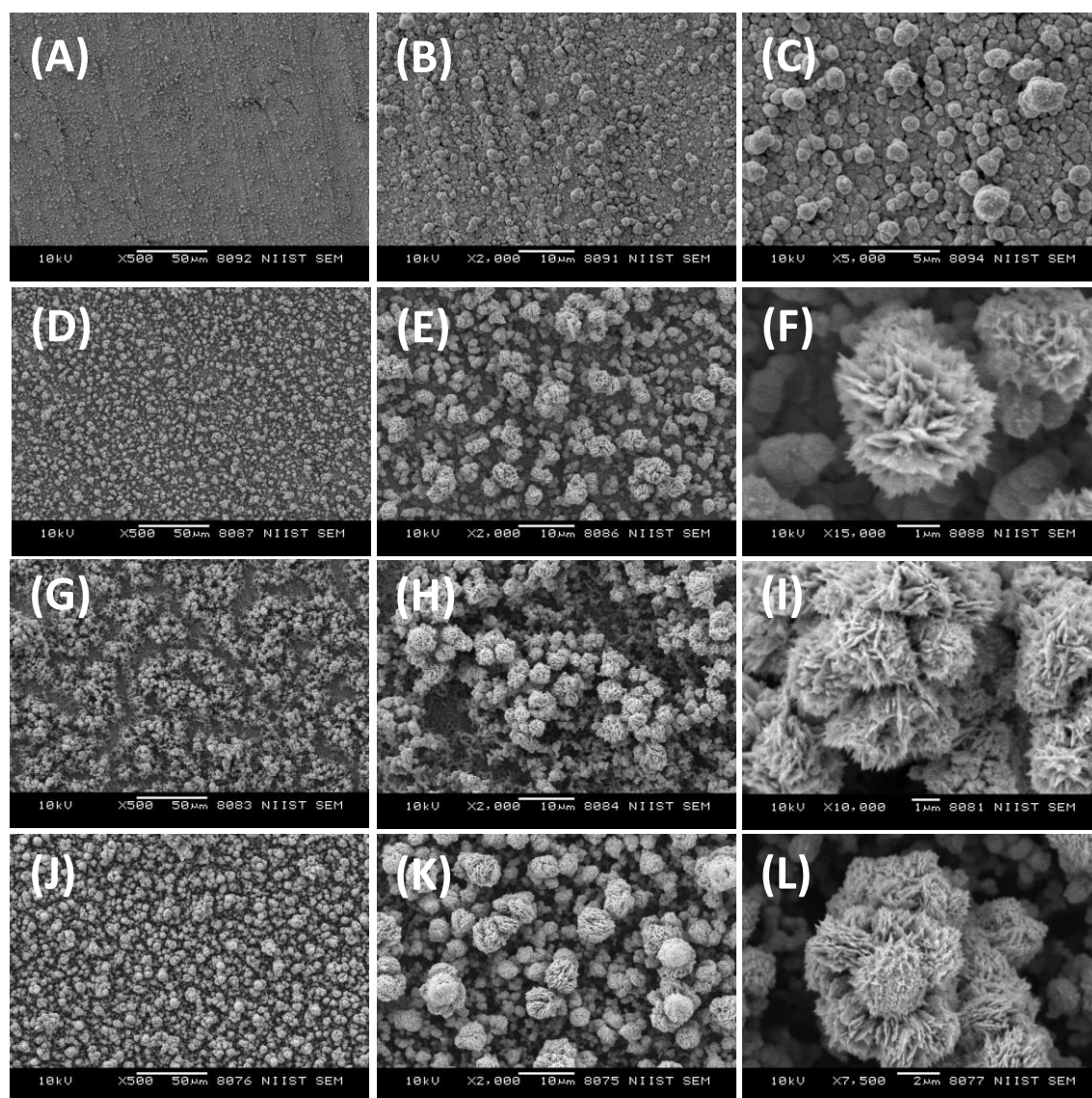


**Figure 4.20.** SEM images of gold mesoparticles obtained by dipping Cu substrates for 3 h in different concentrations of  $\text{Au}^{3+}$ . (A-C) 1 mM, (D-F) 3 mM, (G-I) 5 mM and (J-L) 10 mM.

Among these, the nanostructures prepared with 1 mM exhibited the highest Raman signal intensity ( $3.4 \times 10^3$ ). However, this is almost one order of magnitude smaller than that obtained for 5 mM, while those obtained with 5 min, 3 mM reaction exhibited almost similar SERS activity. The lowest signal intensity was noted for 10 mM, 3h reaction which is even less than those of 5 mM. This can be attributable to their relatively bigger sizes.

For studying the effect of time, SEM and SERS studies of the substrates obtained after 3h of the reaction were carried out. From the SEM images of Au mesoparticles depicted in figure 4.19, it is clear that well-defined morphologies were yielded for 10 mM and 5 mM concentrations than 1 mM. At 1 mM concentration, nanoparticle formation and their overgrowth start to appear, and from 3 mM concentration onwards mesoparticles attain urchins like morphology and clearly visible throughout the substrates. The corresponding SERS studies showed the first raise and then a slight decrease in the enhancement as the concentration used for Cu-Au substrate was varied from 1-10 mM. Thus, higher Raman signal strengths are observed for urchins having size  $\sim 1 \mu\text{m}$  whereas underdeveloped and overgrown bigger urchins exhibit lower intensity (size  $> 5 \mu\text{m}$ ) (Figure.4.21).

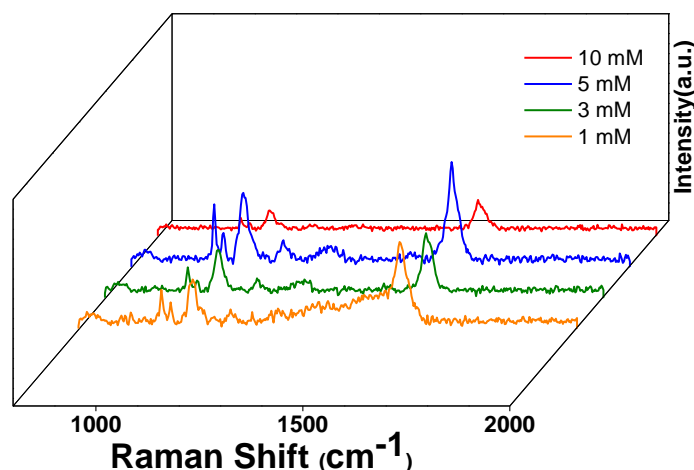


**Figure 4.21.** SERS spectra of Cu-Au hemi-mesoparticles obtained by dipping Cu substrates for 3 h in  $\text{HAuCl}_4$  of varying concentrations.

#### 4.4.3.3. The topography transformation mechanism

In order to study the different stages of Au mesostructure formation, we monitored the morphological transformations as a function of time. Figure 4.22 shows the SEM images of Au particles formed with 5 mM  $\text{HAuCl}_4$  at different time intervals. In the initial stages of the reaction (1-5 min), we noted mainly the appearance of small but less densely populated particles over the underlying layer like structures. As time progress, more and more particles are formed and are spread over the entire surface. It could be seen that density of particles is higher for 1-hour reaction when compared to that of 30 minutes. Further, aggregates of a group of smaller particles resembling that of a flower bud start to appear as the reaction time proceeds to 1 h. Further growth of these buds into well-defined sea-urchin-like morphology occurs above this time period, i.e 2 h.

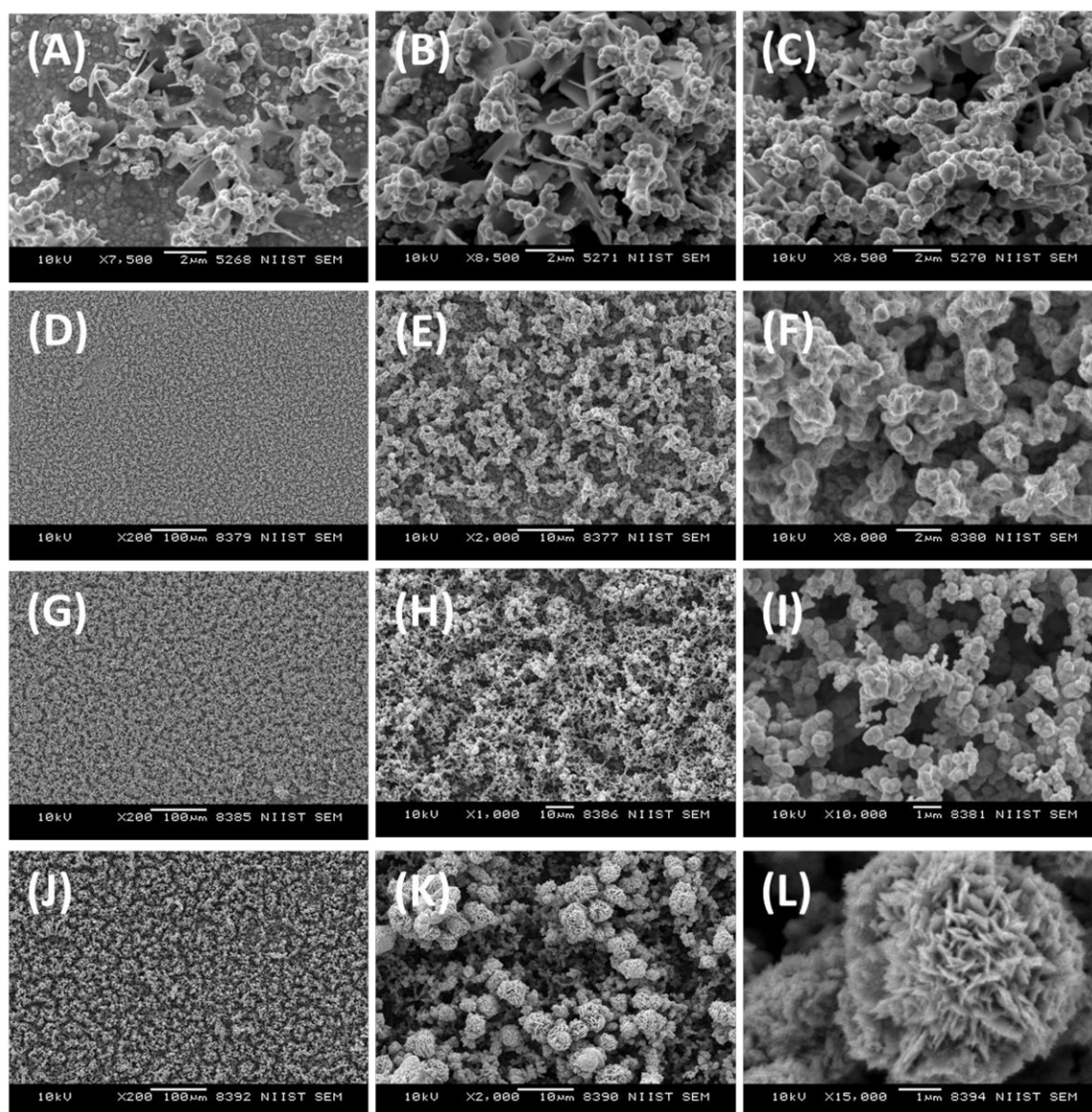


**Figure 4.22.** SEM images of gold mesoparticles obtained by dipping Cu substrates in 5 mM  $Au^{3+}$  for different time interval- (A-C) 5 min, (D-F) 30 min, (G-I) 1 h and (J-L) 3 h.

#### 4.4.4. The growth mechanism of mesoparticles formation

The growth mechanism for the formation of hemi-mesoparticles can divide into four stages. In the first stage, the Ag or Au ions in their solutions are reduced into their atoms by Cu through galvanic displacement reaction (scheme 4.4). As the reaction proceeding, the concentration of Ag or Au atoms on the surface of Cu foil gradually increases. In the second stage, when the concentration of the atoms



exceeds the supersaturation point they tend to aggregate to form a stable nucleus through mass transfer. Thus, enormous numbers of nanoparticles are formed on the surface of the Cu foil. In both the cases of Ag and Au mainly spheroid particles are formed at the initial stages of the reaction. Also, anisotropic nanoparticles are formed at a faster rate for Ag than Au. This is evident from the presence of spike-like morphologies at the initial stages of the growth process which immediately transforms to leaf-like morphologies. The major peaks obtained in the XRD data are those corresponding to (111) planes of fcc crystal lattices. Thus, during galvanic displacement the preferential growth is along (111) direction.

#### 4.4.5. Uniformity of SERS substrate

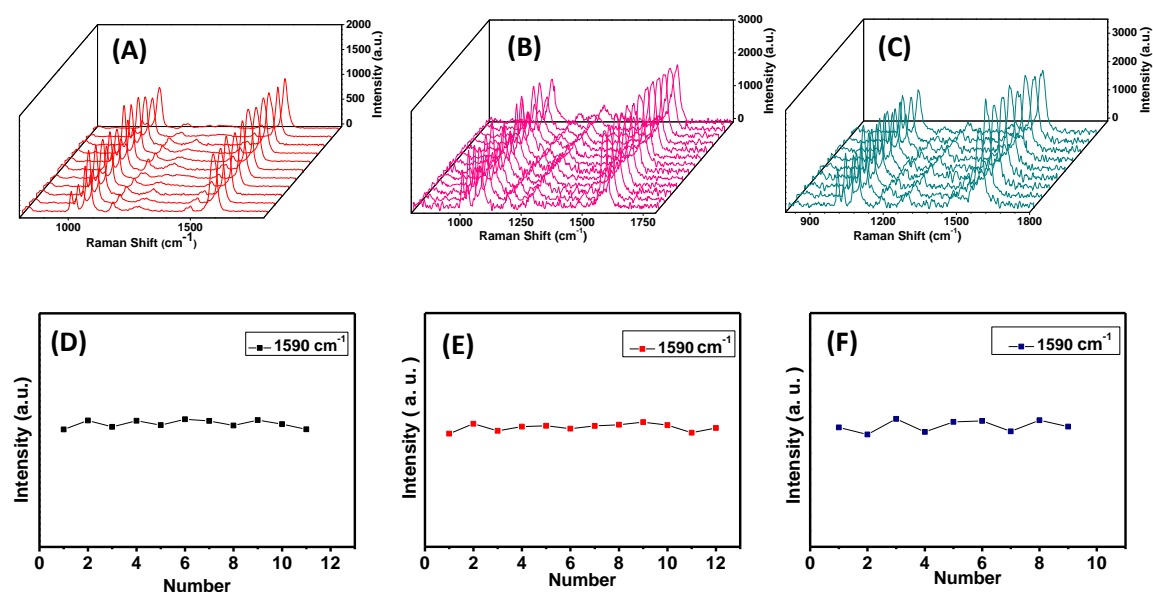


**Figure 4.23.** SERS spectra of MPBA on (A) Cu (B) Cu-Ag and (C) Cu-Au at different positions and (D-F) Their corresponding intensity change of MPBA Raman bands centered at  $1590\text{ cm}^{-1}$ ; substrate preparation condition  $5\text{ mM AgNO}_3$  or  $\text{HAuCl}_4$  and the dipping time 5 min

The uniformity of the substrate is one of the essential parameters for generating quantitative SERS data. Nonuniformity leads to poor reproducibility of

the SERS signals. In order to check this aspect, the prepared substrates were first dipped in a 10 mM ethanolic solution of MPBA (2 mL) for 2 min. These substrates were then thoroughly washed to remove any unbound/physisorbed molecules. Figure 4.23 represents illustrative examples of Raman spectra collected from randomly selected points of each of these SERS substrate. It can be seen that the Raman spectra of MPBA are quite similar in terms of spectral profile, peak position, and intensity. For example, figure 4.23 (D-F) represents the variation of intensity at  $1590\text{ cm}^{-1}$ , the most intense Raman band of MPBA. A close analysis of this reveals that a maximum of 15% variation is observable for peak intensity from point to point.

#### **4.4.6. Application**

To illustrate the potential of the current system in disease diagnosis, we investigated the efficiency of the currently developed SERS substrates in quantitative estimation of creatinine, a protein metabolite which serves as a biomarker for renal clearance test (i.e. kidney functioning). The normal concentrations of creatinine in the blood are  $\sim 0.6 - 1.2\text{ mg/dl}$  and  $\sim 0.5 - 1.1\text{ mg/dl}$  in adult males and females respectively, from which daily  $\sim 500-2000\text{ mg}$  of it is excreted through urine. Thus, accounting the fact that an adult male pass  $\sim 1-2\text{ L}$  of urine in a day, the minimum concentration of creatinine in urine of a healthy person can be calculated to be  $\sim 25\text{ mg/dL}$ . Presently, at diagnostic centers, these are estimated through well known Jaffe reaction. It is a colorimetric-kinetic technique involving the mixing of extracted body fluid with picric acid and NaOH which yield yellow-orange complex (Scheme 4.5). The concentration of creatinine is then determined by measuring absorbance at  $505\text{ nm}$ . The main disadvantage of this

techniques is (i) interference from noncreatinine chromogens which yield similar reaction and coloured complex and (ii) high dependency on the relative concentration of reagents as well as pH of the medium. These lead to imprecise data and wrong diagnosis. Therefore, it is highly required to develop alternative detection and quantification strategies.



**Scheme 4.2.** Schematic representation of Jaffe's test.

In this context, we thought of developing strategies based on Raman spectroscopy, as it provides fingerprint information and hence is highly specific. The normal concentrations of creatinine in blood and urine are ~ 0.1 mM and ~ 2.2 mM respectively (vide supra) which makes it difficult to detect through normal Raman spectroscopy and one need to implement enhancement methodologies. Recently, SERS has evolved as a simpler alternative platform for many points of care applications. Herein we try to explore the utility of these newly prepared SERS substrates for the sensing of creatinine.

#### 4.4.6.1. SERS studies of creatinine solutions in water

Figure 4.24 represents the comparison of normal Raman spectrum and SERS of creatinine. The major Raman peaks corresponding to bond vibrations in creatinine were evident in all of them. The peaks at 681, 838, and 900  $\text{cm}^{-1}$  are assigned to the symmetric stretching of C–N, C–NH<sub>2</sub> and C=O of creatinine molecule and were clearly visible in both normal and SERS modes of acquisition. To estimate the potential capability of SERS substrate fabricated herein for renal

clearance test, we dissolved varying quantities of creatinine in water and Raman spectral measurements were carried out under identical conditions. The typical instrument parameters were 633 nm, 10 mW laser, 10 sec CCD integration time, 20X objective lens and the data averaged over 10 acquisitions. It could be noted that even at very low concentrations (e.g. 1 nM) the current SERS substrates are capable of yielding characteristic Raman spectrum of creatinine. This indicates the high sensitivity offered by them. A plot of concentrations vs intensities, both in logarithmic scale ( $\log C$  and  $\log I$ ) gave a nearly linear correlation with a high correlation coefficient  $R^2$  value of 0.960. These studies clearly suggest the potential of the current system in quantitative measurements.

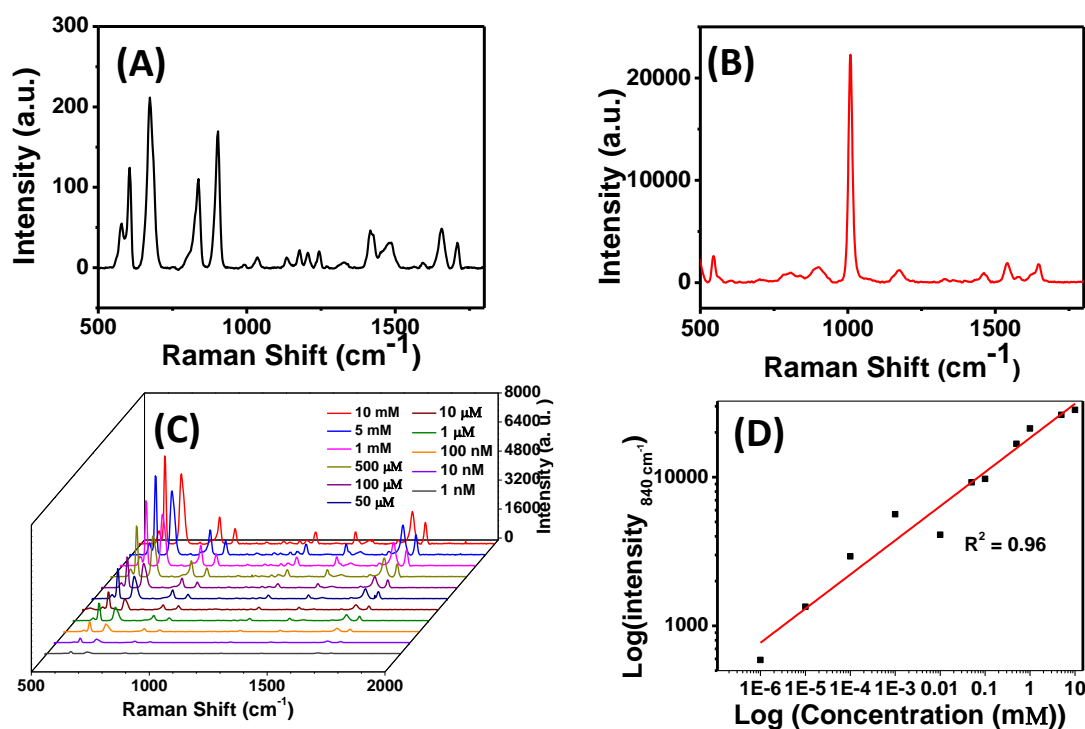


**Figure 4.24.** (A, B) The solid-state Raman spectrum of (A) creatinine, (B) urea. (C) SERS spectra of different concentrations of creatinine in water and (D) the plot illustrating the linear correlation between  $\log(\text{intensity})$  and  $\log(\text{concentration})$ .

#### 4.4.6.2 SERS studies of artificial urine

To evaluate the detection of creatinine in complex mixtures, we prepared artificial urine in the lab and by adding the creatinine concentrations from 5 mM – 1 nM. The averaged SERS spectra are shown in figure 4.25.

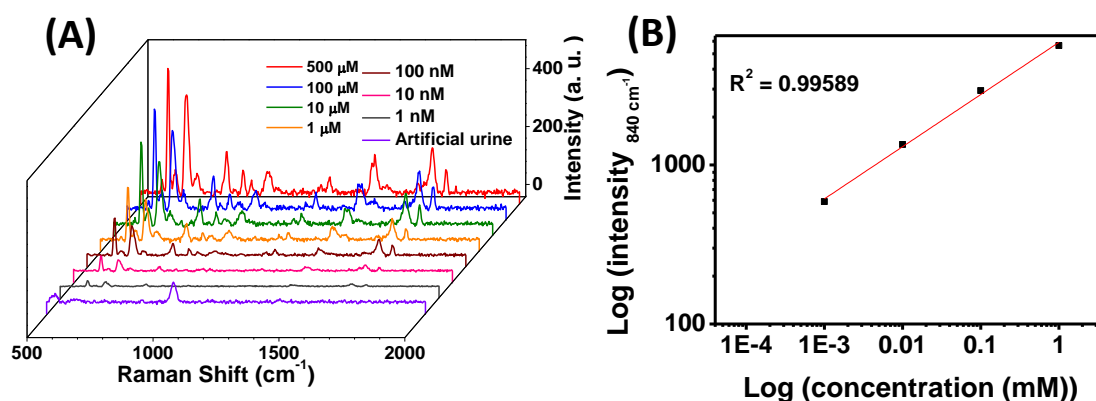


**Figure 4.25.** (A) SERS spectra of artificial urine containing different concentrations of creatinine and (B) the plot illustrating the linear correlation between  $\log(\text{intensity})$  and  $\log(\text{concentration})$ .

The main content of urine is urea which has got Raman peaks at 544, 807, 901, 1009, 1175, 1462, 1541, 1646 cm<sup>-1</sup>, of which the peak at 1006 is having the highest intensity and serve as signature Raman peak for its quantitative analysis. It can be noted that these peaks do not interfere with that of creatinine which allows their estimation without many complications. At different concentrations of creatinine, peak at 1006 cm<sup>-1</sup> shows a low-intensity variation from substrates to, which indicates the reproducibility and further potential for practical applications. In addition, it was observed that with an increase in concentration of creatinine, the major peaks at 840 artificial urine cm<sup>-1</sup> and 900 cm<sup>-1</sup> of creatinine got intensified. A plot of concentrations vs intensities, both in logarithmic scale ( $\log C$  and  $\log I$ )

gave a nearly linear correlation with a high correlation coefficient  $R^2$  value of 0.995.

#### **4.5. Conclusion**

In summary, we illustrated the utility of chemical etching and galvanic displacement reaction for the preparation of hierarchical Ag and Au mesoparticles. In addition to the wide and cheap availability of brass, the simplicity of the procedure allows the preparation of high-quality SERS substrates as and when required with minimal investments. The observed high uniformity and SERS performance illustrate their potential in practical applications. Though the initial nanostructured Cu itself qualify as ideal SERS substrates, their performance can be further improved through simple galvanic displacement reaction. The detailed studies presented here show that surface topographies can be well-tuned by controlling both concentration and reaction time. Further, by combining advantages of fingerprinting ability of Raman spectroscopy and signal enhancement through SERS, a reagent-free method to detect and quantify creatinine from urine was demonstrated. The studies conducted herein demonstrated good linearity for creatinine water solutions and the detection limit can be as low as 1 nM. Together with this, the availability of portable and cost-effective Raman spectrometer can really elevate their potential for point of care diagnostic applications.

#### **4.6. References**

- (1) Sapsford, K. E.; Bradburne, C.; Delehanty, J. B.; Medintz, I. L. *Materials Today* **2008**, *11*, 38-49.

- (2) Sikirzhytski, V.; Virkler, K.; Lednev, I. K. *Sensors* **2010**, *10*, 2869-2884.
- (3) Regan, J. F.; Makarewicz, A. J.; Hindson, B. J.; Metz, T. R.; Gutierrez, D. M.; Corzett, T. H.; Hadley, D. R.; Mahnke, R. C.; Henderer, B. D.; Breneman Iv, J. W.; Weisgraber, T. H.; Dzenitis, J. M. *Analytical Chemistry* **2008**, *80*, 7422-7429.
- (4) Wachsmann-Hogiu, S.; Weeks, T.; Huser, T. *Current Opinion in Biotechnology* **2009**, *20*, 63-73.
- (5) Camp, C. H.; Lee, Y. J.; Heddleston, J. M.; Hartshorn, C. M.; Hight Walker, A. R.; Rich, J. N.; Lathia, J. D.; Cicerone, M. T. *Nature Photonics* **2014**, *8*, 627-634.
- (6) Jeon, T. Y.; Kim, D. J.; Park, S.-G.; Kim, S.-H.; Kim, D.-H. *Nano Convergence* **2016**, *3*, 18.
- (7) Byun, K.-M. *Journal of the Optical Society of Korea* **2010**, *14*, 65-76.
- (8) Mosier-Boss, P. A. *Nanomaterials* **2017**, *7*, 142.
- (9) Reguera, J.; Langer, J.; de Aberasturi, D. J.; Liz-Marzan, L. M. *Chemical Society Reviews* **2017**, *46*, 3866-3885.
- (10) Bich, H. N.; Van Hieu, N.; Hong, N. T. *Advances in Natural Sciences- Nanoscience and Nanotechnology* **2016**, *7*.
- (11) Solís, D. M.; Taboada, J. M.; Obelleiro, F.; Liz-Marzán, L. M.; García de Abajo, F. J. *ACS Photonics* **2017**, *4*, 329-337.
- (12) Dendisova-Vyskovska, M.; Prokopec, V.; Clupek, M.; Matejka, P. *Journal of Raman Spectroscopy* **2012**, *43*, 181-186.
- (13) Xie, X.; Pu, H.; Sun, D.-W. *Critical Reviews in Food Science and Nutrition* **2017**, 1-14.

- (14) Ko, H.; Singamaneni, S.; Tsukruk, V. V. *Small* **2008**, *4*, 1576-1599.
- (15) Israelsen, N. D.; Hanson, C.; Vargis, E. *The Scientific World Journal* **2015**, *2015*, 12.
- (16) Wang, A. X.; Kong, X. M. *Materials* **2015**, *8*, 3024-3052.
- (17) Suresh, V.; Ding, L.; Chew, A. B.; Yap, F. L. *ACS Applied Nano Materials* **2018**, *1*, 886-893.
- (18) Liu, L.; Zhang, Q.; Lu, Y. S.; Du, W.; Li, B.; Cui, Y. S.; Yuan, C. S.; Zhan, P.; Ge, H. X.; Wang, Z. L.; Chen, Y. F. *Aip Advances* **2017**, *7*, 085103.
- (19) Petti, L.; Capasso, R.; Rippa, M.; Pannico, M.; La Manna, P.; Peluso, G.; Calarco, A.; Bobeico, E.; Musto, P. *Vibrational Spectroscopy* **2016**, *82*, 22-30.
- (20) Abu Hatab, N. A.; Oran, J. M.; Sepaniak, M. J. *ACS Nano* **2008**, *2*, 377-385.
- (21) Chu, H. O.; Song, S. G.; Li, C.; Gibson, D. *Coatings* **2017**, *7*, 26.
- (22) Wu, D. Y.; Li, J. F.; Ren, B.; Tian, Z. Q. *Chemical Society Reviews* **2008**, *37*, 1025-1041.
- (23) Kahraman, M.; Daggumati, P.; Kurtulus, O.; Seker, E.; Wachsmann-Hogiu, S. *Scientific Reports* **2013**, *3*, 3396.
- (24) Zhang, C. P.; Yi, P. Y.; Peng, L. F.; Lai, X. M.; Chen, J.; Huang, M. Z.; Ni, J. *Scientific Reports* **2017**, *7*, 39814.
- (25) Xia, X. H.; Wang, Y.; Ruditskiy, A.; Xia, Y. N. *Advanced Materials* **2013**, *25*, 6313-6333.



- (26) Lu, X.; Chen, J.; Skrabalak, S. E.; Xia, Y. *Proceedings of the Institution of Mechanical Engineers, Part N: Journal of Nanoengineering and Nanosystems* **2007**, *221*, 1-16.
- (27) Zhang, W.; Yang, J.; Lu, X. *ACS Nano* **2012**, *6*, 7397-7405.

## **List of Publications**

1. Shape controlled synthesis of multi-branched gold nanocrystals through a facile one-pot bifunctional biomolecular approach **M. Sajitha**, A. Vindiyasarumi, A. Gopi and K. Yoosaf; *RSC Adv.*, **2015**, 5, 98318-98324
2. Making Gold Nanorod Synthesis Greener with Natural Antioxidants and its Theranostic Application, **M. Sajitha**, N. Narayanan, K. Cottayil, R. B. Nellyil, K. K. Maiti\*, K. Yoosaf\*; Manuscript under submission.
3. Bimetallic Hetero Structures as SERS Substrate for Creatinine Sensing, **M. Sajitha**, R. B. Nellyil and K. Yoosaf \*; Manuscript under preparation.
4. Multi-branched Gold Nanocrystals for Photo- based Diagnostic and Therapeutic Applications, **M. Sajitha**, S. Giridharan, K. K. Maiti\* and K. Yoosaf \*; Manuscript under preparation.
5. Surface-Enhanced Raman Scattering (SERS) Substrate Based on Large-Area with High SERS Uniformity, **M. Sajitha**, A. Soman, K. N. N. Unni\* and K. Yoosaf \*; Manuscript under preparation.

### List of Posters Presented at Conferences

1. *Easy Fabrication of Plasmonic Sensors for Point of Care Diagnostics* **Sajitha Manikandan**, Renjith B. Nellyil and Karuvath Yoosaf; **P06**, Page No.38. **NanoBiotech 2018** organized by IISER-TVM and CSIR-NIIST, Thiruvananthapuram in 2018.
2. *Low Cost SERS Substrates for Reagent Free Creatinine Sensing*, **Sajitha Manikandan**, Renjith B. Nellyil and Karuvath Yoosaf; **P105**, Page No.149, **8<sup>th</sup> East Asia Symposium on Functional Dyes and Advanced Materials** organized by CSIR-NIIST, Thiruvananthapuram in 2017 .
3. *Spectroscopic and Microscopic Investigation of Au Nanostar Formation*; **Sajitha Manikandan**, A. Vindhyasarumi and Karuvath Yoosaf. **P083**, Page No. 127. **Asian Photochemistry 2014**, IISER-TVM and CSIR-NIIST, Thiruvananthapuram in 2014.
4. *Morphological Transformation of Au Nanoparticles to Au Nanostars via In Situ Formed Nanoseeds*; **Sajitha Manikandan**, A. Vindhyasarumi and Karuvath Yoosaf. **9<sup>th</sup> JNC research conference on chemistry of materials**, IISER-TVM and CSIR-NIIST, Thiruvananthapuram in 2014.

### List of Orals Presented at Conferences

1. *Making Gold Nanorod Synthesis Greener with Natural Antioxidants and its Theranostic Application*; **Sajitha M.**, N. Narayanan, S. Chelakkara, K. K. Maiti, K. Yoosaf. **SP-13**, Page No.91. **3<sup>rd</sup> International Conference on Advanced Functional Materials**, CSIR-NIIST, Thiruvananthapuram in 2019.